Characterization of Major Intermetallic Phases in solidified Al-xSi-yFe-zSr (x=2 to 12.5wt%, y=0 to 0.5wt% and z=0 and 0.02wt%) alloys.

By

Anton Gorny, B.Sc., M.Sc.

A Thesis

Submitted to the School of Graduate Studies

in Partial Fulfillment of the Requirements

for the Degree of

Doctor of Philosophy

McMaster University

DOCTOR OF PHILOSOPHY (2012) **McMaster University**

(Mechanical Engineering) **Hamilton, Ontario**

TITLE: **Characterization of Major Intermetallic Phases in solidified Al-xSi-yFe-zSr (x=2 to 12.5 wt%, y=0 to 0.5 wt% and z=0 and 0.02 wt%) alloys.**

AUTHOR: **Anton Gorny**

B. Sc (Technion, Israel Institute of Technolgy, Haifa, Israel)

M.Sc. (Technion, Israel Institute of Technolgy, Haifa, Israel)

SUPERVISORS: **Dr. Sumanth Shankar**

Department of Mechanical Engineering

NUMBER OF PAGES: xiii**, 144**

To My Parents…

Abstract

Al-Si cast alloys have been in the fore-front of commercial casting application for more than a century. Iron containing intermetallic phases that evolve during the solidification of these alloys play a major role in the resultant mechanical properties and performance of the cast products. Changes in alloy composition and casting parameters significantly alter the evolution of the Al-Si-Fe intermetallic phases. There was a lack of clear understanding of the complex relationships between the solidification parameters and nature intermetallic phases in these alloys. Current thermodynamic model predictions for the nature of these intermetallic phases in the Al corner of the Al-Si-Fe ternary system are strikingly different from the experimental results in this project. Trace levels of Sr (about 0.02wt%) are typically added to the Al-Si commercial alloys to effect a morphological modification of the eutectic phases to improve the properties and performance of the cast products.

The nature of the Fe containing intermetallic phases have been characterized as a function of alloy composition (Si, Fe and Sr) and cooling rates during solidification. There was an anomalous evolution of the τ_5-Al_8Fe_2Si phase which transformed into the τ_6-$Al_9Fe_2Si_2$ phase during solidification at lower cooling rates and higher Fe concentration in the alloy, alike. Further, Sr addition to these alloys prevented the evolution of the τ_5 phase and promoted the evolution of an unidentified $Al_5Fe_2Si_3$ phase which was noted as κ in this dissertation; the κ phase also transformed into the τ_6 phase at lower cooling rates and higher Fe concentration in the alloy, alike.

Acknowledgements

I would like to thank my supervisor Dr. Sumanth Shankar for his guidance, patience, valuable support. Through the years of my PhD project after several successes and misfortunes in the research, I was finally able to make an original contribution to science which I am proud of and grateful for.

I would also like to thank my supervisory committee meeting members, Dr. Dmitri V. Malakhov and Dr. Hatem Zurob for their guidance, patience and numerous insightful academic discussions.

I would also like to thank my colleagues at the Light Metal Casting Research Centre (LMCRC) for all their help and insightful discussions as well as critiquing several of my theories. Special thanks go to my colleagues Dr. Xiaochun Zeng and Dr. Manickaraj Jeyakumar for their support.

I would like to thank Doug Culley and Ed McCaffery of the Department of Materials Science and Engineering for their patient assistance in metallography and chemical analysis.

Table of Contents

List of Figures

List of Tables

CHAPTER 1. NOMENCLATURE

1.1 ENGLISH ACRONYMS

Text Notation	Description
SEM	Scanning Electron Microscope
SE	Secondary Electrons
SEI	Secondary Electron Image
BSE	Back Scattered Electrons
TEM	Transmission Electron Microscope
EDX	Energy Dispersive X-Ray Spectrum
FIB	Focused Ion Beam microscope
KeV	Kilo Electron Volts $eVX10^3$
XRD	X-Ray Diffraction
nm	nanometer
μm	micrometer
XRF	X-Ray Fluorescence
2θ	Two θ Bragg angle

1.2 LIST OF INTERMETALLIC PHASES

Phase Notation	Phase Stoichiometry
θ	$Al_{13}Fe_4$
τ_5	Al_8Fe_2Si
τ_6	$Al_9Fe_2Si_2$
τ_4	Al_3FeSi_2
τ_7	$Al_3Fe_2Si_3$
κ	$Al_5Fe_2Si_3$

CHAPTER 2. INTRODUCTION

The thermal data during solidification and microstructure of 168 alloys based on the 3xx series of Al-7 wt% Si casting alloys with compositional variations of 0 to 0.5 wt% Fe, 0 to 0.55wt% Mg and 0 to 4 wt% Cu with three levels of trace additions of Ti and Sr in each alloy composition were investigated at the onset of this project. There were several apparent anomalies in the nature of the Fe containing intermetallic phases in the microstructure of these alloys along with anomalies in the morphology of the eutectic Si phase. The initial goal of this project was to evaluate the anomalies in the evolution of the Fe containing intermetallic phases during solidification of these alloys. The first two years of this project was spent on carrying out solidification experiments, microscopy (optical and SEM/EDX), X-Ray diffraction of powder samples prepared by preferential dissolution of the primary Al phase matrix using both Cu K_α radiation and high energy synchrotron bema source and analysis of TEM sample foils prepared by FIB technique. The initial set of alloys prepared were of Al-xSi-yFe-zSr (x=5,7,12.5; y=0.05,0.25,0.5 and z=0,0.01,0.03,0.05 and 0.1) composition ranges (all in weight %) and solidified at three uniquely different cooling rates of the liquid during solidification. The characterization of the intermetallic phases in these alloys was not repeatable or reproducible even within the same alloy composition and cooling rate during solidification. After about two years into the project, it was evident that a critical factor was overlooked in this study and that was the homogenization of the initial alloy melt at a high superheat temperature above the liquidus temperature. In typical commercial casting practices, these alloy melts are held at a high temperature for several hours and resulted in a homogeneous mixture of alloying elements. The Fe containing intermetallic phases that existed in the initial raw materials such as the Al ingots and Al-Fe master alloy dissolved in the alloy melt at a very sluggish rate and they significantly influenced the nature of intermetallic phases that evolved during solidification. A review of the background literature on this topic also suggested several contradicting evidences presented for the characteristics of these intermetallic phases. Hence, the project was re-started with the various alloys and solidification rates so that the initial alloy liquid was held at 1093 K ± 5K (820 ^oC) instead of the conventional 993 K (720 ^oC) for a period of time greater than two hours to enable compositional homogenization of the alloy liquids prior to the solidification.

The characterization of solidified samples was carried out through microscopy (optical, SEM/EDX and TEM/FIB), thermal analysis during solidification and x-ray diffraction using both the synchrotron and Cu radiation sources. The results fell into a systematic order that presented the specific and predictable anomalies in the evolution of the Fe based intermetallic phases in these alloys.

The results suggest that contrary to popular belief, the τ_5-Al_8Fe_2Si phase first evolved during the solidification of the Al-xSi-yFe (x=2 to 12.5wt% and y=0 to 0.5wt%) alloys followed by a peritectic reaction that transformed the τ_5 phase to the τ_6-$Al_9Fe_2Si_2$ phase; the kinetics of this transformation depended on the cooling rate during solidification and Fe concentration in the alloys such that slower cooling rates and higher Fe concentration yielded the partial or complete transformation into the τ_6 phase. The τ_5 phase was retained at the room

temperature after solidification for higher cooling rates and lower concentration of Fe in the alloys. It was found later in this project, that the first intermetallic phase to form was the θ-$Al_{13}Fe_4$ which underwent a rapid peritectic transformation to from the τ_5 phase during the early stages of the solidification process.

In alloys containing 0.02wt%Sr, the evolution of both the θ and τ_5 phases were prevented and a new phase which was denoted as κ in this project evolved with a stoichiometry of $Al_5Fe_2Si_3$. The project was into its fifth year by the time the κ phase was identified and hence, much effort could not be dedicated to fully characterize the crystal structure of this phase. It was found that at slower cooling rates during solidification and higher Fe concentrations in the alloy, alike, the κ phase transformed into the τ_6 phase similar to the transformation of τ_5 to τ_6 in alloys without Sr.

Initial hypotheses have been presented to explain the anomalies observed in the evolution of the intermetallic phases in these alloys without and with Sr addition to them. Further work is required to verify and validate these hypotheses.

In summary, this thesis presents emphatic evidences that our knowledge of the evolution of the Fe containing intermetallic phases in the commercially important Al-xSi-yFe-zSr (x=2 to 12.5 wt%, y=0 to 0.5 wt% and z=0 to 0.02wt%) alloys during solidification are not complete and the evidences presented by simulations of equilibrium phase diagrams do not accurately represent the nature of these intermetallic phases evolved.

CHAPTER 3. REVIEW OF THE PRIOR-ART

The background literature information relevant to this project was broadly categorized as follows:

- Al-Si cast alloys
- Fe in Al-Si cast alloys
- Modification of eutectic phases by Sr addition

Each of the above-mentioned categories is elaborated in separate respective sub-sections of this chapter.

3.1 Al-Si CAST ALLOYS

Al alloys are one of the most economically viable light metal alloys for a variety of commercial application in automotive, aerospace, military and domestic products [1,2,3]. Among them the Al-Si alloy system is more predominantly utilized due to the inherent benefits of being the most cost effective for near net shape manufacturing and recyclability [1,2]. Al-Si cast alloys are used in most commercial automotive gasoline and diesel engine and powertrain components [4,5,6]. Al alloys in general and Al-Si cast alloys in particular are found in many applications some of them bearing critical structural importance and some simply décor elements. Al-Si cast alloys are a cheaper alternative to magnesium alloys and a more expensive but light weight alternative to ferrous alloys. They fulfil design parameters in an application by providing suitably sound mechanical properties combined with economically affordable, light-weight and environmentally friendly solution.

Donahue et al [5] describe advances in all aluminum engines made by German manufacturers such as BMW, Mercedes and Porsche achieved high quality and high volume production of engine blocks cast entirely out of Al-Si alloys. Additionally, US automotive company such as Ford, GM and Chrysler, partially fueled by Japanese carmaker's success in reducing weight of the car, have continued to increase the use of Al-Si alloys for their engine blocks and cylinder heads so much so that even their most powerful V8 engine such as in the Ford Mustang Shelby 500 (2013 model year) is an Al engine [7] .

Military applications are limited to low strength light weight items including personal gear, furniture, interior elements of the battleships, etc.. One of the famous armor applications of the Al is M2/M3 Bradley armoured troops carrier [8] which was equipped with Al armour to lower overall weight of the tank.

Aerospace applications of Al alloys are numerous due to their significantly low cost to weight ratio as compared to other suitable materials. Passenger seats in aircrafts are entirely made of Al-Si cast alloys and about 5-15% of structural components in a military aircraft are made of Al alloys [9]. Figure 3-1 shows that Al alloys form nearly 70% of all metal in a typical large passenger aircrafts such as the Boeing 777.

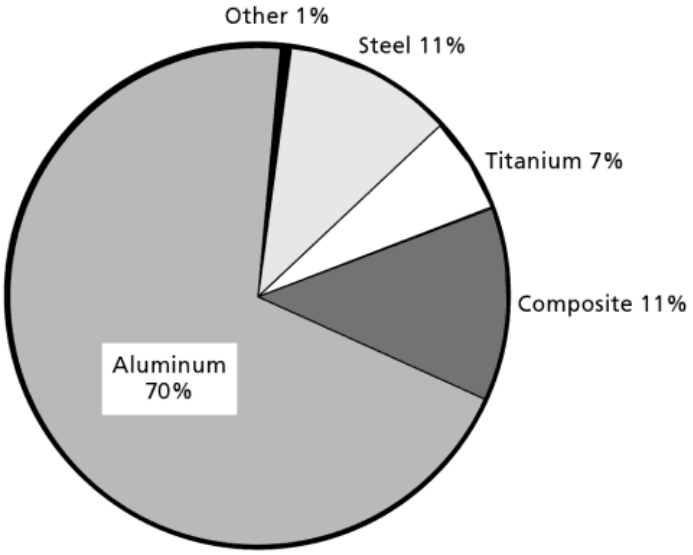

Figure 3-1: Material distribution in a Boeing 777 large passenger airliner [9].

In smaller aircrafts such as the Cessna Skycatcher, the entire exterior body is made of Al alloys [10].

Civil and domestic applications of Al alloys are numerous; furniture, small boats, consumer electronic, exterior finishing material for buildings, electrical wires, bicycle frames, home security systems and doors and windows are some typical examples [11].

Although the application of Al alloys in automotive structural components such as body, support structure and chassis seem to be on the increase lately, it is still a major challenge to substitute the high strength steel alloys typically used for these applications [12,13]. Presently, the density of the Al alloys is nearly three times lower than that of steel and the strength is about four to five times lower than their steel counterparts in the automotive structural components [2,11,12,13]. Hence, the substitution of Al alloys instead of steel in this application would increase the wall thickness of the component significantly rendering the process economically and aesthetically ineffective. Recently, there has been an increased thrust for academic research to design and develop new families of Al alloys with significantly higher (nearly three times) strengths and ductility than those presently available to explore their use as automotive structural components in the aim of further light-weighting the vehicle [13].

Fe is an unwanted and unavoidable impurity in all Al alloys [1, 14,15,16]. One of the detrimental factors in the existing Al-Si casting alloys is the presence of the Fe based intermetallic phases in the solidified casting which plays a significant role in reducing the strength and ductility of the cast component [13]. To design and develop newer Al alloys with superior properties and performance, it is imperative to better understand the nature and type of these Fe based intermetallic phases as a function of solidification parameters to control their evolution and morphology favourable. Further, a trace level of Sr is added to most commercial Al-Si alloys to refine the morphology of the eutectic Al and eutectic Si phases in order to

alleviate the detrimental effect of the plate-like morphology of the eutectic Si phase on the strength and ductility of the castings [2, 17].

It is the aim of this dissertation to present a fundamental understanding of the nature and morphology of the Fe based intermetallic phases evolving in the commercially important Al-Si alloys during solidification and the effect of Sr addition on them, as well. Albeit such information is available in several sources of open academic literature, this information is unclear and in most cases erroneous. This can be attributed to the lack of sophisticated experiments and analysis procedures until the last decade, and the quantum leap in technological advances globally in the last twenty years. An example will be the advances in the EDX (Energy Dispersive X-Ray Spectroscopy) method in the SEM; the advances in the last decade has now enabled researchers to confidently identify stoichiometry of intermetallic phases with a precision of less than 0.5%.

3.1.1 Classification of Al alloys

There are two types of Al alloys described by The Aluminum Association [18]: Cast alloys and wrought alloys. Cast alloys are suitable for use in manufacturing near net shaped components by solidification of the liquid metal and wrought alloys undergo stages of solid-state transformation such as extrusion, forging and drawing subsequent to casting of an initial billet or rod. One of the most common denominations in North America is the American National Standard Alloy and Temper Designation System for Aluminum ANSI H35.1 [19].

3.1.1.1 Cast Al alloys classification and common impurities

Al cast alloy classifications are based on the “pink sheets” from the aluminum association [20] and data from the book titled “Aluminum and Aluminum Alloys” by Davis [1]. There are 8 families of cast alloys. One family index 6XX is unused and reserved for future alloys.

Alloy indices consists of the alphabet letters such as A,B,C, etc., as prefix or extensions to indicate compositional changes of certain minor but critical alloying elements. The first digit indicates the major alloying elements and the second and third are for designation of specific alloy compositions. The forth digit (.X) gives the casting (0) or ingot (1 or 2) designation.

- 1XX.X family is pure aluminum of 99% or greater purity.
- 2XX.X family is the Al-Cu alloys.
- 3XX.X family is Al-Si-Mg-(Cu) combination and most widely used series of cast alloys.
- 4XX.X family is the Al-Si alloys.
- 5XX.X family is the Al-Mg alloys.
- 6XX.X family reserved for future alloys.
- 7XX.X family is the Al-Zn alloys.
- 8XX.X family is the Al-Sn alloys.

Critical elemental additions can include Ti, B, Be, Sb, B, Cd, Pb, Ca, Ag, Hg, P, Na, and Sr.

Table 3-1 summarizes the composition ranges of the major elements in the various series of the cast aluminum alloys.

Table 3-1: Composition ranges of major alloying elements in Al cast alloys.

Alloy	Si	Fe	Cu	Mn	Mg	Cr	Ni	Zn	Sn	Ti	impurities
100	0.1-0.15	0.25-0.8	0.05-0.1	<0.025	…	<0.025	…	0.05	…	<0.025	0.1
200	0.05-3.5	0.05-1.2	3.5-10.7	0.05-0.6	0.03-6.5	…	0.03-1.7	0.05-2.5	0.05	0.07-0.3	0.1-0.5
300	0.13-20	0.04-2	0.03-5	0.03-0.8	0.05-1.5	0-0.35	0-3	0.03-3	0-0.5	0-0.25	0.1-0.5
400	4.5-13	0.6-2	0.05-1	0.05-0.5	0.01-0.1	0-0.25	0-0.5	0.01-0.5	0.01-0.15	0-0.25	0.1-0.35
500	0.15-2.2	0.12-1.8	0.05-0.3	0.5-0.6	3.5-10.6	0-0.25	0-0.4	0-2.2	0-0.15	0-0.25	0.05-0.25
700	0.1-0.3	0.1-1.4	0.1-1	0.5-0.7	0.25-1.8	0-0.6	0-0.15	2.7-7	0-0.15	0-0.25	0.05-0.25
800	0.7-6.5	0.5-0.7	0.7-4	0.1-0.5	0-0.9	0-0.05	0-0.05	0.3-1.5	5.5-7	0-0.25	0-0.3

3.1.1.2 Wrought Al alloys classification

Eight families of wrought alloys are designated by the Aluminum Association “teal pages” (2009 version) [21].

- 1XXX family is 99% or more op pure Al with Si and Fe as major alloying elements.
- 2XXX family is Al alloyed with 3.8 - 6% of Cu with Si, Fe and Mn as secondary alloying elements.
- 3XXX family is Al alloyed with Mn, Mg, Fe and have as low as 0.6wt% Si.
- 4XXX family is Al with addition of up to 6 wt% Si, 0.8 wt% Fe.
- 5XXX family is Al alloyed with up to 5.5 wt% Mg rest of the Fe, Si, Mn are kept below 0.6 wt% mark.

- 6XXX family is Al alloyed with Mg-Si 0.8-1.8 wt% Si, 0.4-1.2 wt% Mg, 0.1-0.7 Fe and Mn.
- 7XXX family is Al alloyed with Zn and Mg ranging up to 7.3 wt% and 3.7 wt% respectively. Some alloys in the series have up to 2.4wt% of Cu. Fe, Mn and Si kept low.
- 8XXX family is Al alloyed with Li, Cu and Mg.
- 9XXX family is reserved for future alloys.

In addition to the designated ranges of composition of the minor alloying elements, there are several other additional minor elements added to these alloys as customized by the user.

3.1.2 Al-Si cast alloy system

The Al-Si binary system has been described in numerous publications and most aspects of the system behaviour has been studied in-depth and documented. The Al-Si phase diagram is a simple binary eutectic system with the eutectic point at about 12.5 wt% Si and 851K (578°C) as shown in Figure 3-2.

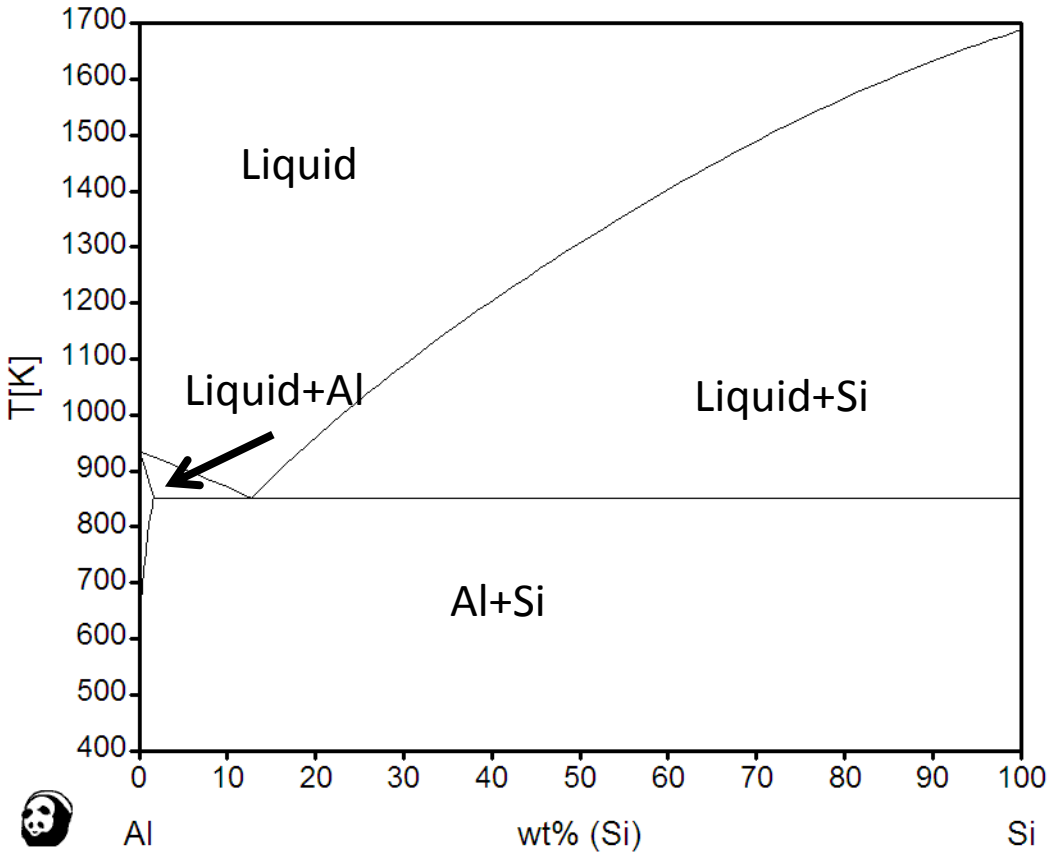

Figure 3-2: The Al-Si binary phase diagram as simulated by the thermodynamic software Pandat with PanAl8 database.

The Al-Si binary system was reviewed by several researchers since the year 1908 [3,16,22,23, 24] by both experimental data (Figure 3-3) and theoretical thermodynamic simulations.

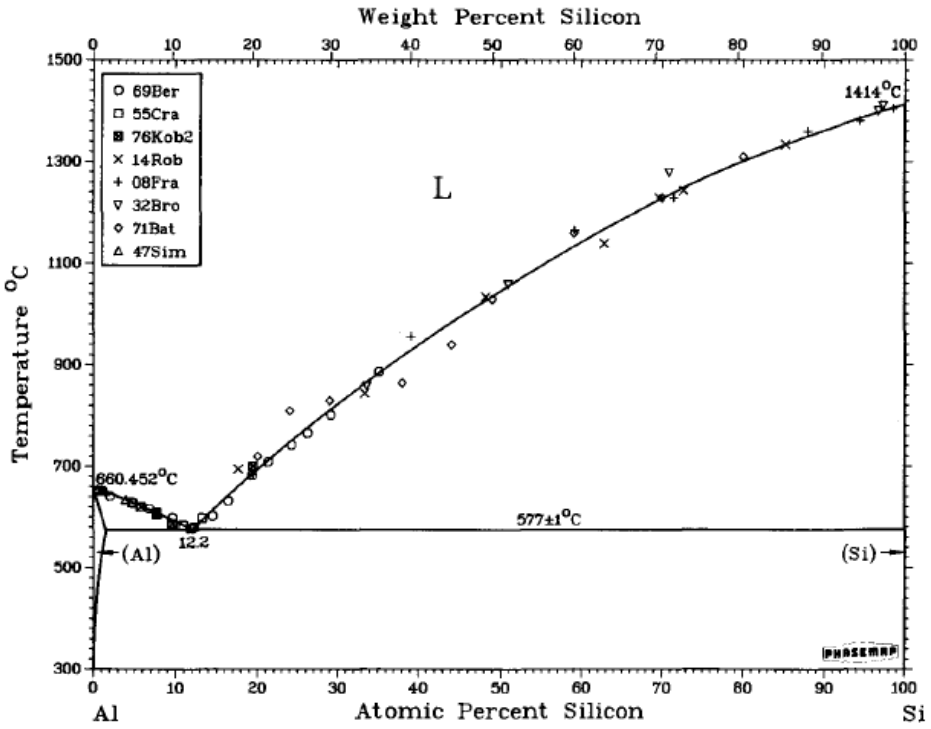

Figure 3-3: Calculated Al-Si phase diagram compared to experimental data [23]

There are three regions in the Al-Si binary phase diagram: 2-11wt%Si is termed hypoeutectic, 11-13wt%Si is termed eutectic and 13-100% Si is termed hypereutectic regions. The elemental Si phase (primary and eutectic) in these solidified alloys are brittle plates which are detrimental to the mechanical properties of these alloys. However, addition of Si to Al makes the alloys castable into near net shape components with reasonably sound properties and performance and economic viability, as well. The hypoeutectic Al-Si alloys with alloy additions such as Mg, Mn, Zn, Cu, Sr, Ti, etc., form the majority of commercial application for these alloys. The morphology of the eutectic Si phase has been one of the heavily debated academic topics for the last century [17,25,26,27,28]. Day and Hellawell (1968) [29] and later Makhlouf and Guthy (2001) [30] are typical examples of elaborate reviews on the evolution and morphology of eutectic Si phase. The morphology of the eutectic Si phase could be refined by increasing the cooling rates of the liquid alloy during solidification [29], however, these cooling rates are limited by the casting processes. Another way to alter the morphology of the eutectic Si phase is by the addition of certain elements such as Sr and Na [30,31,32], and more recently, with other rare-earth elements such as Y, Yb and the La series [33] to the Al-Si alloys . These additions change the morphology of the Si phase from a plate-like to a refined fibrous one [1, 2,17,16, 34]. Another element that plays a critical role in affecting the morphology of the eutectic Si phase is Fe [14,35]. Shankar et al [14] showed that in equilibrium solidification condition, nearly 40 ppm levels of Fe in the alloy resulted in the evolution of the β (Al,Si,Fe)

intermetallic phase along with the eutectic phases (ternary system) and in alloys with less than 30 ppm Fe levels, the morphology of the eutectic Si phase was fibrous and refined. It was further concluded that the β (Al,Si,Fe) intermetallic phase acted as the inoculant for the evolution of the eutectic Si phase and the absence of which rendered the eutectic phases to solidify with a significant undercooling and hence, refining the Si and Al phases. Figure 3-4 shows an isopleth from the low Fe region of the ternary phase diagram of the Al-Si-Fe system with increasing levels of Fe to the Al-7wt%Si alloy.

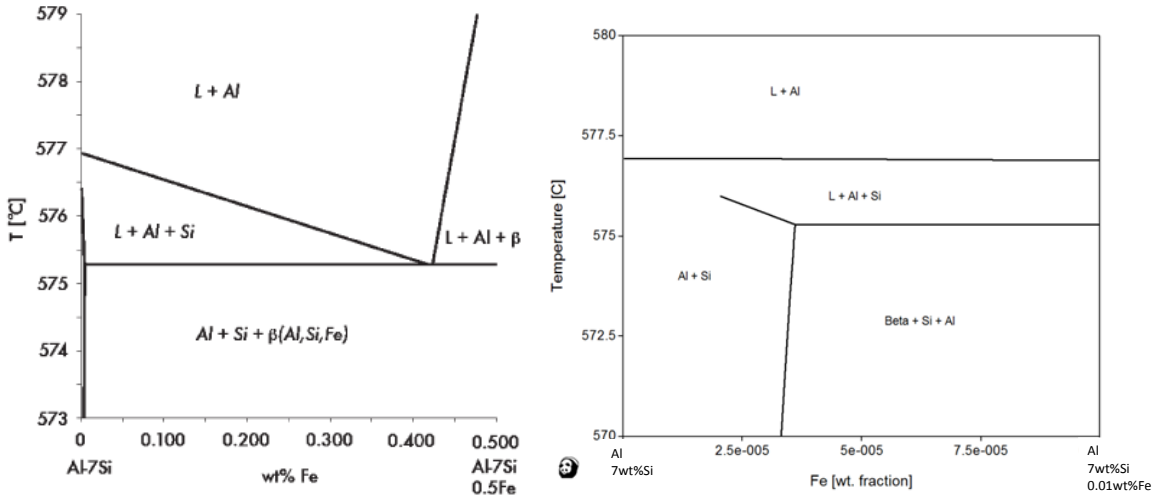

(a) (b)

Figure 3-4: Isopleths from the ternary Al-Si-Fe alloy phase diagram showing the Al-7wt%Si section with increasing levels of Fe in the alloy. (a) 0 to 0.5wt% Fe region and (b) 0 to 0.01 wt% Fe. "Beta" in the figure represents the τ_6-$Al_9Fe_2Si_2$ phase [15].

Further discussion on the mechanism of evolution and modification of the eutectic Si phase and the role of Fe based intermetallic phases will be presented in sub-sections below.

3.2 Fe IN Al-Si CAST ALLOYS

It is hard to evaluate casting techniques and peculiarities of the process from data provided by majority of the publications. Only for the papers there such data is sufficient for judgements papers will be commented and evaluated.

As validated earlier [14,15,17], there is a clear connection between iron containing intermetallic and Al-Si eutectic phases. In pure alloys with less than 0.0032 wt% Fe, the eutectic Si reaction waits for $Al_9Fe_2Si_2$ (τ_6) phase to evolve before the Si can nucleate on the τ_6 phase and grow [17], as shown in Figure 3-5 (a) and Figure 3-4 (b). For alloys with commercially nominal Fe content such as 0.24 wt%Fe, the τ_6 phase evolves prior to the eutectic reaction and the eutectic Si phase nucleates at a eutectic temperature close to that predicted by the alloy phase diagram as again shown by comparing the isopleths of the phase diagram shown in Figure 3-4 (b) and the

thermal analysis curve shown in Figure 3-5 (a) [15]. The eutectic Si phase would not be able to nucleate on the primary Al phase without a very large undercooling and hence, requires the presence of the τ_6 ($Al_9Fe_2Si_2$) phase to act as an inoculant.

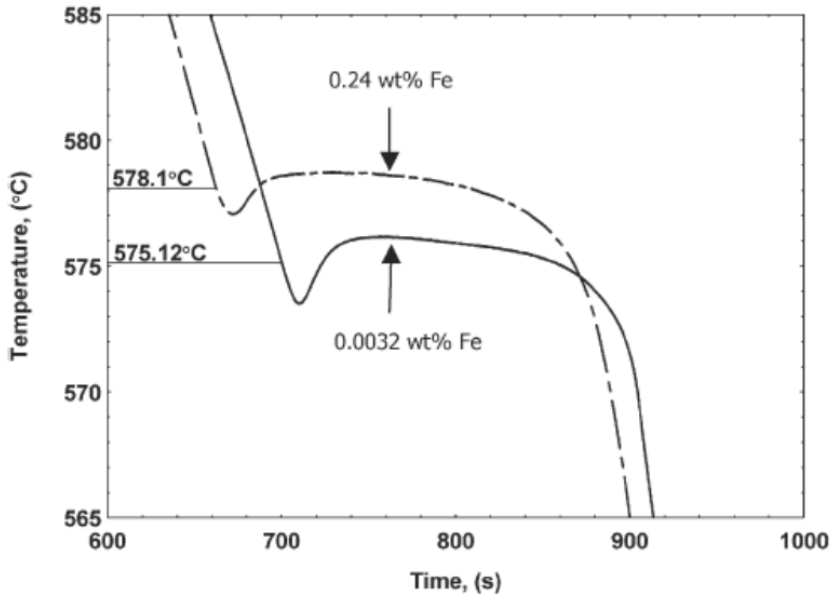

(a)

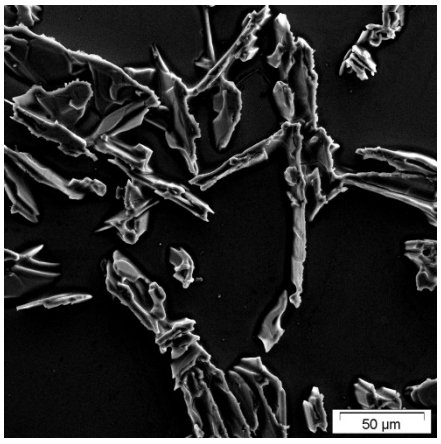

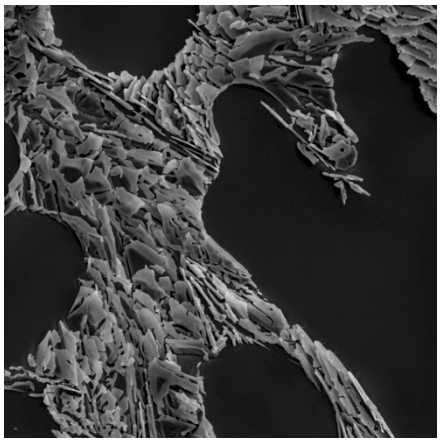

(b) (c)

Figure 3-5: Effect of Fe level in high purity Al-Si alloys. (a) thermal data obtained during solidification, (b) SEM secondary image of Al-7wt%Si-0.24wt%Fe alloy and (c) SEM secondary image of Al-7wt%Si-0.0032wt%Fe alloy [15].

The β-AlSiFe intermetallic phase nucleates on the primary Al phase, as shown in Figure 3-6, with a preferred crystallographic relationship between αAl and β-AlSiFe intermetallic phases [14].

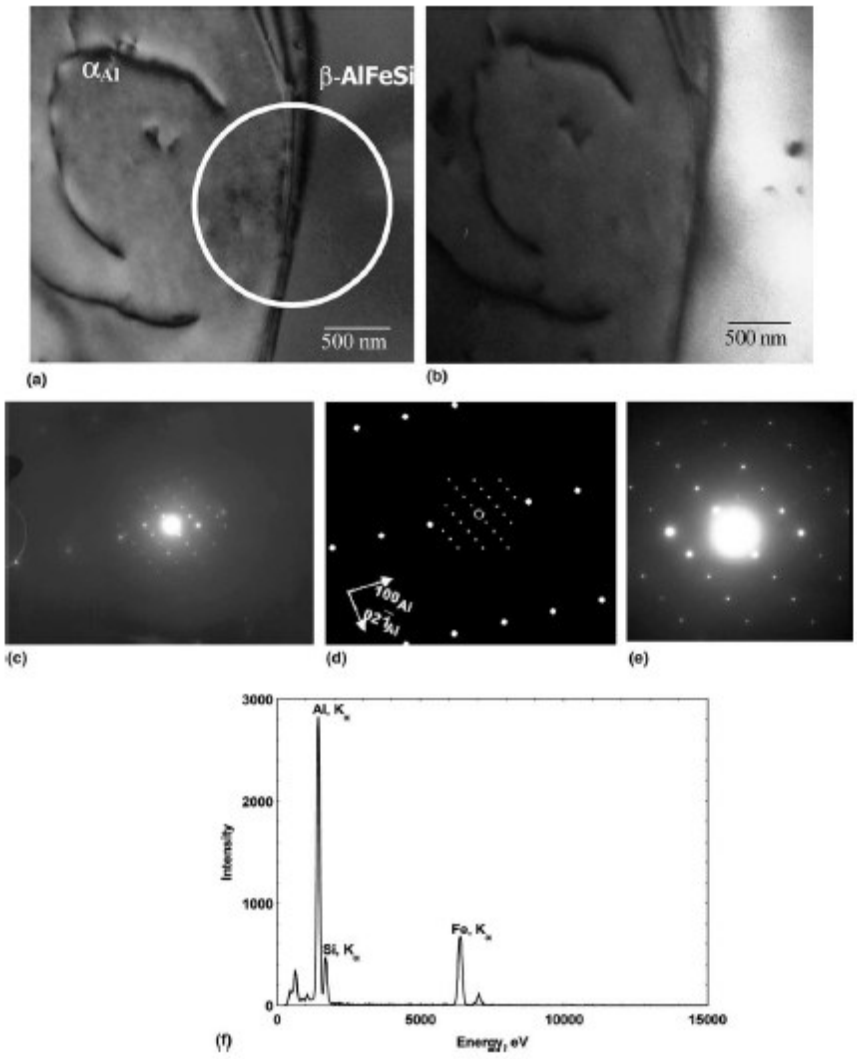

Figure 3-6: Interface between a-aluminum dendrite (αAl) and β- $Al_9Si_2Fe_2$: (a) bright field TEM image; (b) centered dark field image showing the β- $Al_9Si_2Fe_2$ phase; (c) SAD pattern taken in the encircled region in (a), (d) digital replication of (c) for better visualization; (e) SAD pattern from the β-$Al_9Si_2Fe_2$ phase brought to a zone axis; (f) EDS spectrum obtained from the β-$Al_9Si_2Fe_2$ particle [14].

Another piece to the puzzle is the mutual relation between β-$Al_9Si_2Fe_2$ and eutectic Si attached to these phases. It was found by Shankar et al [14,15,17] that there is relation between the β-$Al_9Si_2Fe_2$ and eutectic Si phases. TEM diffraction work shown in Figure 3-7 is a proof of definite crystallographic relation between β-$Al_9Si_2Fe_2$ and eutectic Si. The β-$Al_9Si_2Fe_2$ plays key role in triggering eutectic reaction in unmodified Al-Si-Fe alloys.

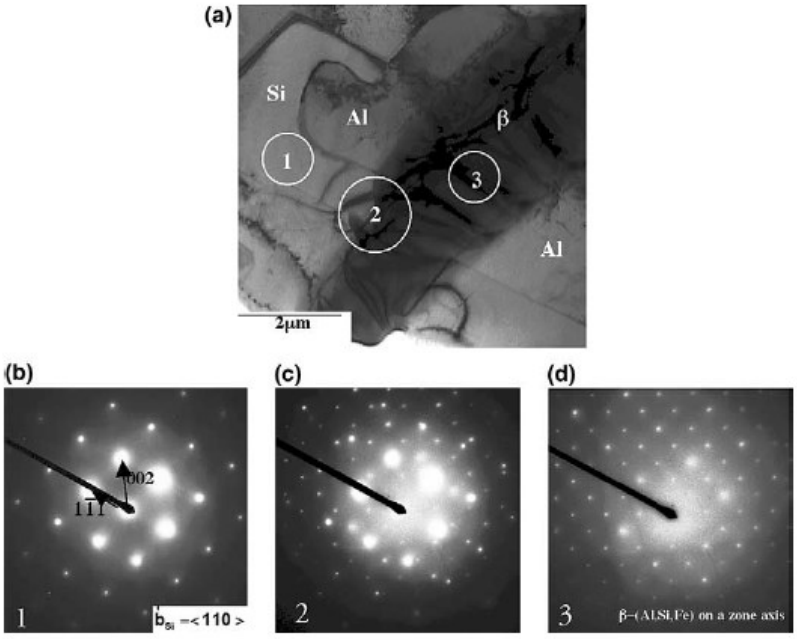

Figure 3-7 : Crystallographic relationship between β-(Al, Si, Fe) and Si. (a) Bright field TEM image. (b), (c), and (d) selected area diffraction patterns from the regions marked 1, 2 and 3 in (a). The region marked ''1'' is on Si, the region marked ''2'' is on the interface between b-(Al, Si, Fe) and Si, and the region marked ''3'' is on β-(Al, Si, Fe). The diffraction patterns show a distinct crystallographic relationship between β-(Al, Si, Fe) and Si. The sample used to generate this figure is Al–7Si–0.24Fe – air cooled at 48 K.min^{-1} [17].

There are suggestions in the literature by Cao et al [36] that Al-Si-Fe intermetallic phases formed in the beginning of the eutectic reaction or slightly prior to it could serve as nuclei for further evolution of the eutectic phases. They suggested that in commercial Al-Si alloys with alloying additions such as Mg, Mn and Sr, the Fe based intermetallic phases nucleated on the oxide films in the melt and further enabled the evolution of the eutectic Si phase as shown by the schematic in Figure 3-8. The work by Cao et al [36] was merely based on optical and SEM microscopy along with evidences from the EDX analysis; no crystallographic information was provided on the phases and nucleation schemes.

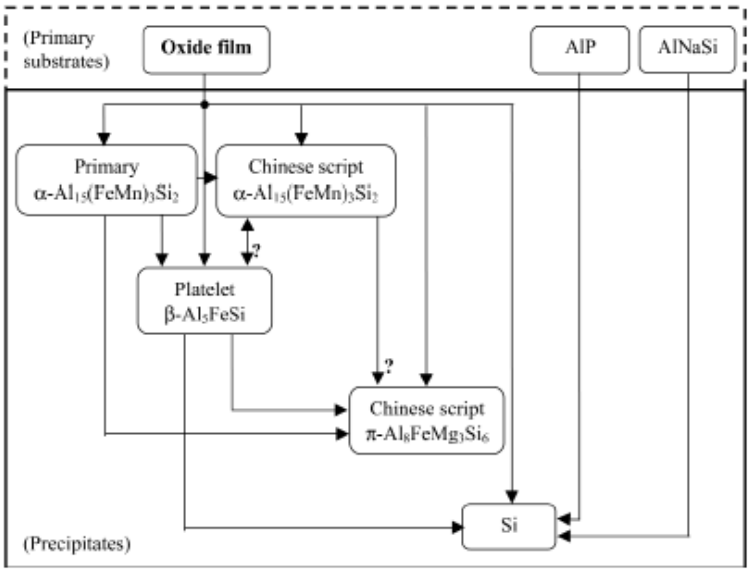

Figure 3-8: Possible nucleation hierarchy among oxide films and solidifying phases in Al-11.5Si-0.4Mg cast alloys containing Fe and Mn (arrows refer to the nucleation process) [36].

Nogita et al [37] suggested that the phosphorous impurity in the Al-Si alloys form the AlP and aluminium oxide containing P; the AlP was suggested to act as an heterogeneous nucleation site for the eutectic Si phase. However in their publication [37], the near eutectic Al-Si alloy composition with 0.004 wt%P was quenched from the liquid phase and an AlP phase was found entrapped inside a bulky polygonal Si phase. This bulky Si phase with the AlP phase nucleating it could only have been the primary Si phase and not the eutectic phase as shown by the Al-Si phase diagram with the metastable extension lines in Figure 3-9 [23] wherein the rapid solidification (quenching) of the Al-9wt%Si alloy will result in a hypereutectic alloy microstructure with primary Si phase because the shift in the eutectic reaction to the low Si levels in the alloy. Further, the nucleation of primary Si phase on the AlP phase has been well documented [38]. As yet, there is no convincing evidence of AlP phase nucleating the eutectic Si phase. Moreover, it would be nearly impossible to prove the crystallographic orientation relationship between AlP and Si, even if there was one, using conventional advanced microscopic techniques such as SEM and TEM or X-ray diffraction experiments because the crystal structure and lattice parameter of these two phases are nearly identical [39, 40].

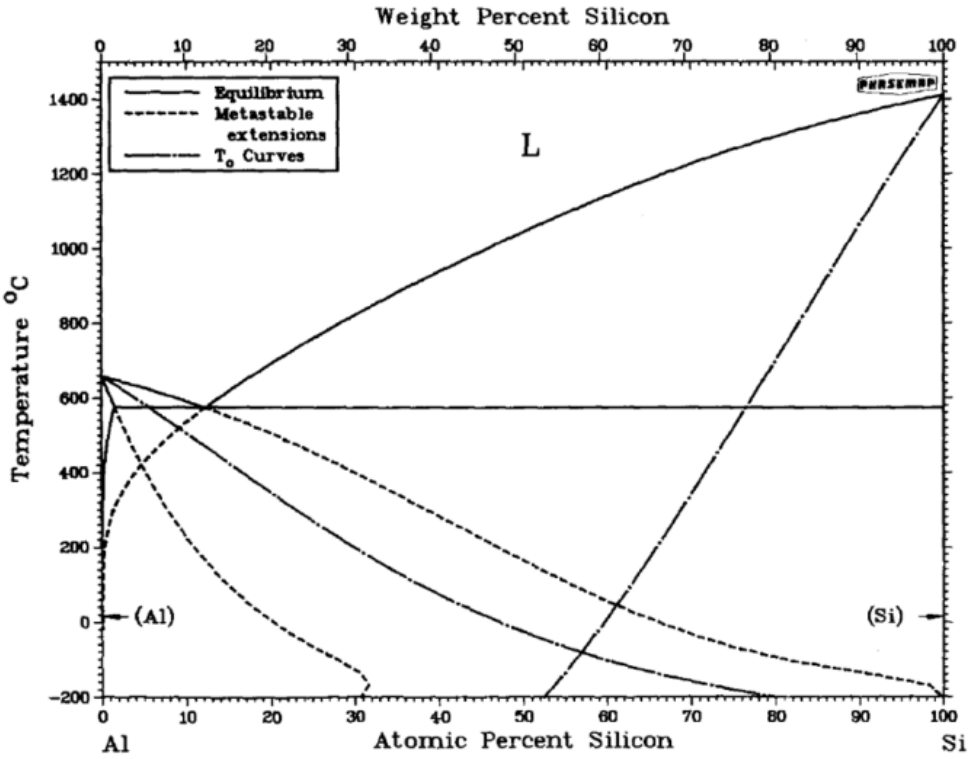

Figure 3-9: Al-Si binary phase diagram with the metastable extension lines [23].

Li et al [41] have shown that during the solid-state precipitation of Si and Fe based intermetallic phases inside the primary Al phase, there is evidence of crystallographic orientation of both the Si and Al-Fe-Si intermetallic phase with the primary Al phase. Li et al [41] further tried to elucidate the effect of trace additions of Sr and Sr+P to the Al-5wt%Si alloy containing 200 ppm of Fe on the precipitating sequences of Si and Al-Fe-Si phases. Due to the lack of a meaningful and elaborate experiment matrix, no significant conclusion could be drawn from this study [41]; however, the authors begin their conclusion in the publication (year 2011) with "*The Fe containing phases are very complex in Al alloy, especially for the high purity Al-Si-Fe alloy*", which is one of the primary motivations for this PhD dissertation.

3.2.1 Al-Fe-Si intermetallic phases

There are typically two schools of thought in naming the Al-Fe-Si intermetallic phases in the Al-Si alloys: one uses the greek alphabet letters such as α, β, ϒ and δ while the other uses letter τ with various numeric subscripts [42,43]. A list of the intermetallic phases found in the Al rich corner of the Al-Fe-Si ternary alloy systems with the two different nomenclature methods is shown in Figure 3-10. The use letters of greek alphabet such as α, β, ϒ and δ is not as precise as using the τ with various numeric subscripts; for example, in commercial Al-Si alloys, Mn is a popular impurity or alloying addition which is soluble in the Al-Fe-Si intermetallic phases and the α phase could refer to both the Al-Fe-Si and Al-Fe-Mn-Si intermetallic phases; these two intermetallic phases have a different crystallographic structure [25,44,45,46,47, 48]. Further, the use of the alphabets α, β, ϒ and δ was based on the morphology of the intermetallic phases

rather than the stoichiometry and reaction during solidification [44, 25, 46, 49, 50], and Takeda and Mutazaki [42] proposed the naming these phase with just letter τ with various numeric subscripts based on the reactions that yielded them during the solidification of the alloys. Examples of such invariant liquid reactions are given in Figure 3-11.

Chemical compound	Chemical formulae Density, *d*	Homogeneity range near 727 °C, at.% (wt.% in parentheses)	Symmetry, structure, cell parameters, nm, diffraction data used for characterization	Decomposition temperature, °C
θ	Al_3Fe $Al_{13}Fe_4$ *d* = 3.90	From Ref 3, 18-20 Fe: 23.5-25 (38.6-41.1) Si: 0-5 (0-4.5)	Monoclinic, *C2/m* *a* = 1.5492(2), *b* = 0.8078(2), *c* = 1.2471(1), β = 107.69(1)° (Ref 19, 21) XRD spectrum recalculated from Ref 21	1152 (Ref 18, 22)
α = τ_5 also referred to as α_H in Ref 24 and α′ in Ref 4	$Al_{12}Fe_3Si_2$ Al_8Fe_2Si $Al_{7.4}Fe_2Si$ *d* = 3.58	From Ref 3, 23, 24 near 600 °C Fe: 18.5-21.5 (32-36) Si: 7-13 (6-11) Refined (Ref 20, this work) Fe: 18-19.5 (31-33.3) Si: 10-12.5 (8.6-10.9)	Hexagonal, *P6₃/mmc* (Ref 23, 25) *a* = 1.2404(1), *c* = 2.6234(2) with 44.9Fe, 167.8Al, and 23.9Si atoms per unit cell (Ref 26) JCPDS 41-894 and 71-238	855 (Ref 9) 715 (Ref 16) 710 (Ref 1)
β = τ_6	Al_5FeSi $Al_{4.5}FeSi$ $Al_9Fe_2Si_2$ *d* = 3.3 to 3.35	From Ref 3, 20, 24, 27 at 640 °C Fe: 15.5-16.5 (27-29) Si: 17-19 (15-17)	Monoclinic, *A2/a* *a* = 0.6161(3), *b* = 0.6175(3) *c* = 2.0813(6); β = 90.42(3)°, (Ref 8, 28) XRD spectrum re-calculated from Ref 28	700 (Ref 1) 694 (Ref 16) 667 ± 5 (Ref 20)
γ termed τ2 in Ref 9 and τ7 in Ref 16, 17	Al_3FeSi $Al_5Fe_2Si_2$ *d* = 3.75	From Ref 3, 25 Fe: 18-23 (31-38) Si: 12.5-22 (11-18.5) Refined (Ref 20, this work) Fe: 19.5-21.5 (33-36) Si: 15.2-25.6 (13-22)	Monoclinic *a* = 1.78, *b* = 1.025, *c* = 0.890, β = 132° (Ref 25) no structure determination JCPDS 20-0032	940 (Ref 9) 850 (Ref 16)
δ = τ_4	Al_4FeSi_2 Al_3FeSi_2 $Al_{2.7}FeSi_{2.3}$ *d* = 3.3 to 3.4	From Ref 29 Fe: 15-17 (26.5-29.5) Si: 27-43 (24-38) Refined (Ref 20, this work) Fe: 15.5-16.5 (27-29) Si: 30.5-38 (27-33)	Orthorhombic, *Pbcn* *a* = 0.6061, *b* = 0.6061, *c* = 0.9525 (Ref 29) XRD spectrum recalculated from Ref 29	865 (Ref 9) 834 (Ref 16)
τ2 in Ref 2, τ3 in Ref 9, τ23 in Ref 16, 17	Al_2FeSi	From Ref 30, 17 Fe: 25 (40.5) Si: 25 (20.4)	Orthorhombic, *Cmma* *a* = 0.7995, *b* = 1.5162; *c* = 1.5221 (Ref 30) XRD spectrum calculated from Ref 30	935 (Ref 2, 9) 920 (Ref 16)
τ″ (Ref 17)	$Al_4Fe_{1.7}Si$	From Ref 31, 17 Fe: 25.4 (41.2) Si: 14.9 (12.1)	Hexagonal, *P6₃/mmc* *a* = 0.7509, *c* = 0.7594 (Ref 31) XRD spectrum calculated from Ref 31	?

Figure 3-10: Stable compounds reported in the Al-rich corner of the Al-Fe-Si ternary system [43]

In the intermetallic phases labelled as τ with numerical subscripts, the number in the subscript increased with decreasing values of temperatures at which the respective phases evolved during solidification. The τ_6 phase is the last to evolve at the eutectic temperature and hence, Takeda and Mutazaki [42] reported only six phases between τ_1 and τ_6. Later additions to the system took subsequent numerical indices as subscripts to τ for phases evolving at higher temperatures than that of τ_6.

Symbol	Temperature, °C	Invariant reaction	Liquid composition, wt-% Al	Fe	Si
U_1†	1120	$L + \epsilon \rightleftharpoons \alpha\delta Fe^{\ddagger} + \eta$	46.0	51.0	3.0
P_1	1050	$L + \alpha\delta Fe^{\ddagger} + \rho \rightleftharpoons \tau_1$	31.0	50.0	19.0
U_2	1030	$L + \alpha\delta Fe^{\ddagger} \rightleftharpoons \eta + \tau_1$	37.5	48.5	14.0
U_3	1020	$L + \eta \rightleftharpoons \theta + \tau_1$	38.0	48.0	14.0
U_4	1000	$L + \rho \rightleftharpoons \omega + \tau_1$	26.0	42.0	32.0
P_2	940	$L + \theta + \tau_1 \rightleftharpoons \tau_2$	41.0	40.0	19.0
P_3	935	$L + \tau_1 + \tau_2 \rightleftharpoons \tau_3$	39.0	39.0	22.0
U_5	885	$L + \tau_1 \rightleftharpoons \omega + \tau_3$	36.0	28.0	36.0
U_6	880	$L + \omega \rightleftharpoons \tau_3 + (Si)$	38.0	26.0	36.0
P_4	865	$L + \tau_3 + (Si) \rightleftharpoons \tau_4$	45.0	23.0	32.0
P_5	855	$L + \theta + \tau_2 \rightleftharpoons \tau_5$	58.0	25.0	17.0
U_7	835	$L + \tau_3 \rightleftharpoons \tau_2 + \tau_4$	56.0	22.0	22.0
U_8	790	$L + \tau_2 \rightleftharpoons \tau_4 + \tau_5$	61.0	18.0	21.0
P_6	700	$L + \tau_4 + \tau_5 \rightleftharpoons \tau_6$	78.0	8.0	14.0
U_9	620	$L + \theta \rightleftharpoons (Al) + \tau_5$	95.0	2.0	3.0
U_{10}	615	$L + \tau_5 \rightleftharpoons (Al) + \tau_6$	93.0	2.0	5.0
U_{11}	600	$L + \tau_4 \rightleftharpoons \tau_6 + (Si)$	85.0	1.0	14.0
E_1	577	$L \rightleftharpoons \tau_6 + (Al + (Si)$	88.4	not measured	11.6

Figure 3-11 : Invariant liquid reactions proposed by Takeda et al cited by Rivlin and Raynor [24]

In present work, to ensure precision and clarity, the use of the symbol τ with various numeric subscripts such as τ_2, τ_4, τ_5 and τ_6 would be used to identify the various Al-Fe-Si intermetallic phases as presented in Figure 3-10. A few additional notations given to the intermetallic phases in the background literature are shown Figure 3-12 [80].

When discussing commercial Al-Si casting alloys, two major Fe containing intermetallic phases are predominantly mentioned: α and β phases [2,51]. Both these phases have solubility of several commercial alloying elements such as Mn and Cr. The α phase has several crystal structures reported depending on the level of alloying elements soluble in it and the solidification conditions prior to its evolution. For example, Kral et al [51] in their work on the commercial Al-11.7Si-0.16Fe-0.13Mn-0.01Mg alloy reported that after addition of 0.06wt% Sr to the alloy, plate like along with chinese script like Al-Si-Fe intermetallic phases co-existed in the solidified microstructure.

Name and Symbol	Model	Crystal Structure	Other Names in Literature
Alpha, α	$Al_{0.66}Fe_{0.19}Si_{0.05}(Al, Si)_{0.10}$	hexagonal[30]	τ_5,[15] K_5,[20] β,[21] M[31]
Beta, β	$Al_{0.598}Fe_{0.152}Si_{0.10}(Al, Si)_{0.15}$	monoclinic[32]	τ_6,[15] K_6,[20] X,[21] L[31]
Gamma, γ	$Al_{0.635}Fe_{0.205}Si_{0.16}$	monoclinic[25]	K[31]
Delta, δ	$Al_{0.49}Fe_{0.16}Si_{0.35}$	tetragonal[33]	τ_4,[15] K_4,[20] δ,[21] A[31]
Tau1, τ_1	$Al_{0.35}Fe_{0.37}Si_{0.28}$	not available	τ_1, [15] K_1,[20] C or D or E[31]
Tau23, τ_{23}	$Al_{0.54}Fe_{0.26}Si_{0.2}$	not available	τ_2, τ_3,[15] K_2, K_3,[20] F or G[31]
Tau, τ	$Al_{0.40}Fe_{0.25}Si_{0.35}$	not available	$Al_8Fe_5Si_7$,[28] B[31]

Figure 3-12: Ternary Intermetallic Compounds in the Al-Fe-Si System according to Liu [80]

The script like phases were identified as α-$Al_{19}Fe_4MnSi_2$ with a BCC structure and the plate-like phases as with a tetragonal structure. However, no information on the solidification method or the rate of solidification was presented in the manuscript Kral et al [51] provided evidence of the α-$Al_{19}Fe_4MnSi_2$ and phases as shown in Figure 3-13 and Figure 3-14, respectively. The plate like phase identified as δ- Al_3FeSi_2 by Kral et al [51] is usually mistakenly identified as the plate like β-$Al_9Si_2Fe_2$ phase in several occasions where the only optical microscopy and SEM with EDX were carried out for phase identification [51].

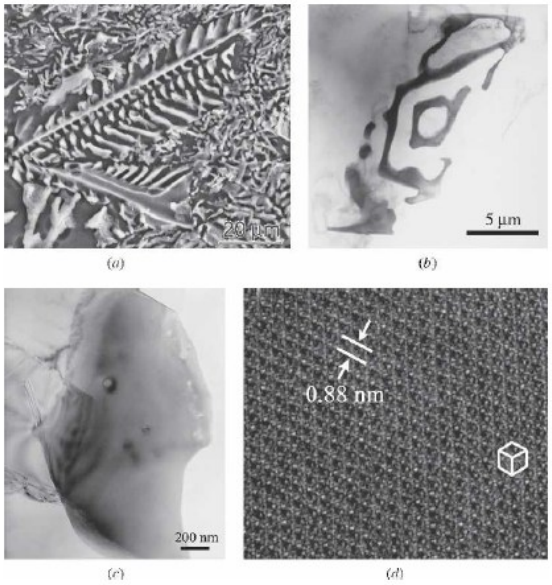

Figure 3-13: The morphology of script particles in an unmodified alloy is revealed by (a) a scanning electron micrograph of a deep-etched specimen, and (b) and (c) transmission electron micrographs and (d) a lattice image from the particle shown in (c) near <111> showing a projection of the unit cell and spacing of the {110} [51].

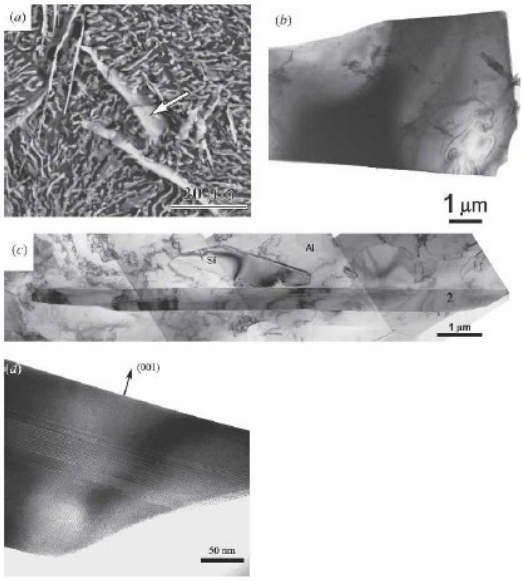

Figure 3-14: (a) An SEM image of a deep-etched sample showing typical plates. (b) A bright-field TEM image of an extracted plate revealing the plate 3D morphology. (c) A montage of bright-field TEM images shows the typical appearance of a plate (designated ''2'') in cross-section. (d) A higher-magnification TEM image of a plate-shaped particle shows the faults often observed and that the normal to the broad face of the plate is parallel to (001).

The β-$Al_9Si_2Fe_2$ phase has significant influence on the mechanical properties of the Al-Si alloys [16,52,] due to their plate morphology with sharp interfaces which act as locations of high stress concentration. TEM and EBSD phase identification of the β-$Al_9Si_2Fe_2$ phase can be seen in Figure 3-15 [51].

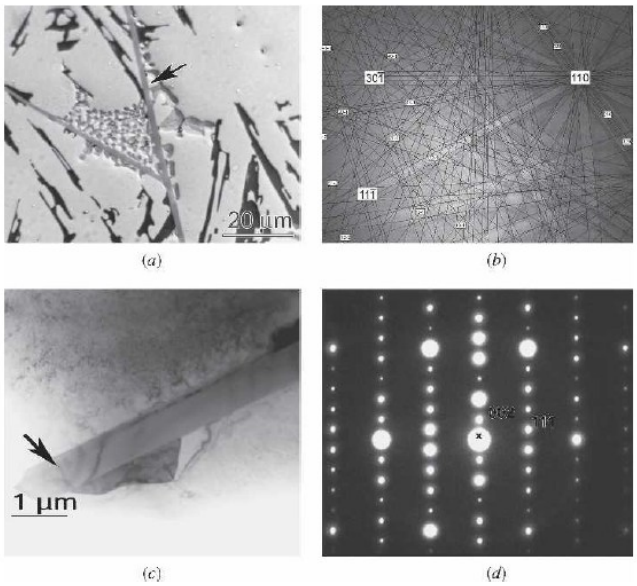

Figure 3-15 : Characterization of the β-$Al_9Fe_2Si_2$ phase in (a) optical micrograph, (b) EBSD pattern indexed as $Al_9Fe_2Si_2$, (c) bright-field TEM image of a β-phase plate, and (d) selected area diffraction of a β-phase plate along [110] [51].

Both δ and β phases have eutectic Si attached to them in the solidified microstructure as seen in Figure 3-14 and Figure 3-15 but the authors did not study the crystallographic orientation relationship between these phases. The reason why Kral et al [51] did not find any β-$Al_9Si_2Fe_2$ in their commercial Al-11.7Si-0.16Fe-0.13Mn-0.01Mg is because the Fe:Mn ratio in the alloy was nearly unity and the Mn phase is known to form a stable α-$Al_{19}Fe_4MnSi_2$ phase with a BCC crystal structure [52] and this would mitigate the formation of the β-$Al_9Si_2Fe_2$ phase in the solidified structure. The results from this dissertation would present the mechanism for the formation of the β-$Al_9Si_2Fe_2$ phase during solidification and the reasons why a near unity ration of Fe:Mn in the alloy prevents the formation of this phase. Kral et al [51] found the β-$Al_9Si_2Fe_2$ phase in another alloy with a high Fe:Mn ratio as in Al-9Si- 1.3Fe-3.3Cu-0.4Mn which is shown in Figure 3-15.

There are other works dedicated to investigation of Al-Fe and Al-Si-Fe intermetallics in commercially pure Al alloys [53]. There are six different intermetallic phases containing Al-Fe in "pure" Al [53]. Hence, it is notable that all commercially pure Al alloys would contain a multitude of Al-Fe and/or Al-Si-Fe intermetallic phases in them. Liu and Dunlop's work deals with Al-0.5/0.25Fe-0.013Si alloys in as cast and heat treated at 873K (600°C). In both the as-cast and heat treated conditions, under slower solidification rates, the presence of the θ-$Al_{13}Fe_4$ phase was dominant and in higher solidification rates, the Al_mSi_x, α-Al,Si,Fe, q_1-AlSiFe and q_2-AlSiFe metastable phases were observed. The most important outcome of the meticulous TEM research [53] is the proof that all these Al-Fe and Al-Fe-Si intermetallic phases nucleated on the primary Al phase during solidification. For example, the crystallographic orientation relationships between the θ-$Al_{13}Fe_4$ and the Al matrix are shown in Figure 3-16.

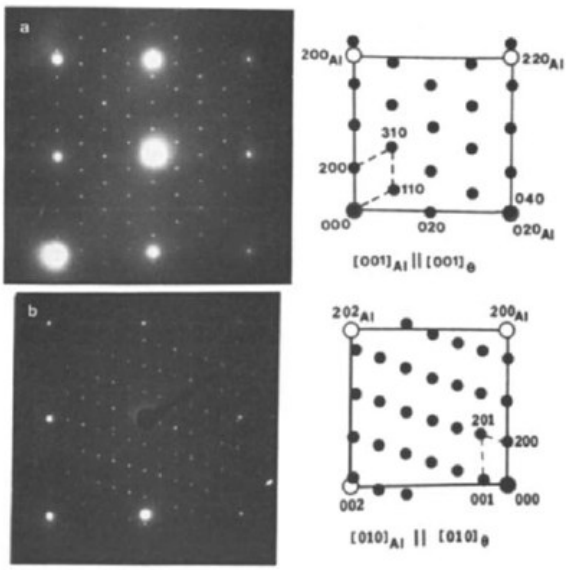

Figure 3-16 : Composite SAED patterns of θ-Al13Fe4 and Al for OR-I with their schematic solutions. (a) $[OO1]_{\theta}$ll$[001]_{Al}$ beam direction; (b) $[O1O]_{\theta}$ll$[010]_{Al}$ beam direction [53].

A comprehensive list of all the crystallographic orientation relationships found by Liu and Dunlop [53] is given in Table 3-2.

There is no cooling curve measurement data reported due to use of commercial ingot, no compositional identification of the phases is reported also full composition of the alloy with all impurities is not provided [53].

Table 3-2: List of mutual orientations between iron containing intermetallic phases and Al [53].

Relation type	**Crystallographic Orientation Relationships**		
Al and θAlFe	$(200)_{\theta}$ll$(200)_{Al}$	$(020)_{\theta}$ll$(020)_{Al}$	$(001)_{\theta}$ll$(001)_{Al}$
Al and θAlFe	$(100)_{\theta}$ll$(100)_{Al}$	$(020)_{\theta}$ll$(020)_{Al}$	$(001)_{\theta}$ll$(002)_{Al}$
Al and θAlFe	$(100)_{\theta}$ll$(10\text{-}1)_{Al}$	$(020)_{\theta}$ll$(020)_{Al}$	$(001)_{\theta}$ll$(202)_{Al}$
αAlSiFe and Al	$(100)_{\alpha}$ll$(100)_{Al}$	$(112)_{\alpha}$ll$(112)_{Al}$	$(111)_{\alpha}$ll$(111)_{Al}$
q_1AlSiFe and αAlSiFe	$(100)_{q1}$ll$(100)_{\alpha}$	$(020)_{q1}$ll$(020)_{\alpha}$	$(002)_{q1}$ll$(002)_{\alpha}$
q_1AlSiFe and Al	$(100)_{q1}$ll$(100)_{Al}$	$(020)_{q1}$ll$(020)_{Al}$	$(002)_{q1}$ll$(002)_{Al}$
q_2AlSiFe and αAlSiFe	$(101)_{q2}$ll$(101)_{\alpha}$	$(010)_{q2}$ll$(020)_{\alpha}$	$(001)_{q2}$ll$(002)_{\alpha}$

The Crystallographic data of the Al-Fe and Al-Si-Fe phases observed by Liu and Dunlop [53] is given in Table 3-3.

Table 3-3: List of crystallographic data acquired by Liu and Dunlop [53]

Phase	**Structure**	**a (nm)**	**b (nm)**	**c (nm)**	**B (°)**
θAl13Fe4	monoclinic - C2/m	1.5489	0.80831	1.2476	107.7
αAlSiFe	BCC – Im3	1.256			
q_1 AlSiFe	C centered orthorhombic	1.27	3.62	1.27	
q_2 AlSiFe	monoclinic	1.25	1.23	1.93	109

In Table 3-3, the structure of the α-AlSiFe phase was identified as BCC [53]. In our work with high purity Al-Si alloys, the structure of the α-AlSiFe phase was hexagonal. Liu and Dunlop [53] may have used commercial purity Al alloys for their study which would include a significant amount of Mn as impurity and this would mitigate the formation of the α-AlSiFe phase with the hexagonal structure and promote the formation of the cubic structure [54]

Westengen [55] reported that there are three possible crystal structures for the α-AlSiFe phase: cubic, hexagonal and tetragonal as shown in Figure 3-17. The main difference between the work of Westengen [55] and Liu and Dunlop [53] is that the former used more variations in solidification rates and may have used a higher purity of commercial alloy ingot.

Phase	Structure/ lattice parameters	Main elements	Refs.
Al	fcc, $a = 0.404$ nm	Al	1
α	bcc, $a = 1.256$ nm	Al, Fe, Si	15
α'	hexagonal $a = 1.23$ nm, $c = 2.62$ nm	Al, Fe, Si	18
α''	tetragonal, $a = 1.26$ nm, $c = 3.70$ nm	Al, Fe, Si	present work
Al_3Fe	monoclinic, $a = 1.549$ nm, $b = 0.808$ nm, $c = 1.247$ nm, $\measuredangle\beta = 107°$	Al, Fe	20
Al_6Fe	orthorhombic, c-centered $a = 0.649$ nm, $b = 0.744$ nm, $c = 0.879$ nm	Al, Fe	4
Al_mFe	tetragonal, body centered $a = 0.884$ nm, $c = 2.16$ nm	Al, Fe	5
Al_xFe	unknown, defect crystal structure	Al, Fe	present work
β'	monoclinic, $a = 0.89$ nm, $b = 0.49$ nm, $c = 4.16$ nm, $\measuredangle\beta = 92°$	Al, Fe, Si	present work
Si	fcc, $a = 0.542$ nm	Si	1

Figure 3-17: Phases observed in a commercial purity Al ingot [55].

Skjerpe [56] confirms the variation in the crystal structure of the various Al-Fe and Al-Fe-Si intermetallic phase sin commercial purity DC cast Al alloys as a function of the cooling rate during solidification. A summary of the observations [56] is shown in Figure 3-18. In Figure 3-18, the cooling rates for distances of 10, 50 and 100 mm are 8, 6 and 1 Ks^{-1}, respectively.

	Al_3Fe	Al_xFe	Al_mFe	Bcc α-AlFeSi α_T-AlFeSi	α''-AlFeSi
10 mm	—	—	6	12	—
50 mm	—	—	3	12	—
100 mm	11	5	4	2	1

Figure 3-18 : Results from Selected Area Diffraction Analysis of Thin Foil TEM Samples. The table shows the number of particles observed at various distances from the Ingot Surface [56]. Please refer to Figure 3-17 for the nomenclature and structure of the phases.

It is a well-known and established fact that the Al-Si-Fe intermetallic phases significantly influence the mechanical properties of the Al-Si alloys [16], however, it not universally accepted yet that such intermetallic phases serve as potent nucleation sites for the eutectic Si; nevertheless, experimental data from the literature [14,15,17,36,51,53] presents a multitude of evidence to support this theory. Additionally, literature [51,53,55] has shown that there is enough evidence to show that the Al-Fe and Al-Fe-Si intermetallic phases could act as potent sites to nucleate each other during solidification and heat treatment of the Al-Si alloys. Further, there are evidences to show that several Al-Fe and Al-Fe-Si intermetallic phases nucleate on the primary Al phase during solidification [53].

It is an aim of this dissertation to throw further light on the nucleation of the Al-Fe-Si intermetallic phases in the Al-Si-Fe high purity alloys and the role these phases play in nucleating the eutectic phases.

In the year 1981, Rivlin and Raynor [24] presented a comprehensive literature review of the solidification and intermetallic phases in the Al-Fe-Si ternary alloy system wherein the number of ternary intermetallic phases reported was ten. In the year 1940, Takeda and Mutazaki [42] suggested six ternary intermetallic phases and numerous invariant reactions in the Al-Fe-Si ternary alloy system. Rivlin and Raynor [24] a detailed chronological history of our understanding of the ternary Al-Si-Fe phase structures, compositions and nomenclatures. The τ_5 (α) and τ_6 (β) are more common stable intermetallic phases observed as end products in the Al rich corner of the Al-Fe-Si system [24]. A list of the variations in the composition and crystal lattice parameters reported in the literature for the prominent ternary intermetallic phases in the Al rich corner of the Al-Fe-Si ternary alloy system was presented by Rivlin and Raynor [24] and shown in Figure 3-19.

Phase	Formula	Analytic composition, wt-% Al	Fe	Si	Symmetry and lattice spacings, nm				Ref(s).
τ_2	...	...	35.3	12.8	**Cubic**				26, 34
					$a = 1.603$				
	...	...	33—38	13—18.5	**Monoclinic**				27
					$a = 1.78 \pm 0.01$ $b = 1.025 \pm 0.005$ $c = 0.89 \pm 0.005$ $\beta = 132°$				
τ_4					**Tetragonal**				
					a	c			
	Al_4FeSi_2	47.08	27.04	25.01	0.616	0.949			22
	...	...	...	...	0.612	0.948			32
	Al_3FeSi_2	...	...	...	0.607	0.950			35
	$Al_{57}Fe_{15}Si_{28}$	...	...	...	0.630 ± 0.0005	0.941 ± 0.0007			36
	$Al_{47}Fe_{15}Si_{38}$	...	...	...	0.612 ± 0.0005	0.953 ± 0.0007			36
					Cubic*				
τ_5	$Al_{20}Fe_5Si_2$	62.4	31.9	5.6	$a = 1.2548$				32
	...	...	...	...	$a = 1.256$ (138 atoms/cell)				37
	...	...	~32.5	8.4—10.3	**Hexagonal**				38
					$a = 1.23 \pm 0.01$ $c = 2.62 \pm 0.02$				
					Monoclinic				
					a	b	c	β	
τ_6	$Al_9Fe_2Si_2$	58.2	27.4	13.6	0.612	0.612	4.15	91°	32
		59.3	27.2	13.5					
	...	...	26.9	15.2	0.611	0.611	4.14	91°	26
	$Al_9Fe_2Si_2$	...	27.2	13.7	**Tetragonal**				39
					$a = 0.618 \pm 0.006$ $c = 4.25 \pm 0.05$				

*Cubic symmetry formed from hexagonal structure attributed in Ref. 27 to trace of dissolved manganese and X-ray powder patterns are reported as identical with those of Ref. 33 (not published). Symmetry and lattice parameters were confirmed by electron diffraction as $a = 1.23$ nm and $c = 2.62$ nm.

Figure 3-19: Variations in composition and crystal structure for the prominent ternary intermetallic phases in the Al rich corner of the Al-Fe-Si alloy system [24].

It is conjectured that the additions of Mn, Cr and/or Cu as minor alloying elements is soluble in the τ_5 phase and change the crystal structure from hexagonal to cubic or orthorhombic [24,57,58,59]. In commercial Al-Si casting alloys the α-Al-Si-Fe observed and reported has a cubic crystal structure and typically the Al-Si-(Fe,Mn,Cr) [60] phase due to the existence of high levels of transition elements in the alloy. However, the τ_5 phase evolved in the pure Al-Fe-Si system through the solidification reaction path proposed by Takeda and Mutazaki [42] has a hexagonal structure and the proposed variation of the τ_5 phase with the cubic structure due to solubility of Mn, Cr and/or Cu presented by Rivlin and Raynor [24] from their literature review may not be accurate. The cubic structure was attributed to a variant of the τ_5 phase simply

because the chine-script morphology of the cubic phase is shared by the τ_5 phase with the hexagonal structure as well. There is no evidence in the literature [24,44,51,53,54,55,56,57,58,59,61,62,63,64,65] that the τ_5 phase with the cubic structure follows the same reaction scheme as that with the hexagonal structure during solidification. It is possible that the τ_5 phase could evolve with either of the hexagonal or cubic structure, however, there is no direct evidence that both these structure variants occur by the same solidification reaction path. Hence, for clarity, we would like to attribute the hexagonal structure to the τ_5 phase and the phase with the cubic structure with the other alloying elements would be named α. Additionally, Cheng et al [63] carried out experiments wherein steel containing Cr was dipped into molten Al-10%Si alloy at 700°C for 10-180 seconds. The typical results obtained from this work [63] is presented in Figure 3-21 where we observe that the τ_5 phase is forming almost immediately on top of the steel (Fe) surface and the cubic Al-Si-Fe-Cr phase (α_c) is forming over the τ_5 phase suggesting that the α_c phase forms after the τ_5 phase and not due to substitution of Fe atoms in the τ_5 phase by Cr and/or Mn. Hence, naming the cubic phase as τ_5 as well [24,63] would be erroneous because they are two separate phases forming by separate solidification reaction paths.

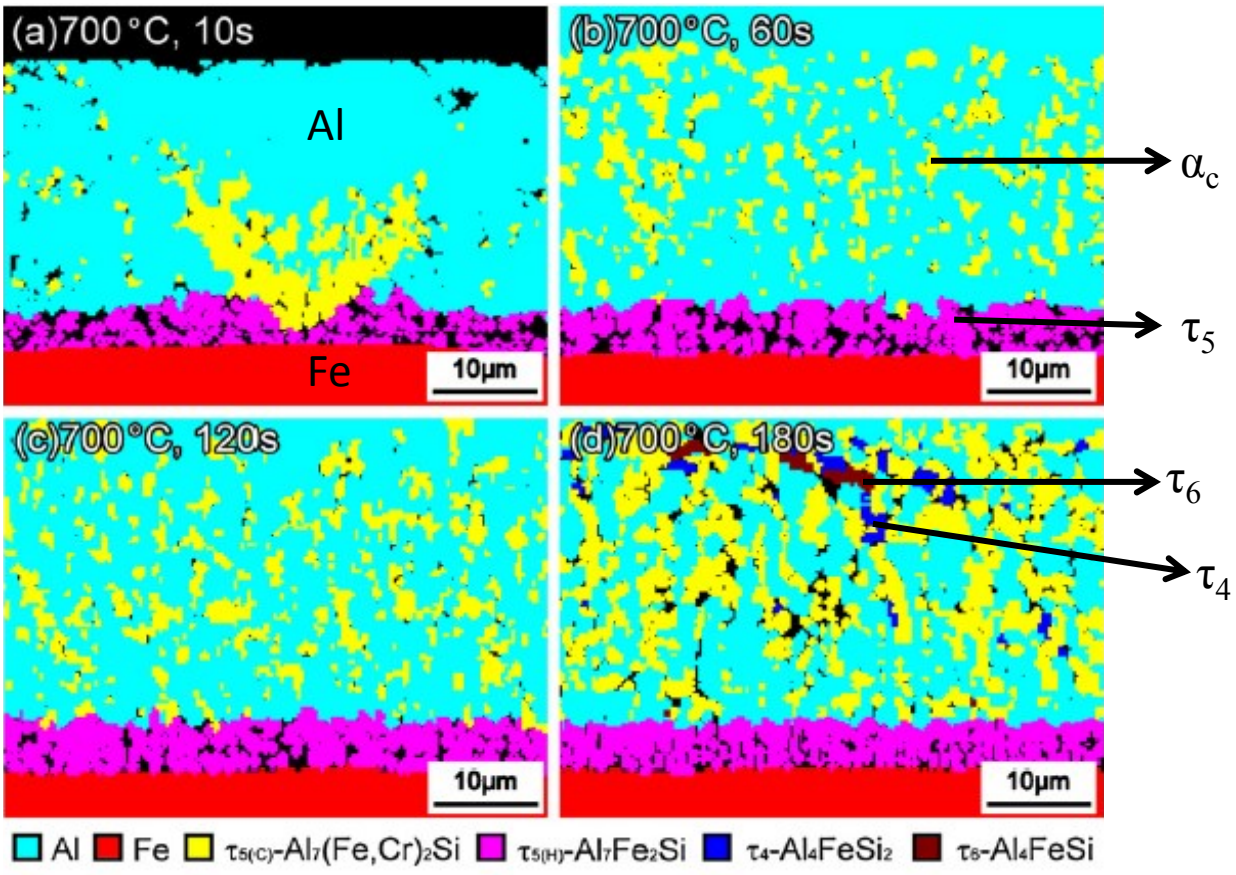

Figure 3-20: Phase maps obtained from an EBSD analysis of the sample of 5Cr–0.5Mo steel hot dipped in a molten bath of Al–10 wt% Si alloy for various immersion times at 700 ◦C. The nomenclature α_c was used to replace $\tau_{5(c)}$ in the bottom of the image [63].

The τ_6 intermetallic phase is also known as β, and this phase is universally accepted to exist with a monoclinic crystal structure [24]. Typically, the stoichiometry of the τ_6 phase could be written as $Al_{4.5}FeSi$, Al_5FeSi or $Al_9Fe_2Si_2$ [44]. Most researchers have reported a monoclinic structure for the τ_6 phase [24,61,67,70,76] with lattice parameters of **a** = 6.18 A, **b** = 6.18 A, **c** = 20.4 A and β = 90.4°. However a few researchers have also suggested a tetragonal structure [24,44] and an orthorhombic structure [44, 66]. Since, the lattice angle β is nearly at 90° and that the lattice parameters **a** and **b** are nearly similar, a few researchers may have mistakenly identified the monoclinic structure a tetragonal or orthorhombic. The evidences from this dissertation also suggest that the τ_6 phase is monoclinic.

In the year 1987, Stefaniay et al [67] presented the ranges of the composition and crystal lattice parameters for all the prominent intermetallic phases evolving in the Al rich corner of the Al-Fe-Si ternary system. They also present the changes to the composition and lattice parameters of these phases as a result of heat treatment of the solidified alloy sample.

In the year 2002, Gupta et al [68,69] carried out several critically controlled diffusion experiments with liquid Al-Si alloy of eutectic composition in contact with solid Fe. Gupta claims use of 99.999 purity metals and 99.95 purity iron. Since description is not involving exact composition of Al and/or Si of 99.999% purity it could be assumed that both Si and Al are 99.999% pure. Therefore the overall system is almost pure but regarding possible presence of Mn and Cr in the solid iron possibility of formation of cubic phases should not be dismissed.The diffusion experiments were carried out at several temperatures well over the liquidus temperature of the Al alloy for several time periods. The samples were solidified either by quenching or furnace cooling to study the effect of solidification rates. The results show that there is a marked difference in evolution of the Fe containing intermetallic phases between a 1h and 4h diffusion experiment at around 1383K (1110 °C) [68] as shown by Figure 3-21. Further, there is a marked difference in the intermetallic phases existing at room temperature between samples quenched and furnace cooled from the diffusion experiment temperature [68], respectively as shown in Figure 3-22. Another notable feature is the marked difference in the intermetallic phases between the diffusion experiments at 1338K (1115 °C) (refer to Figure 3-21) and 1293K (1020 °C) (refer to Figure 3-22) for 4 hours each. These results strongly suggest that the evolution and stability of the Al-Fe-Si intermetallic phases in the Al-Si alloys are significantly sensitive to the melt temperature and the rate of solidification.

Average composition of the intermetallic compounds (at.%)

Intermetallic compound	1 h, 1100 °C, quenched				4 h, 1115 °C, quenched			
	Fe	Al	Si	x	Fe	Al	Si	x
$Fe(Al_{1-x}Si_x)_3$	23.95	70.61	5.42	0.0712	–	–	–	–
$Fe_2(Al_{1-x}Si_x)_5$	27.34	65.06	7.57	0.104	29.35	66.23	4.42	0.0625
$Fe(Al_{1-x}Si_x)_2$	–	–	–	–	–	–	–	–
$Fe_2(Al_{1-x}Si_x)_3$	–	–	–	–	37.33	51.34	11.32	0.18
$Fe(Al_{1-x}Si_x)$	46.36	43.22	10.4	0.194	44.56	43.85	11.58	0.21
$Fe_3(Al_{1-x}Si_x)$	71.69	27.33	1.06	0.037	77.25	20.3	2.45	0.107
τ_1	39.2	40.87	19.56		(Fe_2Al_2Si)			
τ_2	22.89	55.75	21.33		$(Fe_2Al_5Si_2)$			
τ_3	32.24	44.18	23.55		$(Fe_3Al_4Si_2)$			
τ_4	15.02	59.15	25.70		$(Fe_{15}Al_{58}Si_{27})$			
τ_5	20.2	69.09	10.69		(Fe_2Al_7Si)			
τ_6	15.07	67.04	17.86		$(FeAl_4Si)$			
τ_7	–	–	–		$(Fe_{22}Al_{40}Si_{38})$			
τ_9	35.6	35.07	29.31		$(Fe_{36}Al_{36}Si_{28})$			
τ_{10}	26.73	58.86	14.41		$(Fe_{25}Al_{60}Si_{15})$			

Figure 3-21: Effect of time on the Fe based intermetallic phases in the diffusion experiments by Gupta [68].

Intermetallic compound	4 h, 1020 °C, quenched				4 h, 1020 °C, furnace-cooled			
	Fe	Al	Si	x	Fe>	Al	Si	x
$Fe(Al_{1-x}Si_x)_3$	22.95	71.4	5.64	0.073	23.09	71.37	5.53	0.072
$Fe_2(Al_{1-x}Si_x)_5$	28.17	67.42	4.4	0.061	26.55	70.62	2.82	0.038
$Fe_2(Al_{1-x}Si_x)_3$	–	–	–	–	38.45	55.92	5.62	0.091
$Fe(Al_{1-x}Si_x)$	45.13	38.62	16.24	0.296	46.45	36.21	17.33	0.3238
	44.91	42.6	12.48	0.226	32.7	50.44	16.84	0.25
$Fe_3(Al_{1-x}Si_x)$	76.0	18.69	5.31	0.221	76.22	19.89	3.89	0.163
τ_1	–	–	–	–	35.72	41.16	23.12	
τ_2	23.12	55.04	21.79		20.62	59.76	19.6	
τ_4	15.05	58.9	26.04		–	–	–	
τ_5	20.2	69.11	10.69		–	–	–	
τ_6	16.31	66.10	17.59		–	–	–	
τ_7	–	–	–		24.78	36.52	38.7	
τ_9	–	–	–		36.01	36.13	27.85	
τ_{10}	24.2	62.45	13.34		–	–	–	

Figure 3-22 Effect of the solidification rate after the diffusion experiments by Gupta [68].

In the year 2002, another contemporary review of the intermetallic phases in the Al-Fe-Si ternary system was carried out by Raghavan [70]. Summary of the phases reviewed by Raghavan is presented in the Figure 3-24. The only discrepancy observed in the Figure 3-24 was that the composition of the τ_5 phase contradicts all the other reported in the literature. Typical stoichiometry for the τ_5 phase is around $Al_{71}Si_{10}Fe_{20}$ [71]. In present work, several references [71,72,73,74,75,76,77,78] were used to identify and confirm the intermetallic phases observed in the solidified microstructure.

A notable work cited by Rivlin and Raynor [24] is that of Iglessis [79] which suggests that in the Al-Si eutectic alloy with 0.24 wt%Fe, the τ_5 evolves at solidification rates of less than 3 $K.min^{-1}$ and there is no evolution of the τ_6 phase until above the solidification rate of 3 $K.min^{-1}$; increasing the Fe content in the alloy to 0.5 wt% increasing the critical solidification rate to 300 $K.min^{-1}$ and at an Fe content of 0.8 wt% the rate increases to 500 $K.min^{-1}$. Not much discussion was presented of this work by Iglessis [79] by Rivlin and Raynor [24] or by the two other publications [61,64] who have cited this work [79]. A reason for this lapse in the discussion may be attributed the anomalous and singular results reported by Iglessis [79] which contradicts the known phase diagram and solidification paths of the Al-Fe-Si alloy system. Figure 3-23 (a) and (b) show the typical results from Iglessis [79] for the Al-10wt%Si-0.25wt%Fe and Al-10wt%Si-0.5wt%Fe alloys, respectively; wherein a plot of the eutectic temperature versus square root of the cooling rate at the eutectic temperature presents the regions of high cooling rates in which the τ_5 (α in the figure) phase is present in the solidified sample and low cooling rates in which the τ_6 (β in the figure) phase is present. It is notable that the results of our experiments presented in this dissertation corroborate the results presented by Iglessis [79] as explained by Rivlin and Raynor [24].

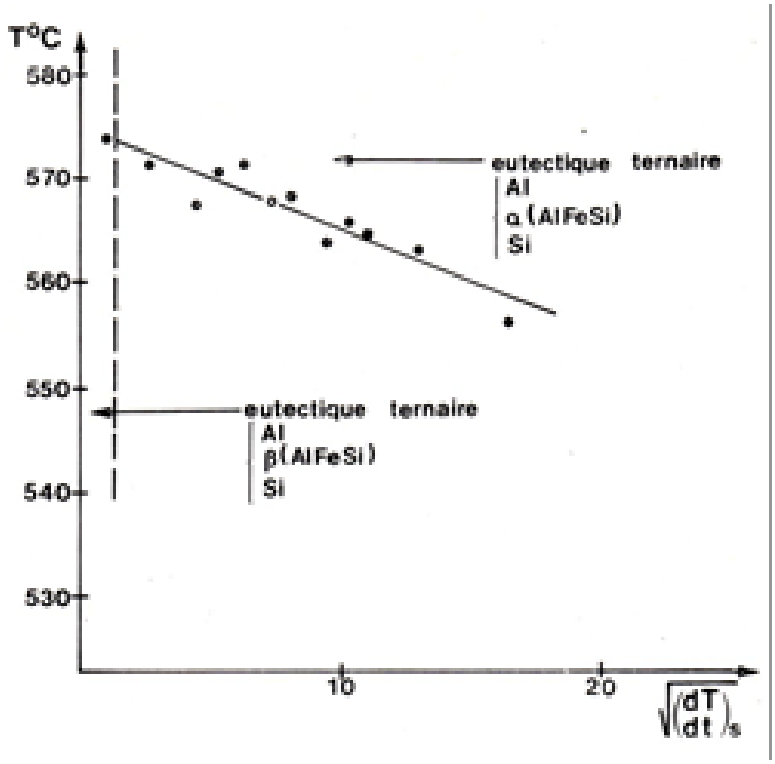

(a)

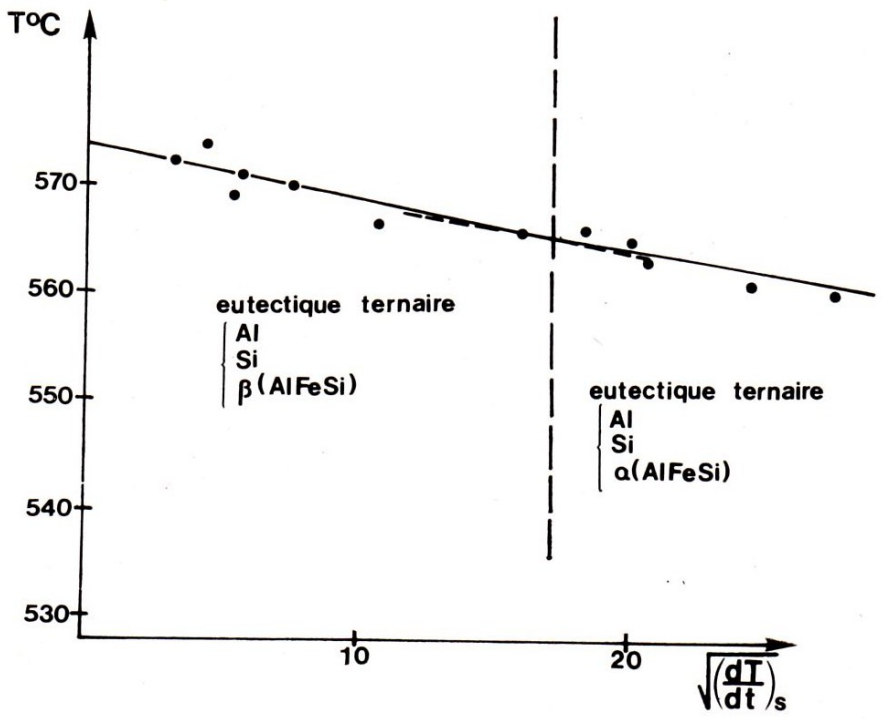

(b)

Figure 3-23: Plot of eutectic temperature and cooling rate during solidification of the eutectic phases showing the regions where the τ_5 (α in the images) and τ_6 (β in the images) were observed in the respective solidified samples. (a) Al-10wt%Si-0.25wt%Fe and (b) Al-10 wt%Si-0.5wt%Fe alloys [79].

Liu and Chang [80] presented a summary of the intermetallic phases in the Al-Fe-Si ternary alloy system through rigorous thermodynamic models and simulations. Their work is quite comprehensive and compare well with several experimental observations on the related topics. One of the major drawbacks of mere thermodynamic models is that anomalous behaviours of solute redistribution during solidification, effect of trace level impurity elements in the alloys on the resultant intermetallic phases and effect of solidification rates on the phase evolution would not be fully captured. Some of the results of this dissertation present typical examples of such differences between the thermodynamic model predictions and experimental observations. It was found in this work that both the Fe and Si atoms in the liquid Al alloy show anomalous behaviour in their distribution in the melt which leads to evolution of intermetallic phases that contradict thermodynamic predictions.

Phase	Composition, at.% Al	Fe	Si	Pearson Symbol	Space Group	Lattice Parameter, nm	Reference
$Al_2Fe_3Si_3$ (τ_1)	25.0	37.5	37.5	*aP*16	$P\bar{1}$	a = 0.46512 b = 0.63261 c = 0.7499 α = 101.375° β = 105.923° γ = 101.237°	1996Yan
Al_2FeSi (τ_{23})	50.0	25.0	25.0	(*o*)	*Cmma*	a = 0.7995 b = 1.5162 c = 1.5221	1989Ger2
$Al_{2.7}FeSi_{2.3}$ (τ_4) (δ)	45.0	16.7	38.3	*tI*24	*I*4/*mcm*	a = 0.607 c = 0.950	1969Pan
				or			
				*oP*24	*Pbcn*	a = 0.6061 b = 0.6061 c = 0.9525	1995Gue1
$Al_{15}Fe_6Si_5$ (τ_5) (α)	57.7	23.1	19.2	(*h*)	$P6_3/mmc$	a = 1.2404 c = 2.6223	1977Cor
$Al_{4.5}FeSi$ (τ_6) (β)	69.2	15.4	15.4	*mC*52	*A*2/*a*	a = 0.6161 b = 0.6175 c = 2.0813 β = 90.42°	1994Rom
$Al_{63.5}Fe_{20.5}Si_{16}$ (τ_7) (γ)	63.5	20.5	16.0	(*m*)		a = 1.78 b = 1.025 c = 0.890 β = 132°	1967Mun
$Al_6Fe_4Si_6$ (τ_8)	37.5	25.0	37.5	*mP*64	$P2_1/n$	a = 0.7179 b = 0.8354 c = 1.4455 β = 93.80°	1995Gue2
$Al_2Fe_3Si_4$ (τ')	22.2	33.3	44.4	*oC*36	*Cmcm*	a = 0.36687 b = 1.2385 c = 1.0147	1996Yan
$Al_4Fe_{1.7}Si$ (τ'')	59.7	25.4	14.9	(*h*)	$P6_3/mmc$	a = 0.7509 c = 0.7594	1989Ger1

(*o*) = orthorhombic; (*h*) = hexagonal; (*m*) = monoclinic

Figure 3-24: Al-Si-Fe crystal structure and lattice parameter data compiled by Raghavan [70].

In the year 2007, Krendelsberger et al [81] published a comprehensive work on the phase identification and characterization in the Al-Fe-Si ternary system by rigorous solidification experiments using the DTA and characterization using the X-ray diffraction and SEM-EDX techniques. Most report data in the literature were verified and validated by Krendelsberger et al [81] with additional new data as shown in Figure 3-25; there are now eleven stable ternary intermetallic phases in the Al-Fe-Si system.

Phase	Composition	Reference	Crystal Structure Data
τ_1	$Al_{21.5–45}$ $Fe_{36.5–37.5}$ $Si_{8.5–41.5}$	6	confirming Refs. 4, 5, 18, and 19
	$Al_2Fe_3Si_3$	20	*P*-1, *aP*16 a = 0.4651(2) nm, α = 101.38(2) deg
			b = 0.6326(2) nm, β = 105.92(2) deg
			c = 0.7499(3) nm, γ = 101.24(2) deg
	other names found in the literature: $Al_3Fe_3Si_2$, K1,[4] D,E,[5,21] τ_9[2,18]		
τ_2	$Al_{53.9–65.3}$ $Fe_{19.5–20.5}$ $Si_{15.2–25.6}$	6	confirming Refs. 5, 9, 10, 18, 19, and 22
	Al_3FeSi	9	..., *mC** a = 1.78(1) nm
			b = 1.025(5) nm, β = 132 deg
			c = 0.890(5) nm
	other names found in the literature: β,[3] α_3,[10] γ,[7,9,22,23] K,[5,21] $Al_5Fe_2Si_2$[2,18]		
τ_3	$Al_{53–56}$ $Fe_{23.5–24.5}$ $Si_{20.5–22.5}$	6	confirming Ref. 4
	Al_2FeSi	24	*Cmma*, *oC*128 a = 0.7995(2) nm
			b = 1.5162(6) nm
			c = 1.5221(6) nm
	other names found in the literature: ζ,[3] $Al_{12}Fe_6Si_5$, K_2,[4] G,[5,21] τ_2,[22] $Al_9Fe_5Si_5$,[2] F,[21] τ_{23}[23]		
τ_4	$Al_{45.5–54}$ $Fe_{15.5–16.5}$ $Si_{30.5–38}$	6	confirming Refs. 4, 5, and 25
	Al_3FeSi_2	26	*I*4/*mcm*, *tI*24, $GaPd_5$ a = 0.607 nm
			c = 0.950 m
	other names found in the literature: δ,[3,7,10,23] K_4,[4] γ,[12] A,[5,21] Al_3FeSi_3,[2,25] $Al_{2.7}FeSi_{2.3}$[27]		
τ_5	$Al_{68–72}$ $Fe_{18–19.5}$ $Si_{10–12.5}$	6	confirming Refs. 5, 12, 18, 19, 22, and 28
	$Al_{7.4}Fe_2Si$	29	$P6_3/mmc$, *hP*(244–7.4) a = 1.2404(1) nm
			c = 2.6234(2) nm
	other names found in the literature: β,[3] K_5,[4] α,[11,12,22,29] α_2,[10] M,[5,21] $Al_5Fe_6Si_5$,[27] Al_7Fe_2Si[18,30]		
τ_6	$Al_{64.5–67.5}$ $Fe_{15.5–16.5}$ $Si_{17–19}$	6	confirming Refs. 5, 12, 18, 19, 22, 28, 31, and 32
	$Al_{4.5}FeSi$	33	*C*2/*c*, *mC*52 a = 2.0813(6) nm
			b = 0.6175(3) nm, β = 90.42(3) deg
			c = 0.6161(3) nm
	other names found in the literature: X,[3] K_6,[4] β,[7,10,11,12,22] L,[5,21] $Al_9Fe_2Si_2$,[2] Al_4FeSi[18]		
τ_7	$Al_{39.2–48.7}$ $Fe_{23.5–24.5}$ $Si_{27.8–36.3}$	6	confirming Refs. 4, 5, 18, and 34
	$Al_3Fe_2Si_3$	34	$P2_1/n$, *mP*64 a = 0.7179(2) nm
			b = 0.8354(2) nm, β = 93.80(2) deg
			c = 1.4455(4) nm
	other names found in the literature: ζ,[3] K_3,[4] τ_3,[1] B,[5,21] $Al_8Fe_5Si_7$,[21] τ_{23},[23] $Al_6Fe_4Si_6$, τ_8[27]		
τ_8	$Al_{24.1–28.6}$ $Fe_{31.9–32.9}$ $Si_{39.5–43}$	6	or $Al_{38}Fe_{32}Si_{30}$[5] or $Al_{44}Fe_{32}Si_{24}$[18]
	$Al_2Fe_3Si_4$	20	*Cmcm*, *oC*48 a = 0.3669(2) nm
			b = 1.2385(7) nm
			c = 1.0147(5) nm
	other names found in the literature: C,[5,21] τ'[27]		
τ_{10}	$Al_{57–59}$ $Fe_{24–25}$ $Si_{17–18}$	6	or $Al_{60}Fe_{25}Si_{15}$[5] or $Al_{59–63}Fe_{24–27}Si_{13–14}$[18]
		this work	*hexagonal* a = 1.5518(2) nm
			c = 0.7297(1) nm
	other names found in the literature: F,[5] τ_{23},[23] $Al_4Fe_{1.7}Si$, τ ",[27] $Al_9Fe_4Si_3$[6]		
τ_{11}	$Al_{64–66.5}$ $Fe_{24–25}$ $Si_{9.5–11}$	6	
	$Al_4Fe_{1.7}Si$	16	$P6_3/mmc$, *hP*28, Co_2Al_5 a = 0.7509(3) nm
			c = 0.7594(3) nm
	other names found in the literature: ζ,[3] F (high-temp. modification),[5] Al_5Fe_2Si[6]		

Figure 3-25: Comprehensive list of the ternary intermetallic phases in the AL-Fe-Si system developed by Krendelsberger et al [81].

In the year 2008, Du et al [82] presented a comprehensive understanding of the solidification phases evolving in the Al-Fe-Si system through rigorous thermodynamic modeling using the CALPHAD approach. They have verified and validate several stable equilibrium intermetallic phases in the literature that were proposed through experiments.

In the year 2004, Bosselet et al [83] followed by Roger et al [84] in the year 2011 presented a comprehensive understanding of the temperature ranges at which the various ternary intermetallic phases are stable in the liquid and solid alloy samples. Their work [83,84] presents the maximum temperature at which each ternary intermetallic phase are stable solid phases and further, present the solid state transformations among these ternary intermetallic phases at various temperatures. Figure 3-26 presents the findings of Bosselet et al [83].

Composé et formule approchée	Domaine d'existence à 1000 K (at%)	Symmétrie, structure, paramètres de maille (nm)	Température de décomposition (K)	Références, commentaires
$\tau 1$–9 $Al_2Fe_3Si_3$	Fe: 36,5-37,5 Si: 18,5-41,5	Triclinique, *P-1*, a = 0,465 ; b = 0,633 ; c = 0,750, α = 101,4° ; β = 105,9° ; γ = 101,2°	1323	[14]
$\tau_2 = \gamma$ Al_3FeSi	Fe: 19,5-20,5 Si: 15,2-25,6	Monoclinique, a = 1,78 ; b = 1,025 ; c = 0,890 ; β = 132°	1213	[15]
τ_3 Al_2FeSi	Fe: 23,5-24,5 Si: 20,5-22,5	Orthorhombique, *Cmma* a = 0,799 ; b = 1,516 ; c = 1,522	1208	[16]
$\tau_4 = \delta$ Al_3FeSi_2	Fe: 15,5-16,5 Si: 30,5-38	Quadratique, *I4/mcm* a =0,6061 ; c = 0,9525 Orthorhombic, *Pbcn* a = 0,6061 ; b = 0,6061 ; c = 0,9525	1138	[17] Surstructure [17]
$\tau_5 = \alpha = \alpha_h$ $Al_{7,4}Fe_2Si$	Fe:18-19,5 Si: 10-12,5	Hexagonal, *P63/mmc* a = 1,2404 ; c = 2,6234	1128	[18]
$\tau_6 = \beta$ $Al_{4,5}FeSi$	Fe: 15,5-16,5 Si: 17-19 (vers 873K)	Monoclinique, *A2/a* a = 0,616 ; b = 0,617 ; c = 2,081 ; β = 90,4°	940±5	[15, 19]
$\tau 7$ $Al_3Fe_2Si_3$	Fe:23,5-24,5 Si: 27,8-36,3	Monoclinique, $P2_1/n$, a = 0,718 ; b= 0,835 ; c = 1,445 ; β = 93,8°	-	[20]
$\tau 8$ $Al_2Fe_3Si_4$	Fe: 31,9-32,9 Si: 39,5-43	Orthorhombique, *Cmcm* a = 0,367 ; b = 1,238 ; c = 1,015	-	[14]
$\tau 10$ $Al_9Fe_4Si_3$	Fe: 24-25 Si: 17-18	Orthorhombique	1050	(présent travail)
$\tau 11$ Al_5Fe_2Si	Fe: 24-25 Si: 9,5-11	Hexagonal, $P6_3/mmc$ a = 0,751 ; c = 0,755	Td > 1150	confondu avec $\tau 10$ dans [21]

Figure 3-26: Composition, structure and stability temperature limits for Al-Si-Fe ternary intermetallic phases [Source : 83].

The data in Figure 3-26 relays a critical message in that, when the Al-Si alloys are prepared commercially, Fe is an unavoidable impurity which exists as dissolved element in the primary Al phase, or as binary or ternary intermetallic phases in the solidified Al ingot used as raw material. Westengen [55], Liu and Dunlop [53] and Skjerpe [56] individually demonstrated that

there several stable Fe containing intermetallic phases (binary and ternary) in a commercial pure Al ingot as shown in Figure 3-17. The Al-Si alloy in the industry made from Al ingots contains a range of Fe based intermetallic phases. The most common phases in the commercial purity Al ingot are the binary θ-$Al_{13}Fe_4$ or the τ_5 ternary Al-Fe-Si phase. According to Rivlin and Raynor [24] the θ-$Al_{13}Fe_4$ remains as stable solid phase in the melt until 1467 K (1194 °C) and Figure 3-26, the τ_5 ternary Al-Fe-Si phase is stable until 1128 K (855 °C) which would mean that these phases could exist after a commercial Al-Si casting alloy is prepared and influence the preferential nucleation of certain ternary intermetallic phases over others during the casting, leading to anomalous deviations from thermodynamic model predictions.

Additionally, the cooling rate during solidification of the Al-Fe-Si alloys significantly influence the intermetallic phases found in the final solidified structure. Griger et al [61] prepared specific compositions of the ternary Al-Fe-Si system and solidified them at various cooling rates to show the variations in the phases obtained in the end sample as shown in Figure 3-27. Griger et al prepared different alloys with different techniques : atomization for fast cooling rates, mechanical alloying for certain compositions since such techniques are different from regular casting it highly possible to get different intermetallic phases than comparing with regular cast alloys with same composition. Young and Clyne [85] carried out similar experiments with binary Al-Fe alloys and reported the influence of cooling rate during solidification on the final solidified intermetallic phase as shown in Figure 3-28.

Phase field	Composition (%)			Cooling rate (°C s^{-1})					
	Fe	Si	Fe/Si	< 10	100	500	1000	10^4	10^5
α-Al	0.9	0.25	3.6	$A_3(A_6)$	–	–	–	–	–
	0.5	0.2	2.5	α_c	α_c	α_c	–	–	α_c
	0.5	0.5	1.0	α_c	–	–	–	–	–
	0.2	0.2	1.0	α_c	–	–	–	–	–
	0.5	1.0	0.5	β	–	n.d.		–	n.d.
Θ	10.9	1.7	6.4	–	–	–	A_3 + Si	$\alpha_c + \alpha_H$	α_c
	10.0	2.0	5.0	–	$\alpha_c + A_3$	α_c	–	–	–
	10.4	2.2	4.7	–	$\alpha_c + A_3$	$\alpha_c + A_3$	$\alpha_c + (\alpha_H)$	–	–
	7.6	2.1	3.5	–	–	–	–	–	α_c
	8.6	2.5	3.4	$A_3 + \alpha_c$	–	–	–	–	–
	7.5	2.4	3.0	–	$\alpha_c + A_3$	$\alpha_c + A_3$	α_c	–	–
	3.3	1.1	3.0	$A_3 + \alpha_c$	–	–		–	–
	5.2	1.9	2.7	$\alpha_c + A_3$	–	–	–	–	–
	4.3	5.0	0.8	$\alpha_H + \alpha_c$	–	–		–	–
α	7.0	13.6	0.5	β + Si	–	–		–	–
	5.0	9.7	0.5	β + Si	–	–	–	–	–
	5.0	12.0	0.4	–	–	–	–	δ + β + Si	Si + δ + β
β	1.5	9.2	0.2	β + Si	–	–	–	–	–

α, β and δ, α-, β- and δ-AlFeSi, respectively; $_c$, cubic; $_H$, hexagonal.

Figure 3-27: Formation of Al-Fe-Si intermetallic phases as a function of Fe and Si contents and cooling rate during solidification [61].

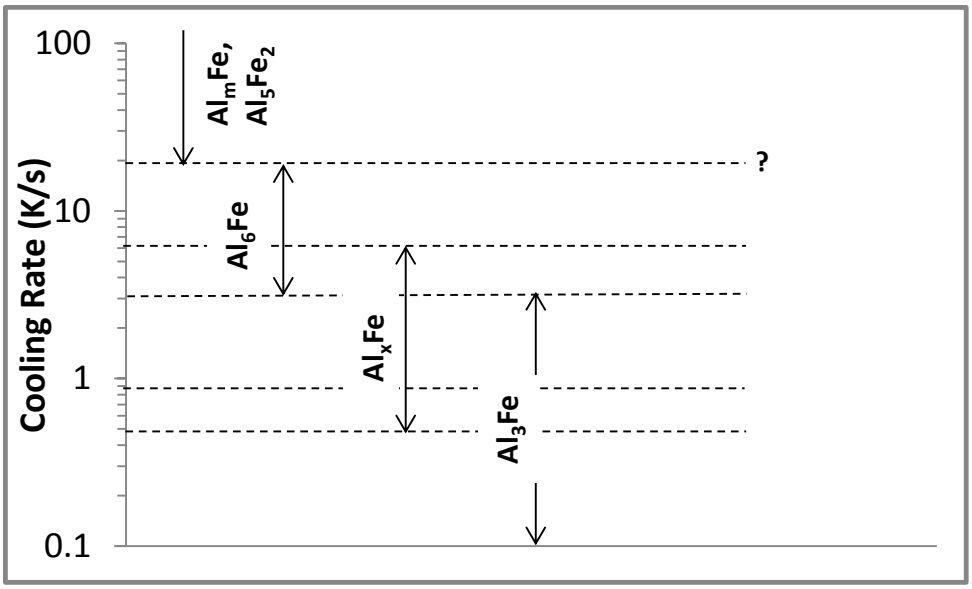

Figure 3-28: Approximate cooling rate regimes for formation of the different binary Al-Fe intermetallic phases in hypoeutectic Al-Fe alloys [85].

Superheat effect upon Al-Fe-Si intermetallic phases was investigated by Awano and Shimizu [86] . Awano and Shimizu showed clear transition between α phase through two phase region to β phase region of Al-Si-Fe and Al-Si-Fe-Mg alloys depending on superheat. For same composition at different superheats Awano and Shimizu observed mostly script like phases for high superheat and plate like phases for small superheat. Effect was observed for different Si concentrations from 6 to 22 wt% [86]. In pure alloy cast from 99.9999% Si and Al and 99.99 % Fe two phases were observed at all superheats. Duration of melt holding time or casting under vacuum ruled out gas dissolution or oxides as source of the change. Phase identification showed compositions which did not resemble τ_5 or τ_6 phases, despite that Awano and Shimizu called these phases α and β. X-ray diffraction of appropriate alloys identified phase called T_2 referenced to 1952 β phase reference which now days is obsolete. No identification for α phase through X-Ray diffraction was made. Awano and Shimizu called some impurities responsible for a change in the phases. Cooling rate was also mentioned to favor α or β – fast cooling favors α and slow favors β. This paper is not presenting any feasible theory to explain transition nor reflects change in cooling rate. Ability to change phases in cast alloy by superheat is important fact to be mentioned in discussion part of this thesis.

In summary, the literature on the subject of the intermetallic phases in the Al-Si-Fe ternary system, specifically, the Al rich corner of the system presents a comprehensive and valid list of all the intermetallic phases that evolve during solidification under near equilibrium conditions. However, there is very little information presented on the identification of the intermetallic phases in the pure Al-Si-Fe system with the Si ranges between 3 and 12.5 wt% and Fe between 0 and 1 wt%, and the effect of the cooling rate during solidification and the effect of initial superheat temperature of the melt above the respective liquidus temperature on the evolution of the intermetallic phases. A large number of researches have been carried out on the

commercial purity Al-Si alloy system where the nature and formation of the intermetallic phases during solidification is significantly affected by the minor alloying elements in the alloys such as Mg, Ti, Sr and transition elements. It is the aim of this dissertation to address the above-mentioned lack of detailed information in the literature to enable a better understanding of the commercially important Al-Si hypoeutectic alloys.

3.3 MODIFICATION OF EUTECTIC PHASES BY Sr ADDITION

Modification of the morphology of the eutectic Si phase in commercial hypoeutectic Al-Si cast alloys by addition of NaCl and/or CaF_2 was patented by Pacz in 1921 [26]. Since then, there has been a significantly number of publications in the literature about the methods and mechanisms of the morphological modification of the eutectic Si phase (plate-like to fibrous) by trace level additions of several elements such as Sr, Na, Yb, Y, La, Ce, etc., [2,16,17,30,31,32,33,]. Several contradicting theories have been presented from nearly a century of research on the topic of modification of the Si phase, among these there are four in-depth literature reviews on this topic [16,29,30,34]. Among these, the review by Makhlouf et al [30] is the most comprehensive.

In the year 1924, Edwards and Archer [87] first proposed that when trace levels of Na is added to the melt, there is a significant undercooling of about 5 K or greater below the eutectic temperature during the evolution of the eutectic phases in the Al-Si binary alloys. In the year 1984, Hanna and Lu [27] presented the liquidus and eutectic temperatures for the binary Al-Si alloys with an without Sr modification, for a range of 1 to 25wt% Si in them, as shown in Figure 3-29; wherein it can be observed that during the cooling of the alloys, the Sr-modified alloys shows marked undercooling of the eutectic temperature which was absent during the heating process. This shows that Sr addition alters the evolution of the eutectic phases during solidification and not during the re-melting of the alloy thereby confirming that the lower eutectic temperatures are not an artifact of the ternary Al-Si-Sr alloy system. Other publications [88,89,90] also validate and quantify the marked undercooling of the eutectic temperature in the Al-Si alloys because of trace level addition of a modifying element such as Sr.

Composition Wt Pct Si	Liquidus °C		Eutectic °C			
	Normal	Modified	Normal		Modified	
	(Cooling Only)		Cooling	Heating	Cooling	Heating
1.94	647.5	647.5	574.2	577.3	568.0	576.3
3.95	632.0	632.0	573.8	577.8	566.4	576.3
6.35	618.5	617.0	574.7	578.0	569.0	578.0
8.08	605.0	605.0	575.2	577.0	568.8	576.0
10.91	588.5	588.0	577.0	579.6	571.4	578.0
12.0	579.0	580.0	576.6	579.0	568.5	577.8
12.60	—	575.5	574.4	578.5	571.0	577.1
13.78	588.0	580.0	576.2	578.4	573.0	577.0
14.56	599.0	585.0	577.3	579.8	572.0	577.1
16.22	623.0	613.0	576.5	578.3	570.0	577.5
18.00	646.0	636.0	575.5	—	569.4	578.0
19.24	664.0	659.0	575.5	578.0	569.0	578.0
21.0	692.0	682.0	574.3	—	568.0	—
23.0	715.0	709.0	574.0	578.0	569.1	577.0

Figure 3-29: Liquidus and eutectic temperatures obtained by thermal analysis for unmodified and Sr-modified Al-Si alloys for both the solidification and re-melting at 4 K/min [27].

In the year 2011, Srirangam et al [91] presented a very concise and comprehensive discussion on the effect of Sr addition on the morphological changes to the eutectic phases in the commercially important Al-Si hypoeutectic alloys. Modification of eutectic Si by addition of Sr or Na was studied by many researchers [14,15,17,92,93,94,95 ,96,97,98,99,100,101]; the proposed theories and mechanisms are contradictive. There is no consensus on the how Sr addition modifies eutectic Si. Srirangam et al [91] proposed that Sr breaks Si-Si clusters in the melt thereby changing the nucleation of eutectic Si during eutectic reaction through changes in the physical properties of the melt such as viscosity and interfacial energy. Since clusters are an essential stage in the process of homogeneous nucleation, delay in cluster formation would delay nucleation of eutectic Si; delayed nucleation will lead to excessive amount of undercooling. Thall and Chalmers [102] proposed that interfacial energy change is responsible for change in morphology of eutectic phases. Gayler [96], Gwyer [97] and Rothery [99] proposed similar theories for modification by Na and Sr elements based upon change in the surface energy in the liquid. No experimental data relating Sr addition to liquid properties was obtained during the 1970-s,80-s or 90-s. The ability of Sr addition to limit Si phase growth was among other explanations of eutectic Si modification [27,92,93] proposed since the 1970-s. Another proposed mechanism was the inhibition of nucleation sites (oxides, phosphorous) by Sr [91–95,101]. Such theories could not explain the refinement of eutectic Al observed by Shankar et al [17]. An additional experimental outcome observed in this project shows that addition of trace level of Sr to the Al-Si alloys significantly altered the nature of the Fe bearing intermetallic phases thereby altering the heterogeneous nucleation sites for the eutectic Si phase during solidification. The details of these observations are presented in the results and conclusions chapter of this dissertation.

Bian et al. [103] reported that based upon scattering data from the liquid melt, the atomic structure of Al–Si eutectic melt changes with the addition of Sr. Malik [*104*] showed that the addition of Sr also changes the melt viscosity of the Al-Si alloys.

The mechanism of Sr modification presented by Shankar et al [17] and later by Srirangam et al [91] where the effect of Sr altering the nucleation environment of the eutectic Si phase in the interdendritic alloy melt during solidification seems to be the more agreeable explanation coupled with the observed experimental evidences. The earlier theory [105] that the morphological modification of the eutectic Si is attributed solely to the induced multiple twinning by atoms of Sr interfering with the growth ledges of the Si phase does not validate several experimental observations. For example, there is an observed undercooling in the nucleation temperature of the eutectic phases in the alloys modified with trace elements are not explained by the latter theory.

In the year 1957,Plumb and Lewis [106] used radioactive Na addition to the Al-Si alloy and found that the atoms of Na resides in the primary Al phase in the solidified sample. Recent work by Siemensen et al [107] used the nanoSIMS technology to confirm the work by Plumb

and Lewis [106] and suggested that the modifying elements such as Na, Ca and Sr segregated in different phases in the solidified microstructure of the Al-Si alloys and further suggested that the mechanism of modification of the eutectic Si phase by each of these elements could be significantly different from each other. Recent work by Timpel et al [28] showed that there are two types of Sr segregation in the Al-Si alloys; one is the elemental segregation and the other in the form of cylindrical Al_2Si_2Sr intermetallic phase. The elemental segregation is suggested as being responsible for "encapsulating" of eutectic Si particles and restricting it growth [28], while Al-Si-Sr intermetallic phase occupies the {111} stacking fault growth steps and induce twinning in the eutectic Si.

Samuel et al [108] have discovered destabilization of β-Al-Si-Fe (τ_6) by Sr modification and Cao and Campbell [109] reported morphological changes in the cubic α intermetallic phases ($Al_{15}(FeMn)_3Si_2$ and $Al_{15}(FeCr)_3Si_2$) due to addition of Sr to the Al-Si commercial alloy. Kumari et al [110] reported the refinement of the β-Al-Si-Fe phase morphology due to Sr addition to the commercial Al-Si alloy, LM25. Eidhed [111] reported that Sr addition to a commercial Al-Si die casting alloy mitigates the evolution of the β-Al-Si-Fe (τ_6) and promotes the evolution of the cubic α-Al-(Fe,Cr)-Si phase in the solidified structure and the total volume fraction of the intermetallic phases in the solidified stricture reduces.

Han et al [50] carried out directional solidification experiments on the Al-7Si-0.9Fe alloy containing 0.03 wt%Sr in them and found that the evolution of the β-Al-Si-Fe (τ_6) is mitigated and the evolution of the δ-Al-Si-Fe (τ_4) is promoted. It is notable that both the β (τ_6) and δ (τ_4) have a similar plate-like morphologies which would be indiscernible when viewed in the microstructure as shown by Figure 3-14 and Figure 3-15. Further, the authors [50] state that the presence and volume fraction of the β (τ_6) and δ (τ_4) intermetallic phases in the solidified microstructure changes with the growth velocity during directional solidification. At a low growth velocity of 4 $mm.min^{-1}$, the β (τ_6) exists in the microstructure while at high growth velocity of 30 $mm.min^{-1}$, the β (τ_6) does not exist while the δ (τ_4) exists. The authors [50] present the results of the X-ray diffraction experiments shown in Figure 3-30 to substantiate their claim.

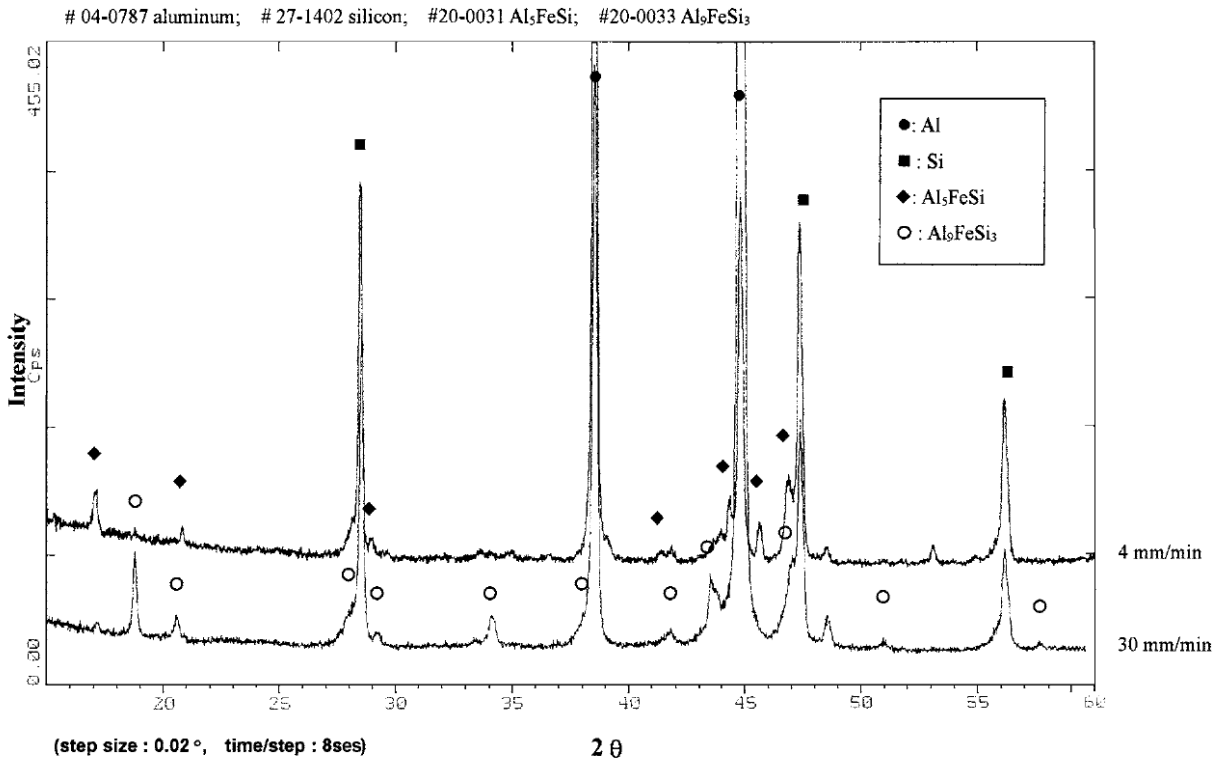

Figure 3-30: X-ray diffraction spectra of directionally solidified Al7Si-0.9Fe alloys with 0.03 wt%Sr at growth rates of 4 and 30 mm/min [50].

In summary, the background literature strongly suggest that the addition of Sr to the Al-Si alloys impacts the atomic arrangement in the melt in addition to change in the nature and evolution of the Fe based intermetallic phases during solidification and the work presented in this dissertation would present further evidences to support this observation. The prior-art in the literature solely discussion on the anomalous clustering of atoms in the liquid Al-Si-Fe alloy system will be presented in the subsequent section to further understand the heredity of the liquid structure during solidification of these alloys and its influence on the evolution of the intermetallic phases.

3.4 ATOMIC CLUSTERING IN LIQUID Al-Si AND Al-Fe SYSTEMS

Liquids have no long range symmetrical order as in solid which have specific long range crystal structure. Short range atomic arrangements in liquid metallic systems with inter atomic bonds which differ in strength depending on chemical elements are called clusters. Clusters are crucial for liquid properties and change in the cluster structure could be attributed to changes in the phase evolution during solidification.

First reported observation of clusters in liquid metals was by Egelstaff [112] in 1962 through Neutron scattering experiments of metallic liquids. The coordination number which is evaluated from the scattering experiments of the liquids indicates the average number of

closest neighbours to a specific atom. Short range order is typical for liquid with no repeatable structure as found in the crystalline solids. Elliot [113] considered 0.2-0.5 nm size of atomic clusters as short range, 0.5-2 nm as medium range and greater than 2nm as long range orders in the liquid state. Structure factors calculated from scattering data obtained from Cu-23%Sn alloy by Xiufang et al [114] is shown in

Figure 3-31; pre-peak observed at 0.145 nm^{-1} is indicative of a medium range order. This medium range order peak was attributed by Xiufang et al [114] to formation of chemical compounds or clusters composed of two different elements. In Figure 3-31, the ordering in the liquid is function of the temperature and the observed medium range order totally disappears at temperature over 1300 °C.

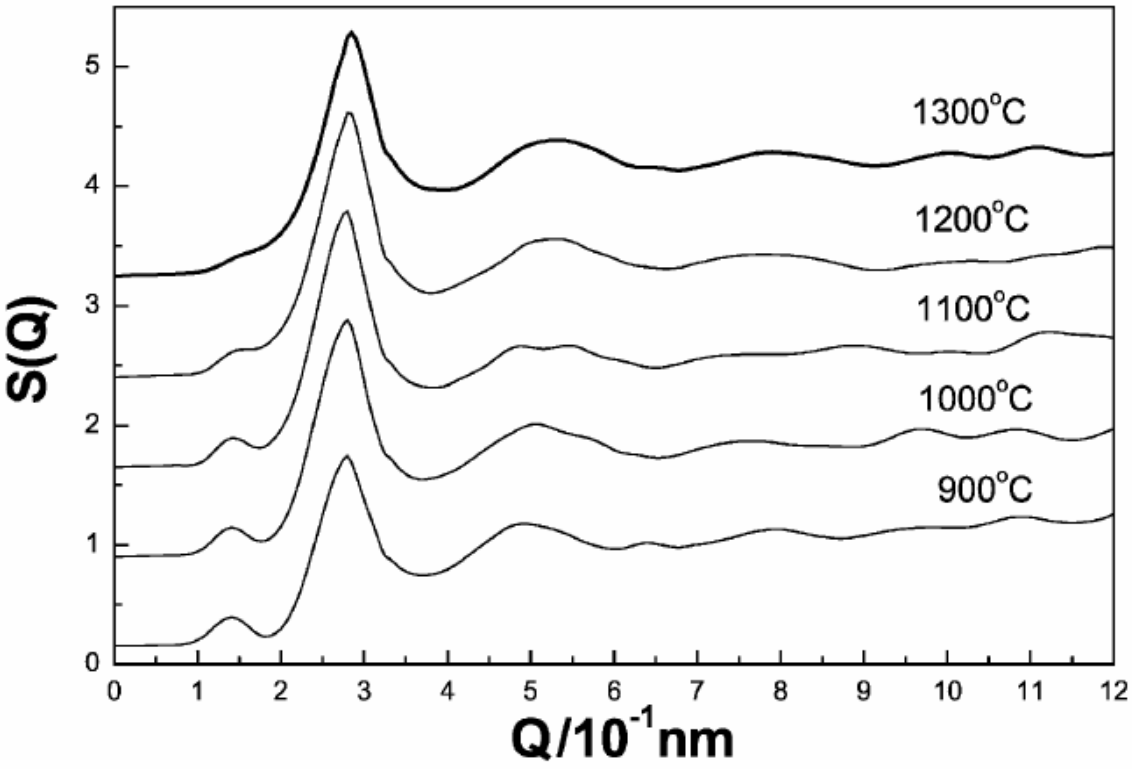

Figure 3-31 : Scattering factors obtained from Cu-23%Sn alloys at different temperatures [114]

Relationship between the change in the order to the physical properties could be illustrated by abnormal changes in the melt viscosity, as shown in Figure 3-32 [114]. The viscosity measurements shown in Figure 3-32 is for the same alloy (Cu-23%Sn) shown in Figure 3-31;

anomalous change in the viscosity of the liquid alloy is correlated with loss of the medium range ordering at high temperatures. Clusters comprising of atoms of same type usually have weaker metallic bonds [114]. Clusters comprising of different atom species could typically form with stronger bonds of the covalent type. It is notable that the amount and type of clusters existing at the initial temperatures prior to the solidification of an alloy is critical to the type of phases evolving during the solidification; initial temperature plays a critical role determining the nature and stability of the clusters in a liquid alloy melt.

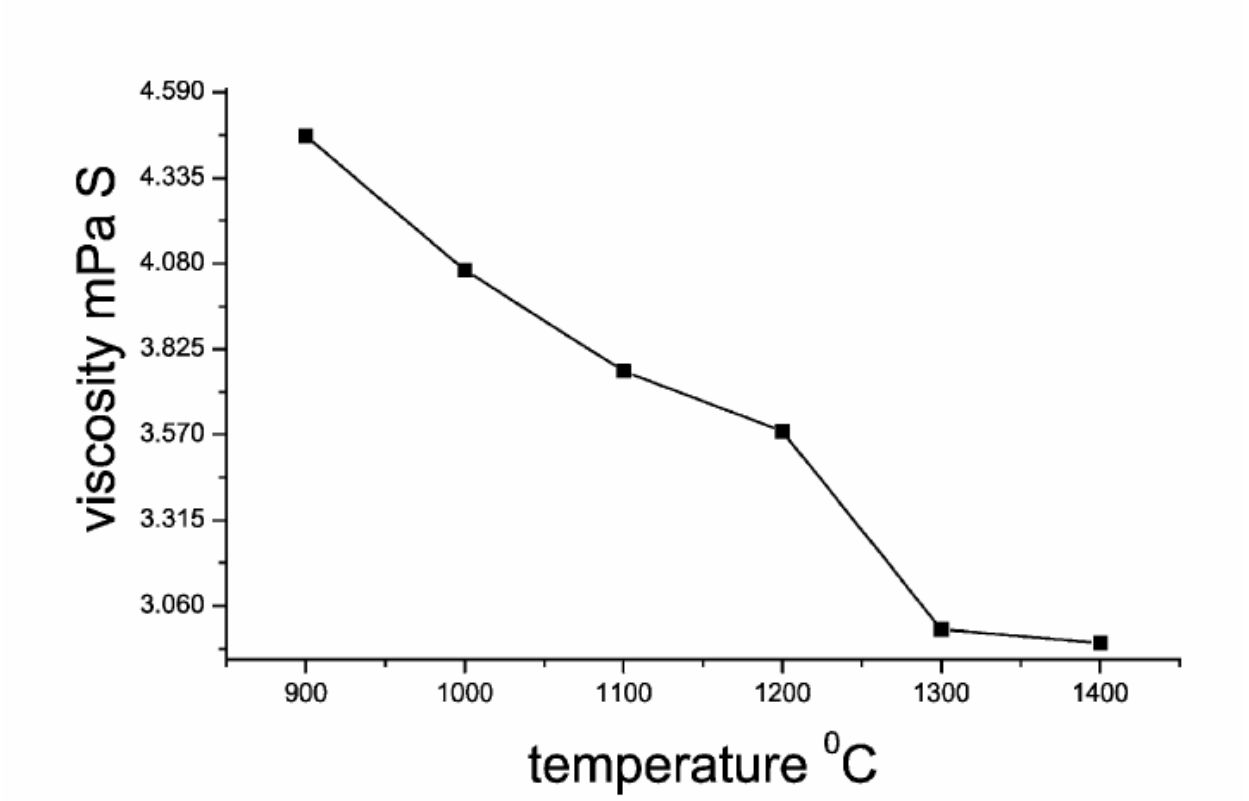

Figure 3-32 : Viscosity of Cu-23%Sn alloy at different temperatures [114]

In this project, the difference of 100 K (993 and 1093 K) in the initial temperature of the Al-Si-Fe alloy melt played a significant role in altering the nature and type of the Fe bearing intermetallic phases evolved during solidification.

3.4.1 Clusters in the liquid Al-Si-Fe alloy system

There is no experimental data for the ternary Al-Si-Fe system describing clustering phenomena and liquid structure. However, there are ample evidence of anomalous clustering phenomena in the binary Al-Si, Al-Fe and Fe-Si systems, independently. It is notable that there is a marked

difference between the liquid structure and clusters in the liquids; the clusters are defined as agglomerates of atoms with inter-atomic bonds stronger than those found in the liquid solution. However there is no general agreement on definition of cluster.

In 2001, Yurkevich [139] performed a series of density measurements in the molten Al-Si alloys with Si concentration between 0.2 and 1.2 wt%; the change in the density as function of temperature and Si concentration is shown in Figure 3-33, wherein the Si-Al bonds were described as donor acceptor bonds with Si accepting electron donated by the Al. Five zones with different micro segregations were identified [139] as shown in Figure 3-34 (a); Gibbs free energy of the alloy for all the proposed bond configurations were calculated as shown in Figure 3-34 (b).

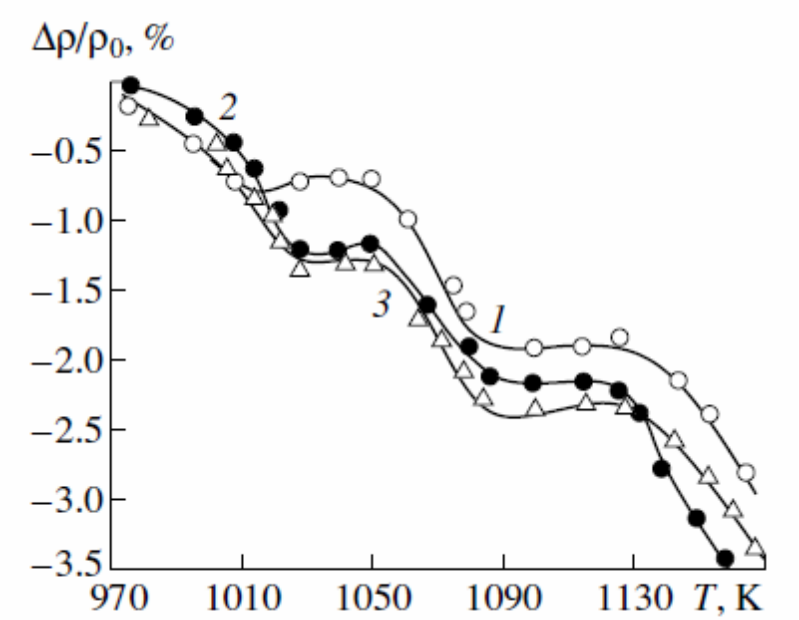

Figure 3-33 : Change in the density as function of temperature and Si concentration for Al (1) 0.2,(2) 0.4 and (3) 0.6 wt% Si molten alloy [139]

Figure 3-34 shows that the Gibbs free energy of the alloy is in direct relation with type of atomic microsegregations and bond type; consequences of change of free energy of the alloy are changes in the stability of the nuclei, driving force for phase formation and phase stability. Reported structural transformation of the Al-Si microsegregations are related to changes in stability of certain configuration at given temperature [139].

In 2002, Il'inskii et al published two works devoted to the liquid Al-Fe and Si-Fe systems [115,116]. In their works [115,116], both theoretical calculations based on the model of micro-inhomogeneous structure and experimental X-Ray scattering data were combined to state that in both the Fe-Si and Al-Fe liquid alloy systems there are stable configurations of atomic clusters in the liquid; an example are the Fe_2Al_5 and Fe_3Al atomic clusters found in the liquid at appropriate compositions [116] as shown in Figure 3-35.

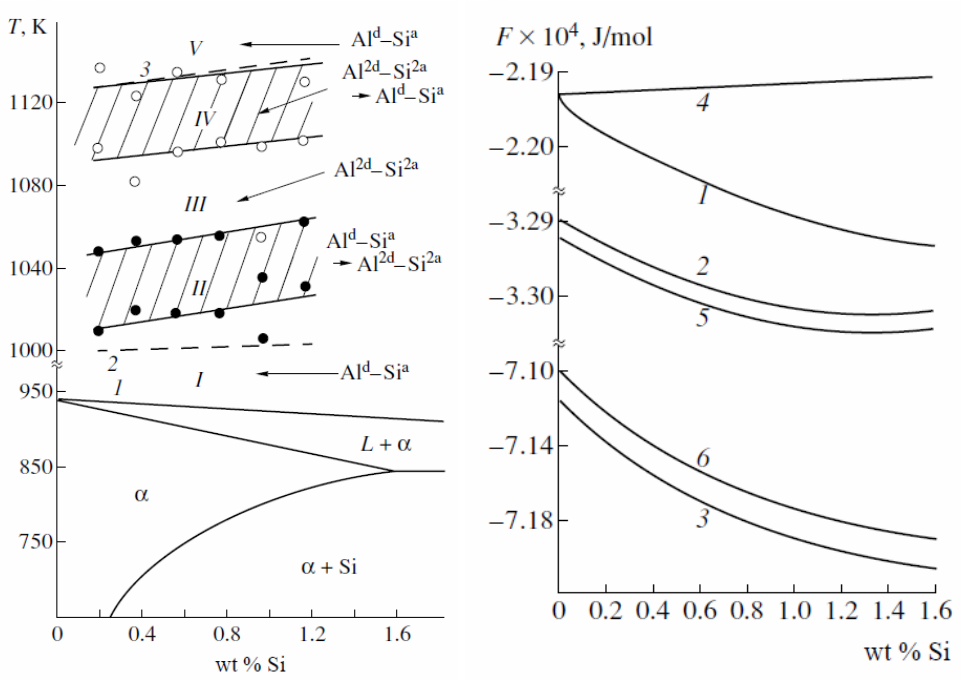

(a) (b)

Figure 3-34 : Anomalous atomic bonds between Si and Al in the Al-Si alloys in the liquid state. (a)Al-Si phase diagram showing micro segregation fields with different bonds and (b) free Gibbs energy of the alloy calculated for different Al-Si bond coordination[139]

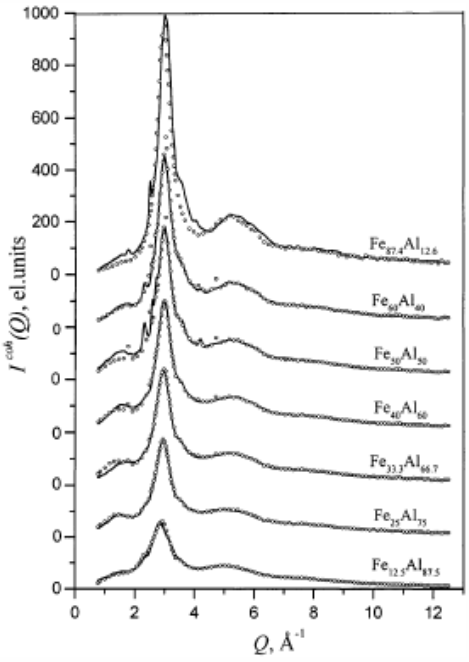

Figure 3-35 : X-Ray scattering data from Al-Fe alloys line – experimental data and circles are calculated at 1820 K [116].

In the Al-Fe system [115], pre peaks observed around 0.1nm^{-1} the medium range order similar to those observed by Xifuang et al [114] in the Cu-23%Sn alloy; the shape and intensity changes in this pre peak indicate changes in the cluster configuration. Similar data obtained in Fe-Si system [116] presents pre peaks at 0.15 nm^{-1} as shown in Figure 3-36; structures attributed to this pre-peak are Fe_2Si_5, FeSi and Fe_3Si. It also was mentioned [115] that typically the average composition of the atomic clusters observed in the liquid do not have a direct correlation to the stoichiometry of the intermetallic phases evolved during solidification of the liquid.

In 2001, Li at al [117] conducted calculation of cluster behavior in Al-Fe alloy. Li et al [117] proposed existence of several cluster configurations in the liquid as shown in Figure 3-37. Existence of several types of co-existing cluster configurations in the alloy melt was proposed and there was a varying amount of each atomic cluster type in the melt at any given temperature [117].

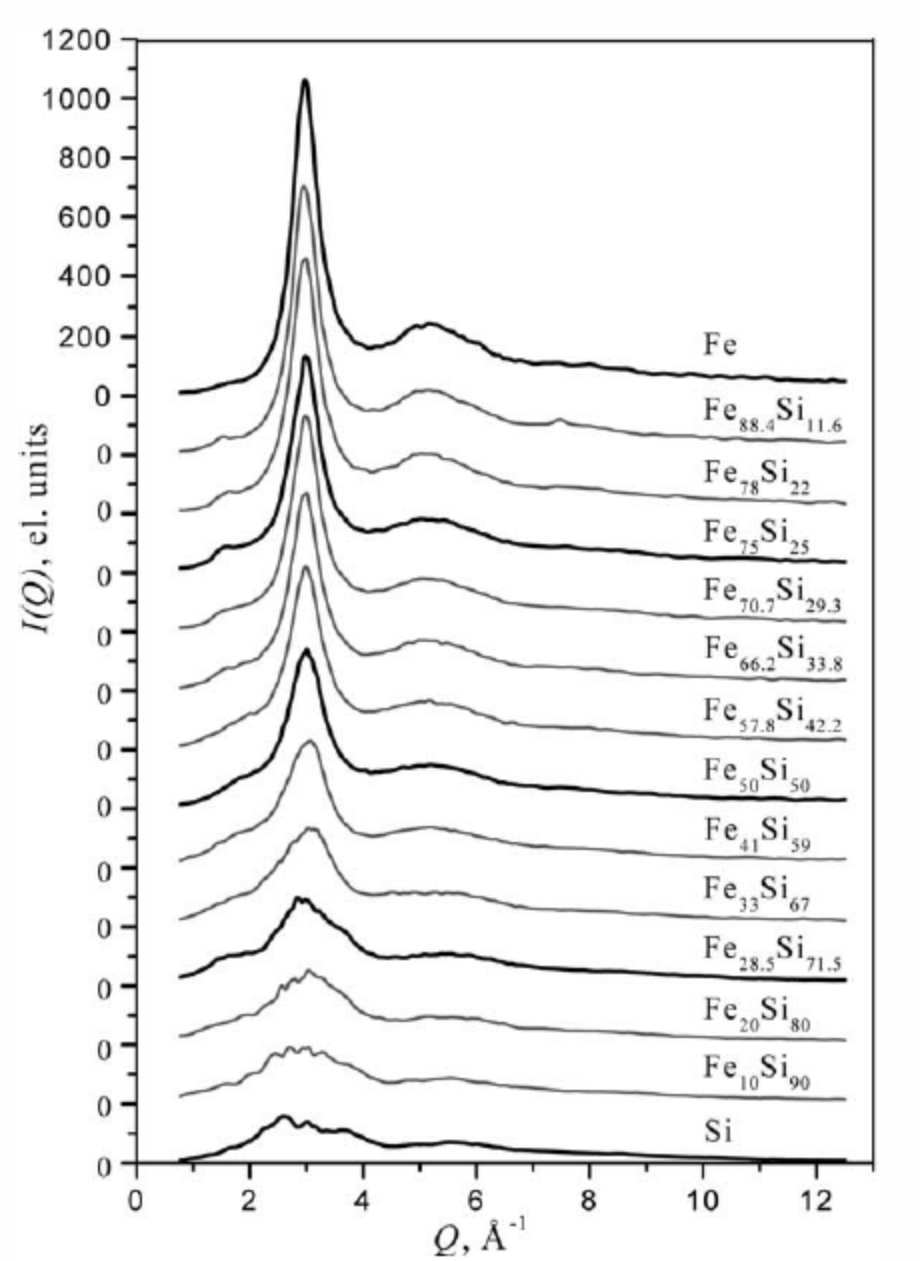

Figure 3-36: Experimental X-ray scattering intensity functions of Fe–Si liquid alloys at 1550 C [115].

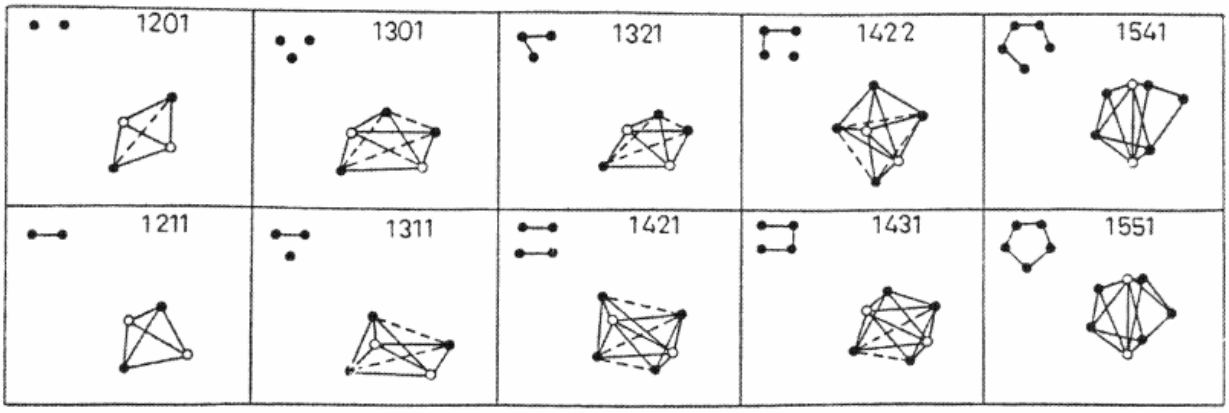

Figure 3-37 : configuration of atomic pairs in Al-Fe alloy [117]

It was reported by Kanibolotsky et al [118] that the enthalpy of mixing in Al-Si-Fe liquid system is exothermic with a calorification of up to -35 kJ/mol. Such behaviour of the system has been related to strong bonding tendencies between the pairs of Al-Fe and Si-Fe atoms and formation of binary Si-Fe clusters. Kanibolotsky et al [118] showed that experimental results demonstrated a dependence of enthalpy of mixing on concentration of the mixed elements but it was stressed that Si-Fe interaction determines the thermodynamics of the Al-Si-Fe system.

Yu et al [119] showed higher energy of activation for diffusion of Fe in a liquid Al compared to other impurities see as shown in Figure 3-38.

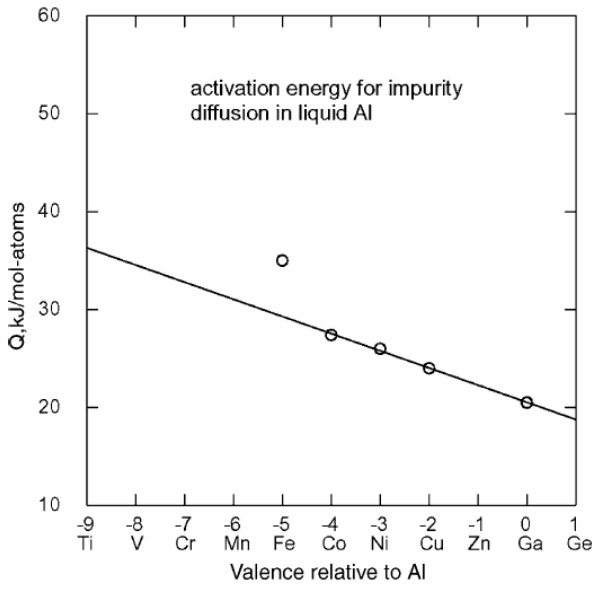

Figure 3-38: Activation energy for diffusion of impurities in liquid Al [119]

Bian et al [120] reported the existence of anomalous medium range order in the liquid Al-Fe alloy and these atomic order disappeared at high melt temperatures of greater than 1700 K. Change in the liquid atomic ordering was related to change in the morphology of Al-Fe phases in solidified samples. Bian et al [120] mentioned that anomalous clusters are $Al_{13}Fe_4$ but no meaningful proof of that had been presented. Considering other works [114,116] clusters should be of the Fe_2Al_5 type but in general Bian did not present sufficient data treatment to substantiate any specific cluster configuration.

Jing-Xiang et al [121] reported that in the Al-Fe-Ce system there is an increase of icosahedral short range atomic order with addition of Ce. Reverse Monte Carlo simulation was performed on the liquid scattering data to match experimental results and it was confirmed [121] that the liquid Al-Fe-Ce alloy have abnormal (compared to Al-Fe) structuring order. Addition of Ce promotes icosahedral ordering and thus, reduces the number of other atomic configurations present in the liquid. Tanaka [122] proposed that local icosahedral ordering acts against crystallization from super-cooled melts and promotes glass formation. Formation of local icosahedral structures reduces the Gibbs free-energy difference between the supercooled liquid and crystal, and also increases the liquid – cluster interfacial energy, γ_{l-c}, which makes crystallization more difficult [122]. Ce is known to modify eutectic Si similar to Sr [123] in the Al-Si alloy; however, it less effective than Sr.

Isono et al [135] showed clear dependence of diffusion of Fe in the liquid Al both by experimental data and theoretical calculations. In their work [135] diffusion experiments were conducted at conditions were convective currents in the solidifying melt were absent. Comparison between diffusion of Cu and Fe in liquid Al (Cu was taken a benchmark) showed 3 times slower diffusion of Fe compared to Cu; however, based on the Einstein's relation for diffusion it should be almost equal. Isono et al [135] attributed it to the formation of anomalous clusters leading to lower mobility of the Fe in the liquid Al. Gebhard et al [132] have reported higher in viscosity of Al-Fe alloys which was explained by cluster formation similarly to that observed by Xiufang et al [114] in the Cu-23%Sn alloy. Viscosity of the alloy is a direct indicator of the nucleus stability in the liquid; therefore, any changes in the viscosity can be attributed to a change in the stability of certain nucleating phases favoring formation of specific phases during solidification.

In summary, it is notable that there are several evidences in the background literature to suggest that anomalous clustering of atoms (both like and dislike pairs) occur in the liquid state of the Al-Si-Fe alloy system, especially in the Al rich corner of the phase diagram. Considering a hypothetical case of a solidification front moving into the liquid phase of an Al-Si-Fe alloy rich in Al, typically, there would be a rejection of the solute atoms of Fe and Si ahead of the growing primary Al phase. The extent of the rejection would be governed by the partition ratio of the respective atom type in the alloy composition; that for Fe being significantly lower than Si. Hence, the rejection of Fe atoms would be more pronounced than the Si counterparts. Additionally, the extent of solute rejection increases with decreasing cooling rate of the liquid phase during solidification. The solute atoms of Fe and Si rejected ahead of the solid/liquid interface would be transported into the liquid phase by two prominent mechanisms: diffusion

and convection. Typically, during solidification, the diffusion mechanism is instantaneous and spontaneous, however, natural convection driven by thermal and density gradients in the liquid is sluggish in the beginning and increases with time of solidification [124]. The velocity of the liquid stream due to natural convection will be higher for slower cooling rates during solidification. Thermodynamic modeling and simulations of phase diagrams based on equilibrium and Scheil-Gulliver assumption of solute redistribution in alloys consider the Gibbs Free energy diagrams of the phases which incorporates the solute redistribution fields ahead of the growing dendrites and predicts the nucleation of stable phases during solidification favoured by the lowest free energy in the system. However, these models fail to incorporate anomalous behaviour of atoms in the liquid alloys which will significantly alter the free energy curves of the system during solidification. In case of the Al-Fe-Si, the only intermetallic phase predicted to evolve for the Al-xSi-yFe (x=2 to 15wt% and y=0 to 0.8wt%) is the τ_6-$Al_9Fe_2Si_2$ for both the equilibrium and Scheil-Gulliver assumption of solute redistribution during solidification as typically shown by the Figure 3-4. The τ_6 phase is characterized by a typical ratio of Fe:Si as approximately 1:1. However, if there were anomalous clusters of any combination of Al,Si and Fe atoms in the liquid ahead of the solidifying primary Al phase, as amply substantiated in the background literature and additionally, if the diffusion of the Fe atoms into the liquid is more than three times slower than that assumed by the thermodynamic models, then there would be a significant difference in the actual map of the Gibbs free energy in the liquid ahead of the solid/liquid interface which may favourably present the lowest free energy to an entirely different intermetallic phase than that modelled and predicted. Isono et al [135] showed that the Fe atoms in the liquid Al-Fe alloy is typically surrounded by 15 Al atoms resulting in an anomalously reduced diffusion of the Fe in the liquid leading to an anomalously higher viscosity of same. If this were to occur in the Al-Fe-Si alloy melts as well, then two situations will occur: firstly, there would be a higher concentration of the Fe atoms ahead of the solid/liquid interface during solidification and secondly the effect of natural convection in a higher viscous liquid would be decreased. This situation will lead to a higher ratio of Fe:Si atoms ahead of the solid/liquid interface which may result in the evolution of a different Al-Fe-Si intermetallic phase such as the τ_5-Al8Fe2Si which would be an anomalous occurrence. It will be later shown in the results of this project that the τ_5 phase with a higher Fe:Si ratio does evolve prior to the τ6 phase with a Fe:Si ratio of unity. Further, the anomalous clustering of the Fe atom by the Al atoms in the liquid could also lead to the initial formation of the binary Al-Fe phase albeit the presence of the Si atoms in the liquid if the free energy of such a phase is the lowest at any temperature during solidification. Similar anomalous clustering of the Fe and Si atoms are also confirmed in the Fe-Si system as presented earlier in this section. This would possibly lead to further deviation from the prediction of the nature of intermetallic phases evolves during solidification of the Al-Fe-Si liquids.

It is notable that there has not been any prior art in evaluating the liquid structure and clustering tendencies in the Al-Si-Fe ternary alloy system, as yet. Hence, it can only be hypothesized based on the anomalous clustering tendencies shown in all of the Al-Si, Al-Fe and Fe-Si binary system, individually that such anomalies could be expected in the ternary Al-Fe-Si

system as well which will lead to evolution of unpredictable solid phases during solidification of these alloys.

The background literature also suggests that clusters present in the liquid state at a high temperature with specific composition of atoms from the various elements in the alloys does not necessitate that these atom compositions will be reflected in the stable solid nucleus that evolves during solidification. It can be safely suggested that the location of such clusters in the liquid presents favourable sites with energy states lower than the surrounding homogeneous liquid and hence, could act as a potent site on which nucleation of the new solid phase may take place. The initial atom composition of the clusters in the liquid state may have an influence on the final composition of the solid nucleus. However, in the case of amorphous or glassy metals, the anomalous clusters of atoms is captured with their original atomic composition and retained at room temperature without any nucleation event for a solid phase during the cooling process.

CHAPTER 4. OBJECTIVES AND PROJECT PLAN

The background literature on the nature and evolution of the Fe based intermetallic phases in the Al-Si hypoeutectic casting alloy strongly suggests that there is several information critical to our comprehensive understanding of the subject matter that are missing. The motivation to carry out this project work is two folds: (1) to better understand the solidification conditions that lead to the evolution of specific Fe based intermetallic phases in the Al rich corner of the Al-Si-Fe system with a range of 2 to 12.5 wt% Si and (2) to better understand the role of trace additions of Sr to the alloy melt on the nature and morphology of the Fe based intermetallic phases in these alloys. With this motivation the objectives are proposed for this research project.

4.1 OBJECTIVES

1. Quantify crystallographic and morphological characteristics of near equilibrium and non-equilibrium intermetallic phases evolved during the solidification of Al-Si hypoeutectic casting alloys while studying the effects of the following independent parameters.

    a. Variations in the compositional levels of Si and Fe.
    b. Superheat of the alloy melt above the respective liquidus temperature.
    c. Cooling rate during solidification.

2. Evaluate the effect of trace levels of Sr additions on the characteristics of the intermetallic phases present in the high purity Al-Si-Fe alloys.

4.2 PROJECT PLAN

The objectives of this project mentioned above entail solidification experiments to be carried out with a variety of independent parameters maintained at several levels. The alloys prepared were of high purity and the following independent parameters were considered for this study.

1. Si Concentration → about 2, 4, 5, 7, 9, 11.5 and 12.5 (eutectic) wt%.
2. Fe Concentration → about 0.05, 0.15, 0.25, 0.5 and 0.8 wt%
3. Cooling Rates During Solidification for the liquid phase→about 0.017, 0.1, 0.8, 5 and 50 Ks^{-1}
4. Liquid alloy superheat above liquidus temperature → about 60, 100 and 200 K

The above mentioned levels of the independent parameters did not deviate more than ±0.25 wt% s of the targeted values. Several combinations of the levels of the independent parameters were used in the experiments. These combinations stemmed from the ongoing

observation of the results from previous experiments to enable explanation of certain specific observed phenomenon in the results.

The combinations of the independent parameters used in this study is presented in Table 4-1

Table 4-1: Combination of independent parameters used in this study.

Parameter	**Levels**						
Si (wt%)	2	4	5	7	9	11.5	12.5
Fe (wt%)	0.25	0.25	0.25	0.05, 0.15, 0.25, 0.5 and 0.8	0.25	0.25	0.05, 0.25, 0.5 and 1
Sr (wt%)	0	0	0	0 and 0.02	0	0	0 and 0.02
Cooling Rate (Ks^{-1})	0.1,0.8, 5 and 50	0.8, 5 and 50	0.8, 5 and 50	0.017, 0.1, 0.8, 5 and 50	0.8, 5 and 50	0.8, 5 and 50	0.1, 0.8, 5 and 50
Liquid Alloy Superheat (K)	200	200	200	60, 100 and 200	200	200	200

Figure 4-1 presents a schematic graphical representation of the experiment matrix with the independent parameters for the solidification experiments with a minimum initial liquid alloy temperature of 1093 K (820 ^{o}C) and held for a minimum of two hours isothermally prior to solidification. Figure 4-1 (a), (b) and (c) are for the Al-Si-Fe system and Figure 4-1 (d) is for the Al-Si-Fe-Sr system. Each point shown in Figure 4-1 is a solidification experiment and there were at least two repetitions of the experiments shown in Figure 4-1 (b) to ensure repeatability and reproducibility of the results. A total of 47 and 13 different solidification experiments were carried out for the Al-Si-Fe and Al-Si-Fe-Sr alloy systems, respectively.

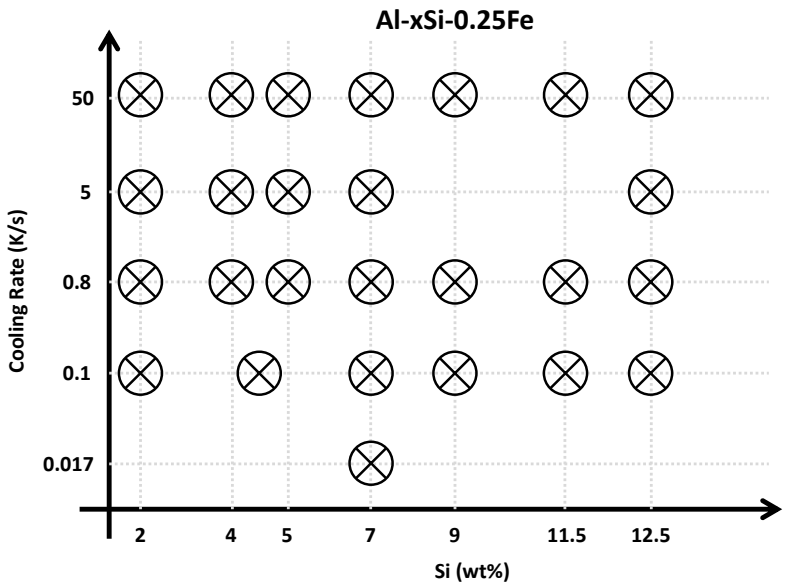
Al-xSi-0.25Fe
Cooling Rate (K/s)
50
5
0.8
0.1
0.017
2
4
5
7
9
11.5
12.5
Si (wt%)

(a)

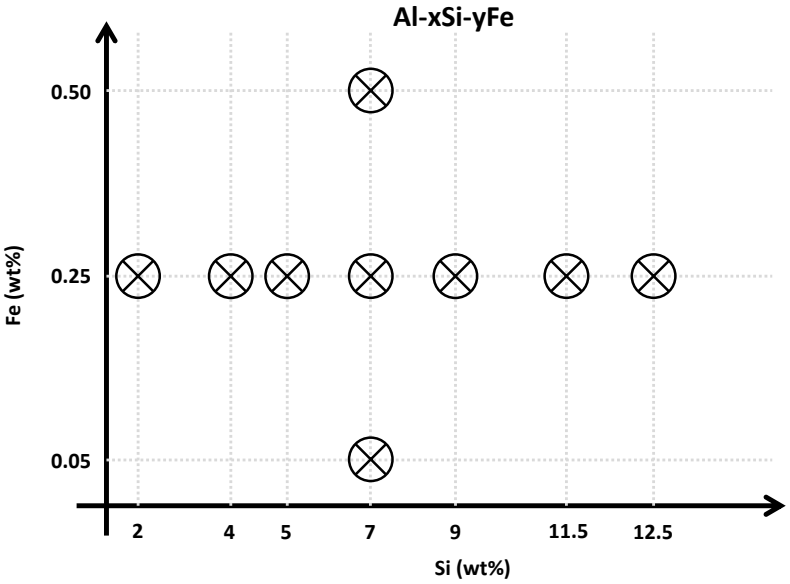
Al-xSi-yFe
Fe (wt%)
0.50
0.25
0.05
2
4
5
7
9
11.5
12.5
Si (wt%)

(b)

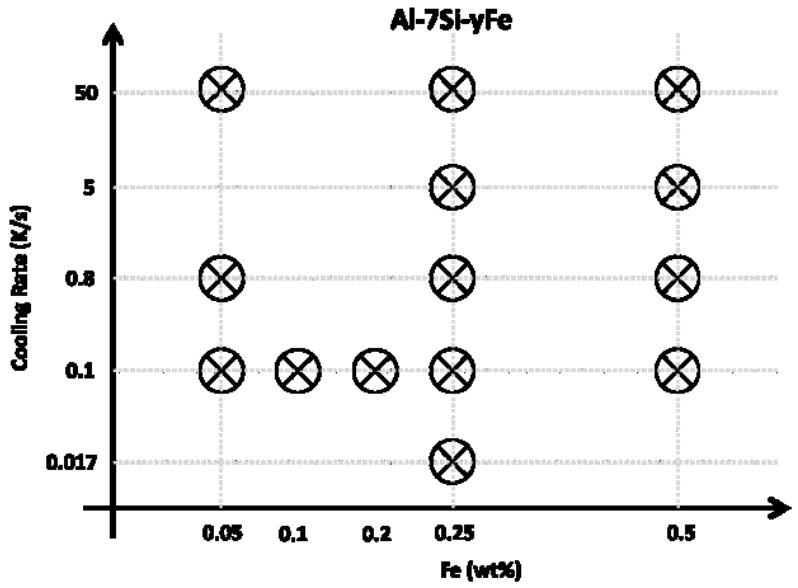

(c)

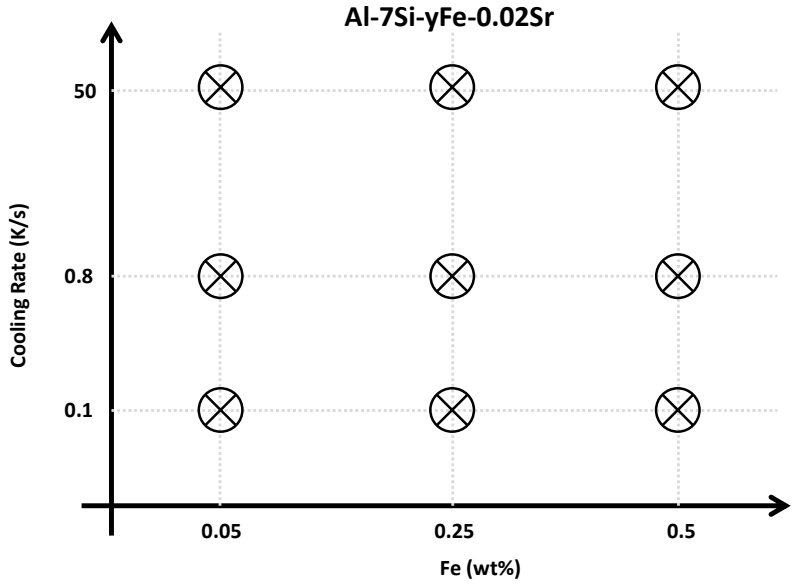

(d)

Figure 4-1: Schematic representations of the experimental matrix with the independent parameters used in this study. The initial alloy temperature was a minimum of 1093 K (820 ^{o}C) and held for a minimum of two hours isothermally prior to solidification. (a) plot of concentrations of Si vs. cooling rate during solidification for Al-xSi-0.25Fe system, (b) plot of concentration of Si vs. Fe concentrations in the Al-xSi-yFe system, (c) plot of concentration of Fe vs. cooling rate for a Al-7Si-yFe system, and (d) plot of concentration of Fe vs. cooling rate for a Al-7Si-yFe-0.02Sr system.

The dependant variables in the solidification experiments were the observations in the microscopes (optical and electron), composition of solidified phases measured with Energy Dispersive X-Ray Spectroscopy (EDX) in Scanning Electron Microscope (SEM), crystal structure of the phases by the techniques in a Transmission electron Microscope (TEM), and X-ray diffraction data obtained from Cu k_α and high energy synchrotron radiation, respectively.

A brief overview of a typical experiment and analysis is presented in Figure 4-2.

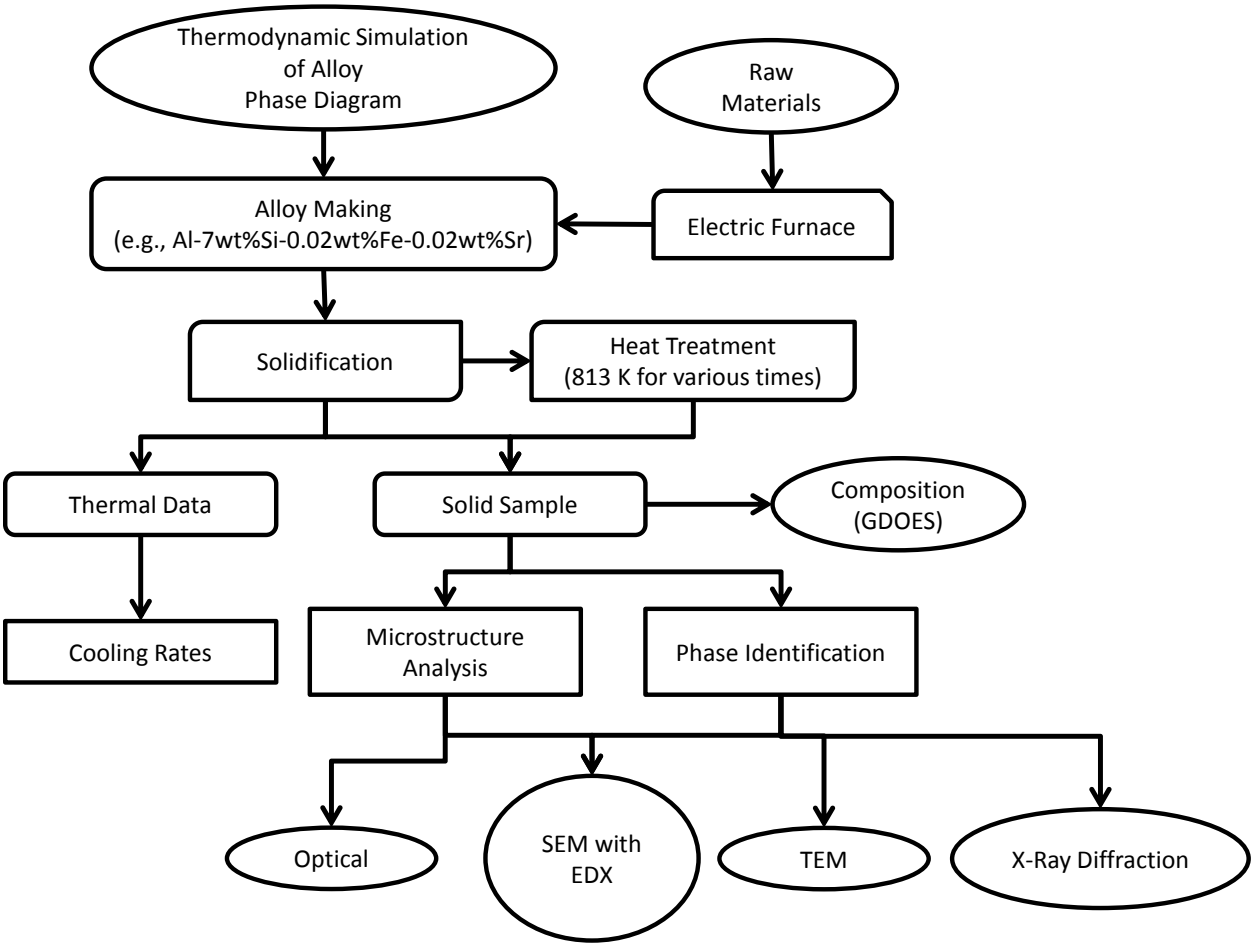

Figure 4-2: A Schematic of a typical solidification experiment and analysis.

A detailed description of the techniques used for the analysis of dependant variable in the experiments will be presented in the next chapter of this dissertation.

CHAPTER 5. EXPERIMENTAL METHODOLOGY

In this chapter, more details will be presented on the several items in the schematic of a typical solidification experiment procedure is presented in Figure 4-2.

5.1 THERMODYNAMIC SIMULATION

The thermodynamic simulations for phase diagrams and solidification were carried out using the PANDAT™*, version 8.1, equipped with the PanAl8 database for aluminum alloys. There are 182 phases for the Al alloy system and 33 phases used to evaluate the Al-Si-Fe-Sr alloy system. The simulations were carried out for normal atmospheric pressure condition. The scan lines for the simulation of 2-D phase diagrams were 0.01 units for both the temperature and composition. PANDAT™ 8.1 uses the CALculation of PHAse Diagram (CALPHAD) [82,125] approach. Both the equilibrium and Scheil-Gulliver conditions were used independently as assumptions in the thermodynamic simulations.

5.2 RAW MATERIALS

The purity of the elements and compositions of the master alloys used in the experiments are presented in Table 5-1.

Table 5-1: Purity and/or composition of elements and master alloys used to prepare the alloys in this study.

Elements	Composition
Al	99 % for commercial and 99.999 % for high purity grade
Si	99.9999 % high purity grade
Fe	Al-25 wt% Fe master alloy with 0.3wt% Si, 0.2wt% Mn and 0.05wt% Cu
Sr	Al-10 wt% Sr master alloy with 1% Ti,0.2wt% B, 0.2wt% Si, 0.3wt% Fe and 0.02wt% Ca

5.3 ALLOY PREPARATION AND HEAT TREATMENT

Electric resistance furnaces were used for alloy preparation from raw materials, melting and holding of liquid alloys, and heat treatment of the solidified alloy samples. The liquid alloy in each experiment was prepared and held in a new high purity alumina crucible.

* Pandat™ version 8.1, Compu Therm LLC., Madison, WI, USA. http://www.computherm.com

5.4 CASTING AND SOLIDIFICATION

The solidification was carried out at five different average cooling rates of the liquid phase during solidification: *about 0.017, 0.1, 0.8, 5 and 50 Ks^{-1}*.

The cooling rate of 0.017 Ks^{-1} was achieved in an electric furnace equipped with a high precision controlled (±0.2K) for temperature ramp up and ramp down cycles. The cooling rate of 0.1 Ks^{-1} was attained when the liquid alloy was placed in a ceramic crucible in the electric furnace and allowed to cool down with a furnace shut down from a high holding temperature of 100 or 200 K superheat above the liquidus of the alloy. The cooling rate of 0.8 Ks^{-1} was achieved when the liquid alloy in a crucible was removed from the electric furnace at the prescribed superheat temperature and placed on an insulating plate to be solidified in normal atmospheric conditions. A cooling rate of 5 Ks^{-1} was achieved by casting the alloy in a pre-heated (673 K (400 ^{o}C)) steel mould equipped with three thermocouples. The liquid alloy was poured into the steel mould with the ceramic crucible,. The cooling rate of 50 Ks^{-1} was achieved by casting the alloy in the steel mould maintained at room temperature without any pre-heat.

5.5 THERMAL DATA ACQUISITION

The cooling rates were evaluated from the thermal data (T versus t) acquired during the solidification experiments with a K-type ungrounded thermocouple (open and/or exposed). The size of the thermocouple was about 1.6 mm. The thermal data acquisition was carried out with the National Instruments[†] SCXI 1600 hardware module equipped with the SCXI 1303 terminal block and coupled with the LabView 2010[‡] software at the rate of 100 data per second. The liquid alloy temperature was also monitored by a similar thermocouple attached to a same temperature monitor.

5.6 CHEMICAL COMPOSITION

The composition of the prepared alloys and master alloys were evaluated using the Glow Discharge Optical Emission Spectroscopy (GDOES). The GDOES unit was calibrated before each measurement procedure using several ASTM standard alloys. Precision of the measurements is ±2% of the measured value.

[†] National Instruments Corporation 11500 N Mopac Expwy Austin, TX 78759-3504
[‡] Product of National Instruments.

5.7 MICROSTRUCTURE ANALYSIS

The microstructure of the solidified samples from preferred sectioned locations were analysed using both the light optical microscope and SEM. Analyses of images from the optical and electron microscopes were carried out by the ImageJ[§] software.

5.7.1.1 Metallographic Sample Preparation

The standard metallographic sample preparation techniques were used for the microstructure analysis of the solidified samples using both the light optical microscope and SEM: sample mounting using thermosetting Bakelite, coarse grinding using SiC papers of increasing grit, polishing using increasing grit levels of diamond polishing suspension and final polish using colloidal silica gel. No chemical etching of any kind was used on the samples.

5.7.1.2 Light Optical Microscope

A Nikon Eclipse LV 100 light optical microscope equipped with the NIS-Elements software was used for image acquisition from the microstructure of the solidified samples.

5.7.1.3 Scanning Electron Microscope

A JEOL 7000 Scanning Electron Microscope (SEM) with a cold Field Emission Gun (FEG) and equipped with an Oxford instruments Energy Dispersive X-Ray Spectrometer (EDX) model 7558 was used. Both the secondary and back scattered electron detectors were used at two working distances of 6 and 10 mm to obtain microstructure images. EDX spectrums were obtained at two accelerating voltages of 10 and 20 KeV and the working distance was maintained 10 mm.

5.8 PHASE IDENTIFICATION

The identification of the phases in the solidified microstructure was carried out by the SEM (EDX), TEM (EDX), TEM (electron diffraction) and X-Ray diffraction (Cu K_α and synchrotron beam source).

5.8.1 TEM

Two TEMs were used for this study: a Philips CM12 with accelerating voltage of 120 KeV equipped with digital and traditional film cameras, and EDX detector and JEOL 2010 High resolution TEM with accelerating voltage of 200 KeV equipped with 2 digital cameras for high resolution and regular imaging, Oxford Instruments Link Pentaflet EDX model 6494, STEM and

[§] Image Processing and Analysis in Java (ImageJ), National Institutes of Health, USA. http://rsb.info.nih.gov/ij

EELS detectors. The samples for the TEM were prepared using the Focused Ion Beam (FIB) milling technique.

5.8.1.1 FIB for TEM

A LEO 1530 dual beam and cross-beam SEM equipped with a FIB milling machine was used to prepare the TEM samples in this study. Using the FIB milling ensures that the TEM sample is taken from a specific place of interest in the microstructure. Specific areas of interest on the microstructure identified in the SEM, protected by 1 to 2 µm thick layer of platinum deposit, milled into thin foils (5 by 20 µm rectangle area and <100 nm thick) using a focussed high energy Ga ion beam. The TEM sample foils were mounted on a holder compatible with the TEM. Figure 5-1 and shows the process of making a TEM sample foil using a FIB.

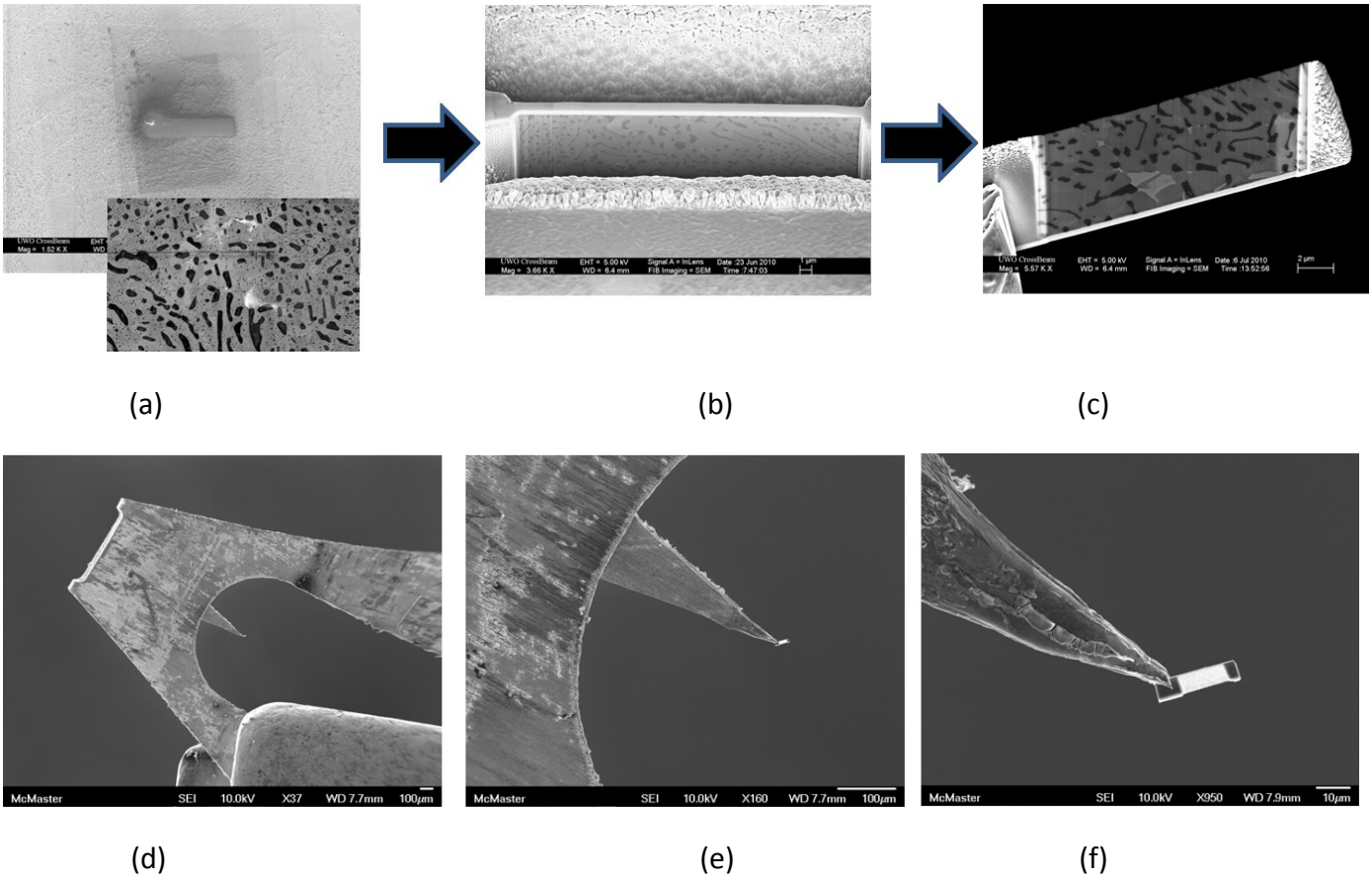

Figure 5-1: Micrographs showing the typical procedure for making Tem sample foils using the FIB milling technique. (a) selection of area of interest on an SEM image, (b) milling with a high energy GA ion beam and (c) to (f) final sample on the holder for further TEM studies.

5.8.1.2 EDX in TEM

The JEOL 2010 High resolution TEM was equipped with an Oxford Instruments Link Pentaflet EDX model 6494 EDX system with INKA data acquisition and processing system.

5.8.2 X-Ray Diffraction

Two methods of X-Ray diffraction experiments were carried out in this study: one using the Cu K_α beam source on powder alloy sample obtained by dissolution process to eliminate most of the primary Al phase that formed the matrix of the solidified sample and the other using the high energy Synchrotron beam source on polished surface of cast alloy samples (micro-diffraction).

5.8.2.1 Powder Diffraction (Cu K_α beam source)

The Al matrix from the solidified alloy samples was preferentially eliminated using a dissolution technique. The analysis of the powder also revealed that the Sr containing intermetallic phases were also dissolved along with the primary Al phase matrix.

5.8.2.1.1 Preferential Dissolution of Al alloys

Different dissolution techniques were reviewed in the Gupta et al [126] work with specific focus on suitability for Al-Si-Fe intermetallic phases extraction. Phenol dissolution technique was chosen as one providing reasonably fast dissolution times and preserving phases of interest. During dissolution reaction between phenol and Al gives soluble aluminum phenolate. Aluminum phenolate is removed by dissolution in benzyl alcohol plus toluene solvent mixture.

5.8.2.1.2 Cu-anode X-Ray Diffraction (XRD)

Conventional XRD experiments were carried out with a Bruker D8 diffractometer equipped with SMART6000 CCD detector and Cu anode generating the standard 0.1541 nm wavelength beam at 40 KeV. The sample powder was mounted with a drop of distilled water on a polymer holder. The goniometer detector was rotated between 10 and 90 degree angles with an angular least count of $0.3^{o}min^{-1}$

5.8.3 Synchrotron radiation experiments

High Energy Synchrotron beam source at the Line D of Sector 2 [127] in the Advanced Photon Source (APS) at the Argonne National Labs, Argonne, IL, USA was used for the diffraction experiments in this study. The energy of the beam was 10.1 KeV with a wavelength of 0.12275 nm. In addition to a goniometer with the sample, a CCD camera detector for the diffracted beam intensities, an X-Ray Fluorescence (XRF) detector was used to obtain elemental map from the microstructure of the solidified specimen surface. The Figure 5-2 shows the photographs of the goniometer with the sample holder, CCD camera detector and XRF detector.

Cast samples were suitably sectioned and polished as for an SEM study. Sample was placed on the sample holder in the goniometer such that the entire beam in entrained on the sample surface.

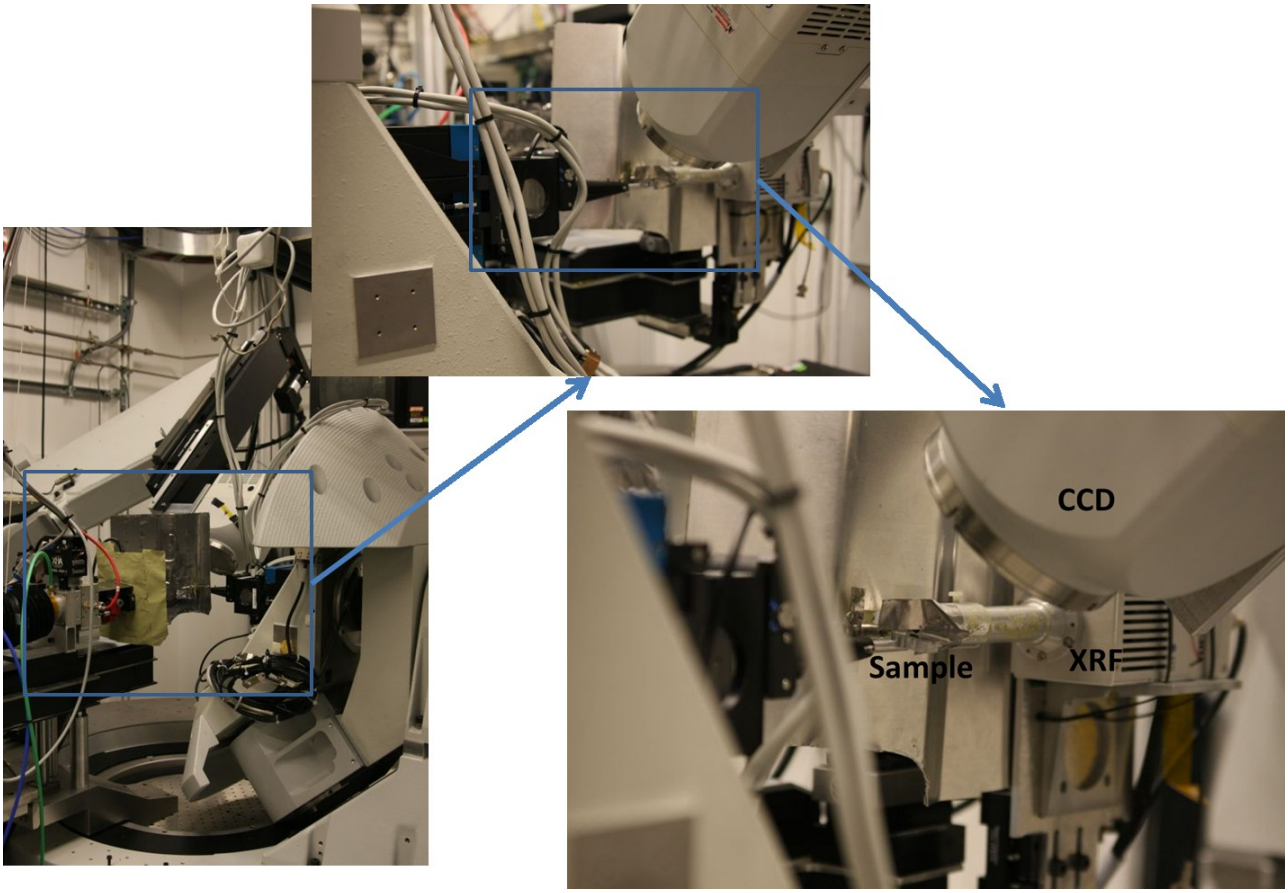

Figure 5-2: Photographs of the diffraction experiment set-up at the Line D of Sector 2 at the APS, ANL, Argonne, IL, USA. The rotating goniometer with the Al alloy sample, CCD camera detector and XRF detector are shown.

An elemental XRF map of the microstructure was initially obtained by the XRF detector and this was used to determine the region of interest (2µm square) to obtain the X-Ray diffraction data from. The size of the incident X-Ray beam is about 50 nm in diameter.

As an example, the XRF maps of Al and Si distribution on a region of the Al-7Si-0.25Fe-0.022Sr alloy sample solidified at 50 K s^{-1} from a superheat of 100 K above the liquidus temperature has been shown in Figure 5-3; wherein the scale of intensities is provided on the right side of each

image. In Figure 5-3 (b) the regions that are blue are nearly devoid of any Si atoms and those that are green and red have higher Si atoms. The entire region in Figure 5-3 is sub-divided into square grids of 2 μm length side. The CCD camera detector is first placed at an angle of 28 ^{o} to the incident beam and the diffraction data is obtained from each of these 2 μm square grid region. The goniometer moves the sample surface such that each of these square grids comes in direct line of the incident X-Ray beam and the diffraction data is collected by the CCD camera as diffraction rings shown in In Figure 5-3 (c). After collecting the data from all the grids in marked on the sample surface, the CCD camera is moved to an angle of 43 and 58 ^{o} to the incident beam, respectively and in each angular location of the camera, the diffraction data is obtained for all the grids in the region of interest. The each of the three angular positions of the CCD camera detector (28, 43 and 58 ^{o} to the incident beam), the detector acquired diffraction data from -12 ^{o} to +12 ^{o} on either side of the angular position.

An SDI application software was used to appropriately translate the intensity images obtained by the CCD camera detector into digital data of intensity versus angular position (I vs 2θ) as shown by a typical example in Figure 5-3 (c). In addition, the CCD camera detector was placed at 0, 3, 6, 9, 12 and 15 ^{o} angles to the incident beam and images of the incident beam were obtained without any sample in the experiment to evaluate the location of the centre beam and the precise distance between the camera and sample surface.

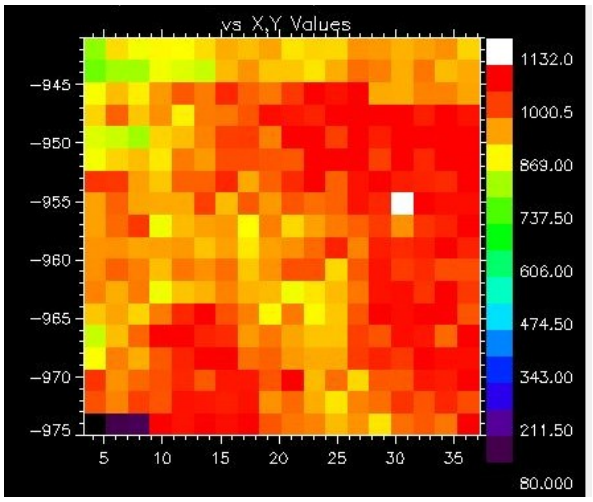

(a)

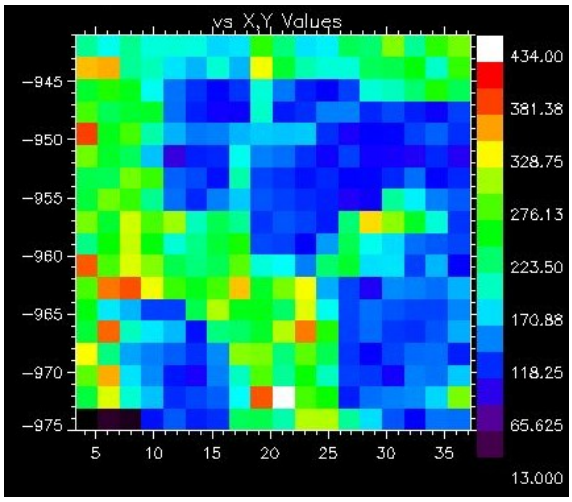

(b)

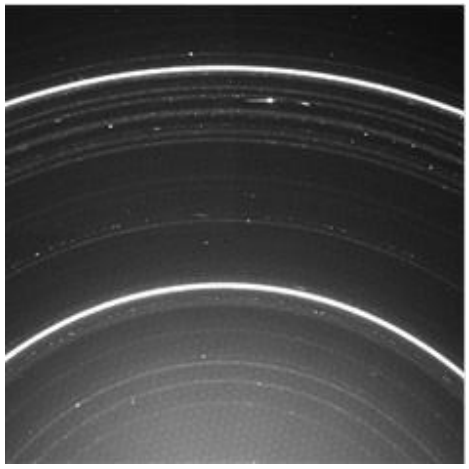

(c)

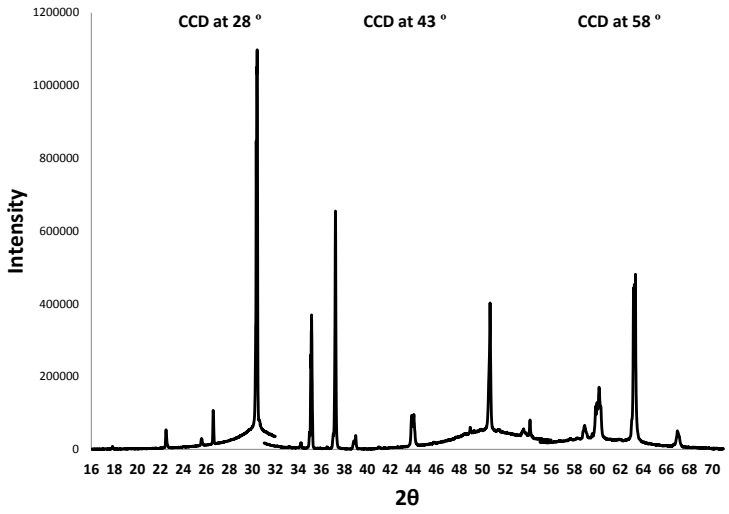

(d)

Figure 5-3: A typical XRF element map of (a) Al and (b) Si obtained from the Al-7Si-0.25Fe-0.022Sr alloy sample solidified at 50 K s^{-1} from a superheat of 100 K above the liquidus temperature. (c) typical X-Ray diffraction pattern obtained by the CCD camera from one location on the grid shown in (a) and (b), and (d) the combined Intensity versus 2θ plots obtained from processing three images as in (c) for the three angles of the CCD camera detector, respectively.

CHAPTER 6. RESULTS AND DISCUSSION: INTERMETALLIC PHASES IN THE AL-SI-FE CAST ALLOYS

The results and discussion section of this dissertation is covered in two chapters: CHAPTER 6 presents the identification and evolution of the intermetallic phases in the Al-Si-Fe alloys and CHAPTER 7 presents the same in the Al-Si-Fe-Sr alloys. The measured chemical compositions of the Al-Si-Fe alloys in this study are presented in a table in APPENDIX A of this dissertation.

To enable a better clarity for the readers, the summary of the identification and evolution of the intermetallic phases in the Al-Si-Fe alloys is presented in the beginning of this chapter followed by evidences and discussion from the various experiment results and analyses to validate the summary.

All the alloy compositions presented in this dissertation from this chapter are in weight percentage of the respective element. However, all the results from the quantified EDX analysis of the phases are in atomic percentage of the respective elements.

6.1 SUMMARY OF ANALYSIS OF RESULTS

One of the critical results obtained in this study of the Al-Si-Fe alloys is that the τ_5 (Al-Fe-Si) intermetallic phase forms in all the compositions of Si and Fe shown in Table 4-1 for all the average cooling rates observed for the liquid phase during solidification of the alloys. This result is contrary to the predictions of the thermodynamic solidification and phase diagram of this alloy system in both assumptions of equilibrium and Scheil-Gulliver conditions, respectively. All the thermodynamic phase simulation during solidification for the Al-Si-Fe alloys with 2 to 12.5 wt% Si and 0 to 0.8 wt% Fe predicts the evolution only the $\tau_6 – Al_9Fe_2Si_2$ phase and not the $\tau_5 – Al_8Fe_2Si$.

Figure 6-1 shows typical isopleths from the equilibrium ternary phase diagram of the Al-Si-Fe system wherein within the compositional ranges of interest for this study the only intermetallic phase predicted to evolve during solidification is the $\tau_6 – Al_9Fe_2Si_2$ phase.

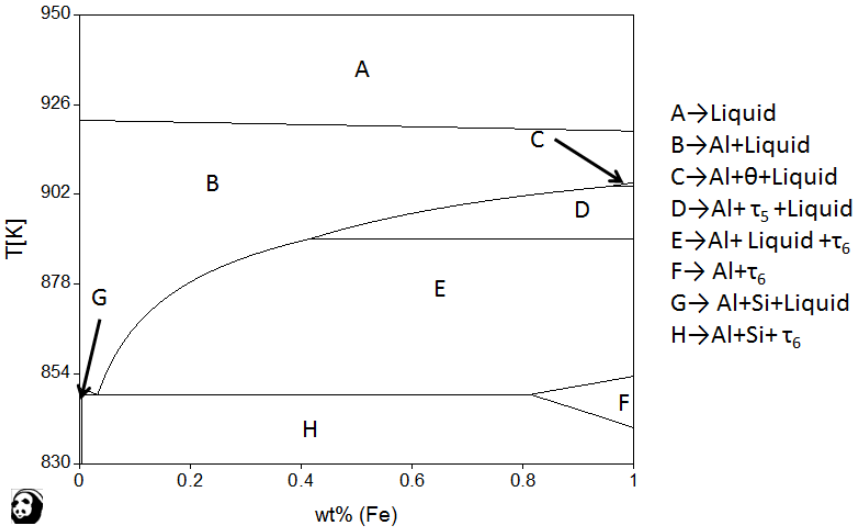
950
926
902
878
854
830
T[K]
0
0.2
0.4
0.6
0.8
1
wt% (Fe)
A
B
C
D
E
F
G
H
A→Liquid
B→Al+Liquid
C→Al+θ+Liquid
D→Al+ τ5 +Liquid
E→Al+ Liquid +τ6
F→ Al+τ6
G→ Al+Si+Liquid
H→Al+Si+ τ6

(a)

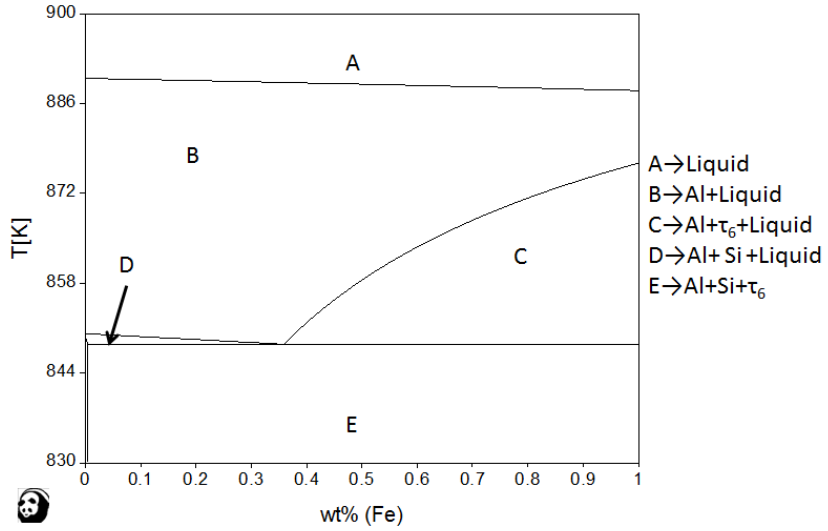
900
886
872
858
844
830
T[K]
0
0.1
0.2
0.3
0.4
0.5
0.6
0.7
0.8
0.9
1
wt% (Fe)
A
B
C
D
E
A→Liquid
B→Al+Liquid
C→Al+τ6+Liquid
D→Al+ Si +Liquid
E→Al+Si+τ6

(b)

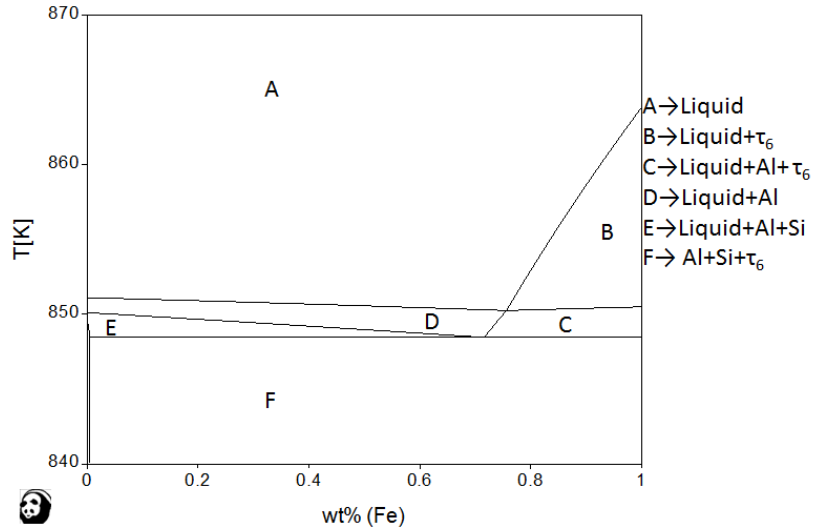

(c)

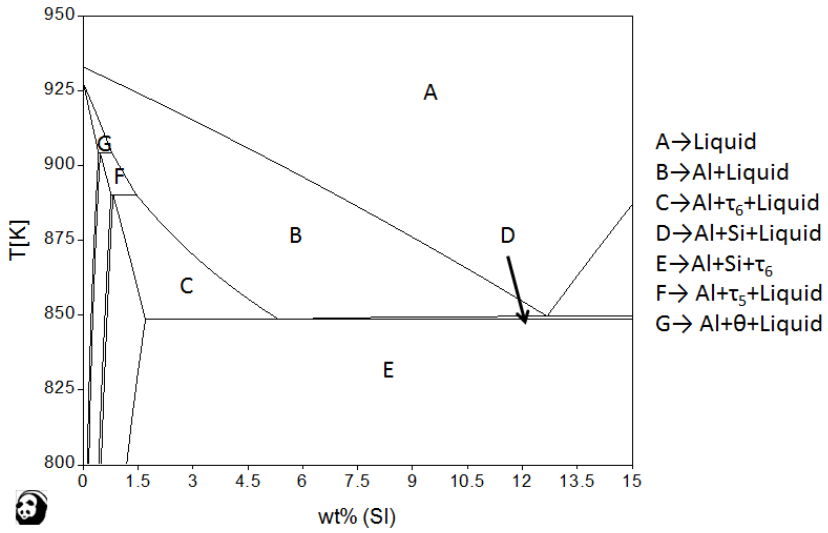

(d)

Figure 6-1: Typical simulated phase diagrams for the Al-Si-Fe system. (a) Al-2Si with increasing Fe, (b) Al 7Si with increasing Fe (c) Al-12.5Si with increasing Fe and (d) Al-0.25Fe with increasing Si content.

Although the terminal phase during "equilibrium" solidification for any combination of the Al-Si-Fe alloy in this study has been observed as the τ_6 – $Al_9Fe_2Si_2$ phase, the τ_5 – Al_8Fe_2Si always evolves prior to the τ_6 – $Al_9Fe_2Si_2$ phase and undergoes a transformation through a peritectic reaction (L + τ_5 – Al_8Fe_2Si → τ_6 – $Al_9Fe_2Si_2$) to enable the formation of the τ_6 phase. In alloys

with cooling rates during solidification that are sufficiently high, the peritectic reaction is suppressed and the τ_5 – Al_8Fe_2Si is retained in the solidified microstructure of the sample at room temperature. The τ_5 – Al_8Fe_2Si phase has a hexagonal crystal structure with a space group of $P6_3/mmc$, and lattice parameters of a = 1.2404 nm and c = 2.6234 nm. The τ_6 – $Al_9Fe_2Si_2$ phase has a monoclinic crystal structure with a space group of C2/c with a0.6161, b= 0.6175, c= 2.0813 and $\beta = 90.42^o$.

The schematic graph between cooling rate and Fe concentration in the alloy shown in Figure 6-2 is a pictorial representation of the type of intermetallic phases that exist in the sample microstructure after solidification of the alloys from a temperature of about 1093 K (820 ^oC). It can be observed that the τ_5 phase is observed at higher cooling rates and lower Fe concentration, and the τ_6 phase is the terminal phase for higher Fe concentrations and lower cooling rates. During solidification, when there is enough time given for the alloy in the two phase region (Liquid + Al) (dictated by the cooling rate), the peritectic reaction (L + τ_5 – Al_8Fe_2Si $\rightarrow$ τ_6 – $Al_9Fe_2Si_2$) will yield the τ_6 as the terminal phase in the solidified sample. Further, higher Fe concentrations in the alloy will enhance the kinetics of the peritectic reaction yielding the terminal τ_6 phase. In Figure 6-2, certain transition cooling rates during solidification and Fe concentration of the alloy results in the presence of both the τ_5 and τ_6 phases in the microstructure; features such as the τ_5 being fully enveloped by the τ_6 phase (symbol “P” in Figure 6-2) could also be observed in the microstructure presenting a direct evidence of the peritectic reaction. Solution heat treatment of the solidified samples containing the τ_5 phase in the microstructure resulted in the transformation of all intermetallic phases to the terminal τ_6 phase which shows that the type of intermetallic phase present in the solidified microstructure is an artifact of the kinetics of the solidification process.

It is evident from Figure 6-2 that there is a band of critical cooling rate above which the τ_5 phase is retained as the stable phase during solidification and below which the peritectic reaction would be completed during solidification yielding the τ_6 phase in the solidified structure. This band of critical cooling rate is a function of the Fe concentration and contains both the τ_5 and τ_6 intermetallic phases in the solidified microstructure: caused either by the solidification arrest during the peritectic reaction or the evolution of an independent τ_6 phase prior to the eutectic temperature for the alloys with 0.5wt%Fe.

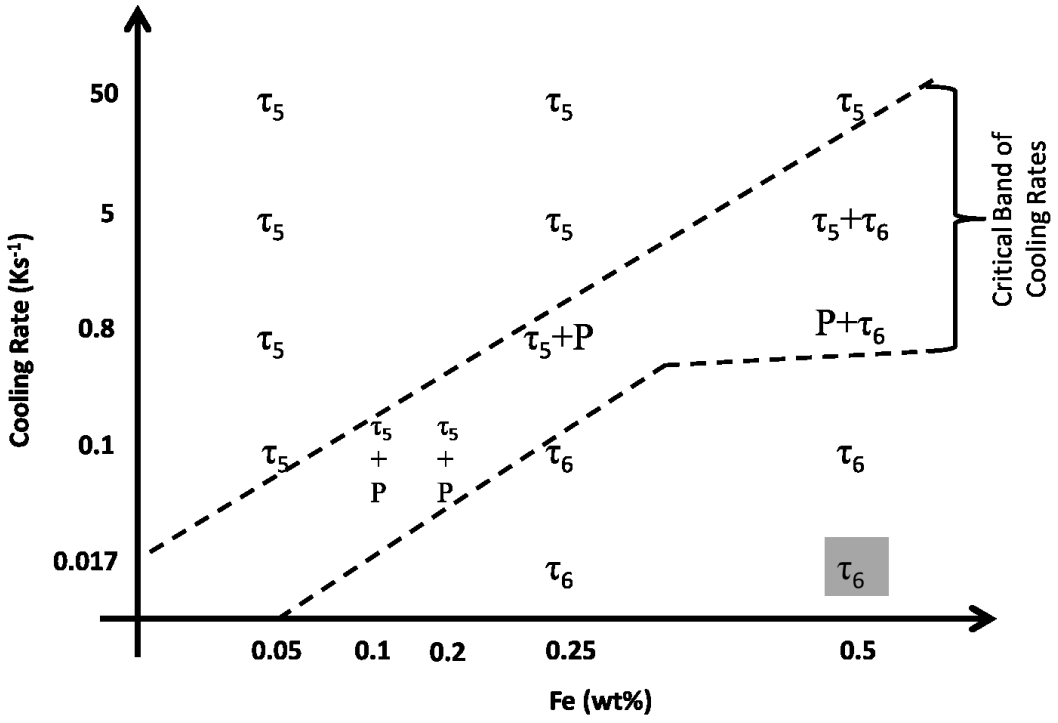

Figure 6-2: Schematic graph of Cooling Rate vs. Fe concentration showing the type of intermetallic phase existing in the sample microstructure after solidification from a temperature of about 1093 K (820 °C) after being held for two hours. The band shown by dotted line presents the conditions in which both the τ_5 and τ_6 phases co-exist in the sample. The symbol "P" represents the τ_5 phase surrounded by the τ_6 phase as arrested during the peritectic reaction: L + τ_5 → τ_6.

The concentration of solute Si is also influences the nature of the intermetallic phase in a solidified structure. The phase diagram in Figure 6-1 (d) presents the equilibrium isopleth for the alloys shown; where the compositions of 2 and 5 wt% Si creates a condition to form the τ_6 phase prior to the eutectic temperature. In addition, the freezing range in the two phase region for the compositions of 2 and 5 wt% Si is quite large compared to the others and it is our hypothesis that apart from the formation of the τ_6 phase and its subsequent transformation to the τ_5 phase by the peritectic reaction during solidification, the solute conditions ahead of the dendrites are favourable for the formation of the τ_5 phase as well prior to the eutectic reaction. Thus, in Figure 6-3, the maximum cooling rate at which the τ_5 phase is retained in the solidified microstructure is increasing for decreasing Si concentrations between 5 and 2 wt%. Further, the critical band of cooling rate that differentiates the type of intermetallic phases in the solidified microstructure is nearly constant between 7 and 12.5 wt% Si as shown in Figure 6-3, because, in this range of Si, the τ_6 phase only appears with the eutectic phases in the equilibrium phase diagram shown in Figure 6-1 (d) and hence, the only intermetallic phase that forms between the liquidus and eutectic temperatures during solidification is the τ_5 phase

which may undergo a peritectic transformation at the slower cooling rates of about 0.8 and 0.1 Ks^{-1}. It is noteworthy that the size of the τ_5 phase decreases with increasing Si concentration between 7 and 12.5 wt% Si in the alloy because of the decreasing freezing ranges of the alloy resulting in a decreasing growth of the τ_5 phase.

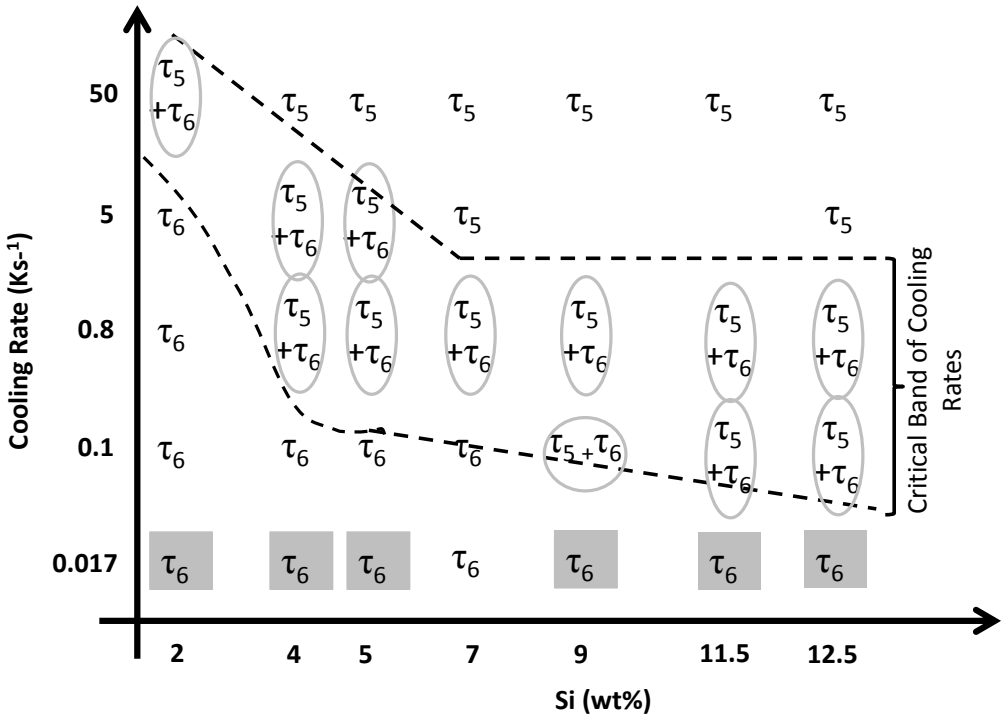

Figure 6-3: Schematic graph of Cooling Rate vs. Si concentration showing the type of intermetallic phase existing in the sample microstructure after solidification of Al-Si-0.25Fe alloys from a temperature of about 1093 K (820 °C) after being held for two hours. The band shown by dotted line presents the conditions in which both the τ_5 and τ_6 phases co-exist in the sample. The grey shaded boxers are hypothesized because these experiments were not carried out.

Alloys solidified from the lower temperature of about 993 K (720 °C) shows the presence of several stable and metastable intermetallic phases and those solidified from a higher temperature of about 1093 K (820 °C) only shows the presence of the τ_5 and/or τ_6 phases (depending on Fe content and cooling rate). The presence of the binary θ-$Al_{13}Fe_4$ intermetallic phase in the commercial purity Al ingot and the Al-Fe master alloys shown in Table 5-1 does not completely dissolve in the liquid alloy maintained at a temperature of about 993 K (720 °C) (about 100 K superheat) unless these alloys are maintained at the superheated temperature for prolonged periods of time to enable the dissolution of the binary phase through diffusion and peritectic reactions. Hence, in alloy solidified from a temperature of about 993 K (720 °C), the presence of solid θ-$Al_{13}Fe_4$ phase particles will trigger alternate solidification paths resulting in

additional stable and metastable intermetallic phase formation during solidification. These phases may include the θ-$Al_{13}Fe_4$, Al_6Fe, τ_7-$Al_3Fe_2Si_3$, and several other metastable phases in addition to the τ_5 and/or τ_6 phases.

The most critical question that needs to be answered in this summary is the reason for the evolution of the τ_5 phase in the microstructure which is contrary to all available thermodynamic model predictions.

In the subsequent sub-sections of this chapter, evidences from the experiment results will be presented to validate the claims in the above mentioned summary and a discussion presented to hypothesize the anomalous observations.

6.2 APPEARANCE AND CHARACTERISTICS OF THE τ_5 AND τ_6 PHASES

The Figure 6-4 shows four magnifications of the light optical micrographs for the Al-7Si-0.25Fe alloy that was solidified form a temperature of about 1093 K (820 ^oC) at a cooling rate of 0.8 K/s^{-1}. The intermetallic phase observed in this condition is the τ_5 – Al_8Fe_2Si phase which typically has an irregular script-like morphology in three dimensional space and commonly observed as a Chinese-script morphology in a two dimensional microstructure (pointed out in Figure 6-4 (d)).

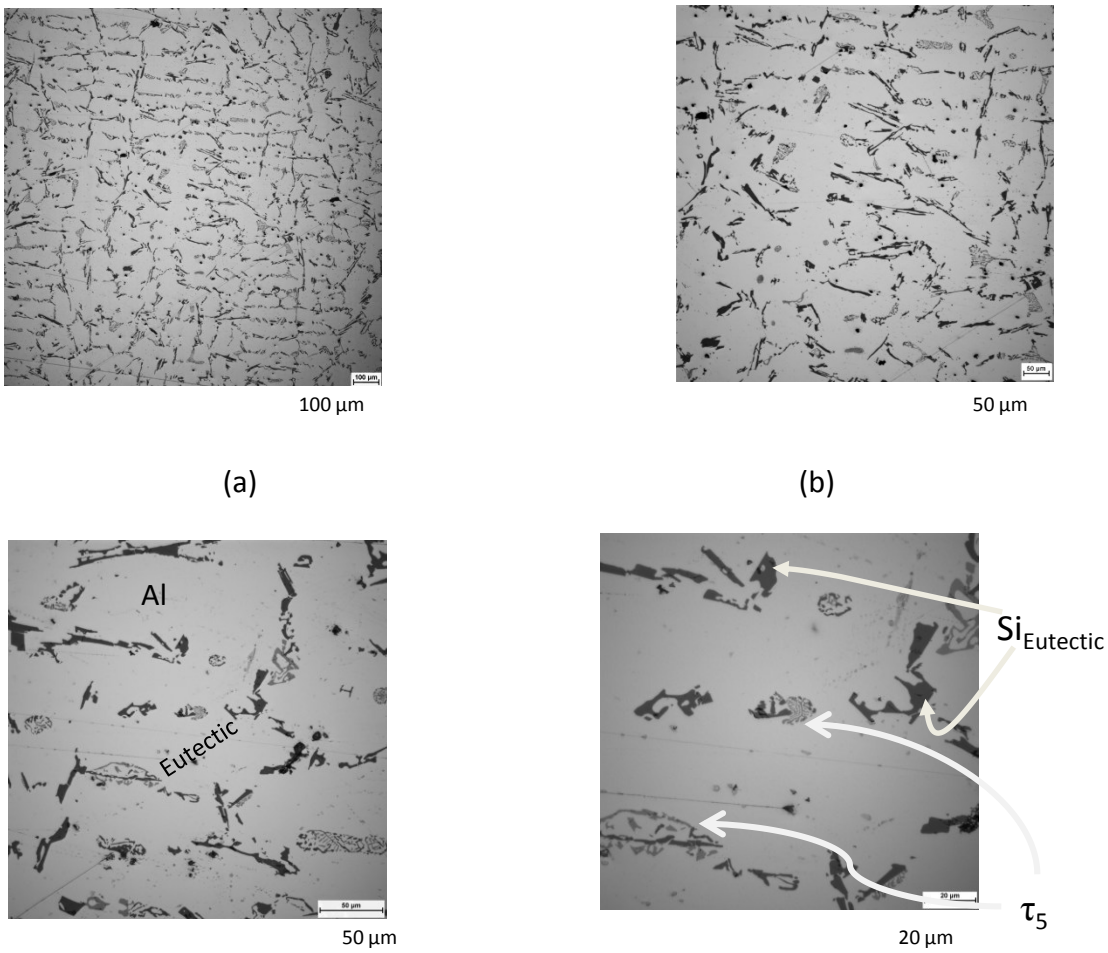

Figure 6-4: Typical microstructure obtained in a light optical microscope of the Al-7Si-0.25Fe solidified from about 1093 K (820 °C) at a cooling rate of 0.8 K/s^{-1}. (a) to (d) shows increasing magnification images wherein the light grey phase is primary Al matrix, dark grey phase is the script-like τ_5 – Al_8Fe_2Si phase and black phase is eutectic Si.

The Figure 6-5 shows four magnifications of the light optical micrographs for the Al-7Si-0.25Fe alloy that was solidified form a temperature of about 1093 K (820 °C) at a cooling rate of 0.1 Ks^{-1}. The intermetallic phase observed in this condition is the τ_6 – $Al_9Fe_2Si_2$ phase which typically has a morphology of a plate in three dimensional space and commonly observed as an acicular morphology in a two dimensional microstructure (pointed out in Figure 6-5 (d)).

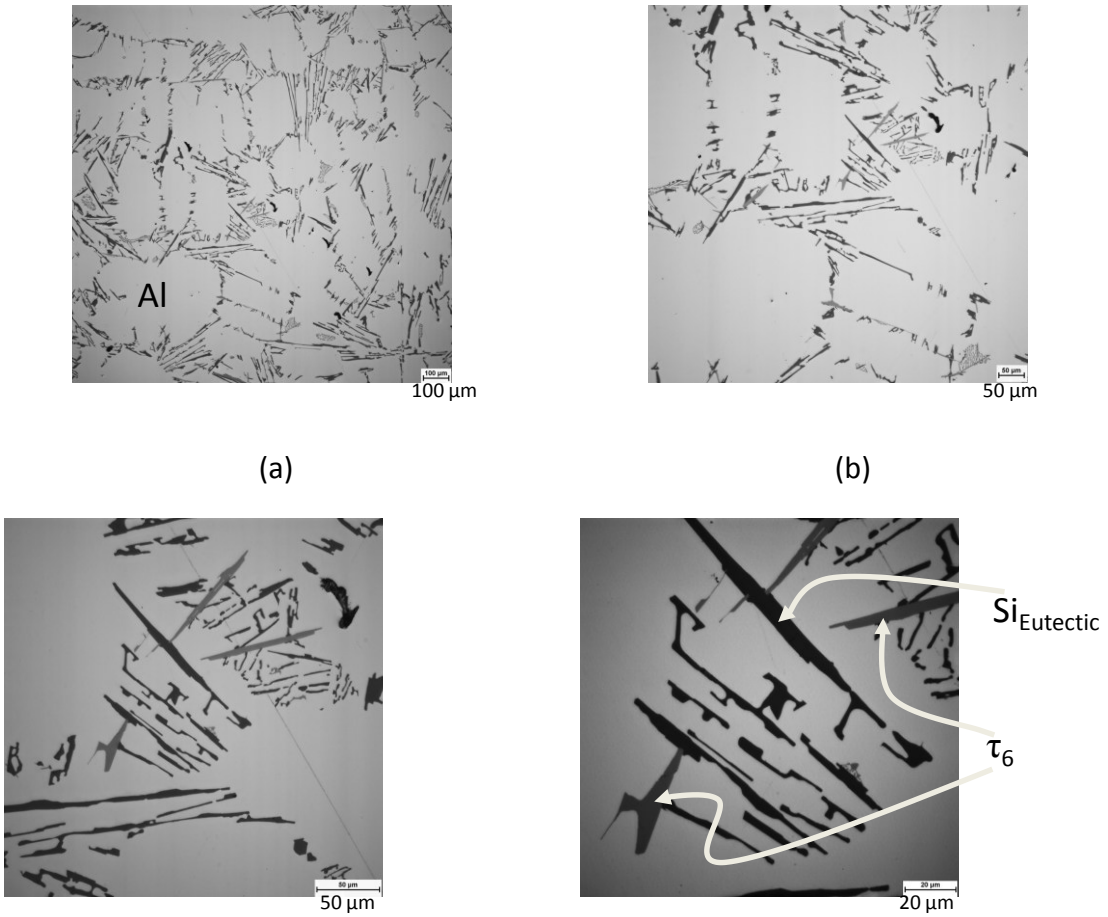

Figure 6-5: Typical microstructure obtained in a light optical microscope of the Al-7Si-0.25Fe solidified from about 1093 K (820 °C) at a cooling rate of 0.1 K/s^{-1}. (a) to (d) shows increasing magnification images wherein the light grey phase is primary Al matrix, dark grey phase is the plate-like τ_6 – $Al_9Fe_2Si_2$ phase and black phase is eutectic Si.

Typical morphologies of the τ_5 and τ_6 phases observed in a SEM is shown in Figure 6-6

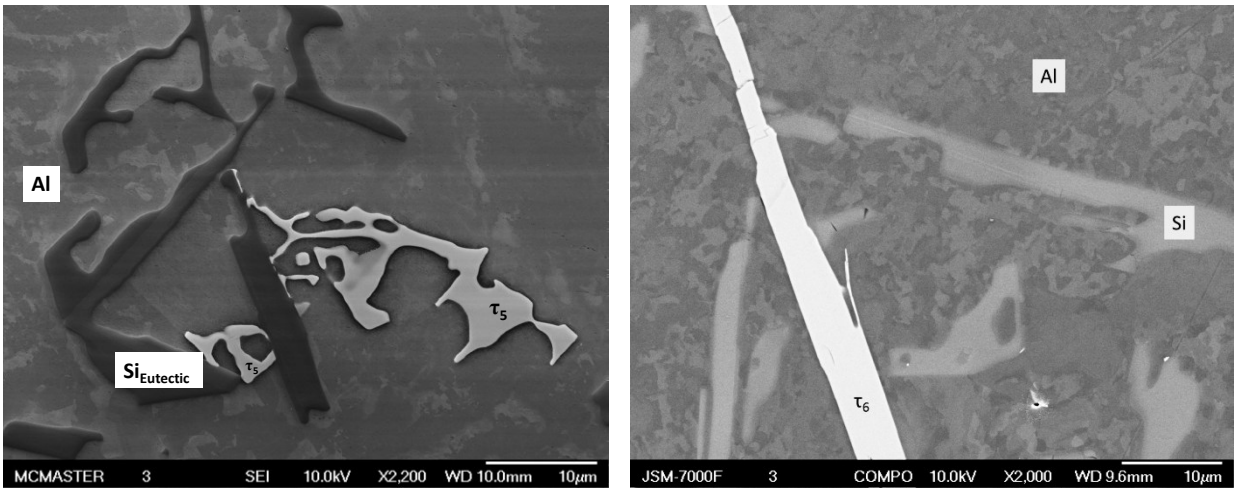

(a) (b)

Figure 6-6: Typical morphologies of the τ_5 and τ_6 phases observed in an SEM. The alloy is Al-7Si-0.25Fe solidified from about 1093 K (820 °C) at a cooling rate of (a) 0.8 Ks^{-1} showing the τ_5 – Al_8Fe_2Si phase and (b) 0.1Ks^{-1} showing the τ_6 – $Al_9Fe_2Si_2$ phase.

Figure 6-7 (a) and (b) presents the typical quantified data from the EDX analysis of the τ_5 and τ_6 phases, respectively, in the Al-7Si-0.25Fe alloy solidified from about 1093 K (820 °C) at 0.8 Ks^{-1} and 0.1 Ks^{-1}, respectively. The typical ratio of Fe:Si atoms in the τ_5 phase is 2:1 and that in the τ_6 phase is 1:1.

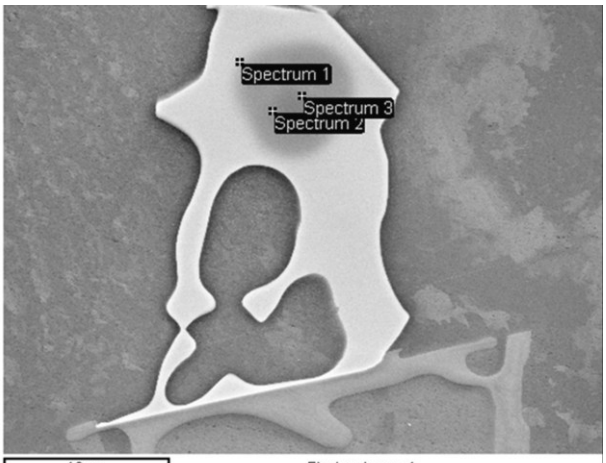

Spectrum	Al	Si	Fe
	(Atomic %)		
Spectrum 1	68.67	10.16	21.16
Spectrum 2	68.15	10.71	21.14
Spectrum 3	67.83	10.90	21.26
Mean	**68.22**	**10.59**	**21.19**
Std. Dev.	0.42	0.38	0.07
Max.	68.67	10.90	21.26
Min.	67.83	10.16	21.14

(a)

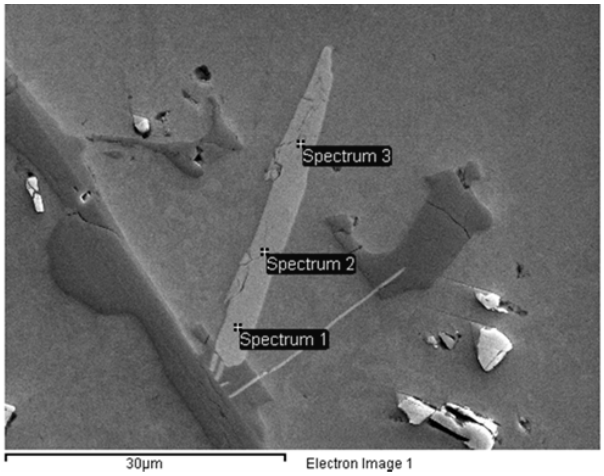

Spectrum	Al	Si	Fe
	(Atomic %)		
Spectrum 1	63.17	18.66	18.17
Spectrum 2	62.79	17.81	19.40
Spectrum 3	63.42	18.25	18.34
Mean	**63.13**	**18.24**	**18.63**
Std. Dev.	0.32	0.42	0.66
Max.	63.42	18.66	19.40
Min.	62.79	17.81	18.17

(b)

Figure 6-7: Typical quantified data from the EDX analysis in the SEM for (a) τ_5 – Al_8Fe_2Si phase and (b) τ_6 – $Al_9Fe_2Si_2$ phase obtained from the microstructures of AL-7Si-0.25Fe alloy shown in Figure 6-6. The ratio of Fe:Si in τ_5 is nearly 2:1 and that in τ_6 is nearly 1:1.

6.3 HOMOGENIZATION OF THE AL ALLOY LIQUID

In the initial couple of years of this project, all the Al alloys in this study were melted at about 993 K (720 °C) and 953 K(680 °C), and held at that temperature for an hour or two prior to the solidification. It was later observed that the Fe bearing intermetallic phases that were present in the solid raw materials used for preparing the final alloy composition or present in the solidified alloy stock used for re-melting did not completely dissolve into the alloy liquid at 993 K (720 °C) in an hour or two. It was observed that a critical stage in effecting a valid study of the phase evolving during solidification of the Al-Si-Fe alloys is the complete homogenization of the alloy melt at high temperature. Hence, the study was carried out in alloys solidified from about 1093 K (820 °C) or more (held for at least 2 hours) to ensure complete compositional homogeneity in the liquid phase prior to solidification. As an example, Figure 6-8 shows the typical difference between the observed intermetallic phases in the Al-7Si-0.25Fe alloy solidified at 0.8 Ks^{-1} from two different initial temperatures of the liquid alloy. The alloy solidified from 953 K (680 °C) has a multitude of metastable intermetallic phases in addition to

the stable τ_5 and τ_6 phases, as well (refer to Figure 6-8 (a)); the alloy solidified from 1093 K (820 ^oC) only showed the presence of the τ_5 intermetallic phase in the solidified microstructure,

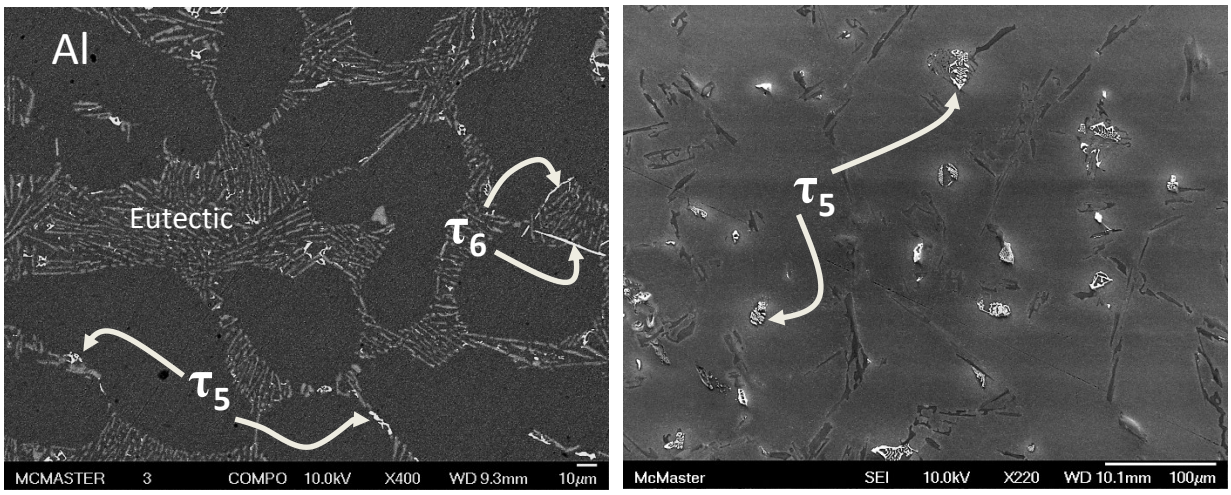

(a) (b)

Figure 6-8: Typical microstructure of the Al-7Si-0.25Fe solidified at a cooling rate of 0.8 Ks^{-1} from an initial liquid alloy temperature of (a) 953 K (680 ^oC) showing several types of stable and metastable intermetallic phases and (b) 1093 (820 ^oC) showing the existence of only the τ_5 phase. The small white phase in (a) are the various metastable binary and ternary intermetallic phases in the Al-Fe-Si system. Both the alloys were held for two hours in their respective melt temperatures.

The aim of this research study is to enable a clear understanding of the intermetallic phases evolving during solidification of Al-Si-Fe pure and homogeneous liquid alloy and hence, the initial alloy temperature prior to solidification was maintained at greater than 1093 K (820 ^oC) for a minimum of two hours. All the results from this point onwards in this dissertation are for alloys solidified from this temperature alone unless otherwise mentioned.

6.4 EFFECT ON SI IN THE AL-SI-FE ALLOYS ON THE INTERMETALLIC PHASES

There are two stable intermetallic phases, τ_5 and τ_6, that could evolve during the solidification of the Al-Si-Fe alloys with 2 to 12.5 wt% Si and 0 to 0.8 wt%Fe in them. The effect of Si was studied for the Al alloys containing 0.25Fe at several cooling rates during solidification as shown in Figure 4-1 (a) and (b). Figure 6-3, which shows the schematic of the observations of the intermetallic phases in the solidified microstructure has been presented again as Figure 6-9 to enable easy reading of this dissertation.

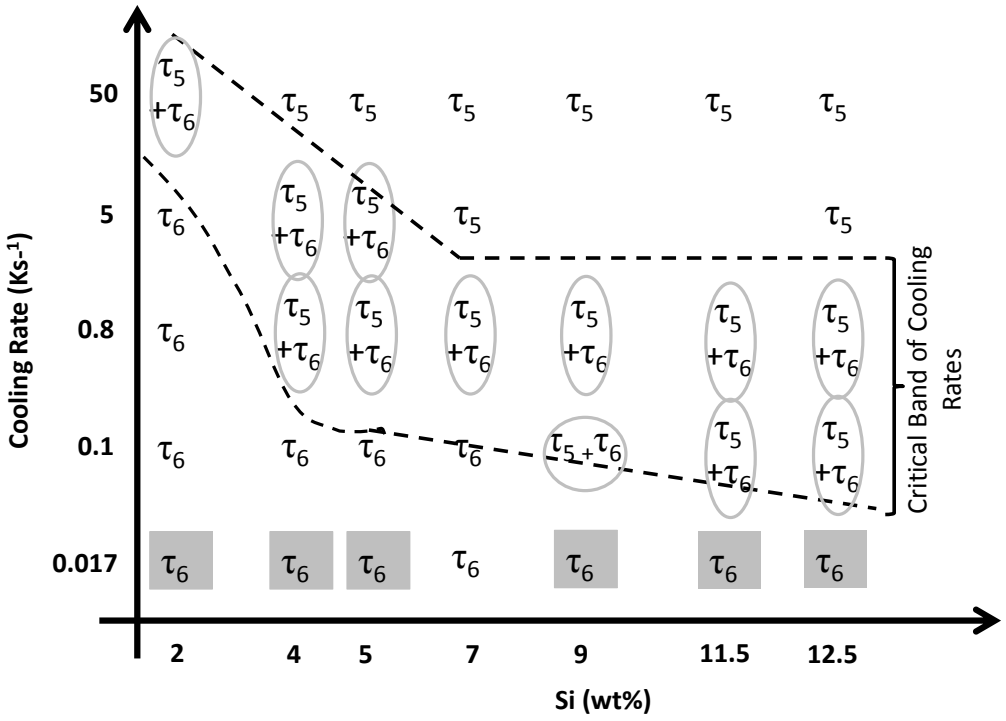

Figure 6-9: Schematic graph of Cooling Rate vs. Si concentration showing the type of intermetallic phase existing in the sample microstructure after solidification of Al-Si-0.25Fe alloys from a temperature of about 1093 K (820 ^{o}C) after being held for two hours. The band shown by dotted line presents the conditions in which both the τ_5 and τ_6 phases co-exist in the sample. The grey shaded boxers are hypothesized because these experiments were not carried out.

The results presented in this sub-section will be microstructure images of the solidified samples with cooling rate just above, within and below the critical band shown in the matrix presented in Figure 6-9.. Typical microstructures of the solidified Al-Fe-Si alloy showing the morphology of the critical solidification phases in both the SEM and light optical microscope are shown in Figure 6-10.

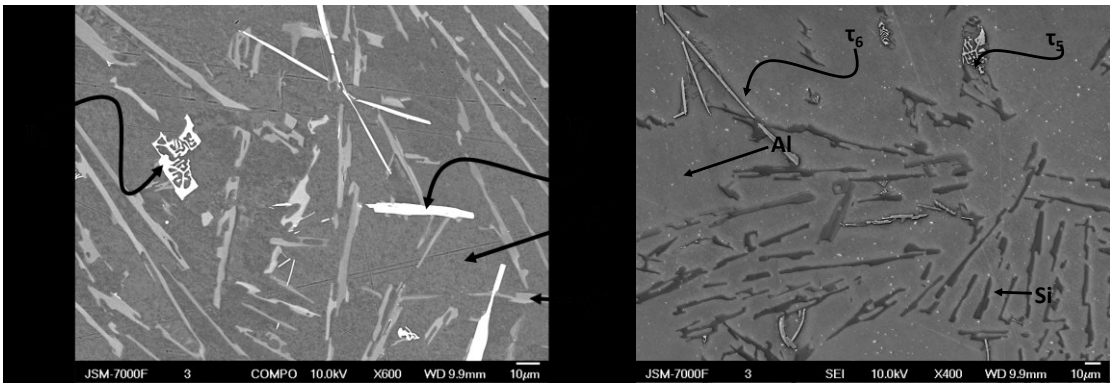

(a) (b)

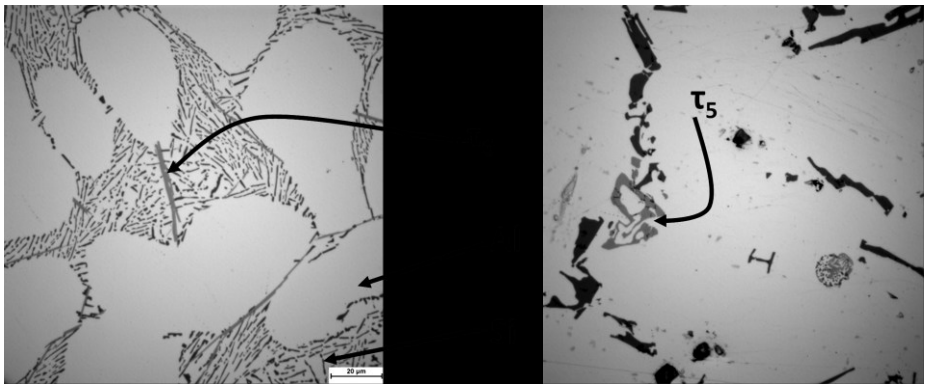

(c) (d)

Al → Primary Aluminum
Si → Eutectic Si
τ_5 → Al_8SiFe_2 hexagonal
τ_6 → $Al_9Si_2Fe_2$ monoclinic

(e)

Figure 6-10: Typical morphology of the critical phases evolved during solidification of the Al-Fe-Si alloy in the Al rich corner of the phase diagram. (a) SEM Backscatter Electron Image (BSEI), (b) SEM Secondary Electron Image (SEI), (c) and (d) light optical microscope images, and (e) nomenclature of the observed phases.

In the results of the microstructure images shown in this chapter, a combination of light optical microscope, SEM/SEI and SEM/BSEI microstructure images will be presented and readers are advised to refer to Figure 6-10 as a typical example of identifying the images obtained by these individual microscopy techniques.

Figure 6-11 presents the SEM electron image of the Al-**2Si**-0.25Fe alloy solidified at 50K/s^{-1} (Figure 6-11 (a) and (b)) and 5 Ks^{-1} (Figure 6-11 (c) and (d)); the presence of both the τ_5 and τ_6 phases are observed in the 50 Ks^{-1} cooling rate whereas, only the τ_6 phase was observed in the lower 5 Ks^{-1} cooling rate during solidification. Further, only the τ_6 phase was observed in the lower cooling rates of 0.8 and 0.1 Ks^{-1}.

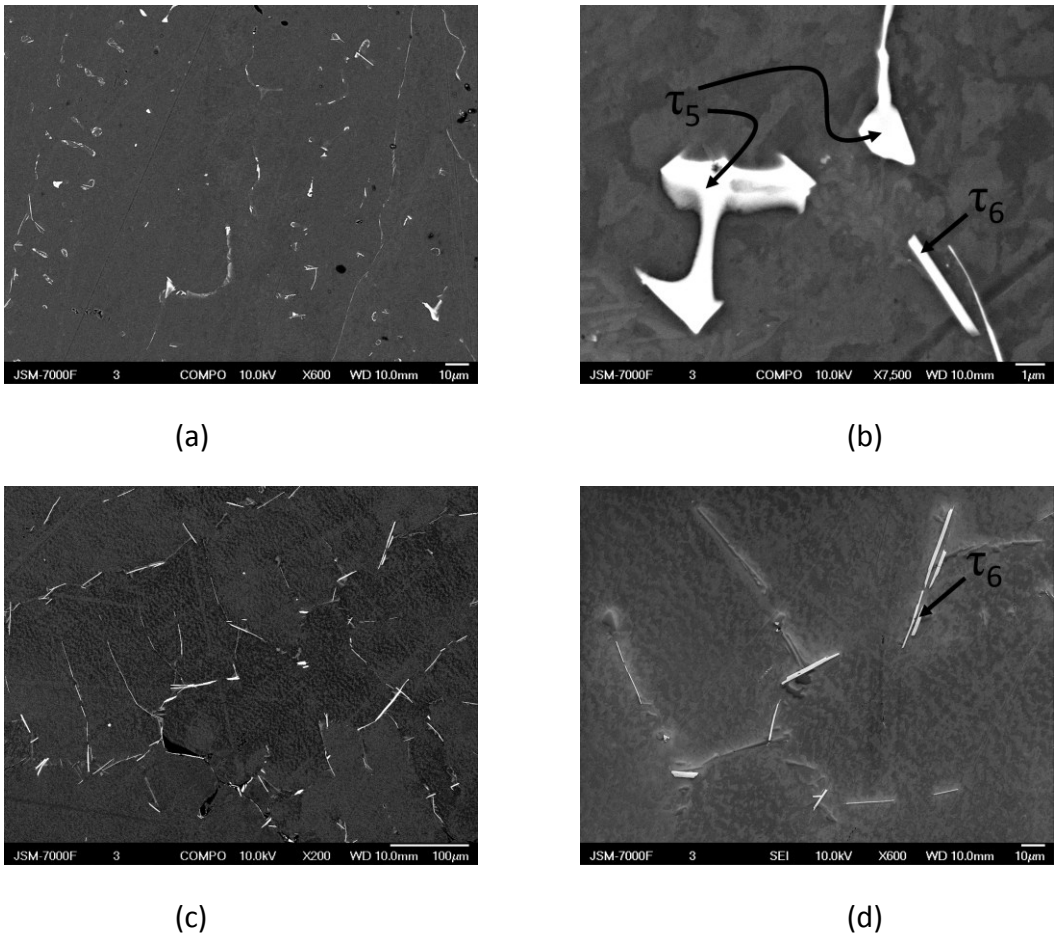

Figure 6-11: Typical microstructure images of Al-2Si-0.25Fe solidified at (a) and (b) 50K/s-1 showing the presence of both the τ_5 and τ_6 phases; and (c) and (d) 5 K/s-1 showing the presence of only the τ_6 phase.

Figure 6-12 presents the SEM images of the Al-**4Si**-0.25Fe alloy solidified at 50Ks^{-1} (Figure 6-12 (a) and (b)) and 5 Ks^{-1} (Figure 6-12 (c) and (d)); the presence of only the τ_5 phase is observed in the 50 Ks^{-1} cooling rate whereas, only the τ_6 phase was observed in the lower 5 Ks^{-1} cooling rate during solidification. Further, only the τ_6 phase was observed in the lower cooling rates of 0.8 and 0.1 Ks^{-1}, as well.

Figure 6-13 to Figure 6-17 show the typical microstructure images of the solidified samples of the Al-Si-0.25Fe alloys for the various Si levels of 5, 7, 9, 11.5 and 12.5 wt%, respectively. In Figure 6-13 to Figure 6-17, the images (a) and (b) show the higher cooling rate at which only the τ_5 phase exists,; (c) and (d) show the intermediate cooling rate at which bot the τ_5 and τ_6 phases co-exist; and (e) and (f) show the lower cooling rate in which only the τ_6 phase exists in the solidified microstructure.

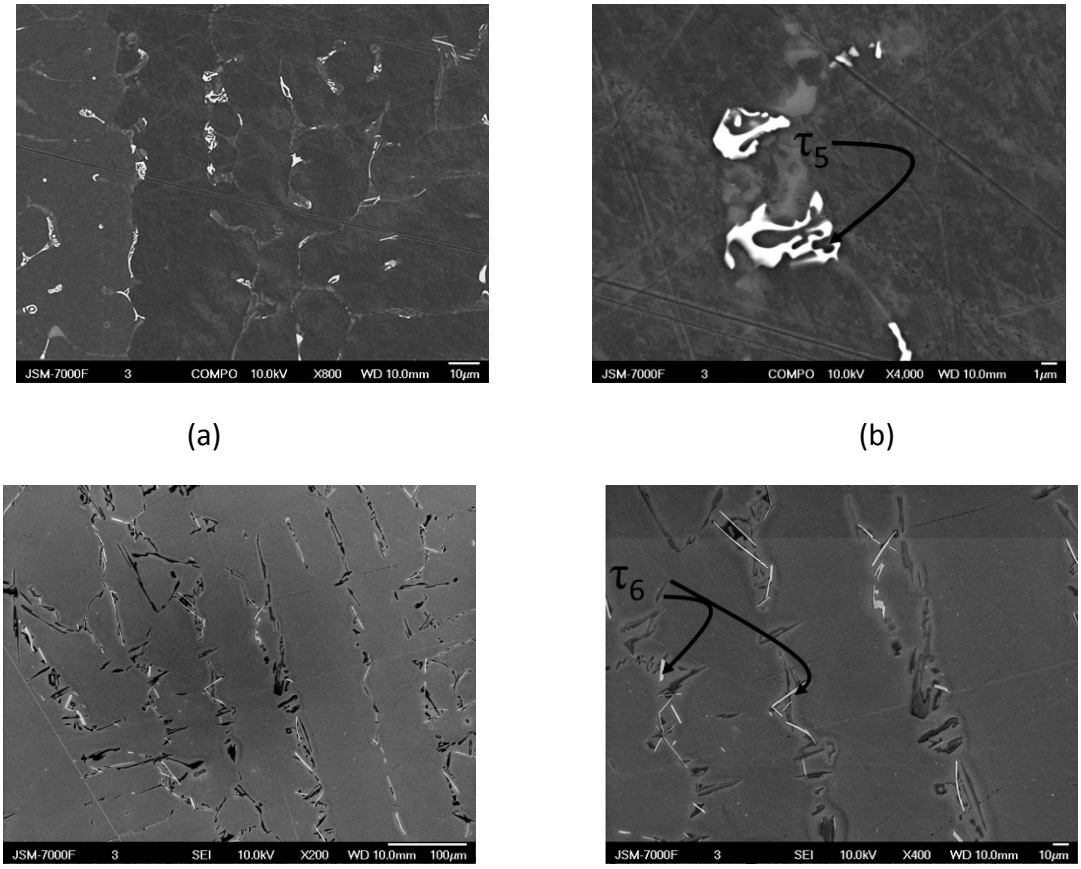

Figure 6-12: Typical microstructure images of Al-4Si-0.25Fe solidified at (a) and (b) 50Ks^{-1} showing the presence of only the τ_5 phases; and (c) and (d) 5 Ks^{-1} showing the presence of only the τ_6 phase.

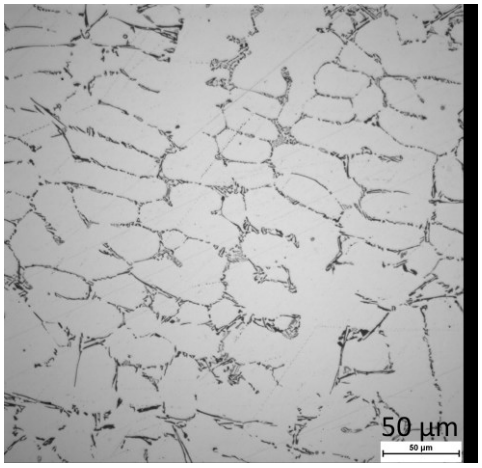

(a)

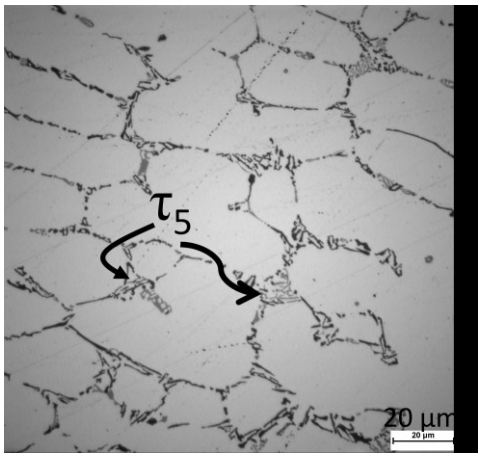

(b)

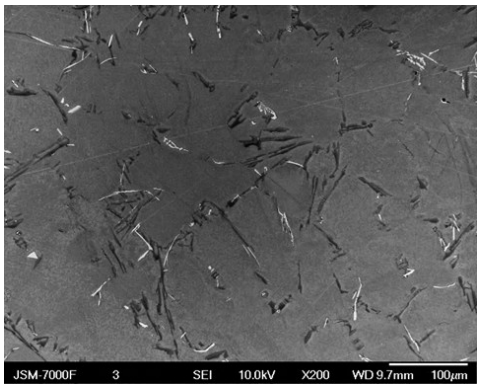

(c)

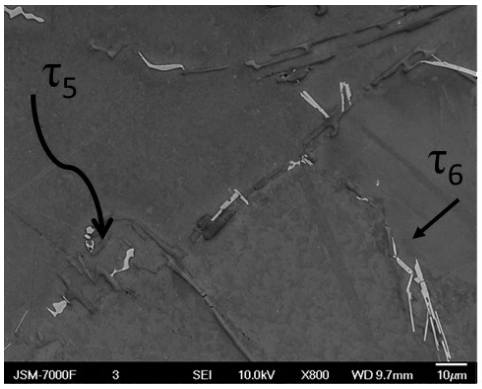

(d)

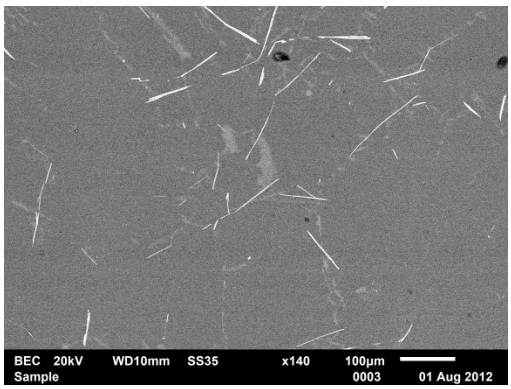

(e)

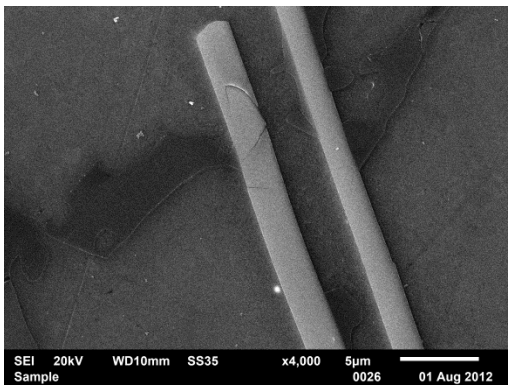

(f)

Figure 6-13: Typical microstructure images of Al-5Si-0.25Fe solidified at (a) and (b) 50Ks^{-1} showing the presence of only the τ_5 phases; (c) and (d) 5 Ks^{-1} showing the presence of both the τ_5 and τ_6 phase; and (e) and (f) Al-4.5 Si-025Fe 0.1 Ks^{-1} showing the presence of only the τ_6 phase.

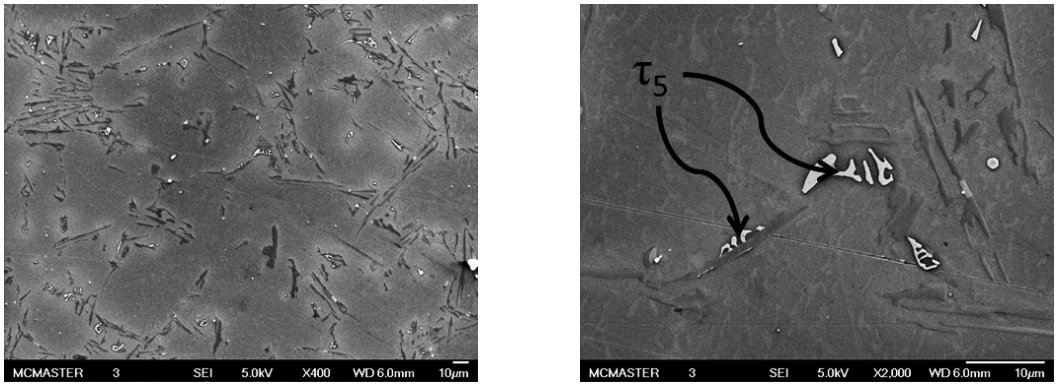

(a) (b)

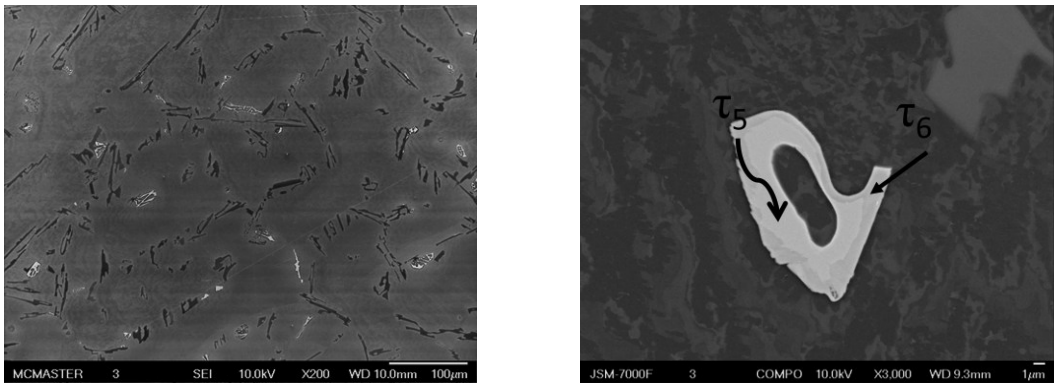

(c) (d)

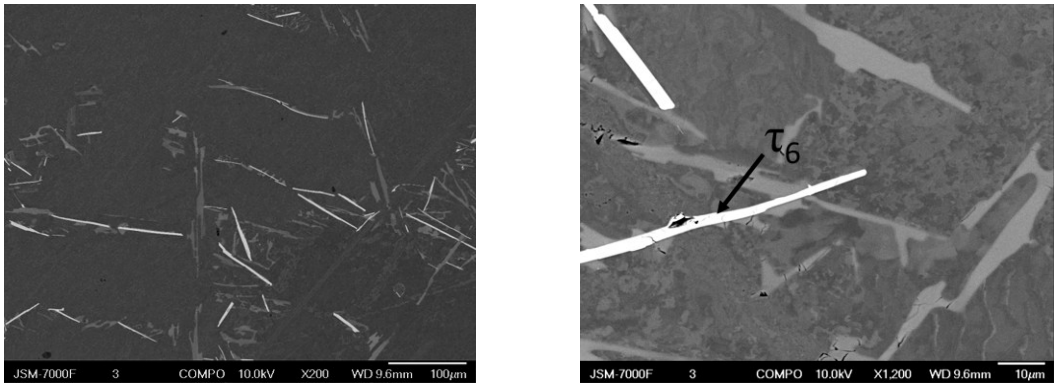

(e) (f)

Figure 6-14: Typical microstructure images of Al-7Si-0.25Fe solidified at (a) and (b) 5Ks^{-1} showing the presence of only the τ_5 phases; (c) and (d) 0.8 Ks^{-1} showing the presence of both the τ_5 and τ_6 phase; and (e) and (f) 0.1 Ks^{-1} showing the presence of only the τ_6 phase with very sparse presence of small τ_5 phase morphology.

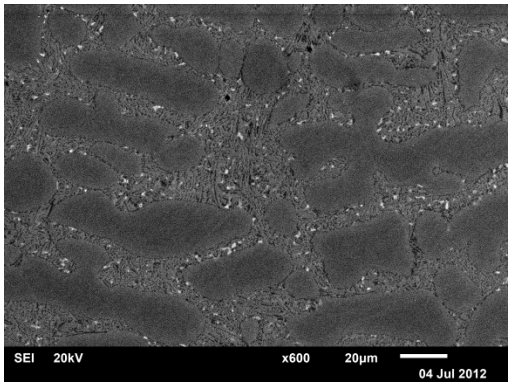

(a)

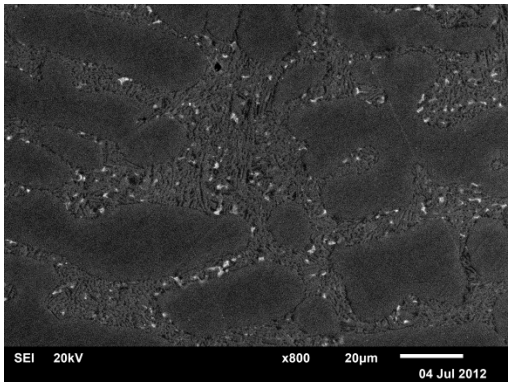

(b)

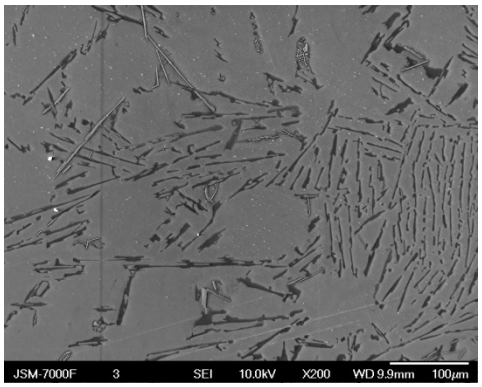

(c)

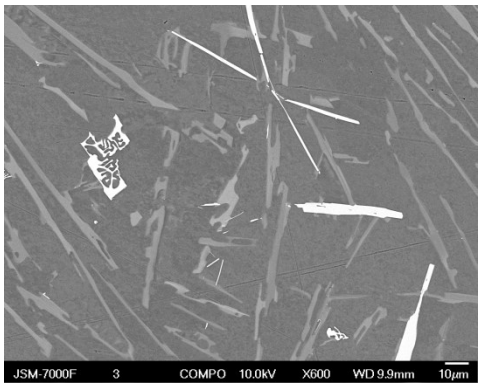

(d)

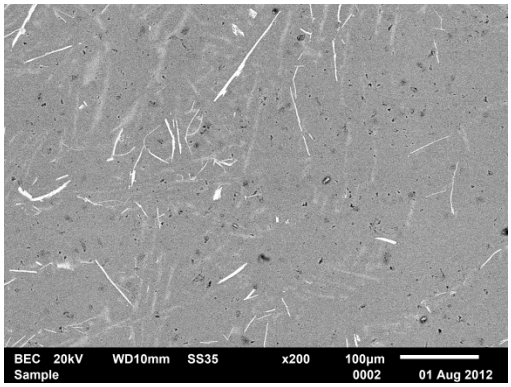

(e)

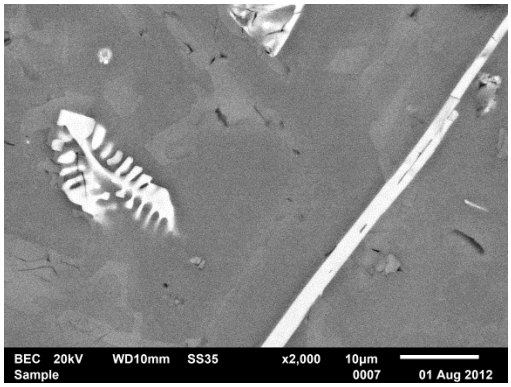

(f)

Figure 6-15: Typical microstructure images of Al-9Si-0.25Fe solidified at (a) and (b) 50Ks^{-1} showing the presence of only the τ_5 phases; (c) and (d) 0.8 Ks^{-1} showing the presence of both the τ_5 and τ_6 phase; and (e) and (f) 0.1 Ks^{-1} showing the presence of both the τ_6 (majority) and τ_5 phases.

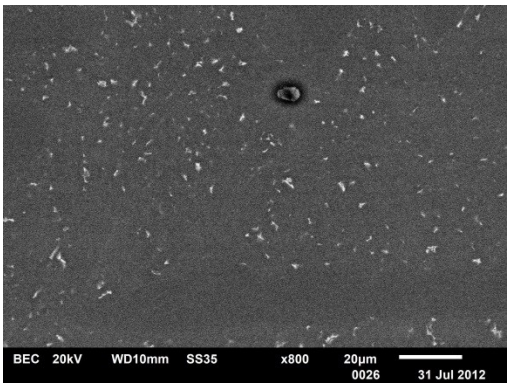

(a)

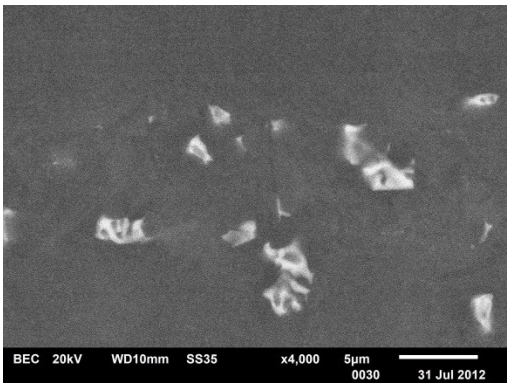

(b)

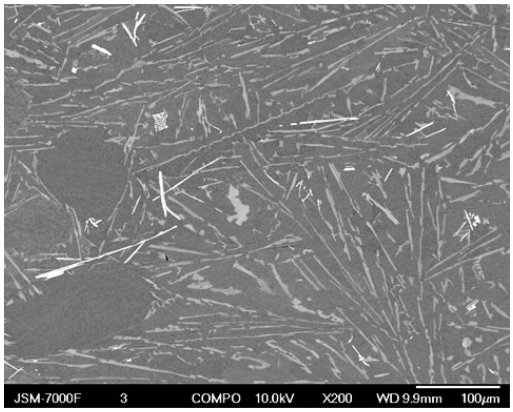

(c)

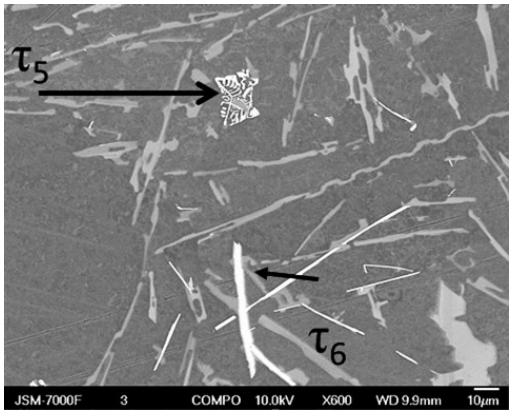

(d)

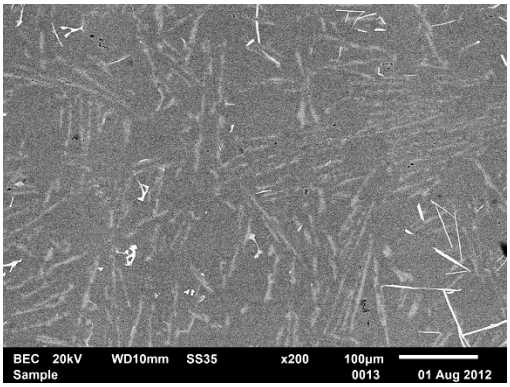

(e)

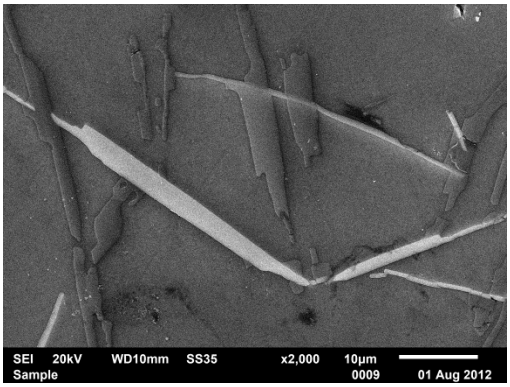

(f)

Figure 6-16: Typical microstructure images of Al-11.5Si-0.25Fe solidified at (a) and (b) 50Ks^{-1} showing the presence of only the τ_5 phases; (c) and (d) 0.8 Ks^{-1} showing the presence of both the τ_5 and τ_6 phase; and (e) and (f) 0.1 Ks^{-1} showing the presence of both the τ_6 and τ_5 phases.

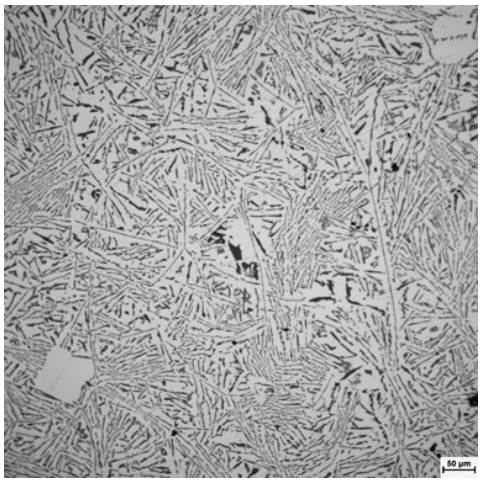

(a)

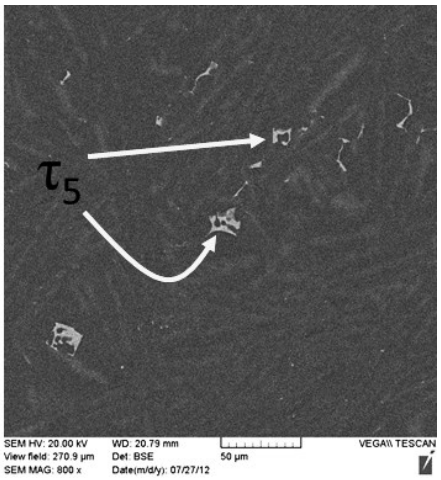

(b)

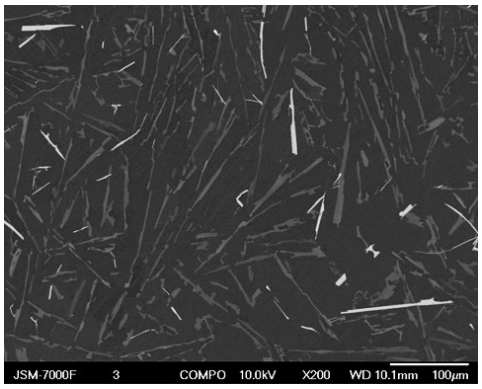

(c)

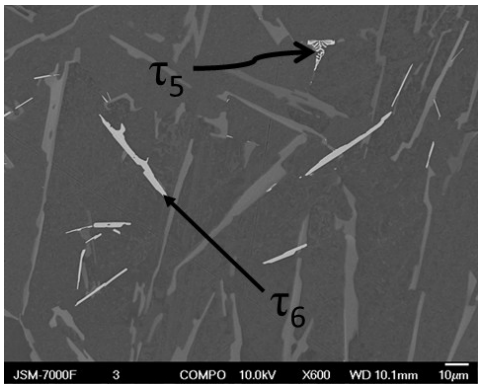

(d)

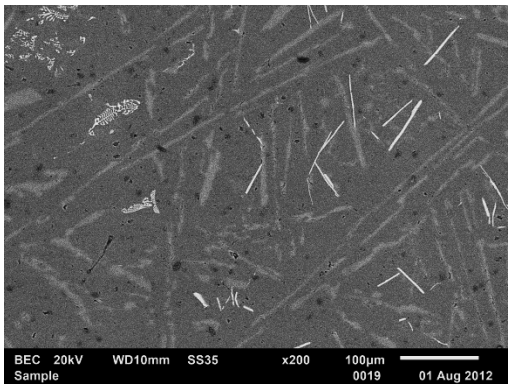

(e)

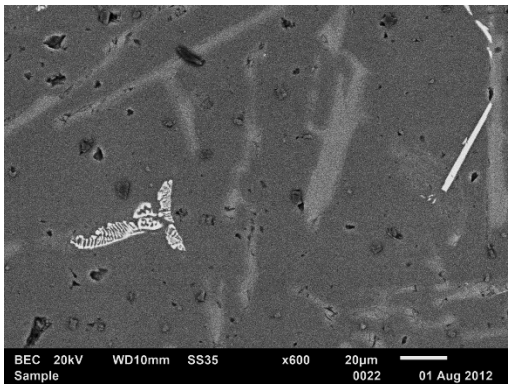

(f)

Figure 6-17: Typical microstructure images of Al-12.5Si-0.25Fe (eutectic alloy) solidified at (a) and (b) 5Ks^{-1} showing the presence of only the τ_5 phases; (c) and (d) 0.8 Ks^{-1} showing the presence of both the τ_5 and τ_6 phases; and (e) and (f) 0.1 Ks^{-1} showing the presence of both the τ_6 and τ_5 phases.

The isopleth phase diagram from the Al-Si-Fe ternary system with Al-xSi-0.25Fe (x=0 to 15 wt%) alloy is presented in Figure 6-18; wherein, the τ_6 phase evolves prior to the eutectic reaction for alloys with 0 to about 5 wt% Si in them. In our alloys of Al-xSi-0.25Fe (x=2,4 and 5), the critical band of cooling rates above which only the τ_5 phase and below which only the τ_6 phase is observed, is shifted to higher cooling rates for lower Si concentration in the alloy, as shown by Figure 6-9, Figure 6-11, Figure 6-12 and Figure 6-13. There are three methods by which the τ_6 phase evolves during the solidification of the Al-xSi-0.25Fe (x=2, 4 or 5) alloys. In one method, the τ_5 phase first evolves after the liquidus temperature because of favourable ratios of Fe and Si atoms in the liquid just ahead of the solidifying primary Al phase. Depending on the cooling rate, this τ_5 phase may further transform into the τ_6 phase during solidification by the peritectic reaction: $L + \tau_5 \rightarrow \tau_6$. In the second method, the thermodynamic phase diagram in Figure 6-18 predicts the evolution of the τ_6 phase at a temperature in between the liquidus and eutectic temperatures, and in the third method, the τ_6 phase evolves with the final eutectic phases. The evolution of the τ_6 phase independently prior to the eutectic temperature is dependent upon the cooling rate during solidification, as well, such that, at high cooling rates, this reaction could be suppressed. Hence, in the Al-xSi-0.25Fe (x=2,4 or 5) alloys, the critical cooling rate for the appearance of the τ_6 phase further increases for decreasing values of Si concentration in the alloy as observed in the schematic shown in Figure 6-3 and the results presented in Figure 6-11 to Figure 6-13.

In Al-xSi-0.25Fe ($5<x\leq12.5$) alloys, the τ_6 phase evolves by two methods: through the peritectic reaction between the liquid and τ_5 phases, and the final eutectic reaction. Further, the maximum cooling rate at which the peritectic reaction occurs prior to the eutectic temperature decreases with increasing Si content because the temperature range of solidification decreases with increasing Si concentration in the Al-xSi-0.25Fe (x=2 to 12.5) alloys; which could be further interpreted as the solidified samples with increasing Si concentration will begin to observe the τ_6 phase obtained from the peritectic reaction at a decreasing value of the cooling rate. Figure 6-19 presents the temperature range of solidification of Al-xSi-0.25Fe (x=2 to 12.5) alloys obtained through both thermodynamic simulation and thermal data during solidification experiments. Additionally, the τ_6 phase evolved along with the eutectic phases in the Al-xSi-yFe (x=2 to 12.5 and y = 0.05 to 0.5) alloys appears to be suppressed at high cooling rates of about 50 Ks^{-1} and results in the evolution of only the τ_5 phase, instead.

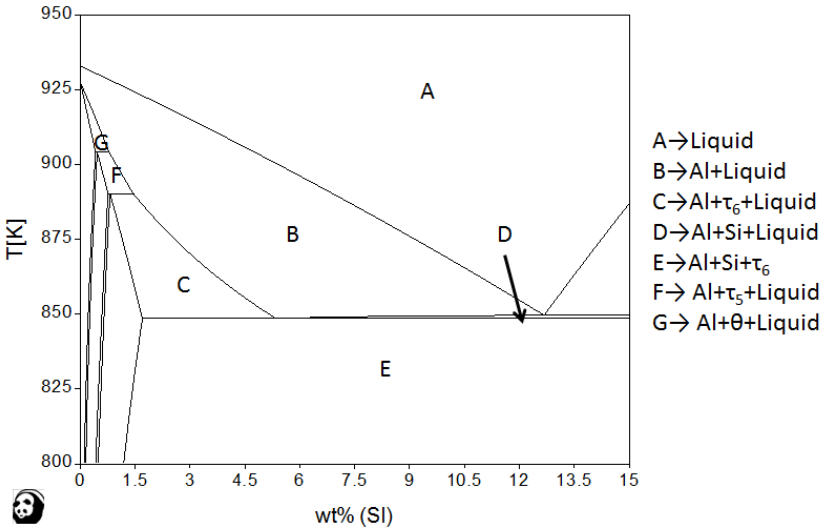

Figure 6-18: Isopleth phase diagram of the Al-Si-Fe system showing the Al-xSi-0.25Fe alloy (x=0 to 15wt%).

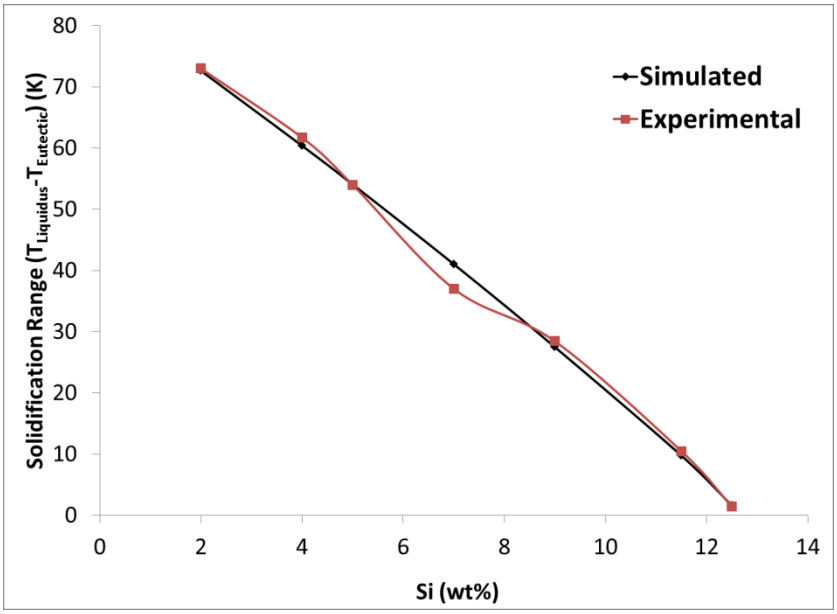

Figure 6-19: Temperature range of solidification of the various Al-xSi-0.25Fe (x=2 to 12.5) alloys evaluated by both thermodynamic simulations using the Pandat software and thermal data obtained during solidification experiments at 0.1 K/s^{-1}. The error in the temperature measurement for the experimental condition is ±0.4 K.

The only fact yet to be verified and validated is the anomalous evolution of the τ_5 phase at any stage during the solidification of the Al-xSi-yFe (x=2 to 12.5 and y = 0.05 to 0.5) alloys. A hypothesis explaining this observed phenomenon is presented at the end of this chapter after presenting all the salient results.

6.5 EFFECT OF FE IN AL-SI-FE ALLOYS ON THE INTERMETALLIC PHASES

Figure 6-2, which shows the schematic of the observations of the intermetallic phases in the solidified microstructure has been presented again as Figure 6-20 to enable easy reading of this dissertation.

The Al-7Si-yFe (y=0.05 to 0.5) alloys were chosen to study the effect of Fe on the evolution of the intermetallic phases during solidification. The results presented in this sub-section will involve microstructure images from samples solidified just above, within and just below the critical band of cooling rate during solidification shown in Figure 6-20. In Figure 6-20, the symbol "P" represents the τ_5 phase enveloped by the τ_6 phase as arrested during the peritectic reaction ($L + \tau_5 \rightarrow \tau_6$); the critical band of cooling rate for each level of Fe concentration contains the τ_5 and P phases for the Fe levels of 0.05 to 2 wt% and τ_6 and P phases for 0.5 wt% Fe in the alloys.

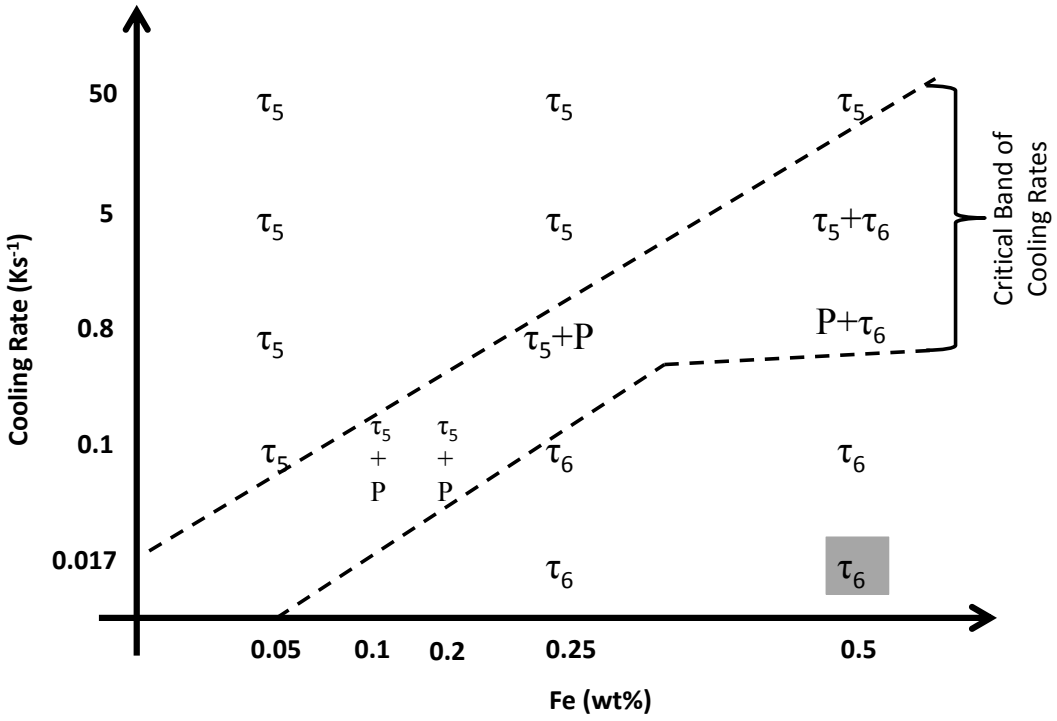

Figure 6-20: Schematic graph of Cooling Rate vs. Fe concentration showing the type of intermetallic phase existing in the sample microstructure after solidification from a temperature of about 1093 K (820 °C) after being held for two hours. The band shown by dotted line presents the conditions in which both the τ_5 and τ_6 phases co-exist in the sample. The symbol "P" represents the τ_5 phase surrounded by the τ_6 phase as arrested during the peritectic reaction: L + τ_5 → τ_6.

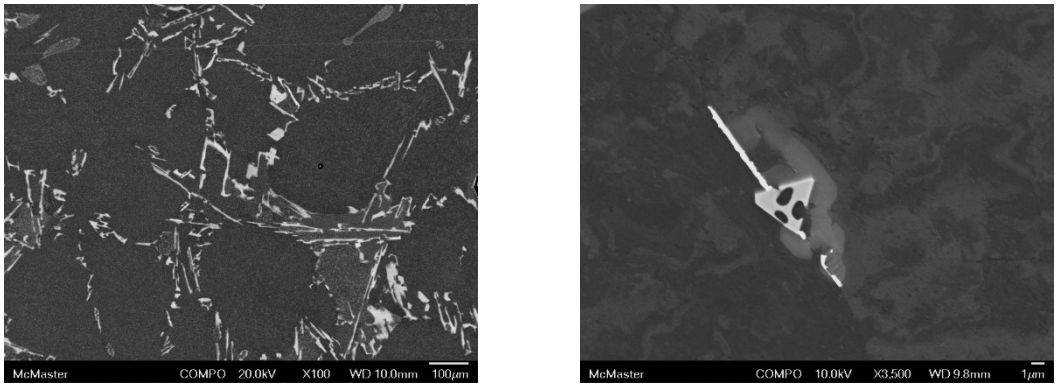

(a) (b)

Figure 6-21: Typical microstructure images of Al-7Si-0.05Fe solidified at (a) and (b) 0.1Ks^{-1} showing the presence of only the τ_5 phase.

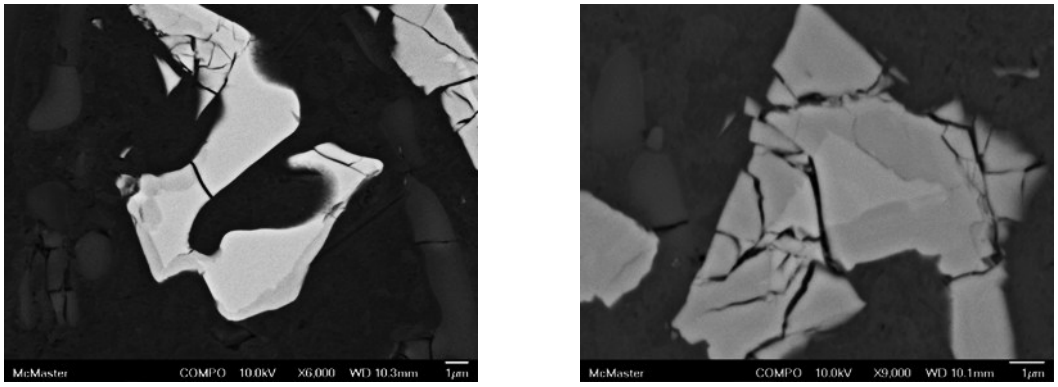

(a) (b)

Figure 6-22: Typical microstructure images of (a) Al-7Si-0.1Fe and (b) Al-7Si-0.2Fe; both solidified at 0.1Ks^{-1} showing the presence of both the τ_5 and P (τ_5 enveloped by the τ_6) phases.

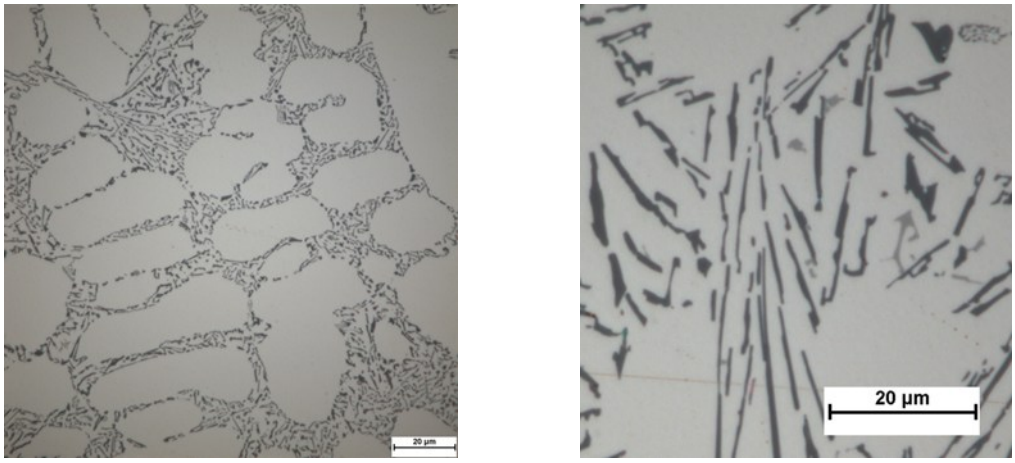

(a) (b)

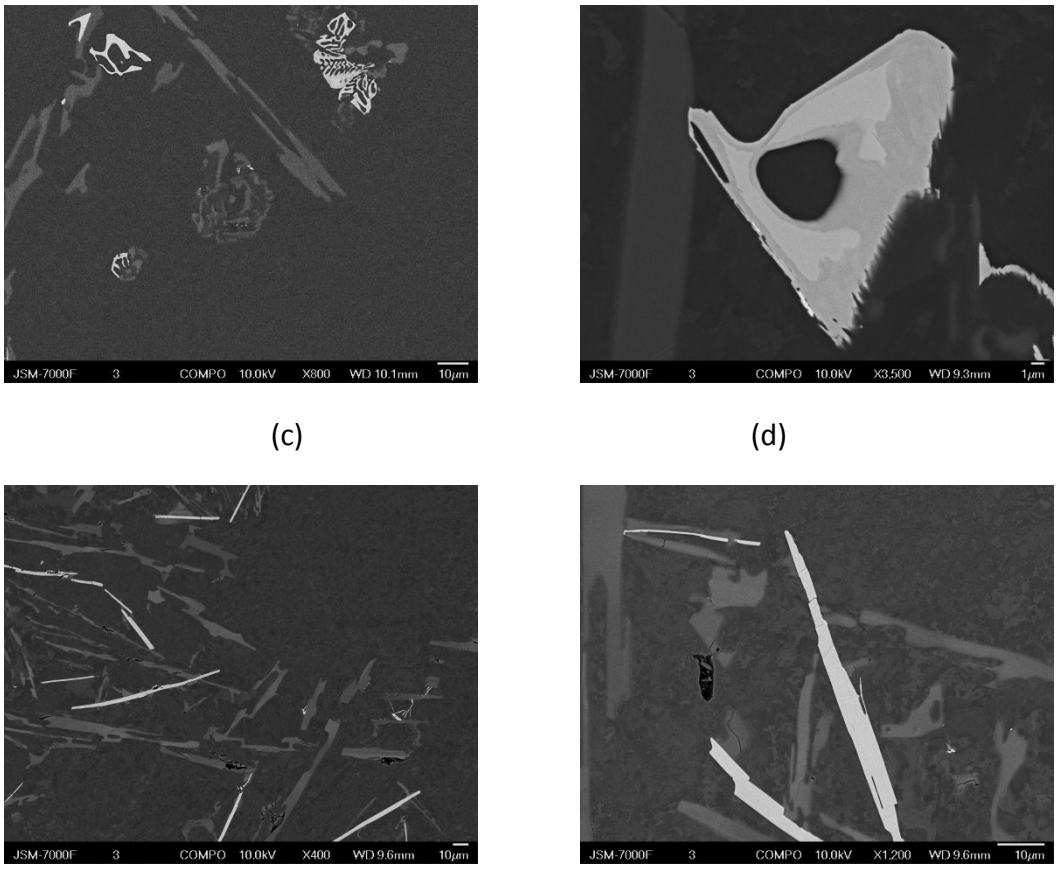

Figure 6-23: Typical microstructure images of Al-7Si-0.25Fe solidified at (a) and (b) 5 Ks^{-1} showing the presence of only the τ_5 phases; (c) and (d) 0.8 Ks^{-1} showing the presence of both the τ_5 and P (τ_5 enveloped by the τ_6) phases; and (e) and (f) 0.1 Ks^{-1} showing the presence of only the τ_6 phase.

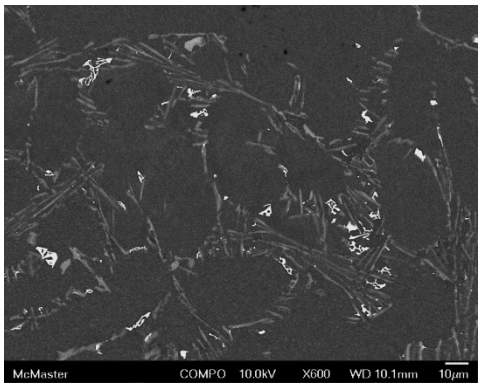
McMaster COMPO 10.0kV X600 WD 10.1mm 10μm

(a)

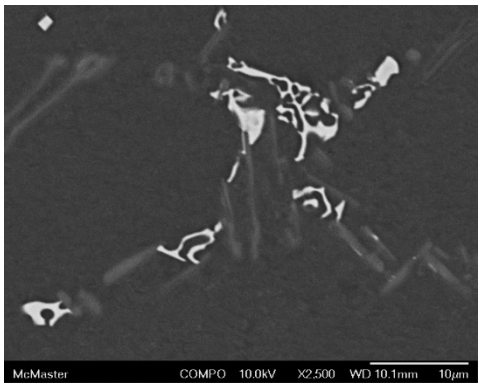
McMaster COMPO 10.0kV X2,500 WD 10.1mm 10μm

(b)

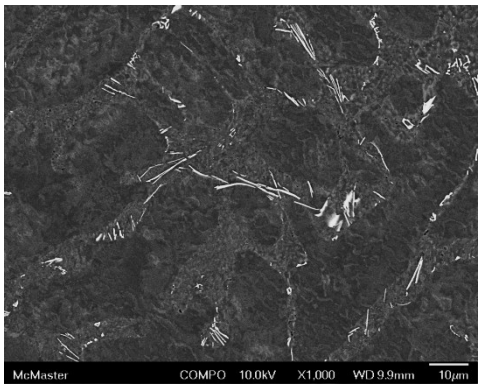
McMaster COMPO 10.0kV X1,000 WD 9.9mm 10μm

(c)

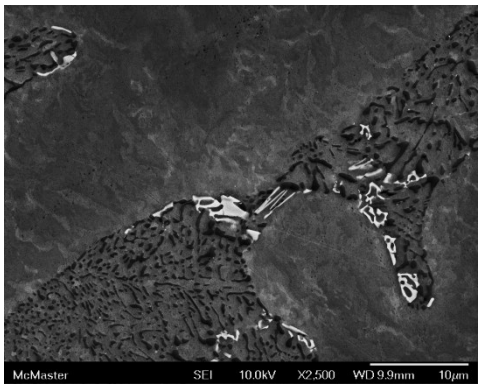
McMaster SEI 10.0kV X2,500 WD 9.9mm 10μm

(d)

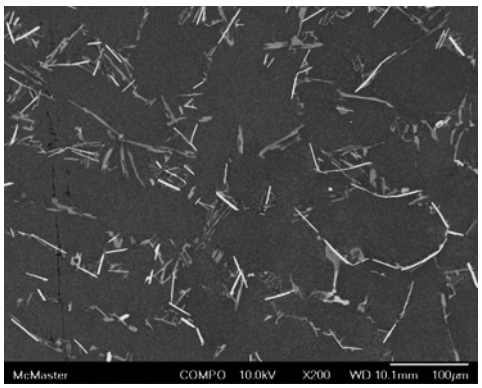
McMaster COMPO 10.0kV X200 WD 10.1mm 100μm

(e)

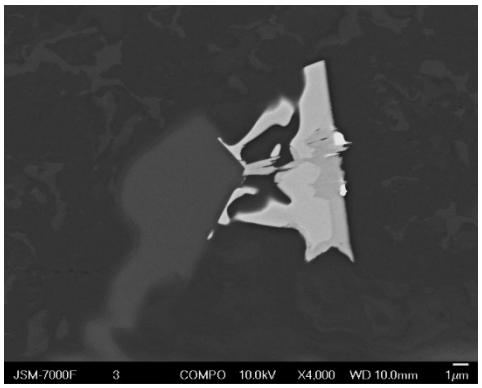
JSM-7000F 3 COMPO 10.0kV X4,000 WD 10.0mm 1μm

(f)

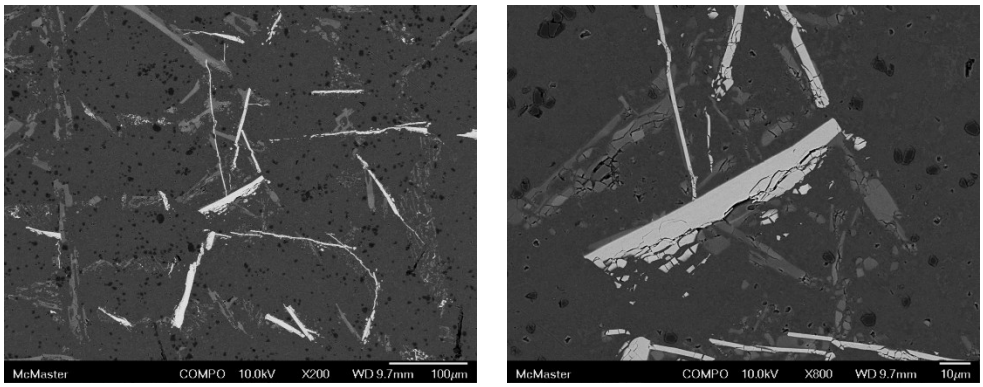

(g) (h)

Figure 6-24: Typical microstructure images of Al-7Si-0.5Fe solidified at (a) and (b) 50 Ks^{-1} showing the presence of only the τ_5 phases; (c) and (d) 5 Ks^{-1} showing the presence of both the τ_5 and τ_6; (e) and (f) 0.8 Ks^{-1} showing the presence of both the τ_6 and P (τ_5 enveloped by the τ_6) phases; and (g) and (h) 0.1 Ks^{-1} showing the presence of only the τ_6 phase.

The effect of Fe in the Al-7Si-yFe (y=0.05 to 0.5) alloys as presented in Figure 6-20 to Figure 6-24 suggests that there is a strong interaction between the Fe concentration and the cooling rate during solidification, influencing the type of intermetallic phases appearing in the solidified microstructure. Figure 6-25 shows the isopleth phase diagram of the Al-Si-Fe system wherein Al-7Si alloy with increasing Fe levels between 0 and 1 wt% is plotted against the temperature showing that only the τ_6 phase is predicted as the intermetallic phase evolving during solidification; and in the alloys with 0.05 and 0.25 wt% Fe, the τ_6 phase evolves with the eutectic phases and in the alloy with 0.5 wt% Fe, it evolves prior to the eutectic phases during solidification. The predictions of the solidification under the Scheil-Gulliver conditions are for the Al-7Si-yFe (y=0.05, 0.25 and 0.5) wherein only the τ_6 phase is predicted to evolve in all the three alloys such that in the alloys with 0.05 and 0.25 Fe, the phase evolves with the eutectic phases and prior to the eutectic temperature in the alloy with 0.5 Fe.

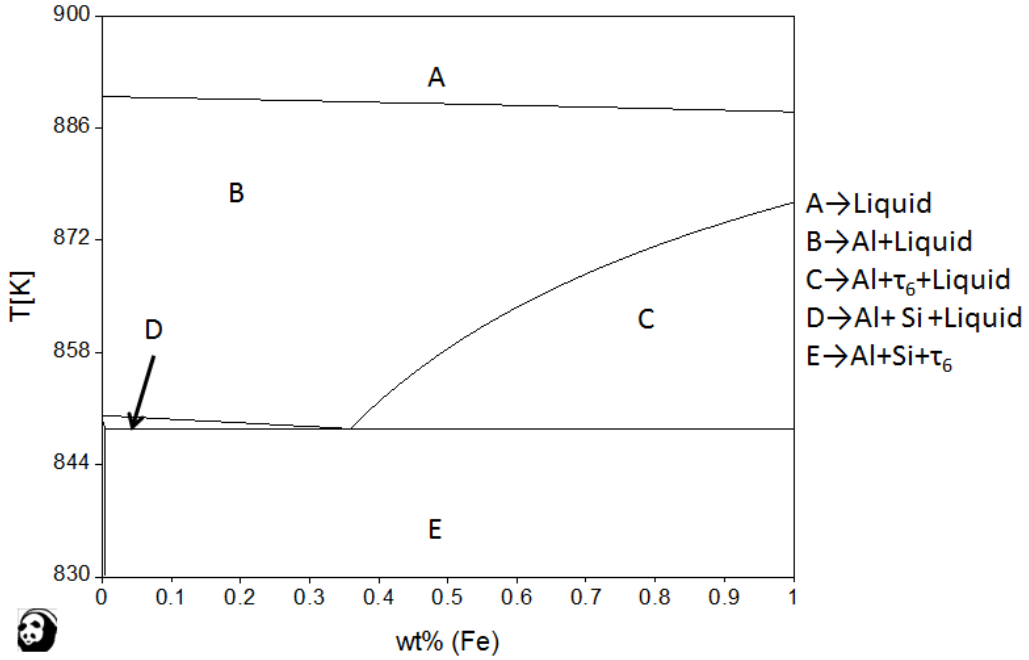

Figure 6-25: Isopleth phase diagram for the Al-7Si-yFe (y=0 to 1) alloy system.

The critical band of cooling rate that demarcates the region above which only the τ_5 and below which only the τ_6 phases exist in the solidified microstructure increases with increasing levels of Fe concentration in the alloy. The τ_5 phase is the first to evolve in all the alloys and cooling rates during solidification presented in Figure 6-20; this phase further transforms into the τ_6 phase during solidification by the peritectic reaction: $L + \tau_5 \rightarrow \tau_6$.

The solidified microstructures of the samples from the Al-7Si-yFe (y=0.05, 0.1, 0.2 or 0.25) alloys show the τ_5 phase along with P (τ_5 enveloped by the τ_6 phase) phases within the respective band of critical cooling rate because, all the τ_6 phases in these alloys will have to evolve from the τ_5 phase through the peritectic reaction. Typical examples of such observations are presented in Figure 6-21 to Figure 6-23.

The solidified microstructure of the alloy sample from the Al-7Si-0.5Fe composition show the τ_6 phase along with the P (τ_5 enveloped by the τ_6 phase) phases within the band of critical cooling rate during solidification; further, this critical band is larger for this alloy as well when compared with that in the alloys with 0.05 and 0.25 wt% Fe in them. In the Al-7Si-0.5Fe alloy, the τ_6 phase evolves independently ahead of the eutectic temperature due to favourable atom fractions of Fe and Si ahead of the primary Al phase during solidification. Hence, in these alloys, the τ_6 phase exists along with the τ_5 phase in the samples solidified at 5 Ks^{-1} cooling rate and with the P phase in the samples solidified at 0.8 Ks^{-1} cooling rate; both the cooling rates of 5

and 0.8 Ks^{-1} exist within the critical band of cooling rates shown in Figure 6-20. The evidences of such observations in the Al-7Si-0.5Fe alloy are shown in Figure 6-24. The Al-7Si-0.5Fe alloys solidified at high cooling rates of 50 Ks^{-1} results in the suppression of the evolution of even the eutectic τ_6 phase and the evolution of the eutectic τ_5 phase is observed instead.

The critical phenomenon that ties all the results and discussion presented in this chapter is the anomalous evolution of the τ_5 phase during the solidification of the Al-xSi-yFe (x=2 to 12.5 and y = 0.05 to 0.5) both in the pre-eutectic temperatures at all cooling rates and eutectic temperature at high cooling rates of about 50 Ks^{-1}. A hypothesis to explain this behaviour is presented in the last sub-section of this chapter; the next sub-section presents the characterization of the τ_5 and τ_6 phases by TEM and X-Ray diffraction techniques.

6.6 CHARACTERIZATION OF THE $\tau_5 - Al_8Fe_2Si$ AND $\tau_6 - Al_9FeSi$ INTERMETALLIC PHASES

The characterization of the intermetallic phases will be presented in the following sub-sections:

- Quantitative EDX Analysis
- X-Ray Diffraction with Synchrotron Beam
- Phase identification by TEM

6.6.1 Quantitative EDX Analysis

To ensure improved accuracy of the quantified results obtained from the EDX spectrum, the Monte-Carlo simulation for the interaction volume for of the incident beam on the sample was simulated and the results are shown in Figure 6-26 (a) and (b) for the general alloy composition of Al-7Si-0.25Fe and intermetallic phase composition of τ_6-$Al_9Fe_2Si_2$, respectively, interacting with an incident beam of 10 KeV voltage, XXX A current and YYY beam aperture size. Figure 6-26 shows that the minimum size of the intermetallic phases to obtain a valid quantitative composition with the EDX spectrum would have to be 2 µm in width and 1 µm in depth; it was ensured that this dimension was maintained as the minimum requirement for the intermetallic phases evaluated with the EDX technique in this project.

There were two intermetallic phases that were evaluated by the EDX technique: τ_5-Al_8Fe_2Si and τ_6-$Al_9Fe_2Si_2$. The average of all the quantitative analyses carried out on the EDX spectra are shown in Table 6-1 for both the τ_5 and τ_6 phases along with the standard deviations of the individual data. EDX interaction volumes have been simulated to evaluate interaction volume for alloy composition in general and each phase separately for composition of the τ_5, τ_6 and Al_2Si_2Sr phases.

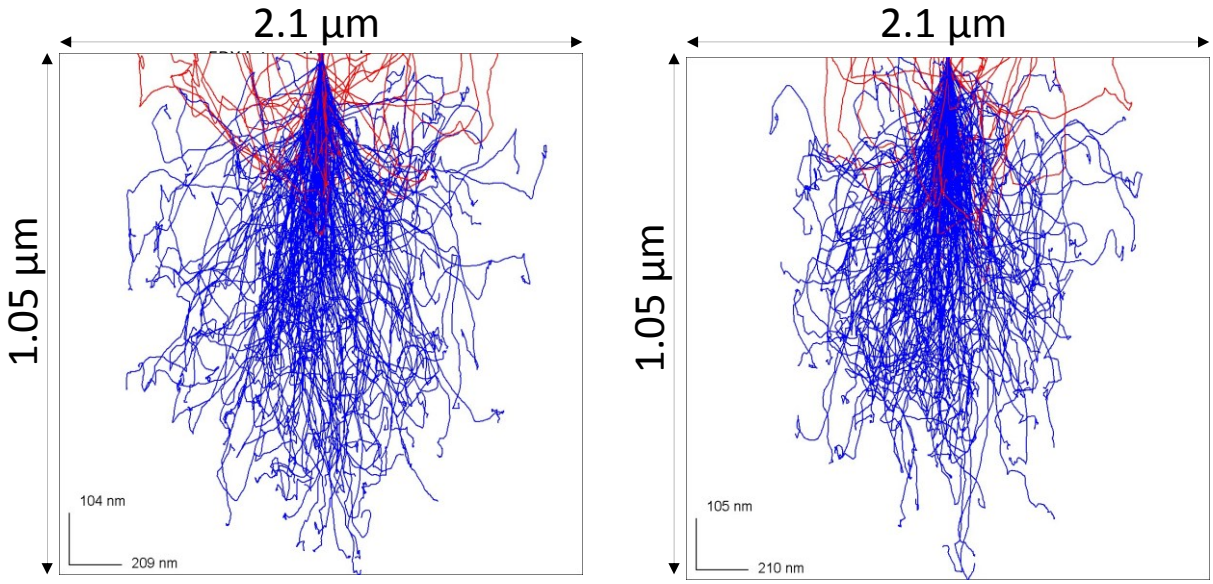

(a) (b)

Figure 6-26 : Monte-Carlo simulations to evaluate the interaction volume of the incident beam and the sample surface. (a) 10 KeV voltage on Al-7Si-0.25Fe alloy composition, (b) 10 KeV voltage on the τ6–Al9Fe2Si2 intermetallic phase composition.

Table 6-1: Typical quantitative analysis of the EDX spectrum obtained from both the τ_5-Al_8Fe_2Si and τ_6-$Al_9Fe_2Si_2$ phases.

Phases	Atomic %	Al	Si	Fe	(Fe/Si) Ratio
τ_5	**Average**	68.92	11.00	19.82	1.80
	Std. Dev.	0.64	0.39	0.55	
τ_6	**Average**	63.76	17.81	18.33	1.03
	Std. Dev.	1.13	0.73	0.69	

6.6.2 X-Ray Diffraction with Synchrotron Beam

The diffraction experiments were carried out on the microstructure of the Al-7Si-0.25Fe alloy solidified at 50 Ks^{-1} using the high energy synchrotron beam source. An X-Ray Fluorescence (XRF) map of element distribution in the microstructure was initially obtained to enable correlation of the diffraction data to the phases in the microstructure.

Figure 6-27 presents the XRF elemental map obtained using the synchrotron beam source of 10.1 KeV voltage, 0.12275 nm wave length and 50 nm beam diameter on the microstructure of the Al-7Si-0.25Fe alloy; the various elements are shown above their respective maps in which the white shade shows the highest relative amount of the respective element in the scanned spot and purple shade shows the lowest.

Figure 6-27 shows that the transition elements such as Mn, Cu, Ni and V occur at the same locations as Fe; which verifies the validity of the maps because the trace levels of transition elements are typically soluble in the Fe based intermetallic phases in the solidified samples of these alloys and the majority of the Fe atoms is present only in the Al-Fe-Si intermetallic phases. Further, in Figure 6-27, the nearly accurate maps of the trace levels of transition metals suggest that the XRF procedure could detect very low ppm levels of these elements in the microstructure.

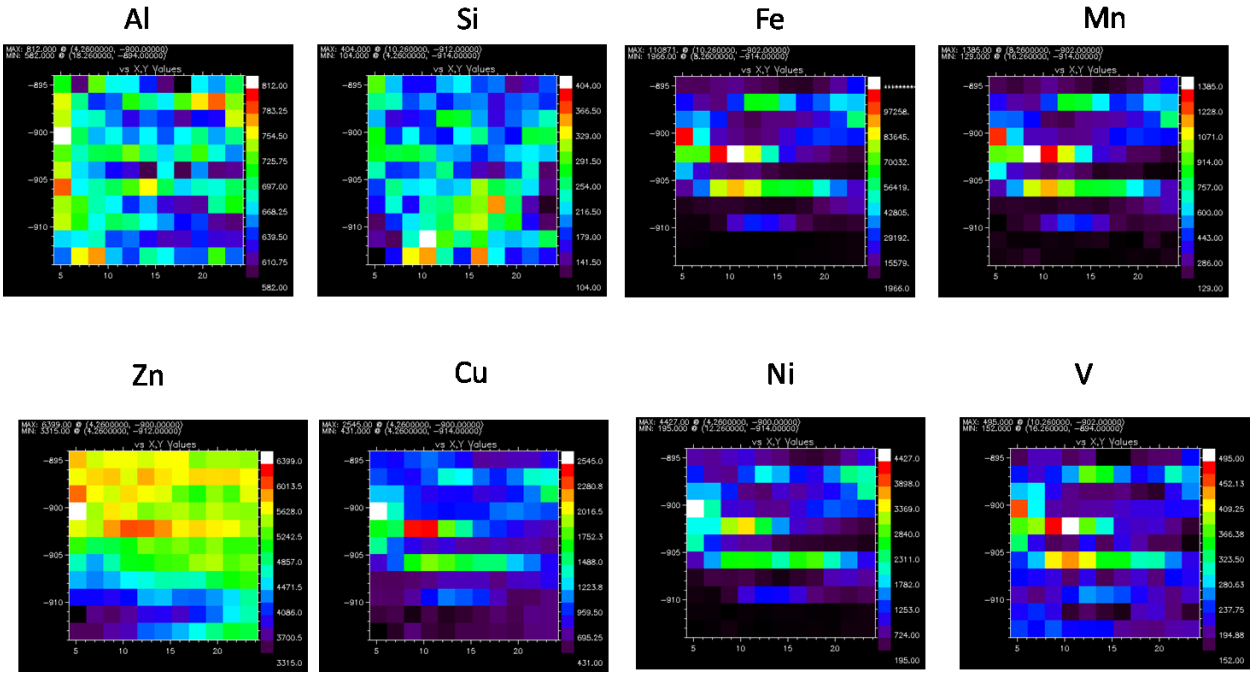

Figure 6-27: Typical XRF elemental maps obtained on the microstructure of Al-7Si-0.25Fe alloy solidified at 50 Ks^{-1}. The elements are shown above their respective maps. Each pixel is a square of 2µm size.

The diffraction data for the entire spectrum of angles between 16 and 71° were obtained from each pixelated grid in Figure 6-27. A schematic of the grid is show in Figure 6-28; wherein the data from all the marked grids were analysed and those from all the marked and shaded grids are presented in this dissertation.

	1	2	3	4	5	6	7	8	9	10	11
11		11-2						11-8			
10					10-5	10-6					
9											
8	**8-1**	8-2									
7	7-1	**7-2**	**7-3**	**7-4**	**7- 5**						
6	6-1		6-3								
5	**5-1**	5-2	**5-3**	**5-4**	**5-5**	**5-6**	**5-7**	**5-8**	**5-9**	**5-10**	5-11
4								4-8			4-11
3											
2				2-4							
1											

Figure 6-28: The pixel grid of the XRF elemental maps shown in Figure 6-27. The marked grids were critically analyzed, and the results from the marked and shaded grids are presented in this dissertation. Each pixel is a square of 2µm size.

There were three angles of the CCD camera at which the entire diffraction spectrum was collected as described in Section 5.8.3. Figure 6-29 shows the typical diffraction data obtained from the three locations of the CCD camera and the corresponding plots of intensity versus angle for each angular location. The data presented in Figure 6-29 was obtained from the grid labelled 5-4 in Figure 6-28 for the Al-7Si-0.25Fe alloy; each ring formed by bright spots in the image corresponds to the diffraction obtained from a specific plane of a specific phase. Each images shown in Figure 6-29 (a) to (c) has a pixel dimension of 0.014° angle and the intensity of all individual pixels were measured and plotted as graphs in Figure 6-29 (d) to (f), respectively.

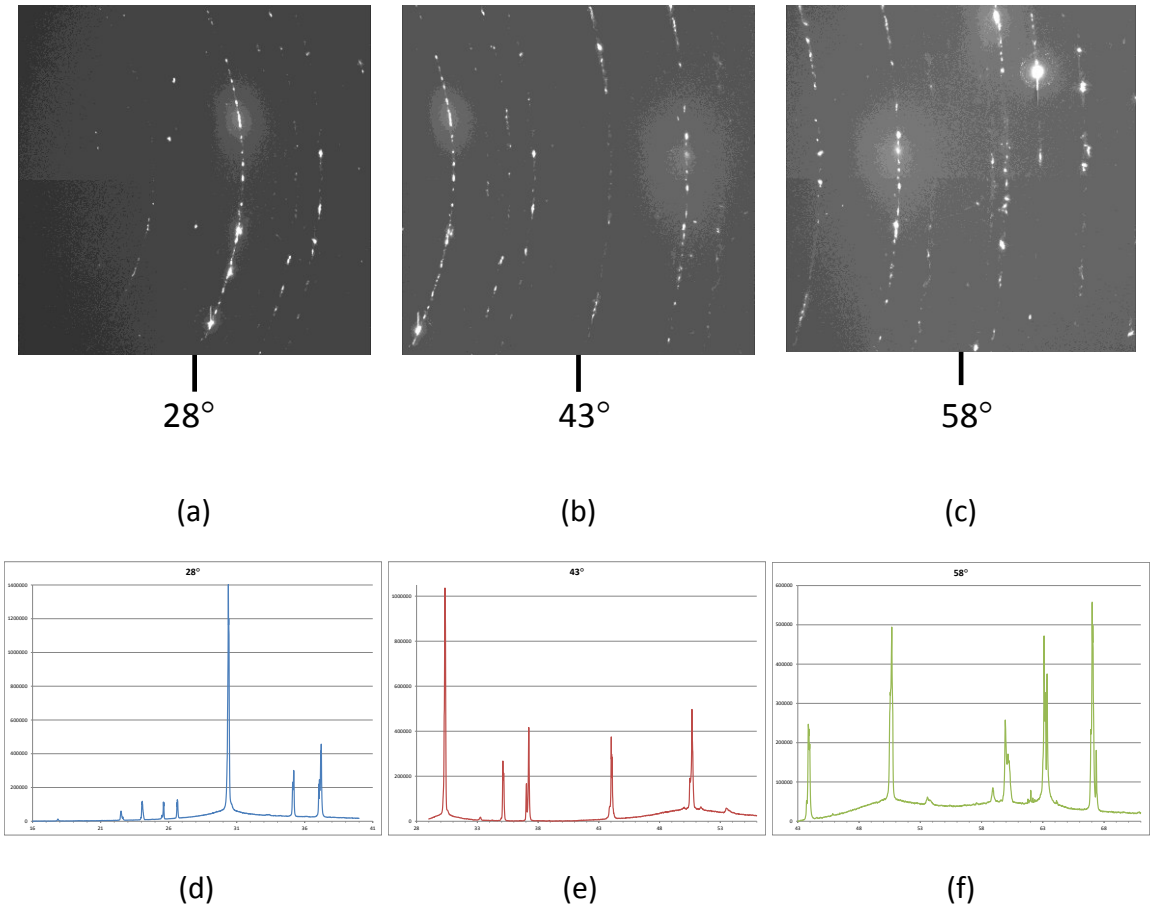

Figure 6-29: Typical diffraction data spectrum obtained from the grid marked 5-4 in Figure 6-28 for the Al-7Si-0.25Fe alloy. There are three spectra obtained at three specific angles of the CCD camera (a) 28^o , (b) 43^o and (c) 58^o. The corresponding converted intensity vs. angle plots is shown in (d) 28^o , (e) 43^o and (f) 58^o. The measurement on the images in (a), (b) and (c) were carried out for each pixel with an angular dimension of 0.014^o.

In Figure 6-28, the grid rows labels 5 and 7 have a strip of Fe rich signals obtained in the XRF elemental maps shown in Figure 6-27. These two strips of data along with a few grid locations from rows 2, 4, 8, 10 and 11 (high Fe signals in XRF) were analysed as labelled in Figure 6-28.

The results of the analysis of the diffraction data for the grid labels 5-4 and 5-10 in Figure 6-28 are presented in this section while the remaining results of the grid locations labelled by a shaded grid box, respectively in Figure 6-28 are presented in Table 6-4. Figure 6-30 presents the results and analysis of the diffraction data obtained from the grid location 5-4 in Figure 6-28; the complete spectrum in shown in Figure 6-30 (a) and the three magnified sections of the complete spectrum along with the analyzed peak phases and plane identities are shown in Figure 6-30 (b) for angular ranges of 16 to 33^o, 33 to 49^o and 49 to 71^o. All possible diffraction peaks (and planes) from the various possible phases in the solidified microstructure of the Al-

7Si-0.25Fe alloy sample were simulated using the crystal structure information from the open literature and the software program PowderCell[**]. Table 6-2 presents a list of the phases used to analyze the diffraction data from the solidified microstructure of the Al-7Si-0.25Fe alloy sample; the specific atom positions of the phases was also used along with the space group and lattice parameter information for improved accuracy of the analysis. Each diffraction data profile was analysed such that the angular locations of specific planes from specific phases matched with an accuracy of ±0.1° (5 pixel width in typical Figure 6-29 (a) to (c)). Further, at least three unique peaks were identified from each phase in a spectrum to confirm the presence of that phase.

Table 6-2: List of the various phases used to analyze the diffraction data from the solidified microstructure of Al-7Si-0.25Fe alloy.

Phase Notation	Phase Stoichiometry	Crystal Structure	Space Group	Lattice Parameters A	Reference
Al	Al	Cubic	Fm3m	a=4.0494	128
Si	Si	Cubic	Fd3m	a= 5.43088	128
θ	$Al_{13}Fe_4$	Monoclinic	C2/m	a=15.489 b=8.083 c=12.476 β= 107.70°	129
τ_5	Al_8Fe_2Si	Hexagonal	$P6_3/mmc$	a = 12.404(1) c = 26.234(2)	84
τ_6	$Al_9Fe_2Si_2$	Monoclinic	C2/c	a = 20.813(6) b = 6.175(3) c = 6.161(3) β= 90.42(3)°	76
τ_4	Al_3FeSi_2	Tetragonal	I4/mcm	a = 6.07 c = 9.50	81
τ_7	$Al_3Fe_2Si_3$	Monoclinic	$P2_1/n$	a = 7.179(2) b = 8.354(2) c = 14.455(4) β = 93.80(2)°	81
Al_4Sr	Al_4Sr	Tetragonal	I4/mmm	a=4.46 c=11.07	130
Al_2Si_2Sr	Al_2Si_2Sr	Hexagonal	P-3m1	a= 4.1872(5) c= 7.427(1)	131

[**] PowderCell Dipl.-Ing. Werner Kraus Phone: +49(0)30 6392 – 5845, Dr. Gert Nolze Phone: +49(0)30 8104 - 3513

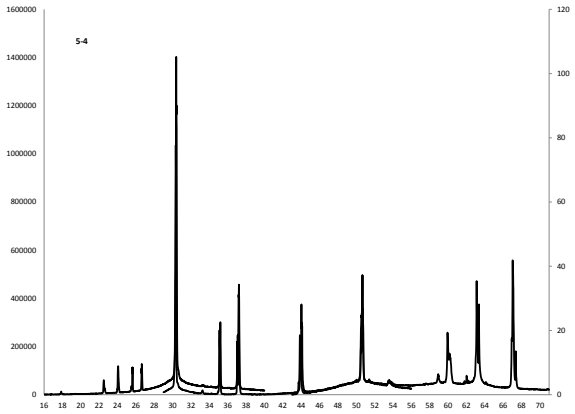

(a)

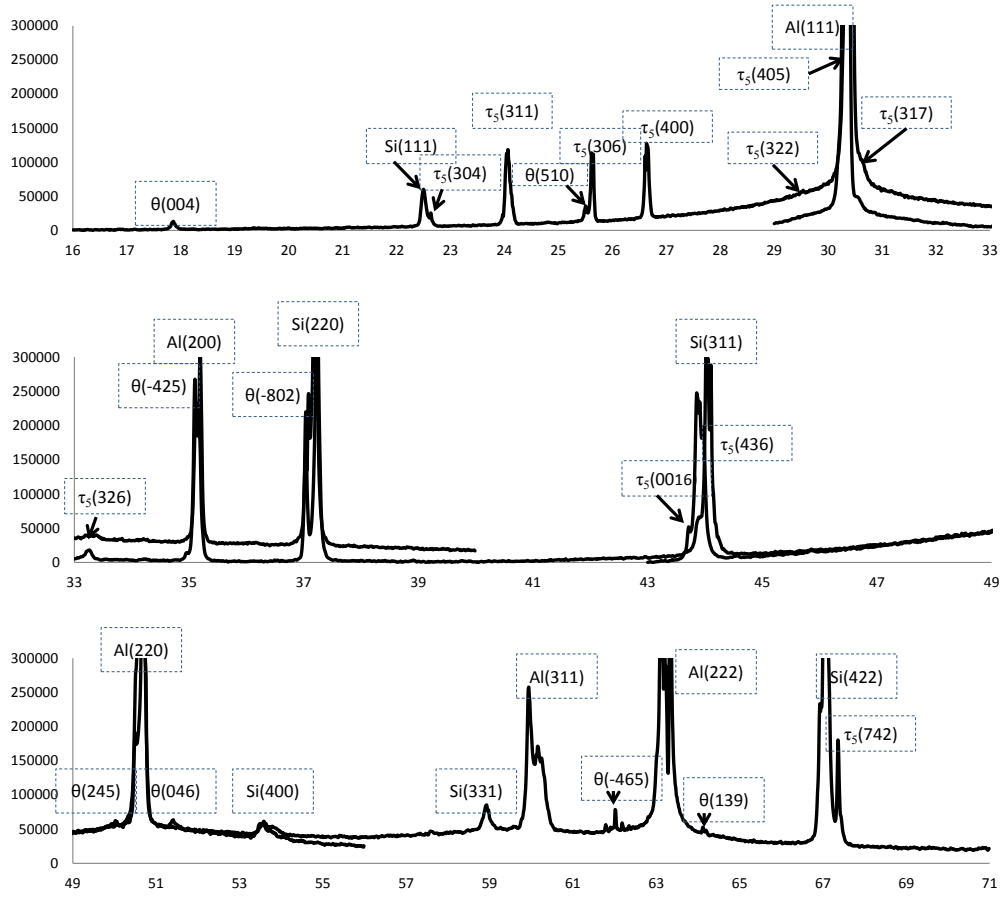

(b)

Figure 6-30: Diffraction data spectrum obtained and analyzed from the grid location labeled 5-4 in Figure 6-28. (a) complete spectrum (16 to 71°), (b) split spectra for clarity of the analyzed peak labels (16 to 33°, 33 to 49° and 49 to 71°).

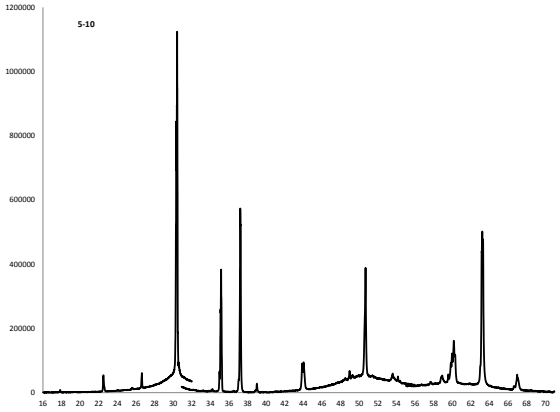

(a)

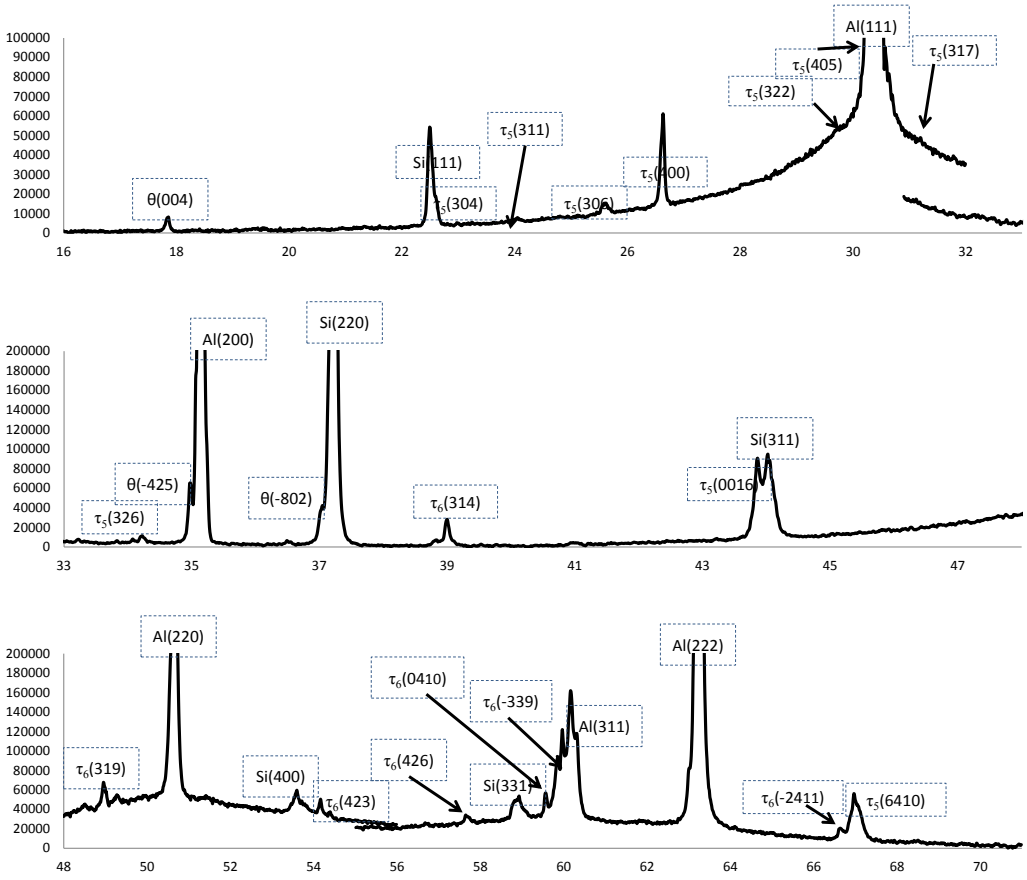

(b)

Figure 6-31: Diffraction data spectrum obtained and analyzed from the grid location labeled 5-10 in Figure 6-28. (a) complete spectrum (16 to 71°), (b) split spectra for clarity of the analyzed peak labels (16 to 33°, 33 to 49° and 49 to 71°).

Apart from the major Al and Si phases in the microstructure, Figure 6-30 shows the presence of both the θ-$Al_{13}Fe_4$ and τ_5-Al_8Fe_2Si in the grid location 5-4 and Figure 6-31 shows the presence of θ-$Al_{13}Fe_4$, τ_5-Al_8Fe_2Si and τ_6-$Al_9Fe_2Si_2$ in the grid location 5-10 from Figure 6-28.

The analysis of results from the grid locations 5-5 to 5-9 of Figure 6-28 is presented in Table 6-4. The analysis of the girds in the row 5 of Figure 6-28 show that the θ and τ_5 phases is present as major phases in 5-4 and the peak intensity of these phases continuously decrease from 5-4 to 5-10 while the peaks of the τ_6 phase appears in grid location 5-6 and increases to a maximum intensity in grid location 5-10. These results suggest that there is are two peritectic transformations: the θ-$Al_{13}Fe_4$ to τ_5-Al_8Fe_2Si phase and subsequently, the τ_5-Al_8Fe_2Si to τ_6-$Al_9Fe_2Si_2$ phase; these reactions are $Liquid_{(Si)}$ + θ-$Al_{13}Fe_4$ → τ_5-Al_8Fe_2Si and $Liquid_{(Si)}$ + τ_5-Al_8Fe_2Si → τ_6-$Al_9Fe_2Si_2$, respectively.

Similar results were observed from the analysis of the diffraction data in the grids from row 7 (7-2 to 7-5) shown in Figure 6-28; wherein, apart from the Al and Si phases, the τ_6 phase was the larger intensity peaks with smaller intensity peaks of both the θ and τ_5 phases. The summary of results of all the analyzed locations is shown by shaded grids in Figure 6-28 are presented in Table 6-4.

Table 6-3: Characteristics of the phases observed in the Al-7Si-0.25Fe alloy shown in Figure 6-30 and Figure 6-31.

Phase Notation	Phase Stoichiometry	Crystal Structure	Space Group	Lattice Parameters	Reference
Al	Al	Cubic	Fm3m	a=4.0494	128
Si	Si	Cubic	Fd3m	a= 5.43088	128
θ	$Al_{13}Fe_4$				
τ_5	Al_8Fe_2Si	Hexagonal	$P6_3/mmc$	a = 12.404(1) c = 26.234(2)	84
τ_6	$Al_9Fe_2Si_2$	Monoclinic	C2/c	a = 20.813(6) b = 6.175(3) c = 6.161(3) β= 90.42(3)°	76

Table 6-4 : Summary of identified phases in Al-7Si-025Fe alloy solidified at 50 Ks^{-1}

Spot	θ	τ_5	τ_6
5_3	X	X	
5_4	X	X	
5_5	X	X	
5_6	X	X	
5_7	X	X	X
5_8	X	X	X
5_9	X	X	X
5_10	X	X	X
7_2	X	X	X
7_3	X	X	X
7_4	X	X	X
7_5	X	X	X
8_1	X	X	X

6.6.3 Transmission Electron Microscopy (TEM)

The TEM was used to obtain Selected Area Diffraction Pattern (SADP) from various zone axes of the intermetallic phases in foils obtained from solidified samples using the Focused Ion Beam (FIB) milling technique.

There are two major phases that were characterized in the alloys of this study (refer to Figure 4-1): the τ_5-Al_8Fe_2Si and τ_6-$Al_9Fe_2Si_2$. Typical sample used to analyze these phases was the Al-7Si-0.25Fe solidified at 0.1 Ks^{-1} wherein both these phases exist in the solidified structure. The characteristics of these phases in all the alloys as analysed with the optical microscope and SEM (with EDX) and presented in Sections 6.4, 6.5 and 6.6.1 of this dissertation show that these two phases evolve during solidification of the alloys depending on the cooling rate during solidification. Hence, in this section, one typical sample with each of the τ_5 and τ_6 phases will be presented for crystallographic characterize these phase. Additionally, crystallographic characterization of the τ_5 and τ_6 phases in these alloys have been carried out and presented using the X-ray diffraction experiments with the synchrotron beam source in Section 6.6.2 of this dissertation.

Figure 6-32 shows the location on the microstructure of the solidified Al-7Si-0.25Fe alloy sample from which the FIB sample was obtained for further TEM analysis of the τ_5 phase.

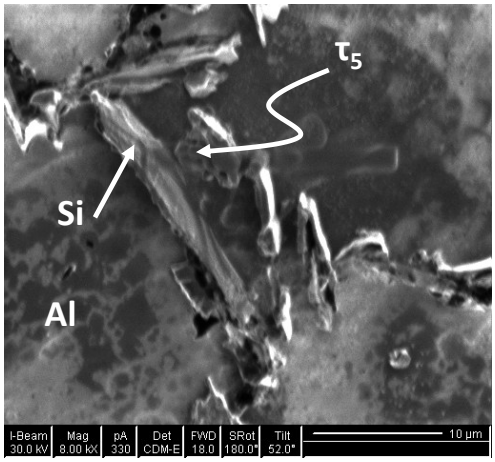

(a)

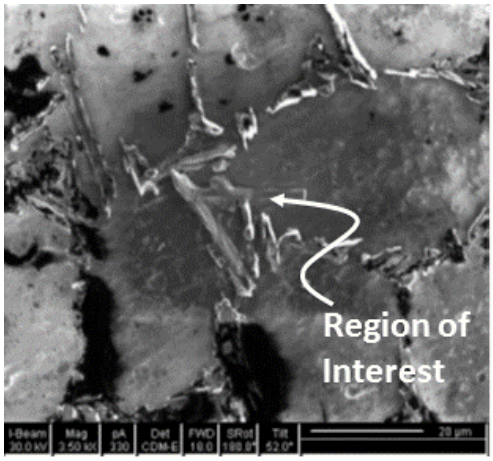

(b)

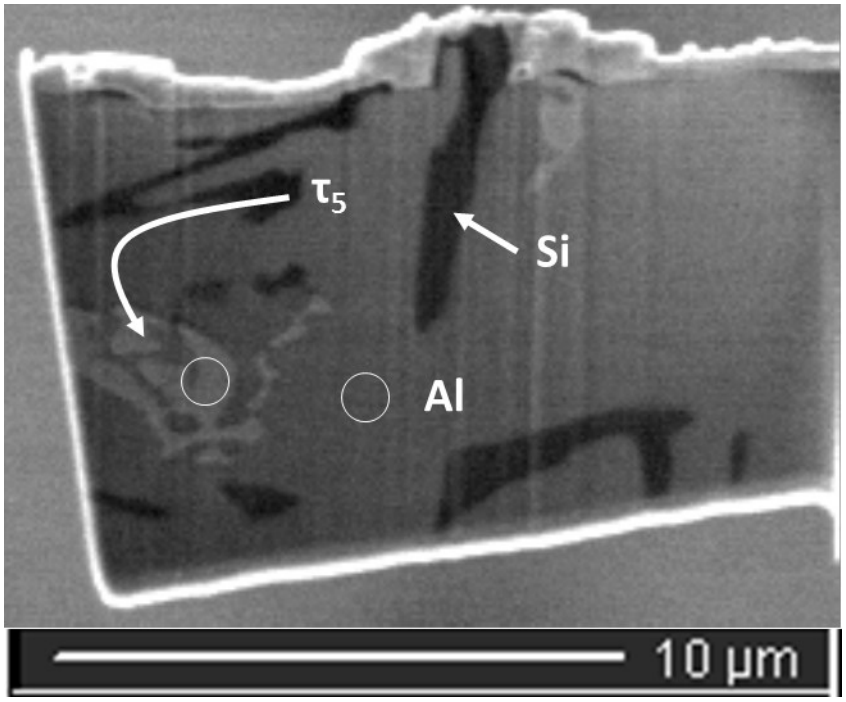

(c)

Figure 6-32: Ga ion beam image in the SEM showing the location in the microstructure with the τ_5 phase from where the TEM sample was prepared using the FIB milling in the Al-7Si-0.25Fe alloy solidified at 5 K/s^{-1}; (a) location of interest with the τ_5 phase, (b) region of interest marked by a layer of Pt deposited. (c) SEM SEI showing the surface of the TEM sample with the τ_5, eutectic Si and Al phases. The circles in (c) denote the locations from which SADP were obtained.

Figure 6-33 (a) and (b) presents the SADP from the Al phase and τ_5 phase respectively as marked by the respective circles in Figure 6-32 (c). The SADP for the Al phase is presented for verification and calibration purposes.

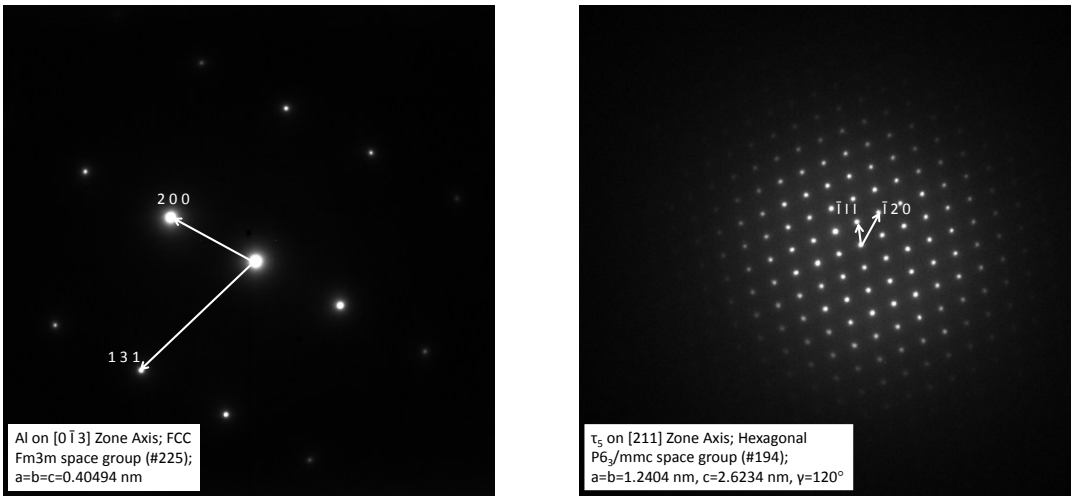

(a) (b)

Figure 6-33: SADP obtained from Al-7Si-0.25Fe alloy solidified at 0.1 Ks^{-1} in TEM from the circles shown in Figure 6-32 (c). (a) Al phase on [0 $\bar{1}$ 3] zone axis and (b) τ_5 on [211] zone axis.

In Figure 6-33 (b) the τ_5 phase was identified by as being on the [211] zone axis and the structure is hexagonal with the space group $P6_3/mmc$ (#194) with lattice parameters of a=b=1.2404, c= 2.6234 and $\Upsilon=120^o$.

Figure 6-34 shows the location on the microstructure of the solidified Al-7Si-0.25Fe alloy sample from which the FIB sample was obtained for further TEM analysis of the τ_6 phase.

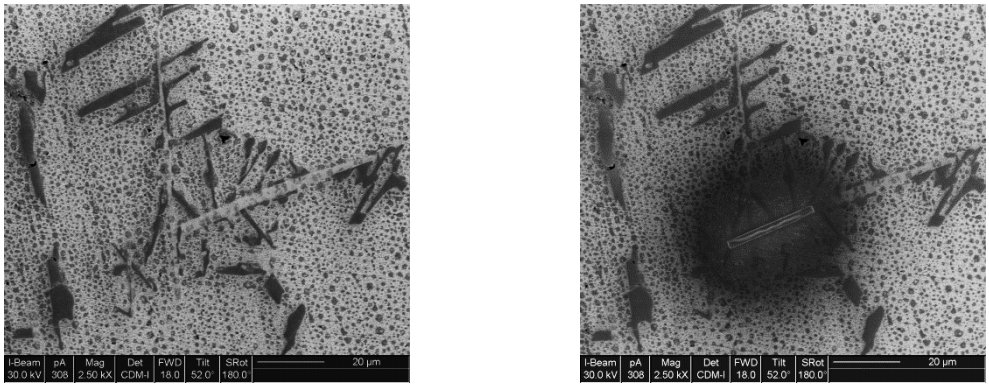

(a) (b)

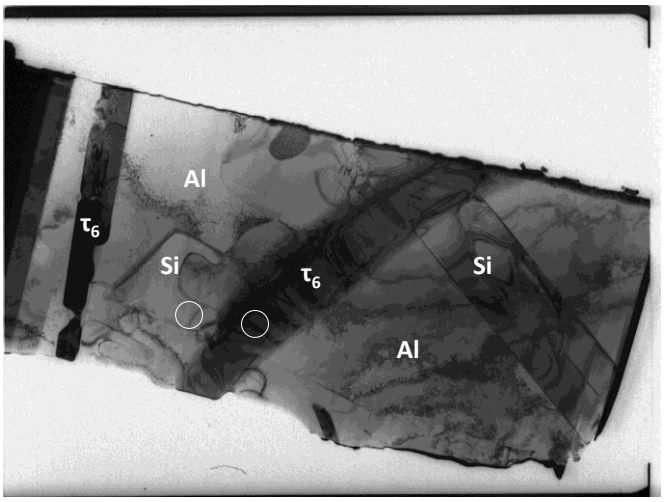

(c)

Figure 6-34: Ga ion beam image in the SEM showing the location in the microstructure with the τ_6 phase from where the TEM sample was prepared using the FIB milling in the Al-7Si-0.25Fe alloy solidified at 0.1 Ks^{-1}; (a) location of interest with the τ_6 phase, (b) region of interest marked by a layer of Pt deposited. (c) TEM image showing the surface of the sample with the τ_6, eutectic Si and Al phases. The circles in (c) denote the locations from which SADP were obtained.

Figure 6-33 (a) and (b) presents the SADP from the Si on [110] zone axis and τ_6 phase on [011] zone axis, respectively as marked by the respective circles in Figure 6-34 (c). The SADP for the Si phase is presented for verification and calibration purposes. Figure 6-33 (a) and (b) were obtained from the same tilt angle of the sample in the TEM and hence, the Si phase is in crystallographic orientation with the τ_6 phase: $[110]_{Si} \parallel [011]_{\tau 6}$.

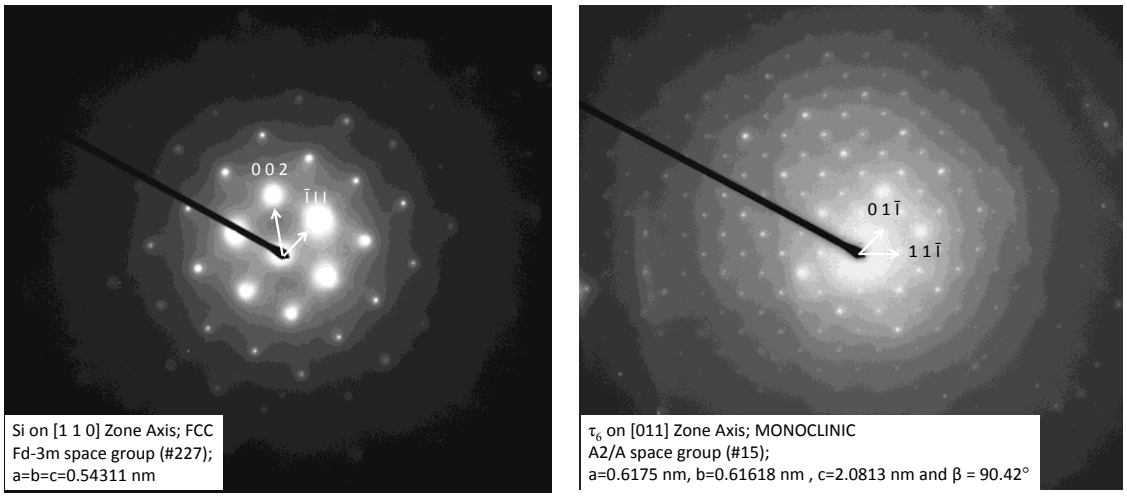

(a) (b)

Figure 6-35: SADP obtained with the TEM from the circles shown in Figure 6-32 (c). (a) Si phase on [110] zone axis and (b) τ_6 on [011] zone axis. The patterns in (a) and (b) were obtained at the same tilt angle of the sample and so Si and τ_6 phases are in crystallographic orientation $[110]_{Si} \parallel [011]_{\tau 6}$.

In Figure 6-35 (b), the τ_6 phase was identified by as being on the [011] zone axis and the structure is monoclinic with the space group A2/a (#15) with lattice parameters of a=0.616, b=0.6175, c= 1.208 and β=90.4°.

It is notable that the crystal structure information obtained for the τ_5 and τ_6 phases in the TEM analysis is identical to the ones used to characterize the peaks from these phases in the X-ray diffraction experiment presented in Section 6.6.2.

6.7 DISCUSSION

The results and analyses thus far presented in this Chapter amply validate the summary presented in Section 6.1. The critical and novel feature of the results is that, contrary to the predictions by the thermodynamic calculations, the τ_5–Al_8Fe_2Si phase with a hexagonal crystal structure (space group $P6_3/mmc$) evolves after the primary Al phase and before the eutectic phases in the Al-Si-Fe system with compositional ranges of 2 to 12.5 wt% Si and 0 to 0.5 wt% Fe. This phase further transforms into the τ_6-$Al_9Fe_2Si_2$ phase by the peritectic reaction: Liquid + $\tau_5 \rightarrow \tau_6$. This transformation is dependent on the cooling rate during solidification and the concentration of Fe in the alloy; slow cooling rates and high Fe concentration promote the kinetics of the peritectic transformation. The τ_6 phase also forms during solidification depending on the cooling rate during solidification and the Fe concentration in the alloy; slower cooling rates and higher Fe concentration promote the evolution of the τ_6 phase during solidification. The τ_6 phase could evolve prior to the eutectic phases and/or with the eutectic phases during solidification; again, this depends on the cooling rate and the concentration of the Fe in the alloy.

In our exhaustive search of the prior art in this subject matter, only Iglessis [79] had presented a similar observation, wherein the τ_5 phase evolves at higher cooling rates during solidification of the Al-10Si-0.25Fe and Al-10Si-0.5Fe alloys; the τ_6 phase evolved in lower cooling rates during solidification in these alloys. No explanation was presented by Iglessis [79] for his anomalous observations and our results are quite similar to the results presented by him.

The reason why the τ_5 phase even evolves during the solidification of the alloys in this study was a conundrum for most part of this research project. Several hypotheses were envisioned, only to be dismissed due to lack of any supporting evidence from the experiments and/or background literature. The only hypothesis that we could propose and not yet dismiss due to any contradicting evidence from our experiments or literature is presented in the following paragraphs.

Anomalous behaviour of the Fe atoms in liquid Al alloys have been reported in the literature by Gebhardt [132, 133] in the year 1953, Turnbull [134] in the year 1990 and finally by Isono et al [135] in the year 1996. Turnbull evaluated that Fe has a negative partial molar volume in liquid Al which translates to decrease in volume of the Al melt when Fe is added to it. Further, Gebhardt reported anomalous behaviour in viscosity [132] and thermal expansion [133] and attributed them to the fact that each Fe atom in the Al alloy is surrounded by a cluster of Al atoms which number between 7 and 12. Isono et al [135] carried out innovative solidification experiments to evaluate the diffusion coefficient of Fe in liquid Al without the influence of the natural convection on the measurements; they proposed that the diffusion coefficient of Fe in liquid Al is significantly less than that expected and predicted by models. Similar results on anomalous low values of diffusion coefficient of Fe in Al was reported by Ejima et al [136,137] in the year 1980.

Isono et al [135] evaluated from their experiments that the number of Al atoms clustering around a single Fe atom in the liquid Al-Fe alloy is 15±7 which agrees with the numbers presented earlier by Gebhardt et al [132, 133]. These anomalous clusters in the liquid alloy tie up the Fe atoms and retard the rate of diffusions of these atoms in the liquid. This clustering also results in the anomalous negative partial molar volume (increase in density of liquid) of the Al-Fe liquid alloy

In the Al-Si alloy system, Wang et al [138] in the year 2001 and Yurkevich [139] in the year 2002 have emphatically shown that there is anomalous increase in the density of the Al-Si alloys due to the clustering and the resultant micro-inhomogeneity of the Si atoms in the liquid alloy. Wang et al [138] showed the anomalous behaviour in hypereutectic alloys with greater than

12.5wt% Si and Yurkevich [139] in alloys with 0.2 to 1.2 wt% Si in them. Kanibolotski et al [118] claimed that Al-Si-Fe system is more determined by Si-Fe interaction than by Al-Fe. There is no data on liquid configuration and clustering phenomena in ternary Al-Si-Fe system.

The results from the background literature presented in the Section 3.4 suggests that there is anomalous clustering of the Al, Fe and Si atoms, independently in liquid Al alloy which leads to significant micro-inhomogeneity of these atoms in the liquid and specifically, slower diffusion rates of the Fe atoms in these alloys. These results form the foundation of our hypothesis to explain the anomalous evolution of the τ_5 phase in the Al-Si-Fe alloys of this project.

During the solidification of the primary Al phase, the Fe and Si atoms segregate at the interface between the solid Al phase and liquid. Typically, these solute atoms would attempt to diffusion from this interface into the bulk liquid so as to equalize their concentration and hence their chemical potential in the liquid. However, the Fe atoms will be tied down by the Al/Si atoms in clusters that significantly retard the diffusion of the atoms into the liquid ahead of the primary Al phase. This will result in an anomalous build-up of the Fe atoms ahead of the primary Al phase at the liquid interface. At some point between the liquidus and eutectic temperatures of the Al-Si-Fe alloys in this study, the concentration of the Fe atoms reach a critical value that would fulfill the thermodynamic conditions required to nucleate a stable binary intermetallic θ-$Al_{13}Fe_4$ phase. Subsequently the θ phase will follow the solidification path and transforms into the τ_5-Al_8Fe_2Si phase, which subsequently reacts with the Si rich liquid and transforms into the τ_6-$Al_9Fe_2Si_2$ and followed by the eutectic reaction yielding the eutectic phases of Al, Si and τ_6 phase as predicted by Takeda and Mutazaki [42], later validated by Krendelsberger et al [81].

Clustering can influence other aspects of solidification. It has been proven that change in the liquid arrangement will change Gibbs free energy of the system [139]. Such change will have tremendous effect on phase evolution. Formation of clusters will alter density [134] and viscosity [132] of the liquid. Changes in viscosity will affect nucleus stability through change in interface energy in homogeneous nucleation. Change in mass transfer will be desirable both in diffusion and convection. Slower diffusion was reported by numerous authors [132,133, 135,136,137]. Change in convection will originate from significant change in density and viscosity of cluster reach liquid. It could lead to formation of dual phase liquid and convection currents will be altered. It will affect both mass and heat transfer. In some extreme cases it can lead to no convection situation as been described in [140]. It is safe to assume that clustering which is temperature dependant [114,115,116,117] will have greater effect toward end of solidification since cluster size grow as temperature lowers. Overall effect will be significant rise in solute concentration.

The altered solidification path from the evolution of the θ phase is shown in Figure 6-36

$$e \Rightarrow \quad L \xrightarrow{928K(655^{\circ}C)} \theta(Al_{13}Fe_4) + (Al)$$

$$U_{15} \Rightarrow \quad L_{(Si)} + \theta(Al_{13}Fe_4) \xrightarrow{909K(636^{\circ}C)} \tau_5(Al_8Fe_2Si) + (Al)$$

$$U_{16} \Rightarrow \quad L_{(Si)} + \tau_5(Al_8Fe_2Si) \xrightarrow{882K(609^{\circ}C)} \tau_6(Al_9Fe_2Si_2) + (Al)$$

$$E_1 \Rightarrow \quad L \xrightarrow{850K(577^{\circ}C)} (Al) + (Si) + \tau_6(Al_9Fe_2Si_2)$$

Figure 6-36: Alternate solidification path resulting in the evolution of the θ,τ_5 and τ_6 phases in the Al-Si-Fe alloy with 2 to 12.5 wt%Si and 0 to 0.5 wt%Fe. The notations for the reaction, e, U_{15}, U_{16} and E_1 are from Krendelsberger et al [81].

The existence of the binary θ phase was not discernible by optical microscopy, SEM or TEM; however the results of the X-ray diffraction experiments with the synchrotron beam (Section 6.6.2) showed the existence of unique peaks from the θ phase in the eutectic region of the solidified microstructure of the Al-7Si-0.25Fe alloy solidified at 50 Ks^{-1}. The τ_5 phase was observed as the script morphology in all of the optical, SEM and TEM techniques in addition to the results from the X-ray diffraction experiments.

The Figure 6-36 suggests that the evolution of the θ phase could take place at a temperature as high as 928 K (655 ^{o}C) and that of the τ_5 phase at 909 K (636 ^{o}C). Hence, during the solidification of the alloys in this project, the thermal condition of the anomalous clusters of Fe surrounded by 8 to 22 Al atoms forming ahead of the solidifying Al phase is sufficient for the evolution of the θ phase to trigger the solidification path shown in Figure 6-36. The results of this project suggest that the transformation of the θ to τ_5 phase by the peritectic reaction shown in Figure 6-36 is fairly rapid because difference in the Fe concentration between θ-$Al_{14}Fe_3$ phase and τ_5 phase are small therefore diffusion of iron into the phase won't take long time, however, the peritectic reaction that transform the τ_5 to τ_6 phase seems to be sluggish due to twice as much difference in Fe concentration between τ_5 and τ_6 and dependant on the Fe concentration in the alloy. In the Al-7Si-0.25Fe alloy solidified at a very slow rate of 0.017 Ks^{-1}, the τ_5 phase morphology is present and compositionally equal to τ_6 phase as shown in Figure 6-37 suggesting that the peritectic reaction was in progress while the sample solidified to room temperature. Other instances of the peritectic reaction are shown in Figure 6-38. The peritectic reaction, U_{16} in Figure 6-36 was captured in a TEM sample by FIB milling and the images are shown in Figure 6-39 (a) and (b) for the TEM bright field and Scanning Transmission Electron Microscope (STEM) images, respectively; wherein, a single grain of the τ_5 phase reacted with the liquid and formed several grains of the τ_6 phase and solid Al. Additionally, a valid evidence of the solidification path shown in Figure 6-36 was observed in the analysis of the results from the diffraction experiments using the synchrotron beam source and presented in Figure 6-30 and Figure 6-31. Figure 6-39 (c) and (d) presents SADPs from the τ_5 and Al phase respectively as marked by locations in Figure 6-39 (a); the crystal structure of the τ_5 phase matches that presented in Figure 6-33 (b).

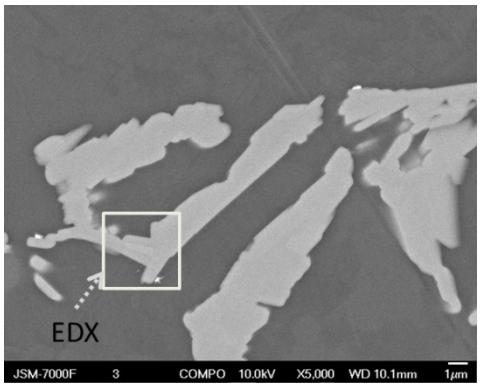

(a)

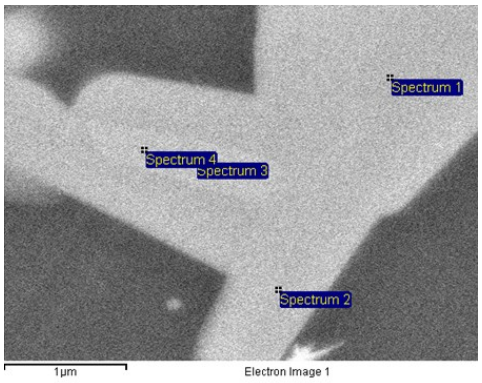

Spectrum	Al	Si	Fe
Spectrum 1	64.31	17.31	18.38
Spectrum 2	66.48	16.65	16.88
Spectrum 3	63.93	17.50	18.57
Spectrum 4	65.44	17.00	17.56
Mean	65.04	17.11	17.85
Std. deviation	1.15	0.38	0.78

(c)

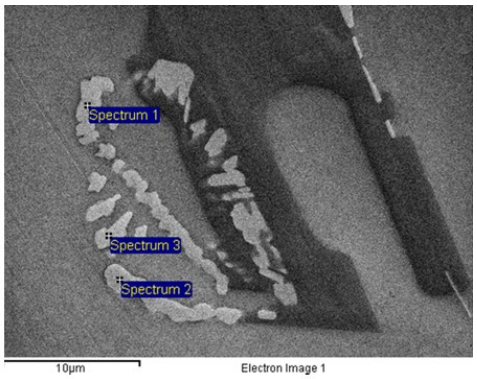

Spectrum	Al	Si	Fe
Spectrum 1	69.53	15.92	14.54
Spectrum 2	63.60	17.84	18.56
Spectrum 3	63.65	16.92	19.43
Mean	65.59	16.90	17.51
Std. deviation	3.41	0.96	2.61

(d)

Figure 6-37: Al-7Si-025Fe alloy solidified at 0.017 Ks^{-1} (a)script like phase with composition checked by SEM EDX (b) equal to τ_6 phase and (c) defragmented phase with script like morphology and composition similar to that of τ_6 phase

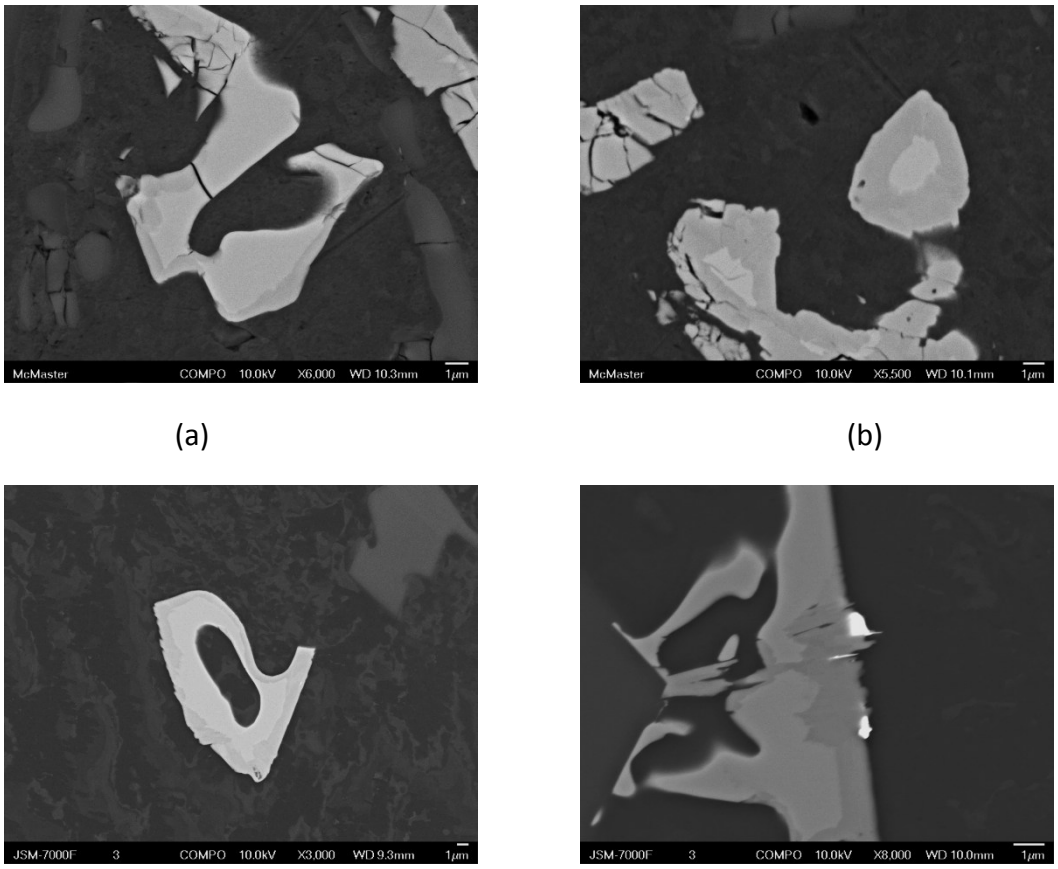

Figure 6-38: Typical microstructure of the progress of the peritectic reaction, U_{16} in Figure 6-36 where the τ_5 phase surrounded by the τ_6 phase. (a) Al-7Si-0.1Fe solidified at 0.1 Ks^{-1}, (b) Al-7Si-0.2Fe solidified at 0.1 Ks^{-1}, (c) Al-7Si-0.25Fe solidified at 0.8 Ks^{-1}, (d) Al-7Si-0.5Fe solidified at 0.8 Ks^{-1}.

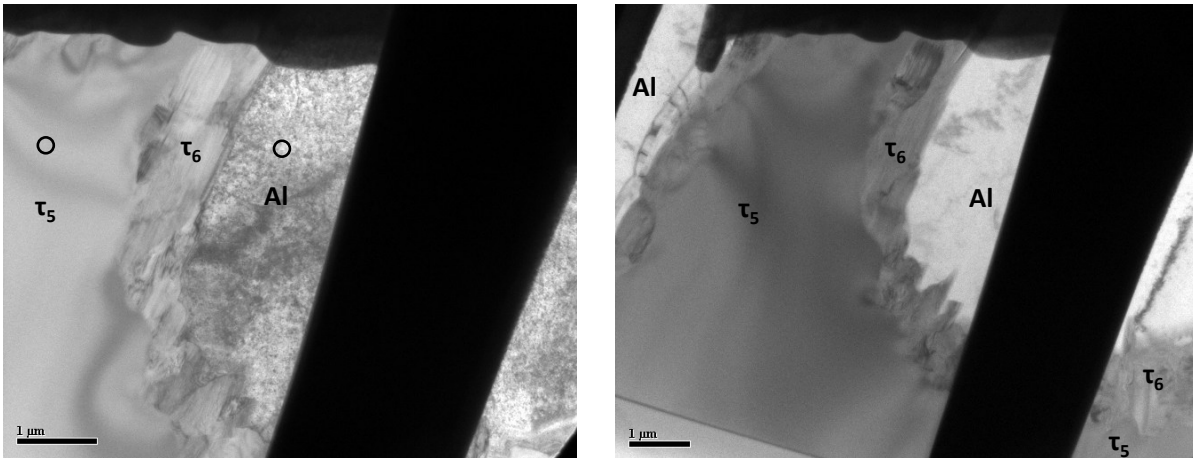

(a) (b)

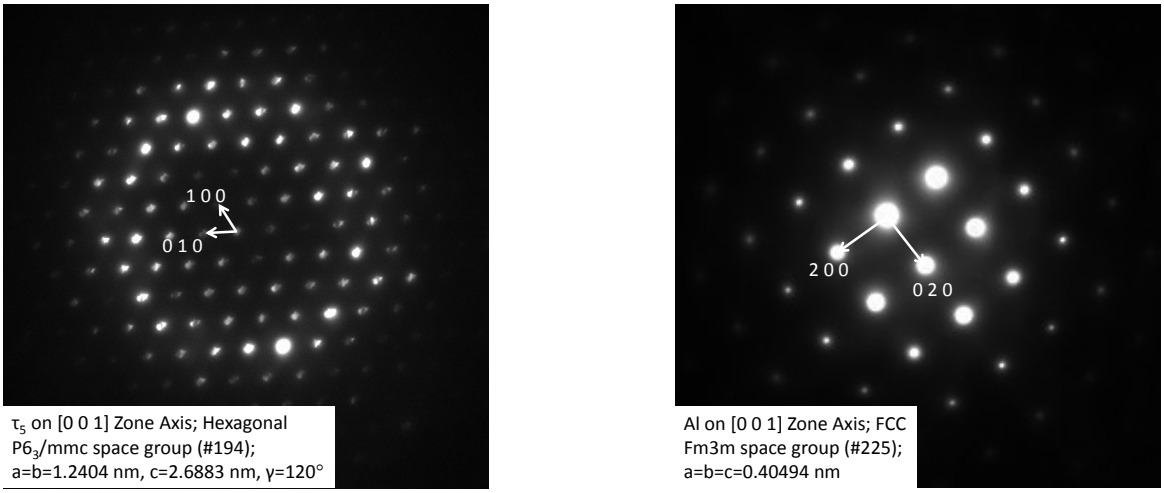

(c) (d)

Figure 6-39: Images showing the progress of the peritectic reaction, U_{16} in in Figure 6-36. A single grain of τ_5 phase reacted with the liquid and formed several grains of the τ_6 phase and (Al). (a) TEM bright field image showing the two locations from which SADP were obtained, (b) STEM image of (a), (c) SADP from the τ_5 phase on [001] zone axis and (d) SADP from the Al phase on

Typically, the kinetics of a peritectic reaction is progressing lower as the reaction proceeds; hence, there is a possibility of a small fraction of the θ phase encapsulated by the τ_5 phase that still remains unreacted in the cooling rates used in this study. The size of this θ phase would be small and in the order of less than 1 µm (or would have been observed in the conventional microscopy techniques used in this study) and required the precise micro-diffraction technique from the solidified microstructure coupled with the XRF elemental map using the synchrotron beam to deduce its presence. Further, it is notable that the existence of the θ phase was observed in the highest cooling rate used during solidification, of about 50 Ks^{-1}.

The predictions by the thermodynamic models and simulations using equilibrium and Scheil-Gulliver solidification conditions do not account for the anomalous clustering of the Al/Si atoms around each Fe atom and hence, would only predict the enthalpy and Gibbs free energy which will further predict the evolution of a specific phase when the Gibbs free energy is low enough to form that solid phase. Anomalous clustering of the Al/Si atoms around the Fe atoms would alter the enthalpy and Gibbs free energy of at the solid Al and liquid interface and could result in favourable conditions for the formation of phases that are not predicted by the thermodynamic models as the case in this study.

CHAPTER 7. RESULTS AND DISCUSSION: INFLUENCE OF STRONTIUM ON THE EVOLUTION OF THE INTERMETALLIC PHASES

The effect of adding about 0.02 wt% Sr to the Al-Si-Fe alloys is presented in this Chapter. Although trace levels of Sr plays a critical role in the Al-Si-Fe alloys, the study of the effect of Sr was not the main focus of this project and hence, only the Al-7Si-yFe (y=0.05, 0.25 and 0.5) with an addition of 0.02 wt% Sr was used for this study. The alloys used to evaluate the effect of Sr addition are shown in the schematic in Figure 4-1 (d). The measured chemical compositions of the Al-Si-Fe-Sr alloys in this study are presented in a table in APPENDIX A of this dissertation.

New $Al_5Fe_2Si_3$ phase was discovered in the Al-7Si-yFe alloys. Phase crystallographic structure is not matching none of the ternary Al-Si-Fe intermetallic phases in the JCPDS database or in reviewed literature. Despite numerous efforts to identify crystal structure of the κ- $Al_5Fe_2Si_3$ phase exact symmetry and unit cell parameters remain unknown.

7.1 SUMMARY OF THE ANALYSIS OF RESULTS

In the similar vein of thought presented in CHAPTER 6 of this dissertation, the summary of the analysis of the results is presented in this section followed by the salient results from the experiments and discussion. Figure 7-1 presents an overview schematic of the intermetallic phases identified in the Sr containing alloys show in Figure 4-1 (d).

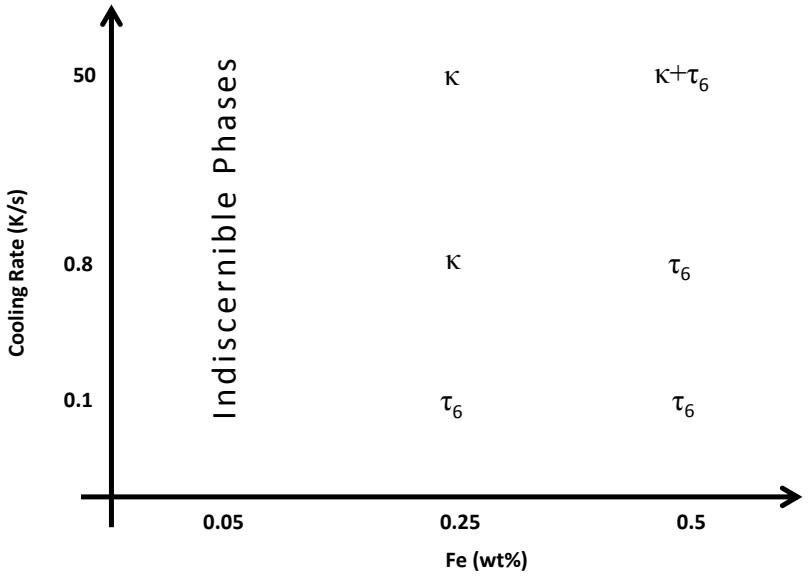

Figure 7-1: Schematic of the identification of the intermetallic phases in the solidified microstructure of the alloys containing Sr used in this study as shown in Figure 4-1 (d). The κ phase in the image is a new term used to identify an unknown Fe intermetallic phase. All the alloys showed an additional Sr containing intermetallic phase (Al_2Si_2Sr).

In Figure 7-1, the κ phase is a new notation used to identify an unknown intermetallic phase with an approximate stoichiometry of $Al_5Fe_2Si_3$; additionally, the Sr containing intermetallic phase, Al_2Si_2Sr was observed in all the nine alloys used in this study along with the Fe containing intermetallic phases. The Al_2Si_2Sr phase was confirmed by the SEM (EDX) and X-ray diffraction with a synchrotron beam and no further characterization of this phase was carried out because our focus in this project was to only analyze the Fe containing intermetallic phases.

Unlike the results of the microstructure analysis of the Al-Fe-Si alloys presented in CHAPTER 6, the τ5 phase did not evolve during the solidification of any of the Al-7Si-yFe (y=0.05, 0.25 and 0.5) alloys solidified at any of 50, 0.8 or 0.1 Ks-1 cooling rates of the liquid, respectively. The new phase was named κ-Al5Fe2Si3 in this study. The addition of Sr to the Al-7Si-yFe (y=0.05, 0.25 and 0.5) alloys altered the solidification path by suppressing the formation of the τ5 phase and promoting the formation of the κ-Al5Fe2Si3 phase during solidification. At cooling rates during solidification that are relatively lower, the κ phase underwent a possible peritectic reaction to transform into the τ6-Al9Fe2Si2 phase which remained as the terminal equilibrium phase in these alloys. Similar to the Al-Fe-Si system, only the τ6 phase is predicted to evolve in the equilibrium phase diagrams simulated using the Pandat thermodynamic software as shown in

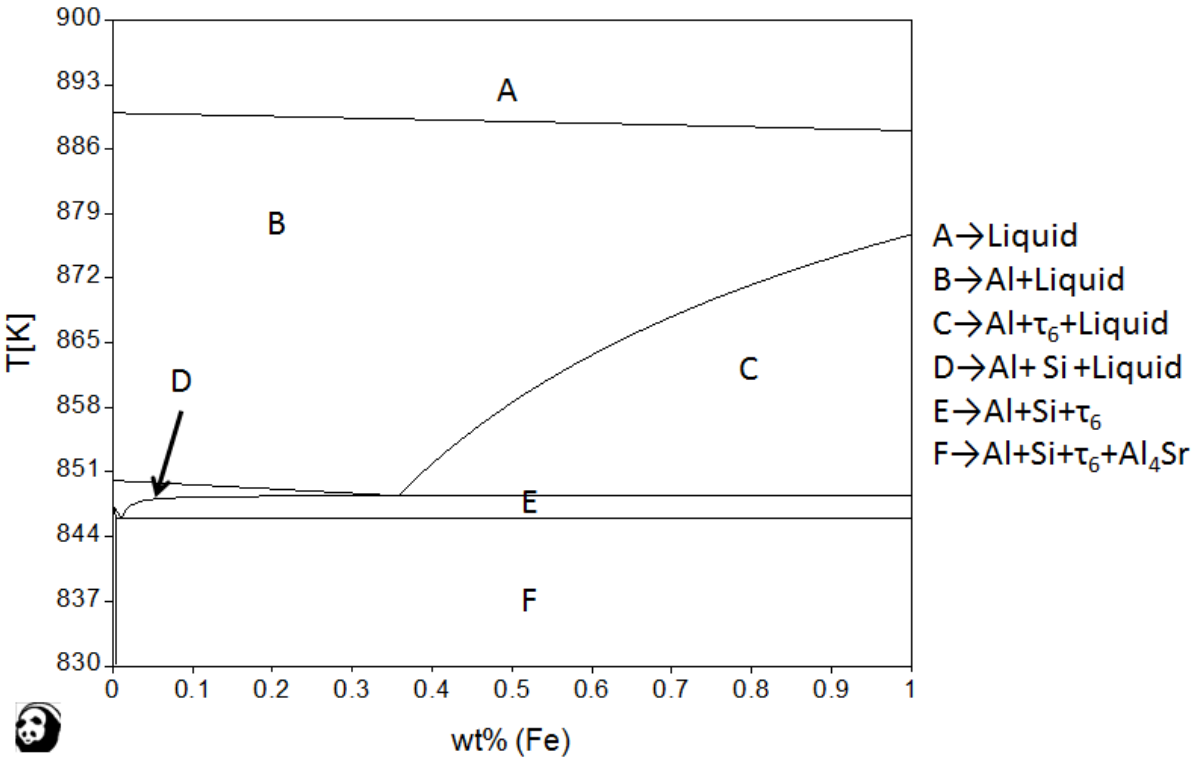

Figure 7-2.

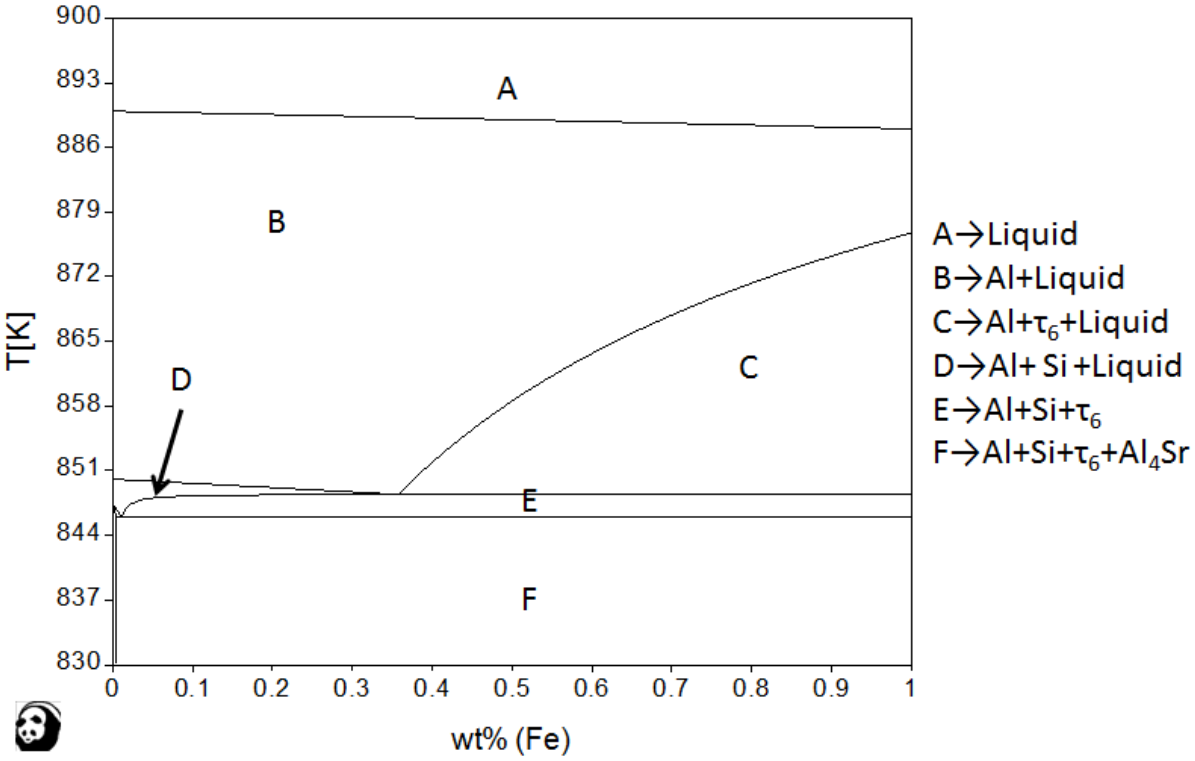

Figure 7-2: Typical isopleth phase diagram of the Al-Fe-Si-Sr system where in Al-7Si-0.02Sr alloy with 0 to 1 wt% Fe is shown as a function of temperature.

In Figure 7-1, the Al-7Si-0.05Fe-0.02Sr alloys showed the presence of several Fe containing intermetallic phases; however, due to the small size of these individual phases, none of them could be characterized by either the SEM (EDX) or TEM analysis. Figure 7-1 also shows that the kinetics of the transformation of the κ phase to the τ_6 phase in the Sr containing alloys are enhanced by the higher Fe concentration in the alloy and slower cooling rates during solidification. When solidified samples containing the κ phase were solution heat treated at 813 K (540 ^{o}C) for 24 h, all the κ phase transformed into the τ_6 phase suggesting that the evolution of κ during the solidification process is an anomaly and the stable equilibrium terminal phase is the τ_6 phase, as predicted by the thermodynamic simulations. It is notable that the Sr containing intermetallic phase predicted to evolve during solidification by the

thermodynamic software Pandat is the Al_4Sr binary phase as shown in

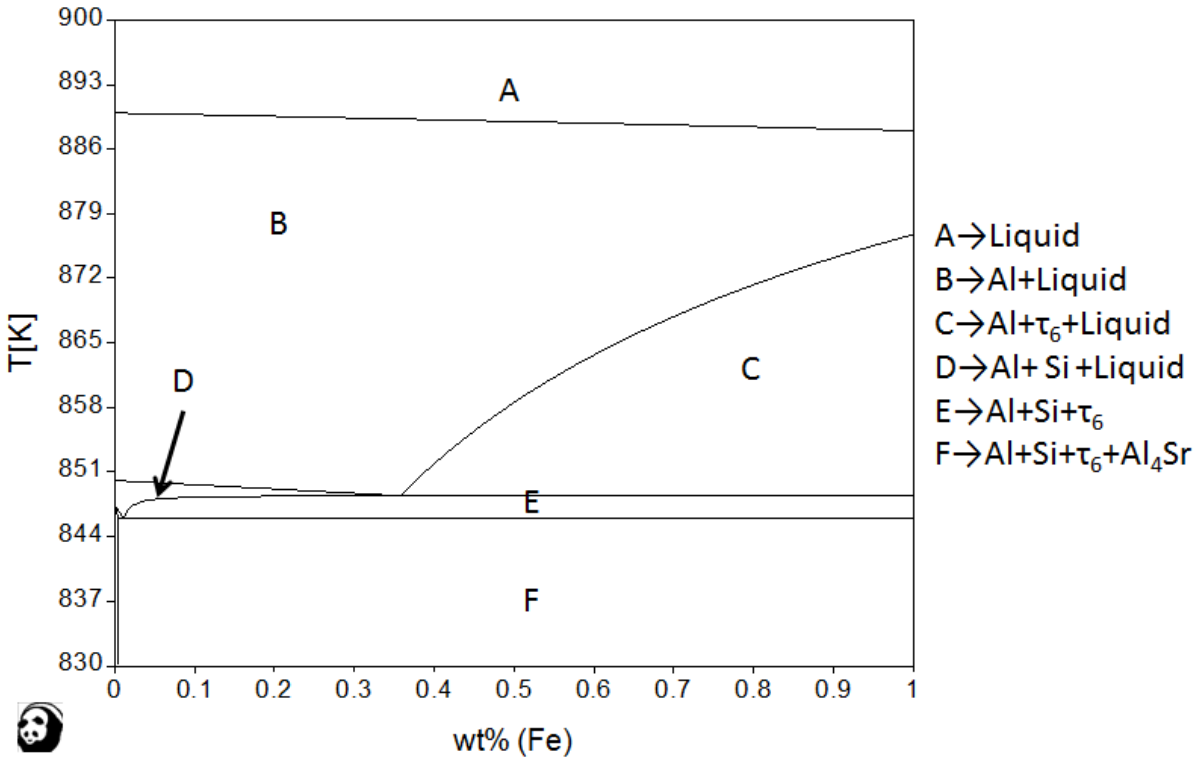

Figure 7-2; however, the observed phase was the ternary Al_2Si_2Sr phase; the Thermo-Calc[††] thermodynamic software with the TTAL7 database was alternatively used to simulate the phase

[††] Thermo-Calc Thermo-Calc Software, Inc 4160 Washington Road, McMurray ,PA 15317 ,USA

diagram shown in

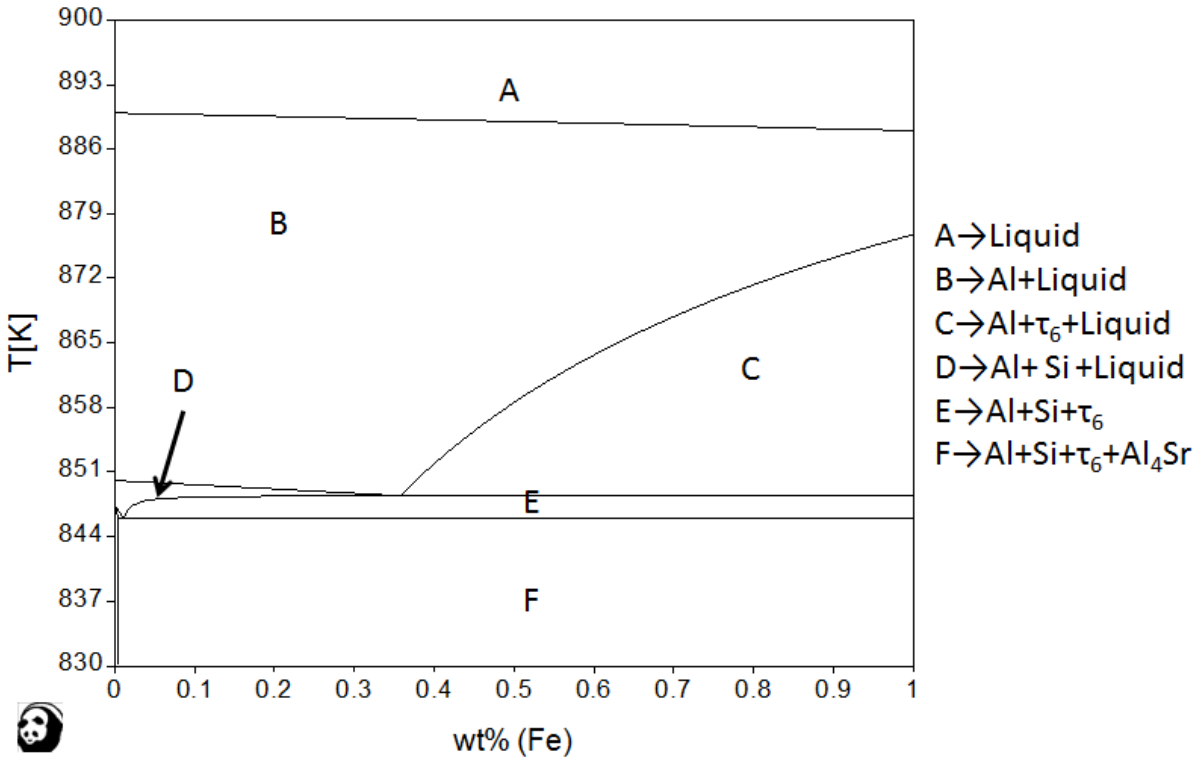

Figure 7-2 predicted the formation of Al_2Si_2Sr instead of the Al_4Sr phase.

7.2 MICROSTRUCTURAL CHARACTERIZATION OF Sr CONTAINING Al-Si-Fe ALLOYS

Figure 7-3 (a) and (b) presents typical SEM BEI of the Al-7Si-0.05Fe alloys for cooling rates during of 50 Ks^{-1} and 0.8 Ks^{-1}, respectively; the bright white phases in the images except the once marked by arrows for the Al_2Si_2Sr phase are the Al-Si-Fe intermetallic phases which are too small to be characterized by the EDX beam or SADP in TEM.

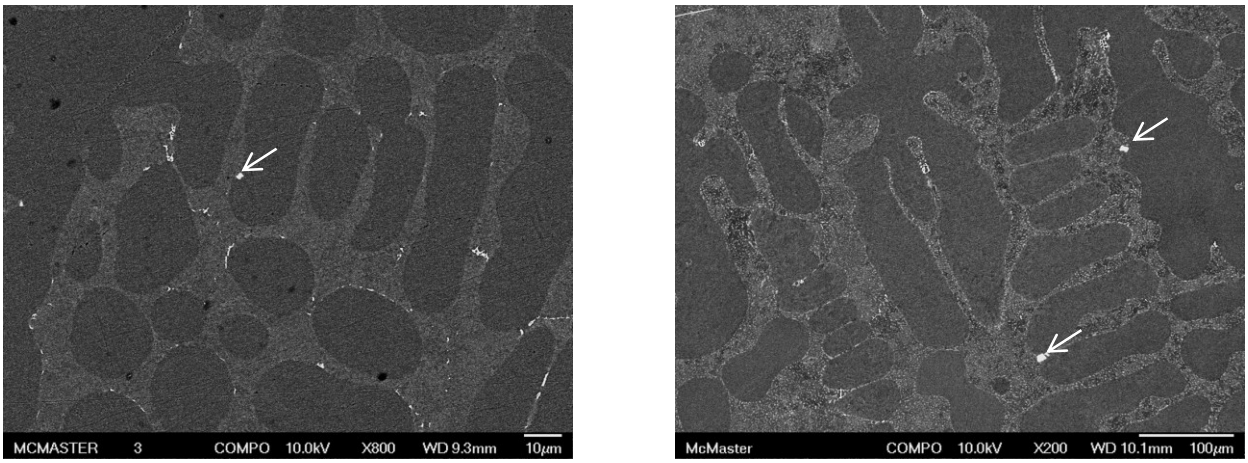

(a) (b)

Figure 7-3: Typical SEM BEI of Al-7Si-0.05Fe-0.02Sr solidified at (a) 50 Ks^{-1} and (b) 0.8 Ks^{-1}; the bright white phases are the Fe containing intermetallic phases except the once shown by arrow for the Al_2Si_2Sr phases.

Figure 7-4 presents the typical microstructure images of the Al-7Si-0.25Fe alloys solidified at the three cooling rates of 50 Ks^{-1} ((a) and (b)), 0.8 Ks^{-1} ((c) and (d)) and 0.1 Ks^{-1} ((e) and (f)); only the κ phase was observed in the samples solidified at 50 Ks^{-1} and only the τ_6 phase in the samples solidified at both the 0.8 and 0.1 Ks^{-1}, alike.

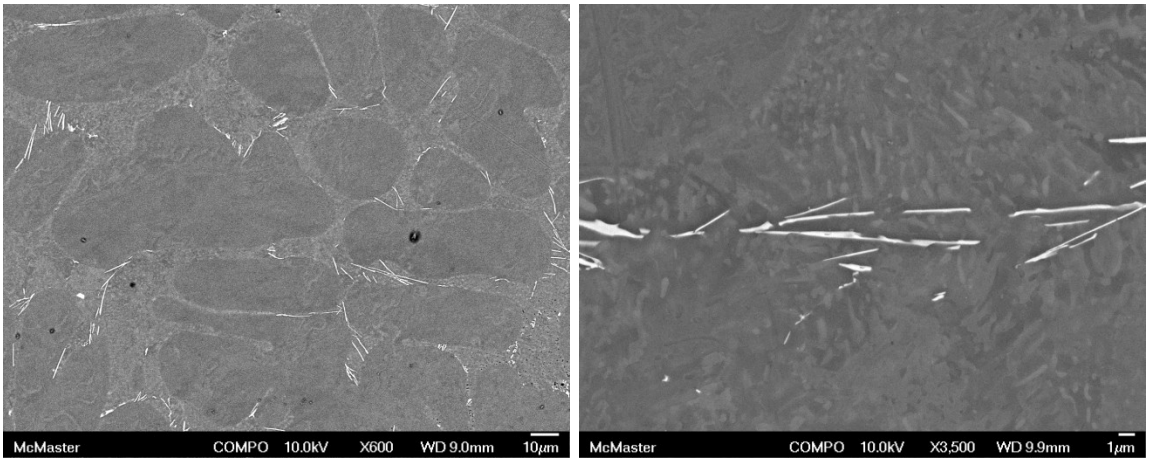

(a) (b)

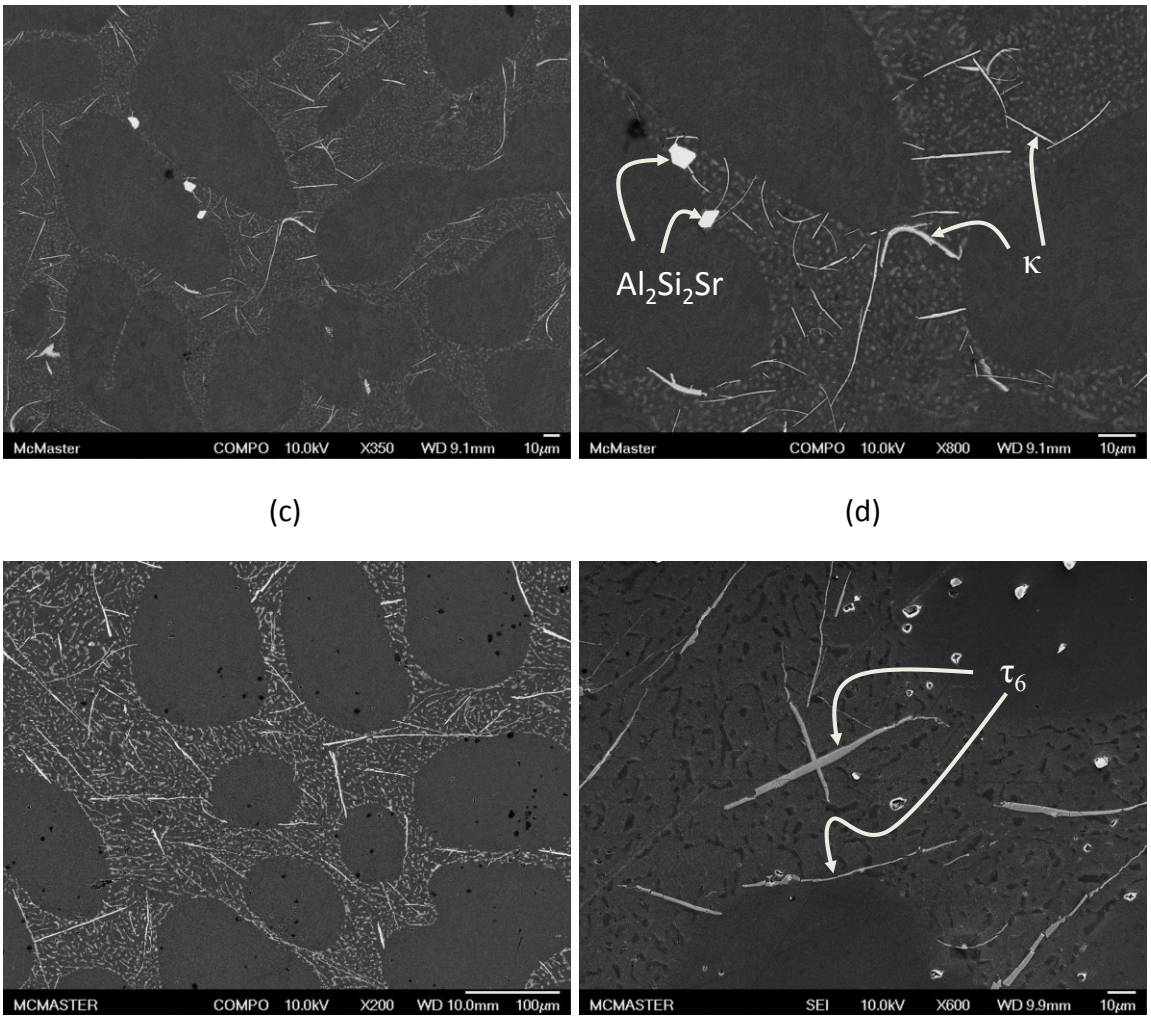

Figure 7-4: Typical microstructure of the Al-7Si-0.25Fe-0.02Sr alloy solidified at (a) 50 Ks^{-1} showing the exiting of only the κ phase, (b) 0.8 Ks^{-1} showing the exiting of only the κ phase and (c) 0.1 Ks^{-1} showing the exiting of only τ_6 phase.

Figure 7-5 presents the typical microstructure images of the Al-7Si-0.5Fe alloys solidified at the three cooling rates of 50 Ks^{-1} ((a) and (b)), 0.8 Ks^{-1} ((c) and (d)) and 0.1 Ks^{-1} ((e) and (f)); only the κ phase was observed in the samples solidified at 50 Ks^{-1}, both the κ and τ_6 phases in the samples solidified at 0.8 Ks^{-1}, and only the τ_6 phase in the samples solidified at 0.1 Ks^{-1}.

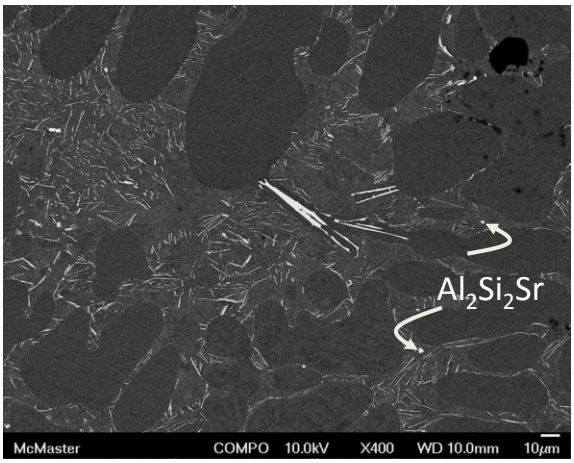
Al_2Si_2Sr
McMaster COMPO 10.0kV X400 WD 10.0mm 10μm

(a)

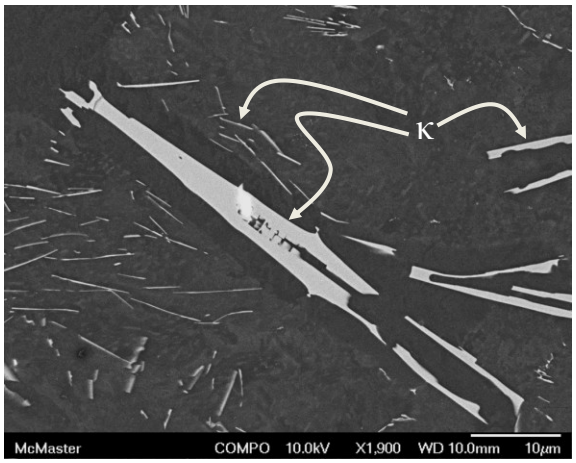
κ
McMaster COMPO 10.0kV X1,900 WD 10.0mm 10μm

(b)

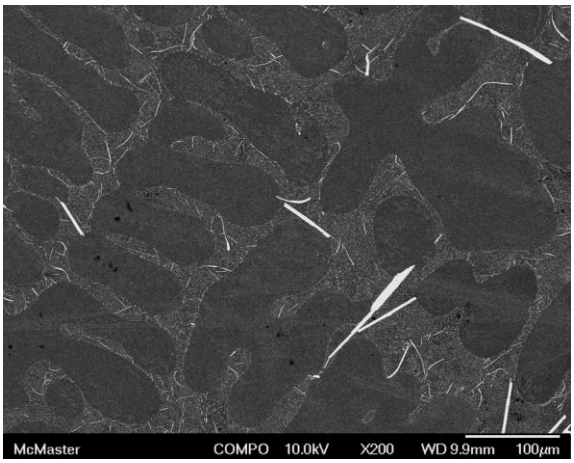
McMaster COMPO 10.0kV X200 WD 9.9mm 100μm

(c)

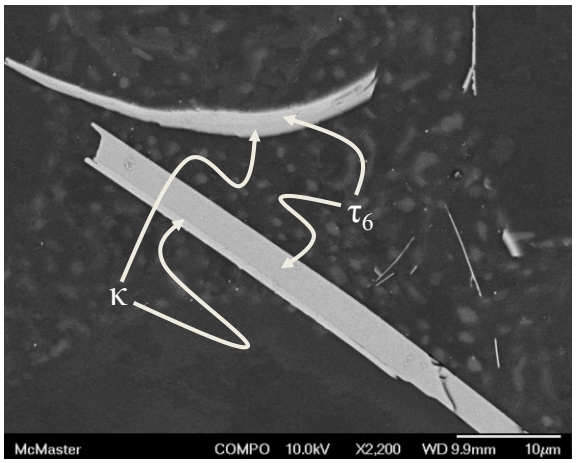
τ_6
κ
McMaster COMPO 10.0kV X2,200 WD 9.9mm 10μm

(d)

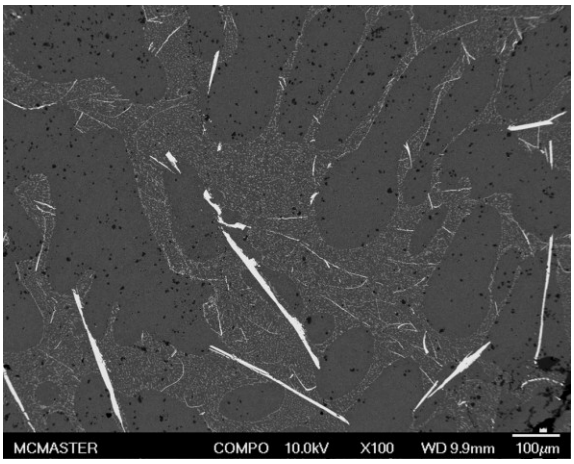
MCMASTER COMPO 10.0kV X100 WD 9.9mm 100μm

(e)

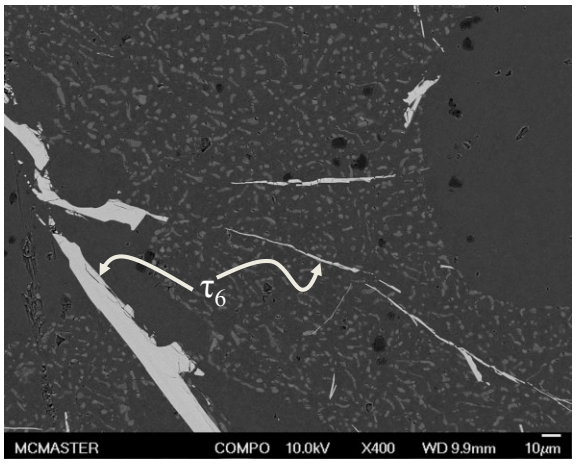
τ_6
MCMASTER COMPO 10.0kV X400 WD 9.9mm 10μm

(f)

Figure 7-5: Typical microstructure of the Al-7Si-0.5Fe-0.02Sr alloy solidified at (a) 50 Ks^{-1} showing the exiting of only the κ phase, (b) 0.8 Ks^{-1} showing the exiting of both the κ and τ_6 phases and (c) 0.1 Ks^{-1} showing the exiting of only τ_6 phase.

The anomaly observed in the microstructure of the Sr containing Al-Si-Fe alloys is that the τ_5 phase fails to evolve when Sr is added and a new phase in κ-$Al_5Fe_2Si_3$ evolves; the κ phase further transforms to the τ_6 phase at lower cooling rates during solidification and the kinetics of the transformation is enhanced by higher concentration of Fe in the alloy. Further characterization of these intermetallic phases are presented in subsequent sections before a plausible hypothesis is presented to explain the mechanisms of such anomalous phase evolutions.

7.3 CHARACTERISTICS OF THE κ AND τ_6 PHASES

The characterization of the κ and τ_6 intermetallic phases will be presented in the following sub-sections:

- Quantitative EDX Analysis
- X-Ray Diffraction of Powder Samples
- X-Ray Diffraction with Synchrotron Beam
- Transmission Electron Microscopy (TEM)

7.3.1 Quantitative EDX Analysis

The quantitative EDX was carried out in the SEM such that the interaction volume of the beam on the surface of the sample was smaller than the volume of the intermetallic phase being evaluated as described in Section 6.6.1. Table 7-1 presents the results of the quantitative EDX analysis of the unknown and new κ and τ_6-$Al_9Fe_2Si_2$ phases observed in a typical microstructure of the solidified samples of Al-7Si-yFe-0.02Sr (y=0.25 and 0.5) alloys in this study.

Table 7-1: Typical results of the quantitative EDX of the unknown κ and τ_6 phases observed in the Al-7Si-yFe-0.02Sr (y=0.25 and 0.5) alloys.

Phases	Atomic %	Al	Si	Fe	(Fe/Si) Ratio
κ	**Average**	61.37	23.06	15.57	0.68
	Std. Dev.	7.64	4.35	3.37	
τ_6	**Average**	62.74	18.41	18.86	1.02
	Std. Dev.	0.20	0.20	0.20	

Table 7-1 shows that the ratio of Fe:Si is still maintained around unity for the τ_6 phases while it is about 2:3 in the κ phase. The typical average stoichiometry for the τ_6 phase in the alloys was evaluated as $Al_9Fe_2Si_2$, while that for the κ phase was $Al_5Fe_2Si_3$.

Table 7-2 presents the typical quantitative EDX results for the Al_2Si_2Sr in the alloys; the stoichiometry of the phase was confirmed by the EDX data presented.

Table 7-2: Typical results of the quantitative EDX of the Al_2Si_2Sr phase in the Al-7Si-yFe-0.02Sr (y=0.25 and 0.5) alloys.

Phases	Atomic %	Al	Si	Sr
Al_2Si_2Sr	**Average**	39.39	40.80	19.82
	Std. Dev.	0.17	0.22	0.10

7.3.2 X-Ray Diffraction of Powder Samples

The X-ray diffraction of the powder samples obtained from the dissolution technique described in Section 5.8.2.1.1 of this dissertation was carried out using the Cu K_α radiation. The Al-7Si-0.5Fe-0.02Sr sample solidified at 5 Ks^{-1} was used for the diffraction experiments. In addition to

obtaining Al free powder from the solidified samples, powder was obtained from samples that were solution heat treated at 540 °C for 24h to explore any phase transformation of the κ phase after solidification.

Figure 7-6 presents the x-ray diffraction spectrum for both the as-cast samples (black line) and heat treated sample (red line) for the Al-7Si-0.5Fe-0.02Sr alloy solidified at 5 Ks^{-1}; all the peaks of Si are labelled and the remaining peaks are labeled in the magnified sections shown in Figure 7-7; the Si peaks were labelled using the JCPDS card file number 27-1402 and the position of the peaks in our spectrum were identical to those in the card file. It is notable that in Figure 7-6, no peaks of Al phase was observed which confirmed the effectiveness of dissolving this major phase; further, there were no peaks of Al_2Si_2Sr observed as well, suggesting that this phase may have been dissolved in our preparation of the powder sample. It would be noteworthy to mention that there is a possibility of certain Fe containing intermetallic phases being dissolved as well in our preparation, however, the results show that the major intermetallic phases have remained intact in the powder sample.

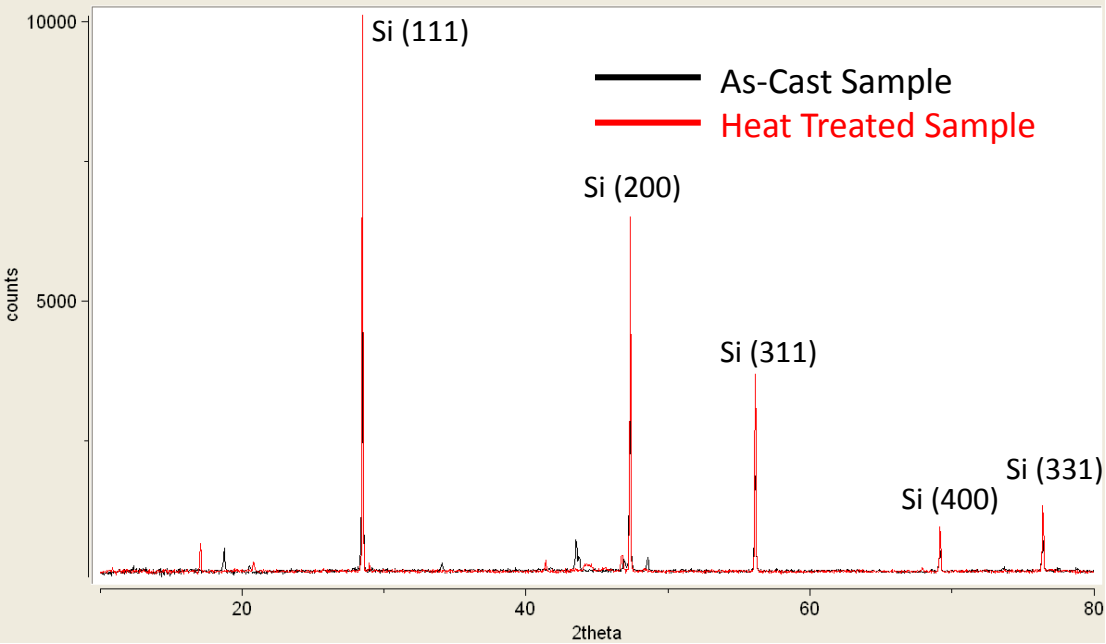

Figure 7-6: X-Ray diffraction spectrum from powder samples of Al-7Si-0.5Fe-0.02Sr alloy solidified at 5 Ks^{-1} showing both the as-cast (in black) and heat treated (in red) samples.

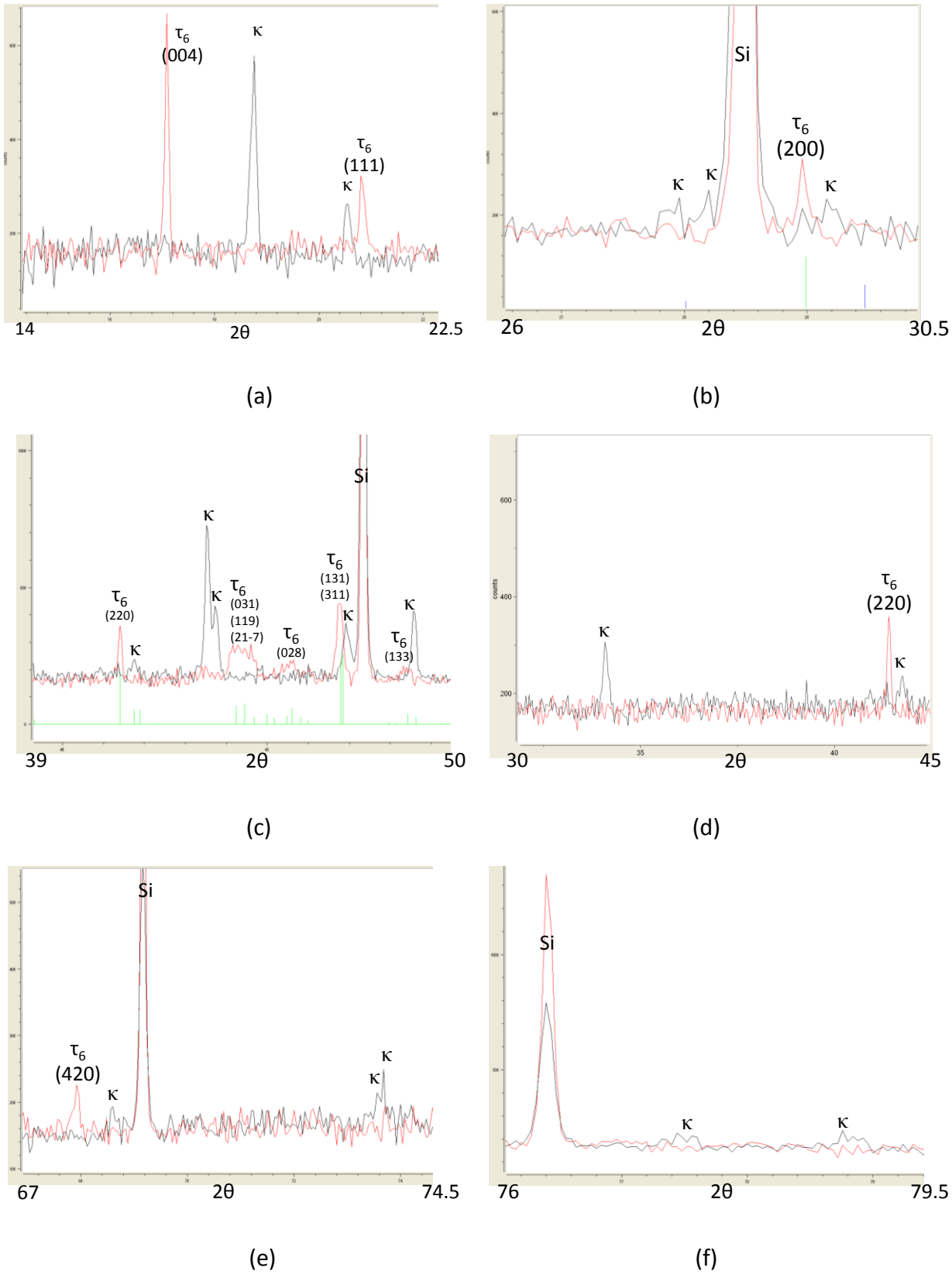

Figure 7-7: Magnified sections of spectrum in Figure 7-6 with phase identification labels.

The peaks from the τ_6 phase in the sections shown in Figure 7-7 was labelled using the JCPDS card file number 82-0546 and it is noteworthy to mention that there was as exact fit of all the angle position of the peaks from the experiments to those in the card file. The peak positions of the κ phase is also shown in the sections shown in Figure 7-7 and none of the crystal structure information from the known intermetallic phases would fit the peaks accurately. A list of the peak positions and intensity ratio are shown in Table 7-3. Table 7-4 presents the comprehensive list of phases along with their crystal structure information used to identify the peaks of the κ phase in the sections shown in Figure 7-7.

Table 7-3: List of peak position, d-spacing and intensity ratio obtained from the κ phase in the sections shown in Figure 7-7.

Peak Position (2θ)	d-spacing (nm)	I/I_{max}
18.76	0.4726	12.31
28.48	0.3132	100.00
34.08	0.2629	6.54
43.52	0.2078	15.50
46.92	0.1935	7.91
47.36	0.1918	67.24
48.56	0.1873	8.81
56.16	0.1636	39.79
69.16	0.1357	12.01
76.4	0.1246	16.87

Table 7-4: List of phases used to identify the peaks marked as belonging to the κ phase in the sections shown in Figure 7-7.

Phase Notation	Phase Stoichiometry	Crystal Structure	Space Group	Lattice Parameters A	Reference
Al	Al	Cubic	Fm3m	a=4.0494	128
Si	Si	Cubic	Fd3m	a= 5.43088	128
θ	$Al_{13}Fe_4$	Monoclinic	C2/m	a=15.489 b=8.083 c=12.476 β= 107.70°	129
τ_5	Al_8Fe_2Si	Hexagonal	$P6_3/mmc$	a = 12.404(1) c = 26.234(2)	84
τ_6	$Al_9Fe_2Si_2$	Monoclinic	C2/c	a = 20.813(6) b = 6.175(3) c = 6.161(3) β= 90.42(3)°	76
τ_4	Al_3FeSi_2	Tetragonal	I4/mcm	a = 6.07 c = 9.50	81
τ_7	$Al_3Fe_2Si_3$	Monoclinic	$P2_1/n$	a = 7.179(2) b = 8.354(2) c = 14.455(4) β = 93.80(2)°	81
Al_4Sr	Al_4Sr	Tetragonal	I4/mmm	a=4.46 c=11.07	130
Al_2Si_2Sr	Al_2Si_2Sr	Hexagonal	P-3m1	a= 4.1872(5) c= 7.427(1)	131
Orthorhombic β	$Al_9Fe_2Si_2$	Orthorhombic	Cmcm	a = 6.18 b = 6.2 c = 20.8	66
β stretched	$Al_9Fe_2Si_2$	Monoclinic	$C_{12}/C1$	a = 12.335 b = 12.3322 c = 41.6186 β= 90.42(3)°	

The diffraction experiments on the solidified as-cast and heat treated samples of the Al-7Si-0.5Fe-0.02Sr alloy solidified at a cooling rate of $5Ks^{-1}$ shown in Figure 7-7 amply demonstrate the following salient results:

- The τ_6 phase does not exist in the as-cast solidified samples. We may have lost some of the small τ_6 phase that may have evolved with the eutectic phases during solidification.

- The κ phase is the only major intermetallic phase existing at room temperature; assuming that there is no more than one unknown phase in the microstructure based on the microscopy images.
- All the κ phase transforms to the τ_6 phase upon solution heat treatment at 813 K (540 ^{o}C) for 24 h. This shows that the terminal phase in these alloys is the τ_6 phase and the solidification conditions and Fe concentration in the alloy alter the solidification path in these alloys to preferentially affect the evolution of the κ phase and its retention at room temperature.

7.3.3 X-Ray Diffraction with Synchrotron Beam

The XRF elemental map and diffraction experiments were carried out on the microstructure of the Al-7Si-0.25Fe-0.02Sr alloy solidified at 50 Ks^{-1}. The conditions for the experiments are presented in Section 6.6.2 of this dissertation and maintained the same for experiments with the Sr containing alloy as well. Figure 7-8 shows the results of the XRF elemental map of the various elements considered showing the region of interest with two primary Al, eutectic phases and three distinct areas of the Fe containing intermetallic phases. Sr was not considered in this XRF map because the beam voltage was 10.1 KeV which was smaller than that required to map Sr element (14.1429 KeV). Each pixel grid in Figure 7-8 denotes the area from which diffraction pattern was collected using the synchrotron beam and the CCD camera detector. Each grid is a square of 1 μm side. Figure 7-8 shows that the transition elements besides the Fe such as Mn, Cu, Ni and V (trace ppm levels in the alloy) all exists along with the intermetallic phase due to their solubility in this phase and this observation corroborates to the confidence in the accuracy of the XRF elemental map. Figure 7-9 show a schematic of the grids to enable ease of visualization for the reader; the grids are numbered and those marked with an 'X' denote the grids from which the diffraction results were analysed and those marked with and 'X' and shaded (8-12, 8-13, 8-14 and 9-14) are those from which the results are presented in this dissertation. There are a total of 324 grids (18 X 18) from which individual diffraction patterns were collected. Typical diffraction patterns look similar to that presented in Figure 6-29.

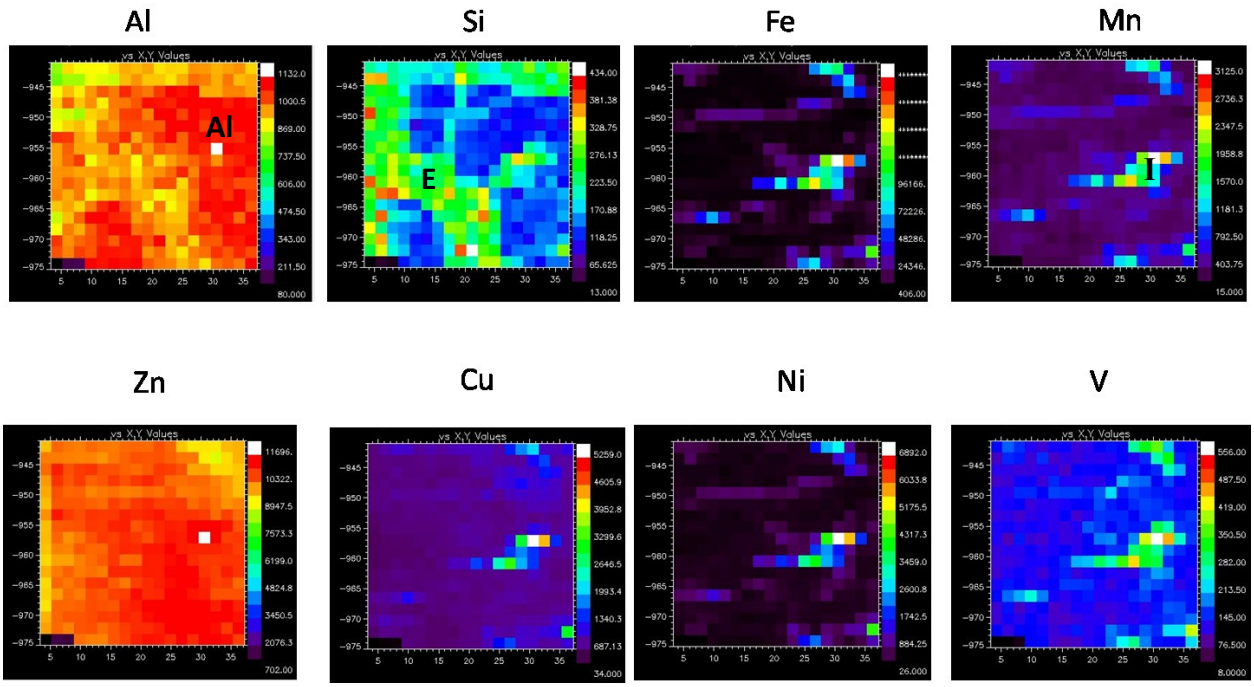

Figure 7-8: Typical XRF elemental maps obtained on the microstructure of Al-7Si-0.25Fe-0.02Sr alloy solidified at 50 Ks^{-1}. The elements are shown above their respective maps. Each pixel is a square of 1µm size. Regions marked Al, E and I denote the primary Al, eutectic and intermetallic phase regions in the microstructure.

	1	2	3	4	5	6	7	8	9	10	11	12	13	14	15	16	17	18
18													X	X	X	X		
17																		
16																		
15																		
14																		
13																		
12																		
11														X	X	X		
10														X	X	X	X	
9														X	X	X		
8											X	X	X	X	X	X	X	X
7																		
6																		
5			X	X	X													
4																		
3																		
2											X							
1												X	X					

Figure 7-9: The pixel grid of the XRF elemental maps shown in Figure 7-8. The marked grids were critically analyzed, and the results from the marked and shaded grids are presented in this dissertation. Each pixel is a square of 1µm size.

The typical diffraction data spectrum from the grid location marked 8-13 in Figure 7-9 is presented in

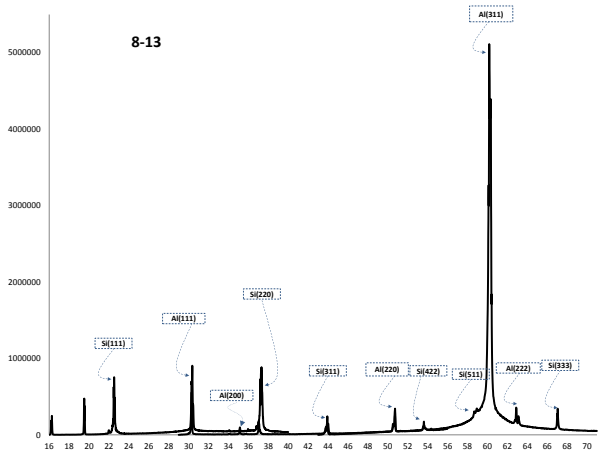

(a)

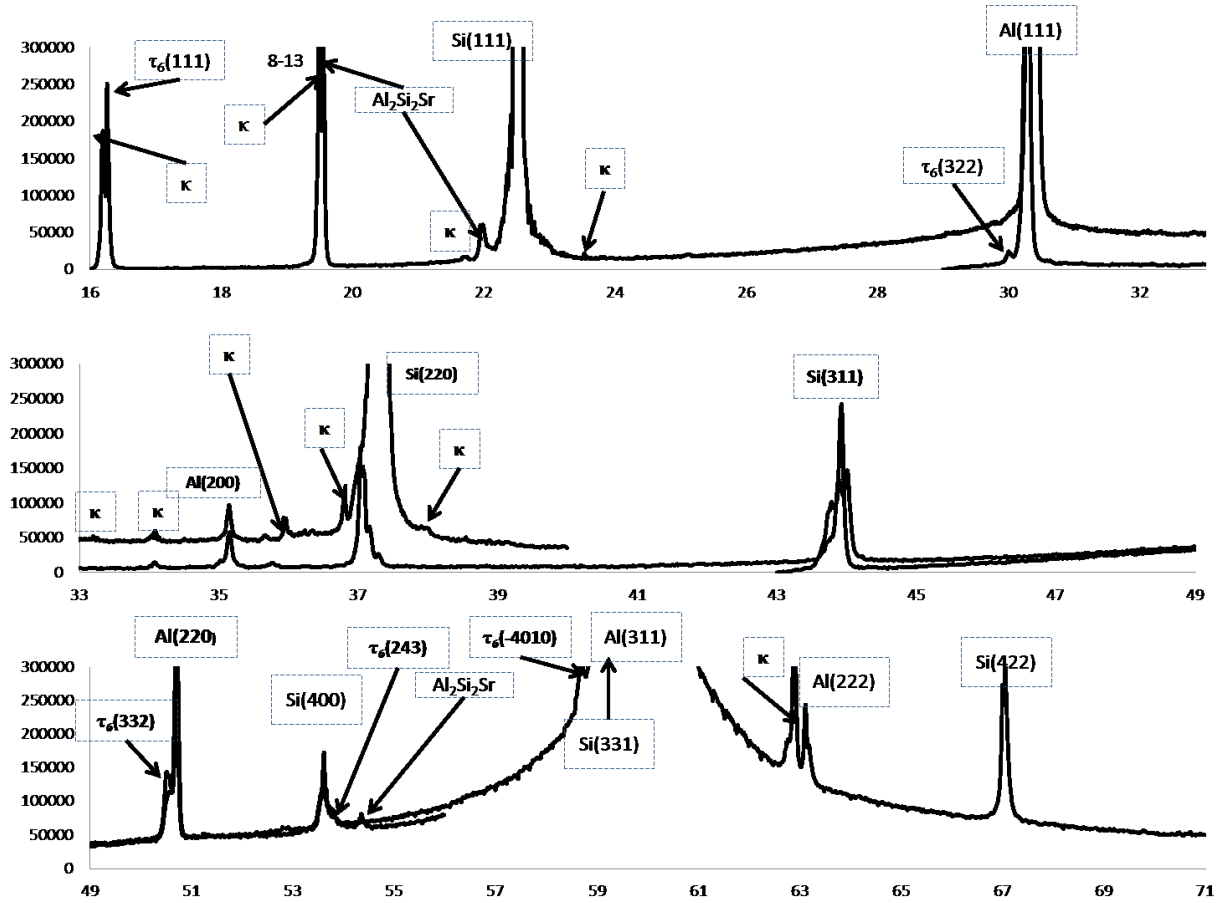

(b)

Figure 7-10: Diffraction data spectrum obtained and analyzed from the grid location labeled 8-13 in Figure 7-9. (a) complete spectrum (16 to 71°), (b) split spectra for clarity of the analyzed peak labels (16 to 33°, 33 to 49° and 49 to 71°).

Figure 7-10 shows that besides the major peaks of Al and Si, the peaks from the τ_6 and Al_2Si_2Sr phases are prominent. There are several peaks that have not been affiliated to any one or more phases; it is plausible that the unidentified peaks stem from the κ phase which has not yet been determined. A list of phases that were used to index the spectra obtained from the diffraction experiments are shown in Table 7-5.

Table 7-5: List of the various phases used to analyze the diffraction data from the solidified microstructure of Al-7Si-0.25Fe-0.02Sr alloy.

Phase Notation	Phase Stoichiometry	Crystal Structure	Space Group	Lattice Parameters A	Reference
Al	Al	Cubic	Fm3m	a=4.0494	128
Si	Si	Cubic	Fd3m	a= 5.43088	128
θ	$Al_{13}Fe_4$	Monoclinic	C2/m	a=15.489 b=8.083 c=12.476 β= 107.70°	129
τ_5	Al_8Fe_2Si	Hexagonal	$P6_3/mmc$	a = 12.404(1) c = 26.234(2)	84
τ_6	$Al_9Fe_2Si_2$	Monoclinic	C2/c	a = 20.813(6) b = 6.175(3) c = 6.161(3) β= 90.42(3)°	76
τ_4	Al_3FeSi_2	Tetragonal	I4/mcm	a = 6.07 c = 9.50	81
τ_7	$Al_3Fe_2Si_3$	Monoclinic	$P2_1/n$	a = 7.179(2) b = 8.354(2) c = 14.455(4) β = 93.80(2)°	81
Al_4Sr	Al_4Sr	Tetragonal	I4/mmm	a=4.46 c=11.07	130
Al_2Si_2Sr	Al_2Si_2Sr	Hexagonal	P-3m1	a= 4.1872(5) c= 7.427(1)	131
Orthorhombic β	$Al_9Fe_2Si_2$	Orthorhombic	Cmcm	a = 6.18 b = 6.2 c = 20.8	66
Tetragonal β	$Al_4Fe_2Si_3$	Tetragonal		a=0.62 c=0.905	

The results of the grid locations marked 8-11, 8-12 and 9-13 are presented in Table 7-6.

Table 7-6: Summary of identified phases in Al-7Si-025Fe-0.03Sr alloy solidified at 50 Ks^{-1}

Spot	κ	τ_6
8_12	X	X
8_13	X	X
8_14	X	X
9_12	X	

Table 7-7 presents the observations of the variations in the peak intensities of the κ, τ_6 and Al_2Si_2Sr phases, individually in each of the grid marked grid locations in Figure 7-9 from where individual diffraction data were analysed

Table 7-7: Observations of the peak intensities of the κ, τ_6 and Al_2Si_2Sr phases in the analyzed diffraction data from the marked grid locations in Figure 7-9.

Grid Location Range	κ	τ_6	Al_2Si_2Sr
8-10 to 8-13	↑	↓	↑
8-14 to 8-18	↓	↑	↓
9-14-9-16	↑	↑	↓
10-14-10-16	↑	↓	↓

The results from the synchrotron beam diffraction experiments show that the τ_6 phase evolves in small proportions with the eutectic phases; the κ phase evolves prior to the eutectic reaction temperature and begins to transform in to the τ_6 phase by possibly a peritectic reaction; and the Al_2Si_2Sr phase exist at the interface of the primary Al and eutectic regions and co-exists with the Al-Fe-Si intermetallic phases. It is emphatically confirmed that contrary to the results from the Al-7Si-0.25Fe alloy solidified at 50 Ks^{-1}, there is no peaks of θ or τ_5 in this alloy.

7.3.4 Transmission Electron Microscopy (TEM)

Figure 7-11 shows the typical results from the TEM analysis of the Al-5Si-0.5fe-0.05Sr alloy showing the presence of the unknown κ phase along with the primary Al and eutectic phases;

also shown is the typical SADP on zone axis obtained from the location shown on the κ phase. Rigorous analyses of SADPs on several zone axes obtained from the κ phase did not yield any favourable clues about the crystal structure of the phase; the known phases shown in Table 7-5 were used for the analyses of the SADPs from the κ phase.

Figure 7-12 shows the typical results from the TEM analysis of the Al-5Si-0.5fe-0.05Sr alloy showing the presence of the τ_6 phase along with the primary Al and eutectic phases; also shown is the typical SADP on zone axis obtained from the location shown on the τ_6 phase. The τ_6 phase was identified to have a monoclinic crystal structure with the space group A2/a (#15) and lattice parameters of a=0.616, b=0.6175, c= 1.208 and β=90.4°.

Further, EDX analysis was also carried out in the TEM and STEM to show that the Fe:Si ratio in the κ phase was close to 2:3 and that in the τ_6 phase was 1:1.

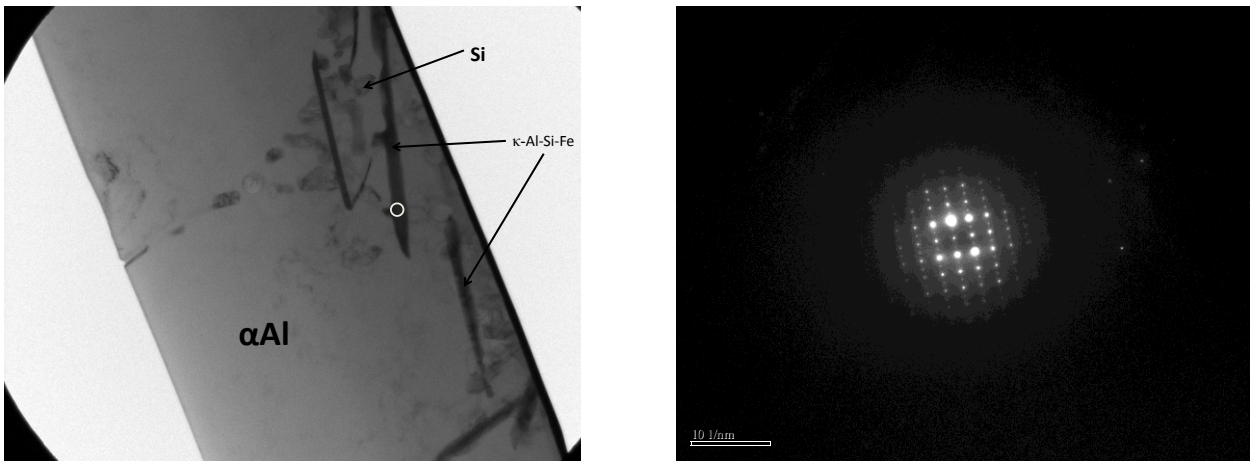

(a) (b)

Figure 7-11: Typical TEM results of Al-5Si-0.5Fe-0.05Sr alloy solidified at 50Ks^{-1} ; (a) bright field low magnification image of the sample showing the κ, eutectic Si and Al phases and (b) SADP pattern on zone axis obtained from the spot shown in (a) on the κ phase.

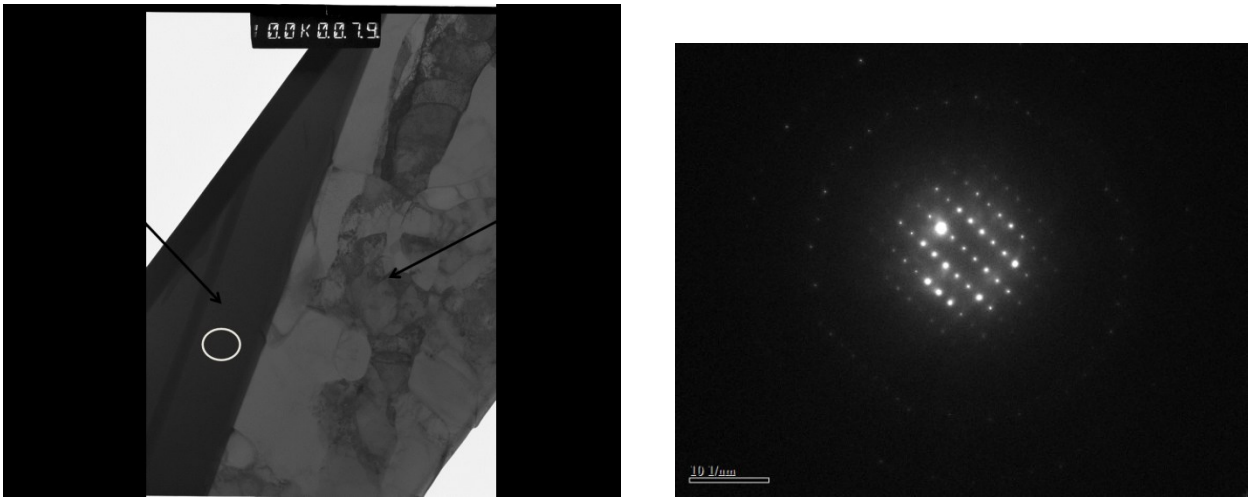

(a) (b)

Figure 7-12: Typical TEM results from the Al-7Si-0.5Fe-0.02Sr alloy sample solidified at 50 Ks^{-1}; (a) bright field image showing the τ_6, eutectic Si and Al phases and (b) SADP pattern on zone axis obtained from the spot shown in (a) on the τ_6 phase.

Figure 7-13 shows the typical bright field STEM image of the Al-7Si-0.05Fe-0.02Sr alloy solidified at 0.8 Ks^{-1} showing the Al_2Si_2Sr intermetallic phase with small morphology and attached to the eutectic Si along with the Al-Si-Fe intermetallic and eutectic Al phases.

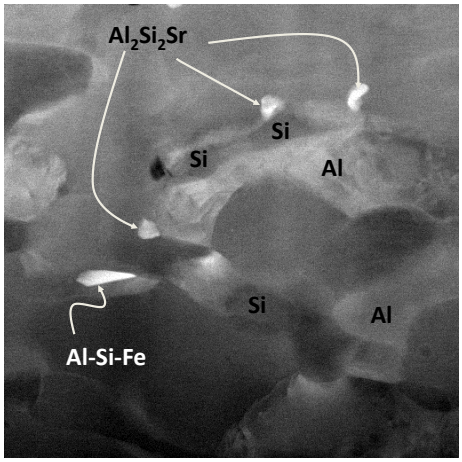

Figure 7-13: Typical STEM bright field image of Al 7Si 0.05Fe 0.02 Sr alloy showing the eutectic region with the Al_2Si_2Sr, Al-Si-Fe intermetallic, Si and Al phases. The identity of the phases was confirmed by EDX analyses.

7.4 DISCUSSION

The addition of trace levels of 0.02Sr to the Al-xSi-yFe (x=2 to 12.5 and y=0 to 0.5) alloys significantly alters the identity of the intermetallic phases that evolve during the solidification process. In CHAPTER 6, it was shown that there is an anomalous evolution of the θ and τ_5 phases followed by the τ_6 depending on the cooling rate during solidification and the concentration of the Fe in the Al-xSi-yFe (x=2 to 12.5 and y=0 to 0.5) alloys. When Sr was added to these alloys, the θ and τ_5 phases did not evolve at any cooling rate or Fe level; however, a new κ phase evolved instead which further transformed into the τ_6 phase depending on the cooling rate and Fe concentration in the alloy. In spite of rigorous analyses to characterize the κ phase, its structure still remains unknown. It is evident from the low magnification microstructure images there is a significant difference in the size, morphology and distribution of the intermetallic phases evolving during solidification of the Al-Si-Fe alloys with and without Sr, respectively.

A plausible hypothesis could not be conceived at this stage to explain the anomalous evolution of the κ phase in the Al-Si-Fe-Sr alloys. However, there are evidences to show that trace levels of Sr addition to these alloys act as potent surfactant. In the recent publication and doctoral dissertation by Srirangam et al [91, 141] it was shown that trace additions of Sr to the Al-xSi (x=0 to 12.5) alloys significantly altered the atomic arrangements of the Si atoms in the liquid by preventing the formation of the Si clusters in the liquid state and hence, delaying the nucleation event of the eutectic Si phases. Further, as mentioned in the Section 6.7, in the Al-Si alloy system, Wang et al [138] and Yurkevich [139], have emphatically shown that there is anomalous increase in the density of the Al-Si alloys due to the clustering and the resultant micro-inhomogeneity of the Si atoms in the liquid alloy. Wang et al [138] showed the anomalous behaviour in hypereutectic alloys with greater than 12.5 wt% Si and Yurkevich [139] in alloys with 0.2 to 1.2 wt% Si in them. From these information in the prior art, we may conclude that there is anomalous clustering of both the Fe and Si atoms, individually in the Al-Si-Fe alloys without Sr and the addition of Sr breaks these clusters and tends to homogenize the Si atoms in the liquid [91, 141] which could lead to the possibility that Sr also has a similar effect on the Fe atoms by altering the typical clustering of 15 ± 7 Al atoms around each Fe atoms in alloys with Sr .

Further, Kanibolotski et al [118] mentioned that thermodynamics of Al-Si-Fe system is primarily governed by the Si-Fe interaction. Turnbull [134] mentioned that clustering effects on partial molar volume would be much stronger in Si-Fe system compared to the Al-Fe system due to stronger interaction between the Si and Fe atom pairs. There is no experimental data describing clusters and liquid structure in Al-Si-Fe system reported, as yet, however, from the information on the significant effect of Sr on the clusters of the Si-Si, Al-Fe and Fe-Si atom pairs in the respective binary alloy systems, it could be safely conjectured that there could be a similar effect on the atom clusters occurring in the Al-Si-Fe ternary system as well. Such an effect will lead to formation of alternate intermetallic phases during solidification as observed in this

project. The fact that the θ and τ_5 phases are prevented from evolving during solidification by the addition of Sr seems to suggest that there is a significant altering of the anomalous atom clusters in the liquid which may lead to an alternate solidification path leading to the evolution of the κ phase. Additionally, the κ phase evolution is an anomaly to the thermodynamic model predictions and it transforms in to the terminal and stable τ_6 phase at slower cooling rates during solidification and higher Fe concentration in the alloy, alike.

Extensive experiments are required in evaluating the clustering tendencies of the atoms in the Al-Si-Fe alloys with and without Sr to verify the hypotheses presented in this dissertation; diffraction experiments of liquid alloys and evaluation of physical properties such as viscosity, diffusion coefficient of atoms in the liquid, and thermal expansion behaviour of these alloys are typical research topics that would have to be explored.

CHAPTER 8. CONCLUSIONS

The results of this project were beyond our expectations from the start of this project. The evolution of Al-Fe-Si intermetallic phases in the Al-xSi-yFe (x=2 to 12.5 and y=0 to 0.5) alloys with and without 0.02Sr is anomalous to conventional wisdom. A detailed scheme of the observed intermetallic phases as a function of the cooling rate during solidification and Fe concentration in the alloy is presented at the beginning of both CHAPTER 6 and CHAPTER 7 of this dissertation for the Al-Si-Fe alloys without and with Sr addition, respectively.

- In the Al-xSi-yFe (x=2 to 12.5 and y=0 to 0.5) alloys:
  - During the solidification of the Al-xSi-yFe (x=2 to 12.5 and y=0 to 0.5) alloys, there is an anomalous evolution of the θ-$Al_{13}Fe_4$ phase at the interface of the primary Al and liquid.
  - The θ phase transforms into the τ_5 -Al_8Fe_2Si phase during solidification through a peritectic reaction: Liquid + θ → τ_5 + (Al). The kinetics of this reaction is fairly rapid because the atom per unit volume of Fe in the θ phase is $1.61E^{-2}$ atoms/$Å^3$ and that for the τ_5 phase is 1.76 E^{-2} atoms/$Å^3$ which is a small difference. Further, the Fe atoms will have to diffuse into the θ phase from the liquid to effect the peritectic reaction.
  - The τ_5 phase grows in the liquid during solidification and transforms to the τ_6-$Al_9Fe_2Si_2$ phase through another peritectic reaction: Liquid + τ_5 → τ_6 + (Al). This peritectic reaction is sluggish because the atom per unit volume of Fe in the τ_5 phase is 1.76 E^{-2} atoms/$Å^3$ and that for the τ_6 phase is 0.938 E^{-2} atoms/$Å^3$ which is a significant difference; the Fe atoms will have to diffuse out of the τ_5 phase and react with the liquid at the surface area of the phase to effect the peritectic reaction.
  - The τ_6 phase also evolves in the eutectic reaction along with the eutectic phases.
  - The crystal structure of the θ, τ_5 and τ_6 phases were evaluated as being monoclinic, hexagonal and monoclinic, respectively.
  - The respective morphologies of the τ_5 and τ_6 phases are Chinese script and acicular in 2-dimension space. The τ_6 phase morphology is plates in a 3-dimension space.
  - Microstructural evidences suggest that the eutectic Si phase nucleates on both the τ_5 and τ_6 phases, alike.

- In the Al-xSi-yFe-0.02Sr (x=2 to 12.5 and y=0 to 0.5) alloys:
  - The evolution of the θ and τ_5 phases is prevented during solidification and instead, there is the evolution of a new phase which has been noted as κ-$Al_5Fe_2Si_3$ in this dissertation.
  - There is no compositional change in Al-Fe phases in Al-Fe-Sr alloys comparing to Al-Fe alloys
  - The κ phase evolves at the interface of the solidifying primary Al phase and liquid, and subsequently transforms into the τ_6 phase at slower cooling rates during solidification and higher Fe concentration in the alloy, alike.

- The τ_6 phase also evolves in the eutectic reaction along with the other eutectic phases.
- The morphology of the κ phase is acicular in the 2-diemensional space.
- There is no microstructural evidence of nucleation of the eutectic Si phase on the κ or the τ_6 phases.
- Liquid structure and clusters in the liquid can play phase determining role during alloy solidification.

CHAPTER 9. RECOMMENDATIONS FOR FUTURE WORK

The results of this project show several anomalies in the evolution of the Fe containing intermetallic phases in the Al-Si-Fe alloys. The hypotheses presented in this dissertation will have to be validated with sufficient experimental evidences.

The following are some of the salient suggestions for the future work stemming from this project:

- A thorough understanding of the liquid structure of the Al-xSi-yFe-zSr (x=2 to 12.5, y=0 to 0.5 and z=0 to 0.04) alloys through diffraction experiments using the neutron and synchrotron beam sources. Critical analyses should focus on any anomalous behaviour in the clustering tendencies of the elements in the liquid state.
- Evaluation of the crystal structure of the κ-$Al_5Fe_2Si_3$ phase in the Al-Si-Fe alloys with Sr addition in them.

CHAPTER 10. REFERENCES

1 Davis JR. Aluminum and Aluminum Alloys. Materials Park, OH, USA: ASM International; 1993.
2 Stevens RH, editor. Aluminum Alloys. Materials Park, OH, USA: ASM International; 1985.
3 Hatch JE, editor. Aluminium. Properties and Physical Metallurgy. Metals Park, Ohio: ASM International; 1984.
4 Ye H, Journal of materials engineering and performance 2003;12:288.
5 Donahue R, Fabiyi P. Society of Automotive Engineers 2000.
6 Miller W, Zhuang L, Bottema J, Wittebrood AJ, De Smet P, Haszler A, Vieregge A. Materials Science and Engineering 2000;280:37.
7 http://www.autoblog.com/2012/04/26/2013-ford-shelby-gt500-certified-at-662-hp-and-630-pound-feet/
8 http://www.army-technology.com/projects/bradley/
9 Campbell FC, Manufacturing Technology for Aerospace Structural Materials. Elsevier Ltd; 2006.
10 http://www.cessna.com/single-engine/skycatcher/skycatcher-exterior.html
11 Mazzolani FM. Aluminium Alloy Structures. Taylor & Francis; 1995.
12 Mega T, Hasegawa K, Kawabe H, JFE Giho 2004;4.
13 Hirsch J, Bassan D, Lahaye C. Materials Transactions 2011:101.
14 Shankar S, Riddle YW, Makhlouf MM. Acta Materialia 2004;52:4447.
15 Shankar S, Riddle YW, Makhlouf MM. Metallurgical and Materials Transactions A 2004;35:3038.
16 Mondolfo LF. Aluminum Alloys : Structure and Properties. London, UK: , Butterworths and Co Ltd; 1976.
17 [1] Shankar S, Makhlouf MM, Riddle YW. AFS Transactions 2005;088.
18 The Aluminum Association 1525 Wilson Blvd, Arlington, VA 22209, USA
19 ANSI H35.1/H35.1M “American National Standard Alloy & Temper Designation Systems for Aluminum”, 2009 American National Standards Institute
20 Registration record of aluminum association alloy designations and chemical composition limits for aluminum alloys in the form of castings and ingot, The Aluminum Association publications 2009
21 International Alloy Designations and Chemical Composition Limits for Wrought Aluminum and Wrought Aluminum Alloys ,The Aluminum Association publications 2009
22 Fraenkel W. Z Anorg Chem 1908;Vol. 58:154.
23 Murray J., McAlister AJ. Journal of Phase Equilibria 1984;5:74.
24 Rivlin V, Raynor GV. International Metals Reviews 1981;3:133.
25 Dahle AK, Nogita K, McDonald SD, Dinnis C, Lu L. Materials Science and Engineering: A 2005;413-414:243.
26 Pacz A. No Title. U.S. Patent 1387900, 1921.

27 Hanna M, Lu S. Metallurgical and Materials Transactions 1984;15:459.
28 Timpel M, Wanderka N, Schlesiger R, Yamamoto T, Lazarev N, Isheim D, Schmitz G, Matsumura S, Banhart J. Acta Materialia 2012;60:3920.
29 Day MG, Hellawell A. Proceedings of the Royal Society A: Mathematical, Physical and Engineering Sciences 1968;305:473.
30 Makhlouf M, Guthy HV. Journal of Light Metals 2001;1:199.
31 Qiyang L, Qingchun L, Qifu L. Acta metallurgica et materialia 1991;39:2497.
32 Lu L, Nogita K, Dahle a. K. Materials Science and Engineering: A 2005;399:244.
33 Knuutinen A, Nogita K, McDonald S, Dahle AK. Journal of Light Metals 2001;1:229.
34 Hegde S, Prabhu KN, Journal of Materials Science 2008;43:3009.
35 Cantor B, Materials Science and Engineering: A 1997:151.
36 Cao X, Campbell J. Metallurgical and Materials Transactions A 2004;35:1425.
37 Nogita K, McDonald SD, Tsujimoto K, Yasuda K, Dahle AK. Journal of electron microscopy 2004;53:361.
38 Jürgen Hirsch, Günter Gottstein BS, editor. Aluminium Alloys: Their Physical and Mechanical Properties, first ed. Wiley-VCH; 2008.
39 Addamiano A. Journal of the American Chemical Society 1960;100:1958.
40 Swanson H, Fuyat R, Ugrinic G, Gilfrich N. 1976.
41 Li J, Zarif M, Peter S. BHM Berg-und Hüttenmännische Monatshefte 2010;155:499–505.
42 Takeda S MK. Tetsu to Hagane 1940;26:335– 61.
43 Pontevichi S, Bosselet F, Barbeau F, Peronnet M, Viala JC. Journal of Phase Equilibria & Diffusion 2004;25:528.
44 Kral MV. Materials Letters 2005;59:2271.
45 Kim BH, Lee SM, Yasuda H. Materials Science Forum 2010;654-656:974.
46 Lu L, Dahle AK. Metallurgical and Materials Transactions A 2005;36:819.
47 Armand M. Revue de l'Aluminium 1954;1:305.
48 Kral M, McIntyre HR, Smillie MJ. Scripta Materialia 2004;51:215.
49 Heath AC, Dix EH. TransAIME 1928;78:164.
50 Han YS, Choi JO, Choi CO, McCartney DG. Metals and Materials International 2004;10:27.
51 Kral MV, Nakashima PNH, Mitchell DRG. Metallurgical and Materials Transactions A 2006;37:1987.
52 Mulazimoglu MH, Zaluska A, Gruzleski JE, Paray F. Metallurgical and Materials Transactions A 1996;27:929.
53 Liu P, DUNLOP GL. Acta Metallurgica 1988;36:1481.
54 Munson D. J Inst Met 1967;95:217.
55 Westengen H. Zeitschrift fur Metallkunde 1982;73:360.
56 Skjerpe PER. METALLURGICAL TRANSACTIONS A 1987;18A:189.
57 Cooper M, Robinson K. Acta Crystallographica 1966;20:614.
58 Cooper M. Acta Crystallographica 1967;23:1106.
59 Li Y, Yang Y, Wu Y, Wei Z, Liu X. Materials Science and Engineering: A 2011;528:4427.
60 Dinnis C, Taylor J, Dahle a. Scripta Materialia 2005;53:955.
61 Griger A, Stefaniay V. Journal of materials science 1996;31:6645–6652.

62 Kim H, Park T, Han S, Lee H. Journal of Crystal Growth 2006;291:207.
63 Cheng W-J, Wang C-J. Applied Surface Science 2011;257:4637.
64 Gustafsson G, Thorvaldsson T, Dunlop GL. Metallurgical Transactions 1986;17:45.
65 Warmuzek M, Gazda A. J Anal At Spectrom 1999;14:535–537.
66 Zheng JG, Vincent R., Steeds JW. PHILOSOPHICAL MAGAZINAE 2000;80:493.
67 Stefaniay V, Griger A, Turmezey T. Journal of Materials science 1987;22:539.
68 Gupta S. Materials Characterization 2002;49:269.
69 Maitra T, Gupta S. Materials Characterization 2002;49:293.
70 Raghavan V. Journal of Phase Equilibria 2002;23:362.
71 Corby R, Black P. Acta Crystallographica Section B: Structural 1977;33:3468.
72 Yanson TI, Manyako MB, Bodak OI, German NV, Zarechnyuk OS, Cerný R, Pacheco JV, Yvon K. Acta Crystallographica Section C Crystal Structure Communications 1996;52:2964.
73 German NV, Zavodnik VE, Yanson TI, Zarechnyuk OS. Sov Phys Crystallogr 1989;34:439.
74 Schubert K, Panday PK. J Less-Common Met 1969;18:175.
75 Gueneau C, Servant C, d' Yvoire F, Rodier N. Acta Crystallographica Section C Crystal Structure Communications 1995;51:2461.
76 Rømming C, Hansen V, Gjønnes J. Acta Crystallographica Section B Structural Science 1994;50:307.
77 Yanson TI, Manyako MB, Bodak OI, German NV, Zarechnyuk OS, Cerný R, Pacheco JV, Yvon K. Acta Crystallographica Section C Crystal Structure Communications 1996;52:2964.
78 N.V. German, V.K. Bel'skii, T.I. Yanson and OSZ. Sov Phys Crystallogr 1989;34:437.
79 Iglessis J., Frantz C, Gantois M. Memoires Scientifique de la Revue de Metallurgie 1977;73:237.
80 Liu Z-K, Chang YA. Metallurgical and Materials Transactions A 1999;30:1081.
81 Krendelsberger N, Weitzer F, Schuster JC. Metallurgical and Materials Transactions A 2007;38:1681.
82 Du Y, Schuster J, Liu Z, Hu R, Nash P, Sun W, Zhang W, Wang J, Zhang L, Tang C. Intermetallics 2008;16:554.
83 Bosselet F, Pontevichi S, Sacerdote-Peronnet M, Viala JC. J Phys IV France 2004;122:41.
84 Roger J, Bosselet F. Journal of Solid State Chemistry 2011;184:1120.
85 Young RMK, Clyne TW. Scripta Metallurgica 1981;15:1211.
86 Awano Y, Shimizu Y. AFS Transactions 1990;98:889.
87 Edwards JD, Archer RS. Chem Met Eng 1924;31:504.
88 Djurdjevic M, Jiang H, Sokolowski J. Materials Characterization 2001;46:31.
89 Chen X, Geng H, Li Y. Materials Science and Engineering: A 2006;419:283.
90 Shabestari S, Ghodrat S. Materials Science and Engineering: A 2007;467:150.
91 Srirangam P, Kramer MJ, Shankar S. Acta Materialia 2011;59:503.
92 Satyapal, H. Prabhum, N. J Mater Sci 2008;43(9):3009.
93 Cho YH, Lee H-C, Oh KH, Dahle AK. Met Mater Trans A2008;39A:2435.
94 G.Sigworth, Int J Met Cast 2008;2(2):19.
95 Sigworth G, Jorstad J, Campbell J. AFS International Journal of Metalcasting Correspondence 2009;3:65.

96 Gayler, MLV. J Inst Met 1927;39:157
97 Gwyer, AGC. J Inst Met 1927;39:184.
98 Rosenhain, W. J. Inst Met 1927;39:184
99 Rothery, H. J Inst Met 1927;39:190.
100 Gayler, MLV. J Inst Met 1927;39:192.
101 Hillert M. Metallurgical and Materials Transactions A 2003;32:1..
102 Thall, B.M. Chalmers, B. J. Inst. Met. 78 (1949) 79.
103 Xiufang B, Weimin W, Shujuan Y, Jingyu Q. Science and Technology of Advanced Materials 2001;19:2.
104 Malik, MM. MASc. Dissertation. McMaster University; 2008.
105 Lu S, Hellawell A. Met Trans 1987;18a:1721.
106 Plumb RC, Lewis JE. J Inst Met 1957;86:393.
107 Simensen CJ, Nielsen Ø, Hillion F, Voje J. Metallurgical and Materials Transactions A 2007;38:1448.
108 Samuel FH, Samuel a. M, Doty HW, Valtierra S. Metallurgical and Materials Transactions A 2001;32:2061.
109 Campbell X, Cao J. Materials Science and Technology 2004;20:514.
110 Sreejakumari S, Pillai R, Rajan T, Pai B. Materials Science and Engineering: A 2007;460-461:561.
111 Eidhed W. J Mater Sci Technol 2008;24:45.
112 Egelstaff, P.A. Advances in Physics, 1962,v.11, p. 203
113 S.R. Elliott, Nature 354 (1991) 445–452
114 Xiufang B, Minhua S, Xianying X, Xubuo Q. Materials Letters 2003;57:2001.
115 Il'inskii A, Slyusarenko S, Slukhovskii O, Kaban I, Hoyer W. Materials Science and Engineering: A 2002;325:98.
116 Il'inskii A, Slyusarenko S, Slukhovskii O, Kaban I, Hoyer W. Journal of Non-Crystalline Solids 2002;306:90.
117 Li H, Wang G, Ding F, Wang J, Shen W. Physics Letters A 2001;280:325.
118 Kanibolotsky D., Bieloborodova O., Kotova N., Lisnyak V. Thermochimica Acta 2003;408:1.
119 Du Y, Changb Y., Huanga B, Gonga W, Jina Z, Xua H, Yuana Z, Liua Y, Hea Y, Xiec F. Materials Science and Engineering A 2003;363:140.
120 Bian XF, Qin JY, Wang WM, Qi XG. Materials Science Forum 2000;331-337:343.
121 Jing-Xiang Z, Hui L, Jie Z. Chinese Physics … 2009;18:4949.
122 Tanaka H. Journal of Physics: Condensed Matter 2003;15:491.
123 Chen Z, Ma C, Chen P. International Journal of Minerals, Metallurgy, and Materials 2012;19:131.
124 Wang, H, PhD Dissertation, McMaster University, 2009.
125 Kaufman, L and Bernstein, H. "Computer Calculation of Phase Diagram," New York: Academic Press Inc, 1970.
126 Gupta A, Marois P, Lloyd D. Materials characterization 1996;37:61–80.
127 Xiao Y, Cai Z, Lai B. Nanotechnology 2005;16:1754.

128 Swanson H, Fuyat R, Ugrinic G, Gilfrich N. 1976.
129 Grin J, Burkhardt U, Ellner M. Zeitschrift für Kristallographie 1994:479.
130 Nowotny, Wesenberg., ZEMTAE, 31, p363 (1939)
131 Visser, J., Technisch Physische Dienst, Delft, Netherlands, ICDD Grant-in-Aid, (1984)
132 Gebhardt, E. Becker, M. and Donner, S. Z. Metallkd., 1953, vol. 44, p. 510.
133 Gebhardt, E. Becker, M. and Donner, S. Z Metallkd., 1953, vol. 44, p. 573.
134 Turnbull D. Acta Metallurgica et Materialia 1990;38:243.
135 Isono N, Smith P., Turnbull D, Aziz MJ. Metallurgical and Materials … 1996;27:725.
136 Ejima T., Yamamura T., Uchida N., Mastuzaki Y., and Nikaido M.: 3. Jpn. Inst. Met., 1980, v. 44, p. 316.
137 Ejima T.and Yamamura T.: J. Phys., 1980, vol. C8, p. 345.
138 Wang W, Bian X, Wang H. Journal of Materials Research 2001;16:3595.
139 Yurkevich N. Inorganic materials 2002;38:243.
140 Nicholas R., Pflug IJ, Mulvaney TR. Food technology 1960;14:205.
141 Srirangam P., PhD Dissertation, McMaster University, 2011.

APPENDIX A. ALLOY COMPOSITION AND THERMAL CURVES

This appendix presents the measured alloy compositions used in this study along with examples of thermal curves acquired during alloy solidification.

A.1. Alloy Compositions

Table A- 1: Typical elemental compositions of the alloys in this study as measured by the Glow Discharge Optical Emission Spectroscopy (GDOES). The targeted compositions are all in weight percentages. Al-x7Si-0.25Fe alloys

Alloy Notation	Al	Si	Fe
Al-2Si-0.25Fe	96.61	3.01	0.3
Al-4Si-0.25Fe	94.89	4.7	0.33
Al-5Si-0.25Fe	94.12	5.48	0.32
Al-7Si-0.25Fe	92.05	7.56	0.31
Al-9Si-0.25Fe	89.95	9.65	0.31
Al-11.5Si-0.25Fe	87.38	12.26	0.31
Al-12.5Si-0.25Fe	86.64	13.01	0.29
Al-7Si-0.05Fe	91.924	7.909	0.097
Al-7Si-0.5Fe	92.27	7.13	0.554

Table A- 2: Typical elemental compositions of the alloys in this study as measured by the Glow Discharge Optical Emission Spectroscopy (GDOES). The targeted compositions are all in weight percentages.Al-7Si-yFe-0.02 Sr alloys

Alloy Notation	Al	Si	Fe	Sr
Al-7Si-0.05Fe-0.02Sr	92.70	7.19	0.05	0.02
Al-7Si-0.25Fe-0.02Sr	92.24	7.45	0.27	0.02
Al-7Si-0.5Fe-0.02Sr	91.51	7.94	0.49	0.03

A.2. Thermal curves

Temperature data acquired during solidification of the alloys will be presented in subsection below. Examples of thermal curves for each cooling rate are presented in section below:

A.2.1 Thermal Curve From Solidification of Al-7Si-0.25Fe alloy at 0.8Ks^{-1}

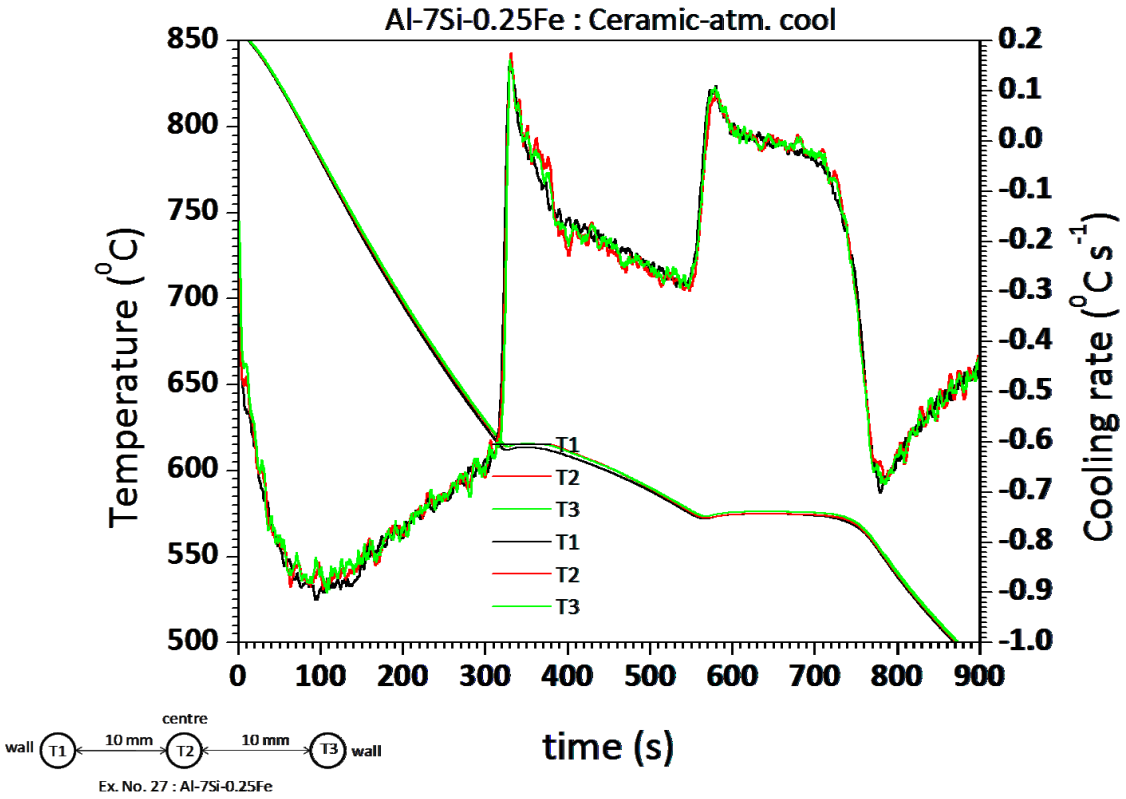

A.2.2 THERMAL CURVE FROM SOLIDIFICATION OF Al-7Si-0.25Fe ALLOY AT 5Ks^{-1}

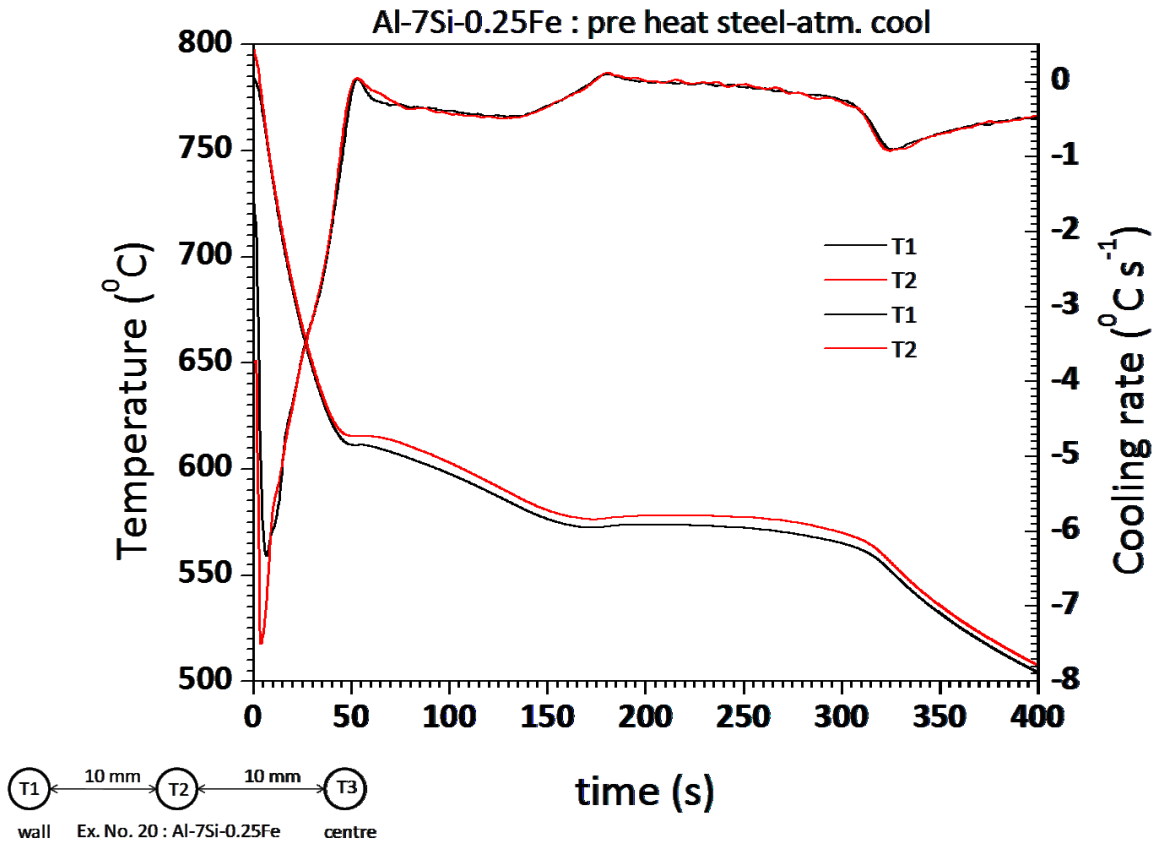

A.2.3 THERMAL CURVE FROM SOLIDIFICATION OF Al-7Si-0.25Fe ALLOY AT 50Ks^{-1}